UNIVERSITY OF SOUTHAMPTON

DEPARTMENT OF ELECTRONICS

TIME-DOMAIN REFLECTOMETRY TECHNIQUES FOR OPTICAL COMMUNICATIONS

BY

ALLEN JAMES CONDUIT

A thesis submitted for the degree of

Doctor of Philosophy

January 1982

UNIVERSITY OF SOUTHAMPTON

ABSTRACT

FACULTY OF ENGINEERING & APPLIED SCIENCE

ELECTRONICS

Doctor of Philosophy

TIME-DOMAIN REFLECTOMETRY TECHNIQUES FOR OPTICAL COMMUNICATIONS

Time Domain Reflectometry Techniques are applied to measurements in optical fibres. The study covers broadly two areas of interest.

Firstly, the Backscatter Technique for attenuation measurements is considered. The resolution requirements of instrumentation are studied and a new 2-channel approach to backscatter waveform analysis is proposed. An optimum operating strategy is described such that the sensitivity and range are maximized. The fundamental accuracy of the backscatter measurement is determined by a comparison with the more-standard cutback technique over a wide spectral range and variations in OH^- impurity along the length of a fibre are tracked by measurements at different wavelengths. The effects on the backscattered power of variations in longitudinal fibre parameters are also demonstrated. In particular, backscatter-loss signatures are presented which clearly show correlation with programmed fibre defects and indicate that in many cases diameter variations are the cause of the previously unidentified features in some back-scatter waveforms. In addition, the backscatter method is used for the first time to track the state of polarization of a pulse propagating in a monomode fibre.

The second application of Time Domain Reflectometry is to the assessment of pulse delay stability against variations in temperature and external stresses. Data from measurements on unjacketed fibres is used to analyse the time delay variations found in jacketed fibres. It is shown that the application of a close-fitting plastic jacket results in a level of residual compressive stress in the fibre and the delay stability is considerably degraded. This may also be influenced by environmental factors.

ACKNOWLEDGEMENTS

I would like to sincerely thank Professor Gambling and the members of the Optical Communications group for the warm welcome which was afforded me as a visitor to the U.K. and I am grateful for the support and encouragement received throughout the course of my studies.

I would especially like to thank Dave Payne for the many discussions, suggestions and constructive criticisms of the work. Also to Arthur Hartog with whom I shared measurements with the dye-laser system and the experiment on pulse delay stability. Arthur's contribution is very much appreciated. Many thanks are due also to John Hullett from the University of Western Australia for his collaboration in early work on instrument limitations.

Thanks also to Francis Sladen, Steve Norman, Bob Mansfield, Max Hadley and Eleanor Tarbox for the many discussions and/or their efforts in fabricating fibres for these experiments.

I am grateful to Jan Ditchfield and Nicky Pink for their many pages of typing and to Chris Nash for his immaculate draughting. I also wish to thank Roy Came and the mechanical workshop staff for their advice and craftmanship.

I wish to acknowledge the support of my parents and family over many years. Special thanks are due to Sheila for her help and encouragement (and most of all for just being there!).

Finally I am grateful to the British Council and the Association of Commonwealth Universities for the scholarship which made possible my postgraduate studies in the U.K. and also to Telecom Australia for their financial assistance.

CONTENTS

		page no.
Chapter 1	Introduction	1
1.1	The Backscatter Technique	2
1.2	Pulse Delay Measurements	4
1.3	Notes on General Layout of Thesis	4
Chapter 2	Theoretical Background of the Backscatter Technique	6
2.1	Loss Mechanisms in Optical Fibres	7
	2.1.1 Absorption	7
	2.1.2 Radiation	8
2.2	Rayleigh Scattering	8
	2.2.1 Rayleigh attenuation	10
	2.2.2 Origin of refractive index fluctuations	11
	2.2.3 Rayleigh radiation pattern	12
2.3	Differential Mode Attenuation (DMA) and the Equilibrium Mode Distribution (EMD)	13
2.4	The Backscatter Characteristic	14
	2.4.1 Impulse response	14
	2.4.2 Response to finite input pulse	16
	2.4.3 Relative backscatter power	17
2.5	Determination of Local Fibre Attenuation	17
2.6	Determination of Loss at a Fault Point	19
2.7	The Backscatter Factor for Multimode Fibres	20
	2.7.1 Approximation	20
	2.7.2 Generalization	21
	2.7.3 Assignment of typical radial characteristics to fibre parameters	21
	2.7.3.1 Core grading	22
	2.7.3.2 Modal energy distribution	22
	2.7.3.3 Local numerical aperture	23
	2.7.3.4 Average scattering loss	23
	2.7.4 Backscatter factor for power law profiles	24
2.8	Errors in Attenuation Measurement Caused by Variations in the Backscatter Factor	25
	2.8.1 Dependence on NA and scattering loss for germano-silicate fibres	25
	2.8.2 Long wavelength measurements	26
	2.8.3 Effect of non-linear scattering mechanisms	26
2.9	Summary	27
Figures 2.1-2.4		
Chapter 3	Theory of Measurement Limitations and the Ultimate Range	28
3.1	Single Channel Sampling, Boxcar Integration and Numerical Averaging	28
3.2	Two Channel Sampling	30
3.3	The Optimum Operating Strategy and Measurement Accuracy Requirements	32
	3.3.1 The attenuation measurement error	32
	3.3.2 Optimum sample separation	33
	3.3.3 Dynamic range utilization	34
	3.3.4 Penalties for non-optimal operation	35
3.4	Timing Sensitivity	36

page no.

3.5 Bandwidth Requirements and Distance Resolution 37
3.5.1 Bandwidth for local attenuation measurement 37
3.5.2 Bandwidth for fault location 37
3.5.3 The minimum distance resolution 38

3.6 Noise Averaging 39
3.7 Effects of Noise Clipping 40
3.8 Non-Linearities 42
3.9 Range Performance 45
3.9.1 The decay in signal-to-noise ratio 45
3.9.2 Design example 46
3.9.2.1 Limits to range 47
3.9.2.2 Range at optimum sample separation 48
3.9.2.3 Extension of range 49
3.10 Measurement Time 49
3.11 Multi-Channel Sampling 50
3.11.1 Maximum span (T_{max}) 51
3.11.2 Range for m-channel sampling 52
3.12 Fault Location 53
3.13 Extension to Long Wavelengths 54
3.14 Summary 55

Table 3.I
Figures 3.1-3.14

Chapter 4 A 2-Channel Implementation with Boxcar Averaging and a Dye-Laser 57
4.1 Basic Experimental Arrangement 57
4.2 Dye-Laser and Optical-Parametric-Oscillator (OPO) 58
4.2.1 Dye-laser 58
4.2.2 Optical-parametric-oscillator (OPO) 59
4.3 Pulse Slicing 59
4.4 Optical Pedestal 60
4.5 Anti-Reflection Cell 60
4.6 Mode-Scrambler 62
4.7 Amplifier 62
4.8 2-Channel Sampling with Boxcar Integrators 64
4.8.1 Aperture duration 65
4.8.2 Analogue averaging 65
4.8.3 Digital averaging 66
4.9 Alignment of a 2-Channel Boxcar System 66
4.9.1 Gain correction 66
4.9.2 Offset compensation 67
4.9.3 Gate triggering 68
4.9.4 Gate non-linearity 68
4.10 Spark-Gap Instabilities and Electrical Interference 68
4.11 Computer Control 69
4.12 Summary 71

Figures 4.1-4.6

page no.

Chapter 5 A 2-Channel Implementation with Fast Sample-Holds, Fast Analogue-Digital Converters and a Semiconductor Laser 73

5.1 Basic Experimental Arrangement 73
5.2 Pulse Laser 74
5.3 Launching and Reception Optics 74
5.4 Amplifier 75
5.4.1 Pre-amplifier 75
5.4.2 Automatic gain control 75
5.5 Computer Interfacing 76
5.6 Sampling System 76
5.6.1 Linearity of sampling system 77
5.6.2 Dynamic performance of sampling system 77
5.7 Computer Control 78
5.7.1 Number of samples 79
5.7.2 Dynamic range utilization 79
5.8 Summary 79

Figures 5.1-5.10

Chapter 6 Cutback Method for Spectral Loss Measurements 81

6.1 Experimental Arrangement 81
6.2 Confidence of Measurement 82
6.3 Measurements on a Plastic-Clad Silica Fibre (PCS) 83
6.3.1 Microbending losses 83
6.3.2 Launch dependent losses 84
6.4 Measurements on a MCVD Fibre 84
6.4.1 Effect of the 'short length' 85
6.4.2 Effect of drift 86
6.5 Summary 86

Figures 6.1-6.4

Chapter 7 Spectral Backscatter Attenuation Measurements and a Comparison with the More-Standard Cutback Method 88

7.1 Fabrication Details of Fibre VD277/L 88
7.1.1 Refractive index profile 89
7.1.2 Diameter control details 89
7.2 Length-Dependent Loss of VD277/L at 1.0 μm 90
7.3 Effect of Launching Conditions on the Backscatter Method 91
7.4 Backscatter Spectral Measurements on Fibre VD277/L 92
7.4.1 Attenuation of the section 500-1500 m 92
7.4.2 Attenuation of the sections 500-1000 m and 1000-1500 m 93
7.5 Evolution of OH^- Along the Length of Fibre VD277/L 94
7.5.1 Steroscan studies of B_2O_3/SiO_2 buffer-layer 95
7.5.2 Thermal history 96
7.6 Absolute Accuracy of the Backscatter Technique by a Cutback Comparison 97
7.6.1 Formulation of a method for comparison 97
7.6.2 Spectral comparison number 1 98
7.6.3 Spectral comparison number 2 99
7.7 Summary 100

Figures 7.1-7.9

page no.

Chapter 8 Interpretation of Features in Backscatter Waveforms 102

8.1 Fluctuations in Length-Dependent Loss 102
8.1.1 Correlated features 103
8.1.2 Scatter centres 103
8.1.3 Anti-correlated features 103
8.1.3.1 Origin of variations in numerical aperture 105
8.1.3.2 Origin of variations in diameter 105
8.2 Effect of Programmed Diameter Changes in Fibre VD277/L 106
8.2.1 Programmed diameter profile 106
8.2.2 Identification of backscatter features and correlation with programmed defects 107
8.2.3 Single-channel measurements 108
8.2.4 High resolution measurements 109
8.3 Modelling the Effect of Diameter Variations 111
8.3.1 Expanding taper 111
8.3.2 Contracting taper with differential mode attenuation (DMA) 112
8.3.3 Contracting taper with cladding effect 113
8.3.4 Computer simulation 114
8.3.4.1 Effect of step changes in fibre diameter 115
8.3.4.2 Effect of cladding loss 116
8.3.4.3 Effect of taper slope 116
8.4 Comparison of Model and Experimental Results 117
8.4.1 Magnitude of features 118
8.4.2 Effect of DMA on contracting tapers 119
8.4.3 Verification of coupling from cladding modes 120
8.4.4 Effect of taper slope 122
8.5 Oscillatory Diameter Variations 122
8.6 Length-Dependent Measurement of Microbending Loss 123
8.7 Summary 124

Figures 8.1-8.22

Chapter 9 Variation of Pulse Delay with Stress and Temperature in Jacketed and Unjacketed Optical Fibres 127

9.1 Theory 128
9.2 Experimental Procedure 129
9.3 Experimental Results 131
9.3.1 Effect of applied tension on unjacketed fibres 131
9.3.2 Effect of temperature on unjacketed fibres 133
9.3.3 Residual fibre stress introduced by jacketing with Nylon 6 133
9.3.4 Delay stability in jacketed fibres 134
9.3.5 Effect of water ingress on jacketed fibres 136
9.4 Summary 138

Tables 9.I-9.II
Figures 9.1-9.6

page no.

Chapter 10 Conclusion 140

10.1 The Backscatter Technique 140
10.1.1 Optimization of measurement 140
10.1.2 Developments in instrumentation 141
10.1.3 Accuracy of the method 142
10.1.4 Analysis of backscatter loss signatures 142
10.1.5 Single mode measurements 143
10.1.6 Current status and future prospects for the backscatter technique 144
10.2 Pulse Delay Measurements 145
10.3 Closing Remark 146

Appendix I Measurement Errors Due to Noise Clipping 147

Appendix II Computer Simulation of Expanding Fibre Section 150

Appendix III Computer Simulation of Contracting Fibre Section 151

Table III.1

Appendix IV Backscatter Measurements in Single Mode Fibres 153

Figures 1-3

Appendix V Stress-Optical Effect 157

V.1 Stress Optical Effect in Bulk Glass 157
V.2 Stress Optical Effect in Glass Fibres 159

Figure V.1

Appendix VI Publications, Conference Papers and Exhibitions 160

Appendix VII References 162

CHAPTER 1

INTRODUCTION

The technology of sources, detectors and multimode fibres for operation in the wavelength region 0.8-0.9 μm has matured sufficiently for optical communications to gain acceptance and assure its commercial exploitation[166]. Low losses, high bandwidths, small size and immunity to electro-magnetic interference are particular advantages of the optical fibre.

Currently, the introduction of fibres is on a small scale and is mainly in high capacity trunk telephony and video circuits where their presence is largely transparent to the subscriber[167]. However, the potential of fibres is to provide a wide range of new services at the subscriber level[168] and this prospect presents an exciting challenge from both technological and sociological viewpoints. The rate of introduction of fibres for telecommunications will depend on economics and to a large extent on demand for digital services and any moves towards all-digital networks. It is expected that costs will decrease dramatically as production quantities increase.

In parallel with the developments in fibre fabrication have been developments in measurement techniques[169]. Now, with the move towards mass production and field applications of fibres, laboratory measurement techniques must be adapted to the factory and field environment and in some cases new and more suitable practices developed.

This thesis considers a measurement technique called Optical Time Domain Reflectometry (OTDR) which is the analogue of the conventional Pulse Echo Tester (PET)[170] used in coaxial cable systems. The study covers broadly two areas of interest. Firstly, the Backscatter Technique[2-7] for measuring fibre attenuation is analysed and constitutes the bulk of the thesis (Chapters 2-8 and Appendices I-IV). Secondly, a modification of the Shuttle Pulse Technique[171] is used to measure the dependence of transit time on stress and temperature in jacketed and unjacketed optical fibres (Chapter 9 and Appendix V).

1.1 The Backscatter Technique

The backscatter technique is a powerful measurement method first demonstrated by Barnoski[2,3] and may be used to determine the overall fibre length, to locate faults and to measure the local fibre loss (i.e. attenuation as a function of length). The principle is to launch a short pulse of light into a fibre and analyse the characteristics of reflected or scattered radiation returning to the source in the ensuing interval.

A major attraction over the more-standard cutback and insertion-loss measurements[148-150] is that it is non-destructive and access to only one end of the fibre is required. This is particularly important in field applications where the fibres cannot be cut for source compensation measurements (as is necessary for the cutback method) and where the opposite end of the cable may be many kilometres away. In addition, the local fibre attenuation cannot be determined by the cutback and insertion-loss methods. This valuable facility provided by the backscatter technique may be utilized for the monitoring of fibre quality and for fault location in the field.

At the time of commencement of this study a number of other researchers had developed the technique further[2-4] and the first commercial instruments, although primitive, were soon to appear on the market[172,173]. However, there had been little consideration given to the absolute accuracy of the backscatter attenuation measurement or to the accuracy requirements of the instrumentation or to the potential range. The prime objective of this thesis is to address these problems. Firstly, the theory of the backscatter process is discussed with particular emphasis on the assumptions which must be valid for the success of the technique. A consideration of the accuracy requirements of the instrumentation shows that an optimum operating strategy exists in terms of the choice of system parameters such that the accuracy with which the local fibre attenuation can be measured is maximized[93].

A new technique called 'The Two-Channel Method' was developed for backscatter waveform analysis[93] and was shown to be capable of measuring local fibre attenuation in much greater detail than had previously been known. The advantages

of a 2-channel technique are numerous and make this approach a very attractive proposition for commercial exploitation.

This development opened the way for an accurate comparison between the backscatter and more-standard cutback method. In particular, the first comprehensive backscatter spectral measurement was performed over a wide wavelength range[94] and produced an excellent agreement when compared to the cut-back method. This result lends a considerable confidence to the efficacy of the backscatter technique.

The 2-channel approach was also applied to the measurement of fluctuations in local fibre losses. The measurement of the length dependence of attenuation at different wavelengths is demonstrated. It is shown that the evolution of an absorbing impurity such as OH^- can be tracked along the length of a fibre[94]. This measurement is important since it may enable the source of a contamination to be identified and lead to modifications and improvements in fibre fabrication methods.

The effects on the backscattered power of non-uniformities in longitudinal fibre parameters is also considered. It is shown that depending on the fibre quality, plots of local attenuation with length (the backscatter-loss signature) frequently exhibit severe fluctuations and anomalies such as negative values. In particular, backscatter-loss signatures are presented which clearly show correlation with programmed fibre defects and indicate, in contrast to conclusions in the literature[7], that in many cases diameter fluctuations are the cause of unidentified features in backscatter waveforms. Moreover, it is possible to infer the nature of the fluctuation from its loss signature[95-98].

Theoretical work[87] has shown that the backscatter technique is also applicable to single-mode fibres, although prior to the commencement of these studies it had only been used for fault location in this type of fibre.[125] It was recently pointed out that the scatter return in monomode fibres contains not only the usual intensity information from which the length-dependent fibre loss may be inferred, but also polarization information, since the backscattered light mirrors the state of polarization (SOP) of the propagating

pulse. A new technique termed Polarization Optical Time Domain Reflectometry (POTDR) has been proposed in which the scatter return from monomode fibres is analysed to determine the SOP along the length[55,56]. Results presented in Appendix IV represent the first measurements of POTDR and clearly demonstrate the feasibility of the technique[57,58].

1.2 Pulse Delay Measurements

Measurements on pulse transit time presented in Chapter 9 were performed with a dual objective. Firstly, the stability of the time delay is evaluated for variations in temperature and axially applied stress in order to provide data for the design of optical delay lines. Both unjacketed and plastic-clad fibres have been tested and it is shown that the application of a secondary coating of Nylon considerably degrades the delay stability.

A second objective results from the observation that the pulse delay is dependent on fibre tension, suggesting the use of the measurement as a diagnostic test for residual stress levels in optical cables. The latter measurement is of some importance to cable designers, since ideally the fibre should be neutrally stressed in order to avoid static fatigue and microbending effects. Refinements to the previously reported delay-measurement technique[42], based on a time-domain reflectometry principle, have resulted in improved long-term stability and this has permitted experiments to be undertaken to determine the residual compressive stress level in a fibre following the application of a Nylon 6 over-jacket. In addition, the effect of water ingress on the cable has been assessed[200-202].

1.3 Notes on General Layout of Thesis

The study of the backscatter technique spans Chapters 2-8 and Appendices I-IV and comprises the bulk of this thesis. Measurements of pulse delay stability are presented in Chapter 9 and Appendix V.

Chapters 2 and 3 cover the theory of the backscatter technique; the former the fundamentals of the process and the latter the measurement considerations, limitations and

ultimate range. Chapters 4, 5 and 6 describe the development and evaluation of the instrumentation. Chapters 4 and 5 detail the backscatter apparatus for multi- and single-wavelength measurements respectively and Chapter 6 describes the more-standard cutback technique. Following, in Chapters 7 and 8 and Appendix IV are the experimental results. Chapters 7 and 8 cover measurements on multimode fibres and the single mode results are presented in Appendix IV.

CHAPTER 2

THEORETICAL BACKGROUND OF THE BACKSCATTER TECHNIQUE

The basic experimental arrangement for a backscatter measurement is shown in figure 2.1. A short pulse of light is launched into an optical fibre and scattering and absorption cause attenuation of the pulse as it propagates. A fraction of the scattered radiation falls within the fibre numerical aperture (NA), and is itself guided[1]. In fact, a backward wave returns to the input after a delay and may be directed to an optical detector[2].

The power backscattered at any point in the fibre depends on the energy of the forward travelling pulse. Thus, as the amplitude of the forward pulse diminishes, so the received backscattered power decays with time[2-4]. For a fibre having a constant loss along its length, an exponential backscatter waveform is observed (see figure 2.2(a)) and at a fault point or joint, the attenuation of the forward-and backward-travelling light causes a sudden drop in backscattered power (see figure 2.2(b)). Reflecting discontinuities are indicated by spikes which are also often associated with a drop in the backscatter level thereafter.

The backscatter technique relies on the existence of a mechanism which scatters light in strict proportion to the energy in the forward propagating pulse. Rayleigh scattering[3-7], to a first order, provides such a mechanism. There are, however, many factors which may cause changes in scattering, and these result in distortion of the ideal backscatter waveforms described above; both the cause and the effect of these variations are described in the following sections. Firstly, however, the fundamental mechanisms of attenuation are considered.

2.1 Loss mechanisms in optical fibres

The attenuation in optical fibres is determined by a combination of absorption and radiative losses[8-11].

2.1.1 Absorption

For silica, molecular vibrations with broad absorption peaks centered at 9, 12.5 and 21 μm in the infrared region (IR)[9,12,13] have tails which extend down to about 1.5 μm and contribute significantly to the loss at longer wavelengths.[9] Dopant materials (e.g. GeO_2, P_2O_5, B_2O_3, F_2O and TiO_2) are used in fibre fabrication to produce the optical guiding structure[10,11] and may contribute to IR absorption[9]. The dopant B_2O_3[14], in particular, causes a shift of the absorption tail to shorter wavelengths and is therefore not used in optical fibres designed for operation in the 1.3-1.55 μm range[9].

The electronic absorption levels associated with the Si-O bonds, on the other hand, are in the ultra-violet (UV). The valence-conduction bandgap is ∿8.9 eV and corresponds to a wavelength of 140 nm[15]. The tails of the absorption extend into the IR, however, the losses at wavelengths longer than ∿700 nm are negligible in comparison to those due to impurity absorption and scattering[8,9,16].

Impurities such as the hydroxyl ion (OH^-), commonly referred to as 'water'[17], and transition metal ions[18], may also contribute to absorption at certain wavelengths. The water has proven a particularly difficult one to eradicate[19-21]. Typically, 1 ppm OH^- produces absorption peaks of 1, 2 and 40 dB km^{-1} at wavelengths of 0.95, 1.24 and 1.38 μm respectively*.

The incorporation of a B_2O_3 buffer-layer in the cladding of MCVD fibres limits OH^- diffusion into the core from the outer substrate tube and reduces the absorption at 0.95 μm to negligible levels[14]. For long wavelength operation, however, B_2O_3 is not suitable due to IR absorption[11] and new techniques must be developed to further reduce the loss at 1.38 μm. Recently reported dehydration techniques using

---

* The fundamental OH^- vibration is at 2.72 μm and harmonics appear at 1.38, 0.95 and 0.72 μm. Combinations with the fundamental vibration of the SiO_2 tetrahedra at 12.5 μm produces absorptions also at 1.24, 1.33 and 0.88 μm[17].

'gettering' agents look promising and some extremely low water content fibres have been produced[22].

2.1.2 Radiation

Radiative losses may result from an intrinsic property of the material or from waveguide effects.

Rayleigh scattering[23,24], caused by fluctuations in the molecular fine-structure of the glass, is the most important and is the dominant loss mechanism in high-quality optical fibres[9]. For a high-grade fibre, operating over the wavelength range ∿0.7-1.4 μm, the total loss α , is approximately equal to the Rayleigh scattering loss α_s, except in bands associated with an absorbing impurity. That is,

$$\alpha \simeq \alpha_s \qquad 0.7 \lesssim \lambda \lesssim 1.4 \ \mu m \qquad \ldots (2.1)$$

The importance of Rayleigh scattering, both in determining the ultimate fibre loss[9] and providing a basis for an optical time domain reflectometer[2], make it worthy of further consideration in the next section.

Further linear scattering may result from waveguide effects or imperfections. For example, high-order modes close to cut-off[25-27] and leaky modes are lossy[28,29]. In addition, core ellipticity[30], variations in diameter[31,32], microbending[32-34], bubbles, point defects[35] and drawing-induced colouration[36] may also contribute to losses. These effects, however, are normally negligible in good quality optical fibres and cables.

Non-linear processes such as Brillouin and Raman scattering may also contribute to fibre loss[(37-40)]. These are characterized by onset-thresholds which are usually above the power levels considered for optical communication[38], and are therefore not normally important. However, in backscatter measurements, high optical power levels are often desirable to obtain increased range or resolution and, particularly in the case of monomode fibres[38], these effects should be considered.

2.2 Rayleigh scattering

The origin and features of Rayleigh scattering are described here in brief. Further details may be found in the literature[23,24].

Consider a dielectric medium of mean permittivity $\bar{\varepsilon}$, exhibiting a variance $\overline{\Delta\varepsilon^2}$. Assume that the spatial width of the permittivity fluctuations is much smaller than the wavelength of light λ/n, where n is the refractive index ($n^2 = \bar{\varepsilon}$).

If the medium is free of current sources[41]

$$\nabla \times \underset{\sim}{H} = j\omega\varepsilon\underset{\sim}{E} \qquad \ldots (2.2)$$

For a small volume element δV, however, the refractive index change $\Delta\varepsilon$, results in the production of an apparent current source $\underset{\sim}{J}$, and equation (2.2) becomes

$$\nabla \times \underset{\sim}{H} = j\omega\bar{\varepsilon}\underset{\sim}{E} + \underset{\sim}{J} \qquad \ldots (2.3)$$

where

$$\underset{\sim}{J} = j\omega(\Delta\varepsilon)\underset{\sim}{E} \qquad \ldots (2.4)$$

This fictitious current extracts power from the incident wave and re-radiates. The radiation or scattering pattern produced is that of a linear current dipole[41].

Consider a set of cartesian coordinates x, y and z in which the light propagates along the z-axis. If the incident radiation of intensity I_{ox}, is polarized with electric vector parallel to x, then the intensity of the scattering from the small volume element is[24]

$$I_x = I_{ox}.\frac{\pi^2\delta V^2}{\lambda^4 r^2}\,\overline{\Delta\varepsilon^2}\,\sin^2\theta_x \qquad \ldots (2.5)$$

where r is the distance from the volume element and θ_x is the angle of the scattering relative to the x-axis.

Similarly, for incident radiation of intensity I_{oy}, with polarization parallel to the y-axis, the intensity of the scattering is[24]

$$I_y = I_{oy}.\frac{\pi^2\delta V^2}{\lambda^4 r^2}\,\overline{\Delta\varepsilon^2}\,\sin^2\theta_y \qquad \ldots (2.6)$$

where θ_y is the angle of the scattering relative to the y-axis.

For natural or unpolarized light of intensity I_o

$$I_{ox} = I_{oy} = \tfrac{1}{2}I_o \qquad \ldots (2.7)$$

Thus, the scattered intensity for unpolarized light is, from equations (2.5), (2.6) and (2.7),

$$I = I_o \frac{\pi^2 \delta V^2}{2\lambda^4 r^2} \overline{\Delta\varepsilon^2}[\sin^2\theta_x + \sin^2\theta_y] \quad \ldots (2.8)$$

Let θ_z be the angle of the scattering relative to the z-axis and with θ_x and θ_y as before

$$\cos^2\theta_x + \cos^2\theta_y + \cos^2\theta_z = 1 \quad \ldots (2.9)$$

Substituting equation (2.9) into (2.8) gives

$$I = I_o \frac{\pi^2 \delta V^2}{2\lambda^4 r^2} \overline{\Delta\varepsilon^2}[1 + \cos^2\theta_z] \quad \ldots (2.10)$$

The total scattered intensity from the whole volume, V, assuming that adjacent scattering elements are independent, can be found by multiplying equation (2.10) by $V/\delta V$. Thus,

$$I_T = I_o \frac{\pi^2 V \delta V}{2\lambda^4 r^2} \overline{\Delta\varepsilon^2}[1 + \cos^2\theta_z] \quad \ldots (2.11)$$

2.2.1 Rayleigh attenuation

Scattering causes a loss of power in the propagating wave and the attenuation coefficient is[24]

$$\alpha_s = \frac{8\pi^3}{3\lambda^4} \frac{\overline{\Delta\varepsilon^2}}{\varepsilon^2} \delta V \quad \ldots (2.12)$$

The strong dependence of loss on wavelength (λ^{-4}) is of particular significance in optical communications where fibre loss should be minimized. This is, in part, the reason for the large research effort into development of fibres and systems for the long wavelengths 1.3-1.55 μm, where losses are lower*[9]. For applications to OTDR, the decrease in back-scatter power at long wavelengths is also significant as it affects instrument accuracy and range (see section 3.13)

---

*The other reason is the low material dispersion in the region of 1.3 μm[42].

2.2.2 Origin of refractive index fluctuations

The Rayleigh Law, described in the above equations, is valid for any medium in which the correlation-distance of the local refractive index variations is small compared to the wavelength of light*[23,24].

The refractive index fluctuation, $\Delta\varepsilon$, can be expressed in general as a function of two independent thermodynamic variables such as the density ρ, and the temperature T, and in the case of a multicomponent medium, the concentration c[23,24].

$$\Delta\varepsilon(\rho,T,c) = \left(\frac{\partial\varepsilon}{\partial\rho}\right)_{T,c}.\Delta\rho + \left(\frac{\partial\varepsilon}{\partial T}\right)_{\rho,c}.\Delta T + \left(\frac{\partial\varepsilon}{\partial c}\right)_{\rho,T}.\Delta c \qquad \ldots (2.13)$$

If the fluctuations in density, temperature and concentration arise independently of each other and are statistically independent, then the variance $\overline{\Delta\varepsilon^2}$ is given by

$$\overline{|\Delta\varepsilon(\rho,T,c)|^2} = \left(\frac{\partial\varepsilon}{\partial\rho}\right)^2_{T,c}.\overline{\Delta\rho^2} + \left(\frac{\partial\varepsilon}{\partial T}\right)^2_{\rho,c}.\overline{\Delta T^2} + \left(\frac{\partial\varepsilon}{\partial c}\right)^2_{\rho,T}.\overline{\Delta c^2} \qquad \ldots (2.14)$$

In the case of silica, microscopic density fluctuations are frozen into the solid below the glass transition-temperature[43-45]. This is an intrinsic feature of glass, independent of any waveguide structure and results in a fundamental lower limit to fibre loss due to Rayleigh scatter[45].

The dopant materials (e.g. GeO_2, B_2O_3, P_2O_5, F_2O and TiO_2[10,11]) used in fibre fabrication may also contribute to Rayleigh scattering[9]; random variations in dopant concentration within the silica contribute to small index fluctuations (see equation (2.13)). Germania, in particular, causes significant additional Rayleigh scatter[9,46] and the power loss in a germano-silicate glass** is given approximately by[47,48]

$$\alpha_s \simeq 1.8 \times 10^{-28}\lambda^{-4}(1 + 100\Delta)\ npm^{-1} \qquad \ldots (2.15)$$

where the refractive index difference

$$\Delta = \frac{NA^2}{2n_1^2} = \frac{n_1^2 - n_2^2}{2n_1^2} \simeq \frac{n_1 - n_2}{n_1} \qquad \ldots (2.16)$$

---

*If the correlation distance of the refractive index fluctuations is comparable to the wavelength, the effect is known as Mie scattering[24].

**The core is GeO_2/SiO_2 of refractive index n_1 and the cladding is SiO_2 of refractive index n_2.

and NA $= \sqrt{n_1^2 - n_2^2}$ is the numerical aperture of the fibre.

The effect on backscatter measurements of fluctuations in the scattering loss due to changes in germania concentration, is analysed in section 2.8.

It should be noted that certain additives can cause a reduction in scattering[49]. This is due to either an improvement in the lattice order or a reduction in glass fictive temperature, however, these effects are yet to be fully clarified.

In addition to the above sources of refractive index variation, other dielectric imperfections can be caused by the presence of phase boundaries, partial crystallization and voids[35], but good fabrication techniques can minimize their contribution to the loss.

2.2.3 Rayleigh radiation pattern

The radiation pattern of the Rayleigh scattered light is described by equations (2.5), (2.6) and (2.10). In the case of propagation of a beam polarized in the x-direction, the angular dependence of the radiation is $\sin^2\theta_x$ which describes a toroid in the y-z plane (see equation (2.5)). If, on the other hand, the beam has no defined polarization then the angular dependence of the scattering is described by the surface $(1 + \cos^2\theta_z)$ (see equation (2.10)).

In the case of multimode optical fibres it has been shown that plane polarized light becomes de-polarized, even in very short lengths[50]. For a weakly-guiding fibre with electric vectors almost perpendicular to the axis[25] the radiation pattern is therefore of $(1 + \cos^2\theta_z)$ dependence. Consider a small volume element within the fibre core and let dE_v be the total scattered energy from the element. Then the energy dE_Ω, radiated into a solid angle Ω, is given by[5]

$$dE_\Omega(r,z,\theta) = \frac{3}{16\pi} dE_v(z,r)\left[1 + \cos^2\theta\right] d\Omega \qquad \ldots (2.17)$$

where r, z, θ define a cylindrical coordinate system and the factor $3/16\pi$ is a normalizing constant such that

$$\frac{3}{16\pi}\int_{4\pi}(1+\cos^2\theta)d\Omega = \frac{3}{16\pi}\int_0^{2\pi}\int_0^{\pi}(1+\cos^2\theta)\sin\theta\, d\theta\, d\phi = 1 \qquad \ldots (2.18)$$

Single-mode fibres, on the other hand, can sustain the polarization properties of the incident beam over a considerable distance[51-54] and therefore the radiation pattern, assuming excitation of only one x-orientated polarization, is given by

$$dE_{\Omega}(z,r,\theta) = \frac{3}{8\pi} dE_{v}(z,r)\sin^{2}\theta_{x}d\Omega \qquad \ldots (2.19)$$

where θ_x is the angle between the electric vector and the incident wave, and the constant of proportionality is determined from the condition,

$$\frac{3}{8\pi}\int_{4\pi}\sin^{2}\theta_{x}d\Omega = \frac{3}{8\pi}\int_{0}^{2\pi}\int_{0}^{\pi}(1 - \sin^{2}\theta\cos^{2}\phi)\sin\theta d\theta d\phi = 1 \qquad \ldots (2.20)$$

In practice, birefringence in the glass results in different speeds of propagation of the x- and y-orientated fields[51-54]. Thus, in general, the state of polarization varies along the length of a single-mode fibre. The Rayleigh scattered light at each point in the fibre also 'mirrors' the polarization of the primary propagating beam[55]. This phenomenon may be exploited in a new instrument called a 'Polarization Optical Time-Domain Reflectometer' (POTDR)[55-58]. The first demonstration of this technique[57,58] is described briefly in Appendix IV.

The discussion of Rayleigh scattering is extended to the application of time domain reflectometry in multimode optical fibres in section 2.4. Firstly, however, the effect known as differential mode attenuation (DMA) is described.

2.3 Differential Mode Attenuation (DMA) and the Equilibrium Mode Distribution (EMD)

Power propagating in a multimode fibre is usually distributed amongst several hundred modes, each being an eigenvalue solution derived from Maxwell's equations, with waveguide boundary conditions. In general, fibre loss depends on modal distribution[59]; high-order modes suffer increased losses due to proximity to cutoff, lossy claddings, finite cladding thickness and bending of the guide[60,61]. The lowest-order modes may also exhibit excess loss due to the central

dip in the index profile commonly observed in MCVD fibres[62,63], or due to the higher dopant concentrations near the core-centre in graded-index fibres (see section 2.2.2).

As a consequence, the mode distribution varies along the length of a fibre[64,65]. Microbending and waveguide irregularities, however, cause coupling between modes[66-68] and after a distance L_c, known as the coupling length, the propagating power stabilizes into an equilibrium mode distribution (EMD)[69,70]. Coupling lengths range, typically, from tens of metres to a few kilometres and depend on fibre/cable quality[71,72].

The attenuation of the equilibrium mode set is a useful quantity in system design in that, if known, it can be extrapolated to predict the attenuation of long fibre links[73]. A similar situation arises with fibre dispersion, due to differential mode delay (DMD), but unfortunately there is somewhat less certainty in prediction of overall link bandwidth[73-76].

Thus, in the measurement of fibre propagation characteristics careful consideration must be given to the mode distribution and in particular, the launching conditions. This is a subject of further discussion in later sections.

2.4 The Backscatter Characteristic

The theory of the backscatter technique, originally developed by Barnoski[3] and Personick[4] has been generalized and extended by Neumann[5,6]. A summary is presented here in order to create a coherent picture of the theory and to emphasise the basic assumptions. The fundamental accuracy of the technique and the specifications for the measurement apparatus are shown to rely implicitly on the characteristics of the backscattered power and the validity of these assumptions.

2.4.1 Impulse response

Consider an impulse of one joule energy, launched at time t=0, into a fibre at position z=0. The pulse will attenuate as it propagates and its energy E(z), can be described at any point z in the fibre as

$$E(z) = e^{-[\bar{\alpha}'(z)]z} \quad \ldots (2.21)$$

where $\bar{\alpha}'(z)$ is the average attenuation up to the point z and is calculated from the local attenuation $\alpha'(z)$, as

$$\bar{\alpha}'(z) = \frac{1}{z}\int_0^z \alpha'(z)dz \quad \ldots (2.22)$$

(Note that, throughout this thesis, the units of attenuation are $np.m^{-1}$ unless specified otherwise.)

The light energy scattered in the backward direction from an element of length dz at position z is given by

$$dE_b = S(z).E(z).dz \quad \ldots (2.23)$$

where S(z), known as the 'backscatter factor', is the fraction of energy scattered in the backward direction. (The properties of S(z) are described in section 2.7).

The energy propagating in the backward direction undergoes attenuation of average magnitude $\bar{\alpha}''(z)$, in returning to the fibre input, where

$$\bar{\alpha}''(z) = \frac{1}{z}\int_0^z \alpha''(z)dz \quad \ldots (2.24)$$

and $\alpha''(z)$ is the local backward loss.

In general, $\bar{\alpha}'(z) \neq \bar{\alpha}''(z)$, since the mode distributions are not identical in the forward and backward direction and therefore the loss is affected by differential mode attenuation (see section 2.3). Furthermore, fluctuations in fibre diameter, numerical aperture and profile are expected to influence the forward and backward losses differently. (These effects are neglected for the moment, but are analysed in later sections.)

The pulse transit time τ, in a fibre of length L, may be found approximately from

$$\tau = \frac{L}{c} N_1 \quad \ldots (2.25)$$

where c is the speed of light in vacuo and

$$N_1 = n_1 - \lambda\frac{dn_1}{d\lambda} \quad \ldots (2.26)$$

is the material group index. Here n_1 is the refractive index at the core centre and λ is the wavelength. Assuming that

the average group velocity, $v_g = c/N_1$, is identical for the forward and backward wave, the energy from the element dz arrives over the time interval $2dz/v_g$, and the power at the fibre input for each scattering point z, is

$$P_i(z) = \frac{dE_i(z)}{2dz/v_g}$$

$$= \tfrac{1}{2}v_g S(z).e^{-\left[\bar{\alpha}'(z)+\bar{\alpha}''(z)\right]z} \quad \ldots (2.27a)$$

Using the variable transformation $t = 2z/v_g$, where the factor '2' accounts for forward and backward travel, equation (2.27a) reduces to

$$P_i(t) = \tfrac{1}{2}v_g S(\tfrac{t}{2}).e^{-\left[\bar{\alpha}'(t/2)+\bar{\alpha}''(t/2)\right]v_g t} \quad \ldots (2.27b)$$

Equations (2.27a and b) represent the impulse response of the fibre. In the latter equation, 't/2' has been substituted for 'z' in the attenuation and scattering terms. This implies that the backscattered power arriving at the input at time t, results from scattering in the fibre at position z, at time t/2. The following discussions will assume a 'z' or 't/2' dependence and it will not be shown explicitly.

2.4.2 Response to finite input pulse

The response to a rectangular input pulse of finite width W(seconds), and a finite power P_o(watts), can be found by convolution with the impulse responses of equations (2.27a and b). Thus,

$$P(z) = \frac{SP_o}{\alpha'+\alpha''}.\left[-1 + e^{\frac{1}{2}[\alpha'+\alpha'']Wv_g}\right].e^{-[\bar{\alpha}'+\bar{\alpha}'']z} \quad \ldots (2.28)$$

or equivalently

$$P(t) = \frac{SP_o}{\alpha'+\alpha''}.\left[-1 + e^{\frac{1}{2}[\alpha'+\alpha'']Wv_g}\right].e^{-\frac{1}{2}[\bar{\alpha}'+\bar{\alpha}'']v_g t} \quad (2.29)$$

Now if

$$W << \frac{1}{(\alpha'+\alpha'')v_g} \quad \ldots (2.30)$$

equations (2.28) and (2.29) reduce to

$$P(z) = \tfrac{1}{2}P_o WSv_g \, e^{-[\bar{\alpha}'+\bar{\alpha}'']z} \quad \ldots (2.31)$$

and

$$P(t) = \tfrac{1}{2}P_o WSv_g \, e^{-\frac{1}{2}[\bar{\alpha}'+\bar{\alpha}'']v_g t} \quad \ldots (2.32)$$

Thus, according to equation (2.30), provided negligible attenuation occurs over the width of the input optical pulse, or equivalently provided the width of the input pulse is far less than the time constant of the backscatter curve, then the response due to a finite pulse of power P_o, and width W, is identical to that for an impulse of energy $P_o W$.

2.4.3 Relative backscatter power

The backscatter factor for a multimode fibre is analysed in section 2.7.4. It is shown that a 0.2 NA graded-index multimode fibre with a scattering loss of 3dB.km^{-1} (6.9 x 10^{-4} np.m^{-1}), has a backscatter factor S $\sim$3.2 x 10^{-6}m^{-1}. Thus, with an input pulse width W = 100 ns, the backscattered power at any point, from equations (2.31) or (2.32), is $\sim$45 dB below the power in the forward travelling pulse or, equivalently, $\sim$31 dB below the 4% Fresnel reflection which occurs at a perfect fibre break.

The power of typical launched pulses is 0.1-1.0 W and thus it is clear that an amplifier must be incorporated into a backscatter instrument for adequate signal recovery.

2.5 Determination of Local Fibre Attenuation

Equation (2.32) shows that the backscattered power depends on the fibre attenuation. The time constant of the back-scatter waveform is

$$\frac{d}{dt}\ln\frac{P(t)}{P_o W} = -\tfrac{1}{2}v_g[\bar{\alpha}'+\bar{\alpha}''] - \tfrac{1}{2}v_g z\,\frac{d}{dz}[\bar{\alpha}'+\bar{\alpha}''] + \tfrac{1}{2}v_g\,\frac{d}{dz}(\ln S) \quad \ldots (2.33)$$

Using equations (2.22) and (2.24), this reduces to

$$\frac{d}{dt}\ln\frac{P(t)}{P_o W} = -\tfrac{1}{2}v_g[\alpha'(z)+\alpha''(z)] + \tfrac{1}{2}v_g\,\frac{1}{S}\,\frac{dS}{dz} \quad \ldots (2.34)$$

Thus, the time constant is determined by both the local attenuation and the length dependence of the backscatter factor, S.

Consider a section of fibre between the points z_1 and z_2 or, equivalently, a section of the backscatter waveform between t_1 and t_2 (see figure 2.3a). Let the forward and backward attenuations across the section be designated respectively as

$$\bar{\alpha}'(t_1,t_2) = \frac{1}{z_2 - z_1}\int_{z_1}^{z_2}\alpha'(z)dz \qquad \ldots (2.35)$$

and

$$\bar{\alpha}''(t_1,t_2) = \frac{1}{z_2 - z_1}\int_{z_1}^{z_2}\alpha''(z)dz \qquad \ldots (2.36)$$

It is clear from equation (2.34) that if

$$\frac{1}{S}\frac{dS}{dz} << [\alpha'(z) + \alpha''(z)] \qquad \ldots (2.37)$$

then,

$$\tfrac{1}{2}[\bar{\alpha}'(t_1,t_2) + \bar{\alpha}''(t_1,t_2)] \simeq \frac{\ln P(t_1) - \ln P(t_2)}{v_g(t_2 - t_1)} \qquad \ldots (2.38)$$

Thus if $dS/dz = 0$, the time constant of the backscatter waveform is equal to the average of the forward and the backward fibre losses, and is independent of S. It is clear from equation (2.38) that the backscatter method is unable to separate the forward and backward fibre attenuations. However, one estimate of the local loss is

$$\bar{\alpha}(t_1,t_2) = \tfrac{1}{2}[\bar{\alpha}'(t_1,t_2) + \bar{\alpha}''(t_1,t_2)]$$

$$= \frac{\ln P(t_1) - \ln P(t_2)}{v_g(t_2 - t_1)} \qquad \ldots (2.39)$$

The mode set comprising the forward propagating pulse initially depends on launching conditions and changes along the fibre due to both DMA and mode mixing, until after a sufficient length, an equilibrium distribution is obtained[69,70] (see section 2.3). The backscattered light undergoes a similar, but not identical transition in propagating back to the input. In the case of backscattered light the guide is more-fully excited at the scattering point[4,6] since the Rayleigh scattering, to a first-order, is isotropic. Thus,

in general, $\bar{\alpha}'$ is not equal to $\bar{\alpha}''$ since the forward and backward mode distributions are not identical and therefore the loss is subject to DMA[59].

The estimate in equation (2.39) may therefore deviate from the actual attenuation due to the difference in the forward and backward losses. This deviation is expected to be reduced for scatter points remote from the fibre input due to the mode stabilization and the mode equilibrium. In general, however, variations in numerical aperture,diameter and profile may result in an additional error (see equation (2.58)).

A major part of this thesis is concerned with testing and identifying the factors which influence the accuracy of this estimate.

2.6 Determination of Loss at a Fault Point

Point discontinuities such as joints, absorption centres and bubbles result in the sudden attenuation of a propagating pulse. The backscattered power also exhibits a decrease, but at time $t = 2z/v_g$, where z corresponds to the position of the fault (see figure 2.3b).

Equation (2.38) requires the backscatter waveform to be differentiated and is not applicable to point defects, where a singularity exists. The loss may, however, be determined from the ratio of the returned power directly before ($P_{b)}$ and directly after (P_a) the discontinuity and is given by

$$\alpha' + \alpha'' = 10 \log_{10} \frac{P_b}{P_a} \quad \text{(dB)} \qquad \ldots (2.40)$$

where α' and α'' are respectively the losses in the forward and backscattered power at the fault. The backscatter technique is unable to separate the two losses. However, one estimate of the actual loss at the discontinuity is

$$\begin{aligned} \alpha &= \tfrac{1}{2}(\alpha' + \alpha'') \\ &= 5 \log_{10} \frac{P_b}{P_a} \quad \text{(dB)} \end{aligned} \qquad \ldots (2.41)$$

This estimate may once again deviate from the actual loss due to differences in the forward and backward attenuations (refer to the discussion in section 2.5).

In the case of a fibre joint, further problems are sometimes encountered due to changes in scattering levels. Figure 2.3c shows a joint between two fibres with backscatter factors S_1 and S_2 respectively, with $S_1 < S_2$. If the joint loss is small, as is usually the case with fusion-splicing[77,78] the backscatter power when measured from fibre 1 may increase at the joint and result in an apparent negative joint loss[79,80]. The effect on a backscatter measurement in the reverse direction, in contrast, is to produce an apparent excess-positive loss. In practice, it is believed that the ambiguity may be eliminated and the actual joint loss determined by adding the results from the two fibre ends[79-81]. However, this may prove inconvenient, especially if the far end of the fibre is many kilometres distant.

2.7 The Backscatter Factor for Multimode Fibres

The ability of the backscattering technique to reveal local attenuation is critically dependent on the constancy of the backscatter factor S, along the length of the fibre, as shown in equations (2.34),(2.37) and (2.38). The nature of S is now considered.

2.7.1 Approximation

The backscatter factor represents the fraction of the forward energy which when scattered, falls within the numerical aperture (NA) of the fibre and is guided in the backward direction. A first order approximation for S, which assumes the scattering is isotropic, can be obtained by calculating the solid angle determined by the NA^4. Thus, for a step-index fibre

$$S = \alpha_s . \frac{\pi (r \sin\theta_{max})^2}{4\pi r^2} \qquad \ldots (2.42)$$

where α_s is the scattering loss ($np.m^{-1}$) and θ_{max} is the maximum acceptance angle inside the glass . Thus,

$$NA = n_1 \sin\theta_{max} \qquad \ldots (2.43)$$

Substituting equation (2.43) in (2.42) gives the backscatter factor

$$S = \alpha_s . \frac{(NA)^2}{4n_1^2} \qquad \ldots (2.44)$$

2.7.2 Generalization

A detailed analysis of the scattering process should account for the slight anisotropy of the Rayleigh mechanism (see section 2.2.3), effects of index profiling, radial dependence of the scattering loss coefficient and the excitation of leaky modes.

Neumann[5,6] developed a more general expression for the backscatter factor given by

$$S(z) = \frac{3}{8}\frac{\int_0^a E(z,r).\theta^2_{max}(z,r).\alpha_s(z,r).r.dr}{\int_0^a E(z,r).r.dr} \quad \ldots (2.45)$$

where $E(z,r)$ is the distribution of optical energy in the fibre, $\theta_{max}(z,r)$ is the half angle of the cone defined by the local numerical aperture, $\alpha_s(z,r)$ is the local scattering coefficient and 'a' is the radius of the core. The numerator represents the energy captured in the backward direction and the denominator the total forward propagating energy. The factor '$\frac{3}{8}$' accounts for the anisotropy of the Rayleigh scattering (see section 2.2.3).

In general, all the parameters in equation 2.45 can vary across the core and along the length of the fibre. Variations in the z-direction are of major concern since a finite dS/dz leads to an error in the calculated attenuation (see equations (2.34) and (2.55). Variations in S along the fibre can result from fluctuations in parameters such as scattering-loss, numerical aperture, index profile, core diameter and modal energy distribution. In addition, these factors are not independent and a change in one is usually associated with changes in others. (For example, in the case of a germano-silicate glass, equation (2.15) describes an approximate relationship between the scattering loss and fibre numerical aperture.)

2.7.3 Assignment of typical radial characteristics to fibre parameters

It is instructive to assign known or typical radial characteristics to the parameters in equation (2.45), in order to analyse S quantitatively.

2.7.3.1 Core grading

A general class of power-law index profiles is given by[82]

$$n^2(z,r) = \begin{cases} n^2(z,0)\left[1 - 2\Delta\left(\frac{r}{a}\right)^q\right] & r < a \\ n^2(z,0)\left[1 - 2\Delta\right] & r > a \end{cases} \quad \ldots (2.46)$$

where r = radius measured from the core centre

$n(z,r)$ = refractive index at (z,r)

$n_1(z) = n(z,0)$

$n_2(z) = n(z,a)$

$$\Delta = \frac{n_1^2 - n_2^2}{2n_1^2} \simeq \frac{n_1 - n_2}{n_1} \quad \ldots (2.47)$$

q = exponent of the power law.

Note that it is more usual for the parameter 'α' to be used instead of 'q' for the exponent of the power law profile. However, the latter is used in this thesis in order to avoid confusion with attenuation coefficients denoted by α .

2.7.3.2 Modal energy distribution

The distribution of optical energy in the core E(z,r), depends on the excitation conditions at the input, mode coupling and mechanisms of differential mode attenuation. In addition, E(z,r) may consist of energy from both bound and leaky modes[28,29]. Usually, however, when sufficiently far from the fibre input and any discontinuities, such as joints, the propagating energy reaches an equilibrium modal distribution and thereafter loses somewhat the dependence on z (see section 2.3).

In order to simplify the evaluation of equation (2.45) it is useful, however, to assume that all bound modes transmit equal power.

Thus,

$$E(z,r) = \begin{cases} E(z,0)\,\dfrac{n^2(z,r) - n^2(z,a)}{n^2(z,0) - n^2(z,a)} & r < a \\ 0 & r > a \end{cases} \quad \ldots (2.48)$$

where E(z,0) is the energy at the core centre.

This equation neglects the presence of leaky modes which would complicate the picture in that each leaky mode possesses a different attenuation coefficient[28,29,30,83]. In practice, however, this omission is expected to cause negligible error, except possibly near the fibre input, since leaky modes are attenuated strongly by microbends and slight ellipticity[30,84] and therefore contribute only a small fraction to the total propagating power. The power contribution of cladding modes is likewise small for sections remote from the launch, and is also neglected.

2.7.3.3 Local numerical aperture

The local numerical aperture determines the capture cross-section for the scattered light. Both bound and leaky modes are excited at the scattering point, however, the latter are attenuated strongly[29,30,83] and, except for scatter points near the fibre input, contribute little to the received power. In fact, equation (2.45) ignores the excitation of leaky modes, since Θ should define an elliptical capture cross-section if they were present[85]. The local numerical aperture for bound modes, in contrast, defines a circular cone and is given by[82]

$$NA = \sqrt{n^2(z,r) - n^2(z,a)} \qquad \ldots (2.47)$$

where $n(z,r)$ is the local refractive index and 'a' is the core radius. The local circular acceptance angle is therefore

$$\Theta_{max}(z,r) = \sin^{-1}\left[\frac{\sqrt{n^2(z,r) - n^2(z,a)}}{n(z,r)}\right]$$

$$\simeq \frac{\sqrt{n^2(z,r) - n^2(z,a)}}{n(z,0)} \qquad \ldots (2.50)$$

The approximation results from the assumption that the fibre is weakly guiding[25].

2.7.3.4. Average scattering loss

It is shown in equation (2.15) that the scattering loss α_s, depends on dopant concentration. Thus, in the case of graded-index fibres the scattering loss is also expected to depend on radius. However, it is useful to assume that the total radial variation is small and that $\alpha_s(z,r)$ can be

replaced by the average loss α_s, across the core. That is,

$$\alpha_s(z) = \frac{1}{r}\int_0^r \alpha_s(z,r).r.dr \qquad \ldots (2.51)$$

2.7.4 Backscatter factor for power law profiles

From equations (2.46)-(2.51) and the assumptions described in section 2.7.3, it can be shown that the backscatter factor in equation (2.45) reduces to

$$S(z) = \frac{3}{8}\alpha_s(z)\frac{[NA(z)]^2}{n_1^2(z)}\left[\frac{q(z)}{q(z)+1}\right] \qquad \ldots (2.52)$$

The backscatter factor for two special cases of index profile is

(i) Step-index fibre ($q = \infty$)

$$S(z) = \frac{3}{8}\alpha_s(z)\frac{[NA(z)]^2}{n_1^2(z)} \qquad \ldots (2.53)$$

and

(ii) Square law fibre ($q = 2$)

$$S(z) = \frac{1}{4}\alpha_s(z)\frac{[NA(z)]^2}{n_1^2(z)} \qquad \ldots (2.54)$$

Thus, for a graded-index multimode fibre with a parabolic profile, the backscatter factor is expected to be less by a factor of 1/3 than that in a step-index fibre with the same NA and scattering loss. The strength of the z-dependence of each parameter in the equations (2.52) to (2.54) depends largely on the quality of the fibre manufacturing[86]. This will be the subject of further discussion in the next section.

The backscatter factor for a single-mode fibre has recently been analysed in the literature[87,88]. Single-mode fibres have a smaller NA ($\sim$0.1) and therefore the capture cross-section for backscattered light is considerably reduced. As a consequence, the range over which measurements can be performed is expected to be smaller than in a multimode fibre (refer to Chapter 3 for a definition of 'range'). An implementation of single-mode backscatter for the study of polarization properties[55-58] is also described briefly in Appendix IV.

2.8 Errors in Attenuation Measurement Caused by Variations in the Backscatter Factor

The backscatter loss is sensitive to variations in the backscatter factor along the length of the fibre (see section 2.5). From equation (2.34), the error in a local loss measurement δ np.m^{-1}, is given by

$$\delta = -\frac{1}{2}\frac{1}{S}\frac{dS}{dz} \qquad \ldots (2.55)$$

Variations in S may result from changes in α_s, NA, n_1 and q (see equation (2.52)). The core refractive index and profile affects S directly, but more important is the indirect dependence through the NA[7]. S may also change due to variations in fibre diameter. This effect is neglected for the moment but is the subject of an intensive investigation in Chapter 8.

2.8.1 Dependence on NA and scattering loss for germano-silicate fibres

Consider a graded-index multimode fibre with a parabolic index profile (q=2). Neglecting the small direct dependence of S on n_1, q and on diameter variations, the error in a local attenuation measurement, from equations (2.54) and (2.55), is

$$\delta = -\frac{1}{2}\frac{1}{\alpha_s}\frac{d\alpha_s}{dz} - \frac{1}{NA}\frac{dNA}{dz} \qquad \ldots (2.56)$$

For a germano-silicate glass, the scattering loss depends on dopant concentration and therefore, in the case of an optical fibre, it depends on the NA. This dependence is described approximately by equation (2.15).
Thus,

$$\frac{d\alpha_s}{dz} = (1.8\times10^{-26})\lambda^{-4}\frac{NA}{n_1}^2\frac{dNA}{dz} \qquad \ldots (2.57)$$

Substituting equation (2.57) in (2.56) gives the error

$$\delta = \delta_1 + \delta_2 \qquad \ldots (2.58)$$

where

$$\delta_1 = -\frac{50NA/n_1^2}{1 + 50NA^2/n_1^2}\cdot\frac{dNA}{dz} \qquad \ldots (2.59)$$

and

$$\delta_2 = -\frac{1}{NA}\cdot\frac{dNA}{dz} \qquad \ldots (2.60)$$

The total error δ, and its components δ_1 and δ_2 are plotted on figure 2.4 for a fibre having a nominal numerical aperture of 0.2. It can be seen that the dominant source of error is that due to δ_2, which describes the variation in the fibre capture cross-section; however, the contribution due to the scattering loss variation δ_1, is also significant. A change in NA of 0.01 over 1 km is not uncommon[86,89] and the error in an attenuation measurement is thus expected to be ∿0.2-0.3 dB km^{-1}. This would appear to be a fundamental limit to backscatter measurement accuracy.

2.8.2 Long wavelength measurements

Optical fibre systems are now being developed for the wavelength region 1.3-1.55 μm, where fibre losses and material dispersion are low[9,42]. Backscatter instruments operating in this wavelength region are therefore also required.

It is interesting to note that except for small variations of NA[90,91], equations (2.58)-(2.60) are independent of wavelength. Hence the error in attenuation measurements, given by equation (2.55), is almost independent of wavelength. Since the fibre loss is smaller at long wavelengths, the fractional error is more significant and represents a considerable distortion to the backscatter waveform.

Operation at longer wavelengths is considered further in section 3.13, where the instrumentation performance is also taken into account.

2.8.3 Effect of non-linear scattering mechanisms

Non-linear scattering mechanisms such as Brillouin and Raman scattering[37-40] can also modify S(z) substantially; α_s then depends strongly and non-linearly on the optical power level, which is a function of z[38]. This would certainly cause a breakdown of the backscatter technique in its present form. Fortunately, both Brillouin and Raman scattering have high

threshold levels, particularly if the source has a large spectral width[38], and are thus not normally important in backscatter measurements. Nevertheless, investigations into a modified form of backscatter, which involves the non-linear scattering mechanisms, are certainly warranted[92].

2.9 Summary

The theoretical background of the backscatter technique is described in this chapter. Rayleigh scattering caused by fluctuations in the molecular fine-structure of the glass is the dominant loss mechanism in high-quality fibres over the wavelength range of interest for optical communications, except in bands associated with an absorbing impurity. A fraction of this scattered light is re-captured by the fibre and propagates back to the input and may be utilized in an optical time domain reflectometer. It is shown that faults can be located and the local attenuation of the fibre determined from the slope of the backscattered power.

The accuracy of local attenuation measurement is shown to depend critically on the constancy of the backscatter factor S, along the length of the fibre. Variations in S may result from changes in scattering loss, NA, fibre diameter, index profile and mode-energy distribution. An estimate of the ultimate accuracy of the method, based on the distortion of the backscatter waveform due to variations in NA and scattering loss is calculated in section 2.8 to be $\sim$0.2-0.3 $dB.km^{-1}$.

It is the objective in the following chapters to determine the accuracy and the limitations of the backscatter technique. Chapter 3 considers the theory pertaining to the specification of the instrumentation[93] and Chapters 4, 5 and 6 describe the implementation. In Chapter 7, the measurement accuracy of the backscatter technique is tested by performing a comprehensive spectral comparison with the more-standard cutback method[94]. Following, in Chapter 8, the effect of variations in the backscatter factor is considered, and the likely causes are identified[95-98].

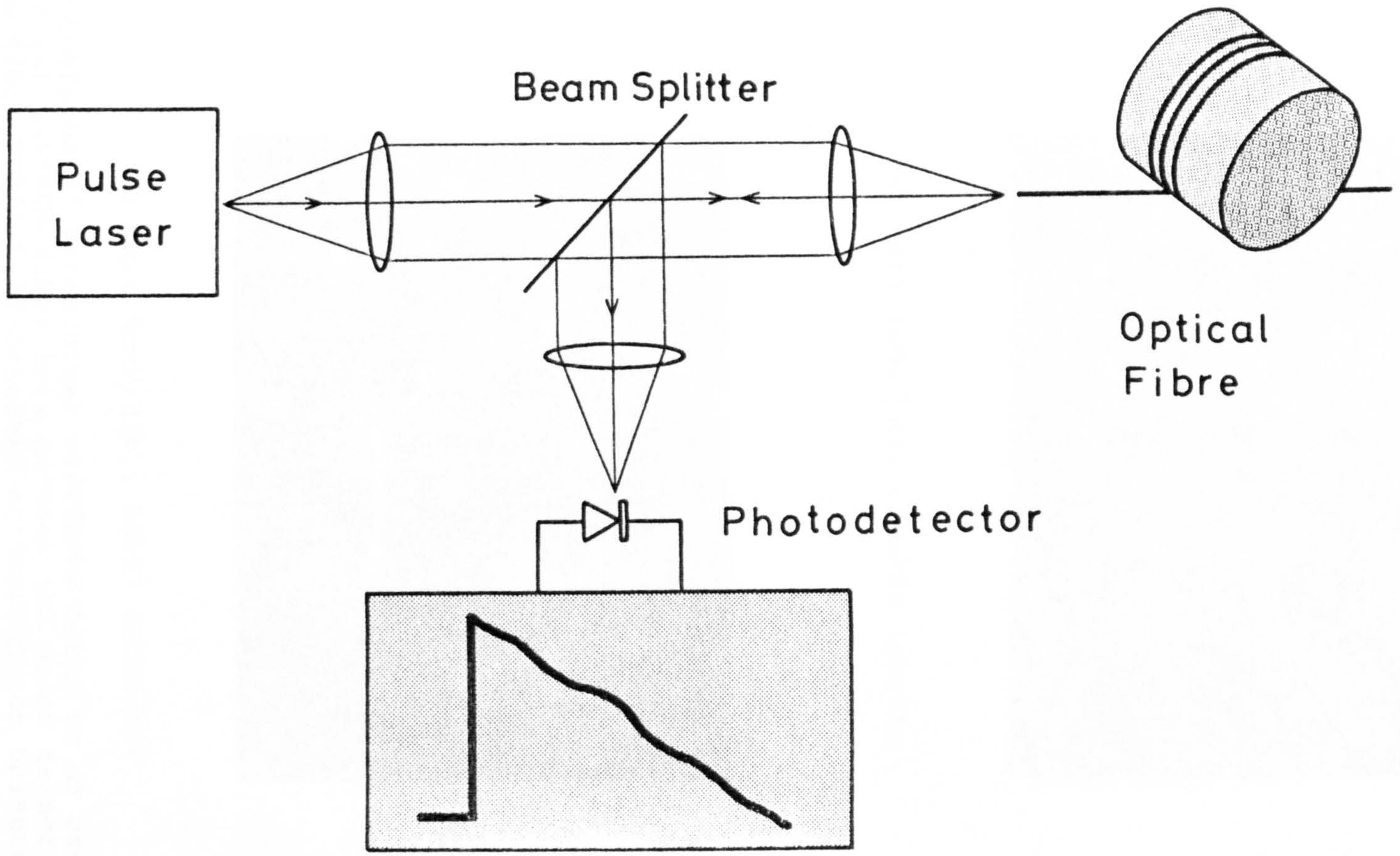

Fig. 2.1 Optical time domain reflectometry

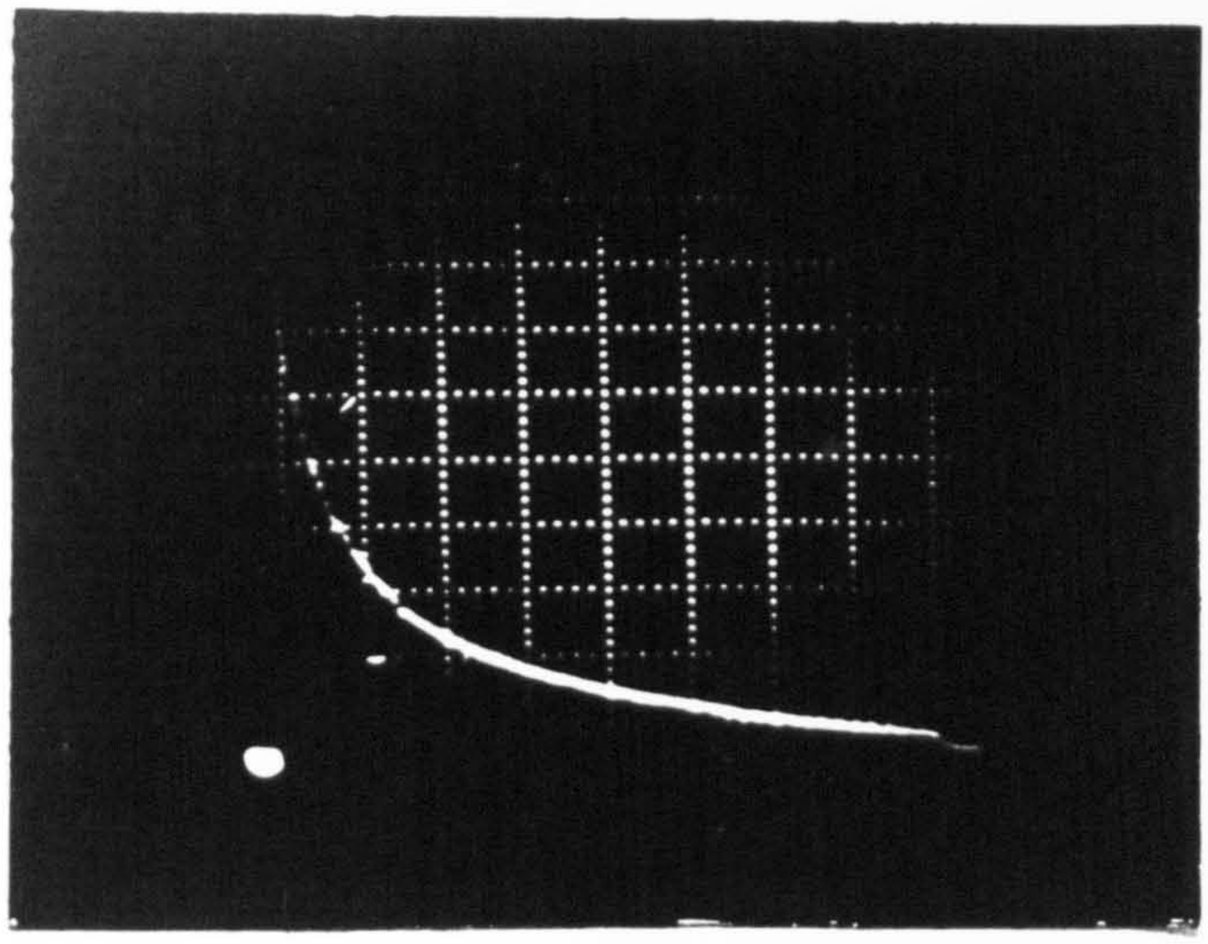

(a) vert 100mV/div , horiz 2μs/div

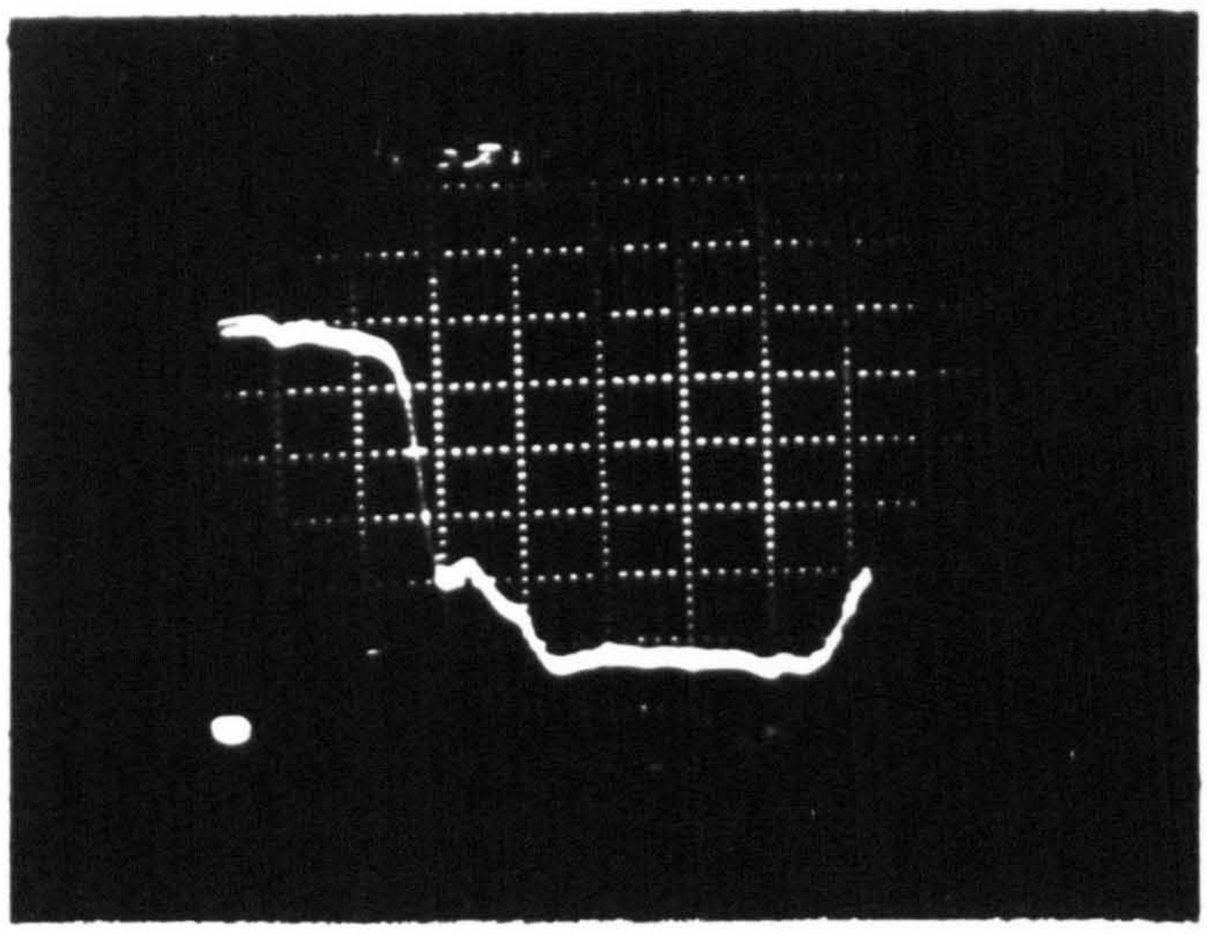

(b) vert 50mV/div , horiz 200ns/div

Photographs of Backscatter waveforms taken on an oscilloscope for (a) uniform fibre loss section (b) point defect or fault. The fibre VD237/L, fabricated at Southampton University is of graded index, 0.2NA and is 1.8km in length. The position of the fault is at approximately 50 metres from the far end of the fibre.

FIGURE 2.2

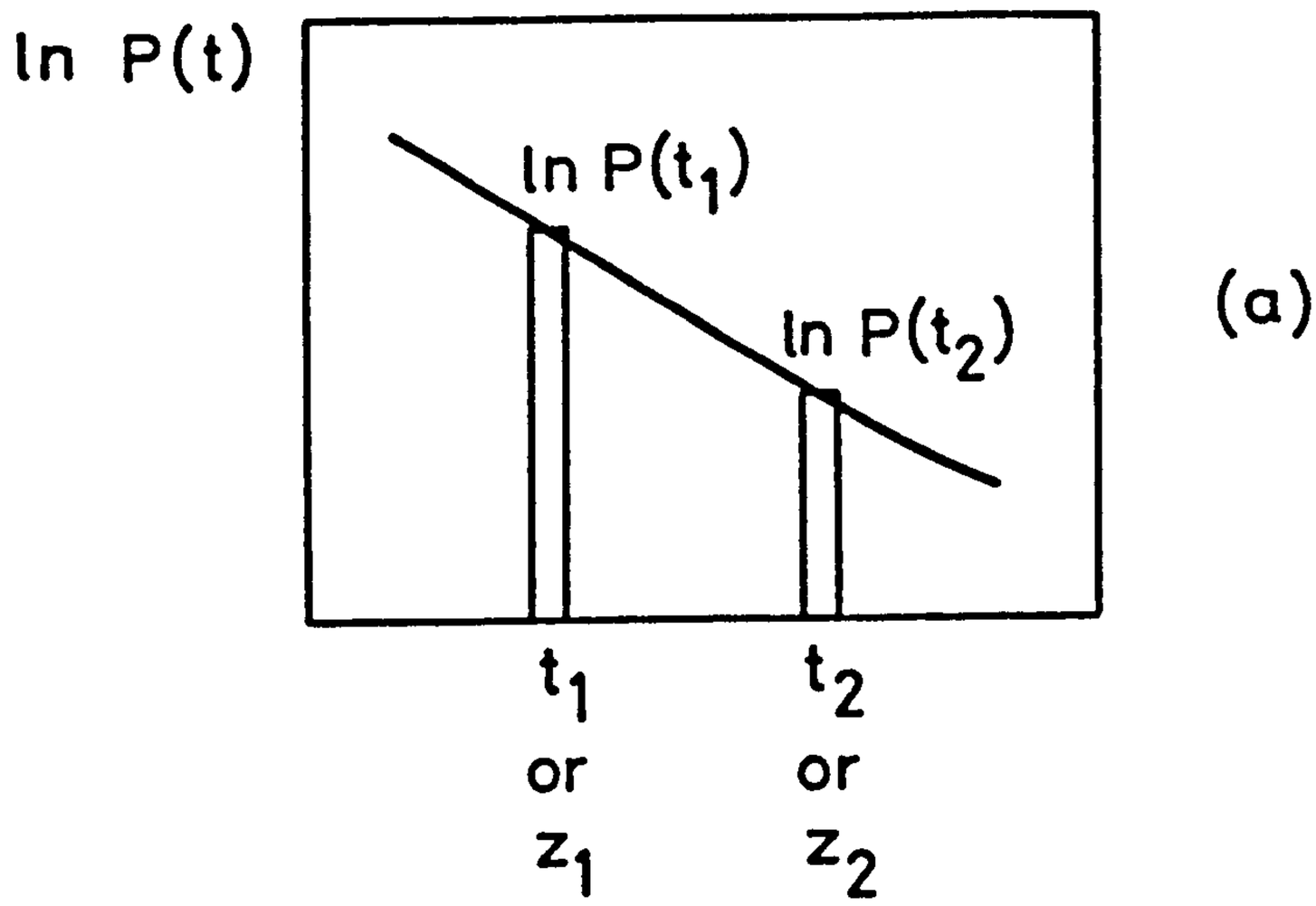

(a)

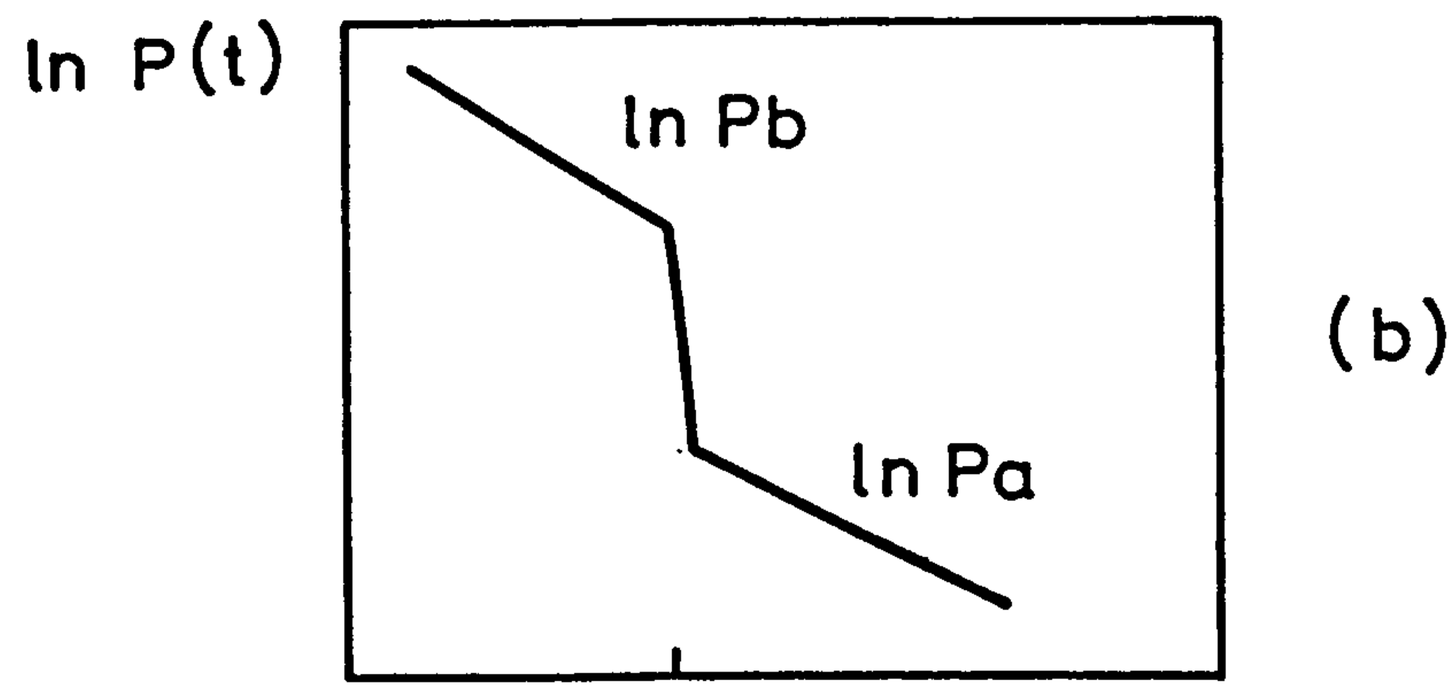

(b)

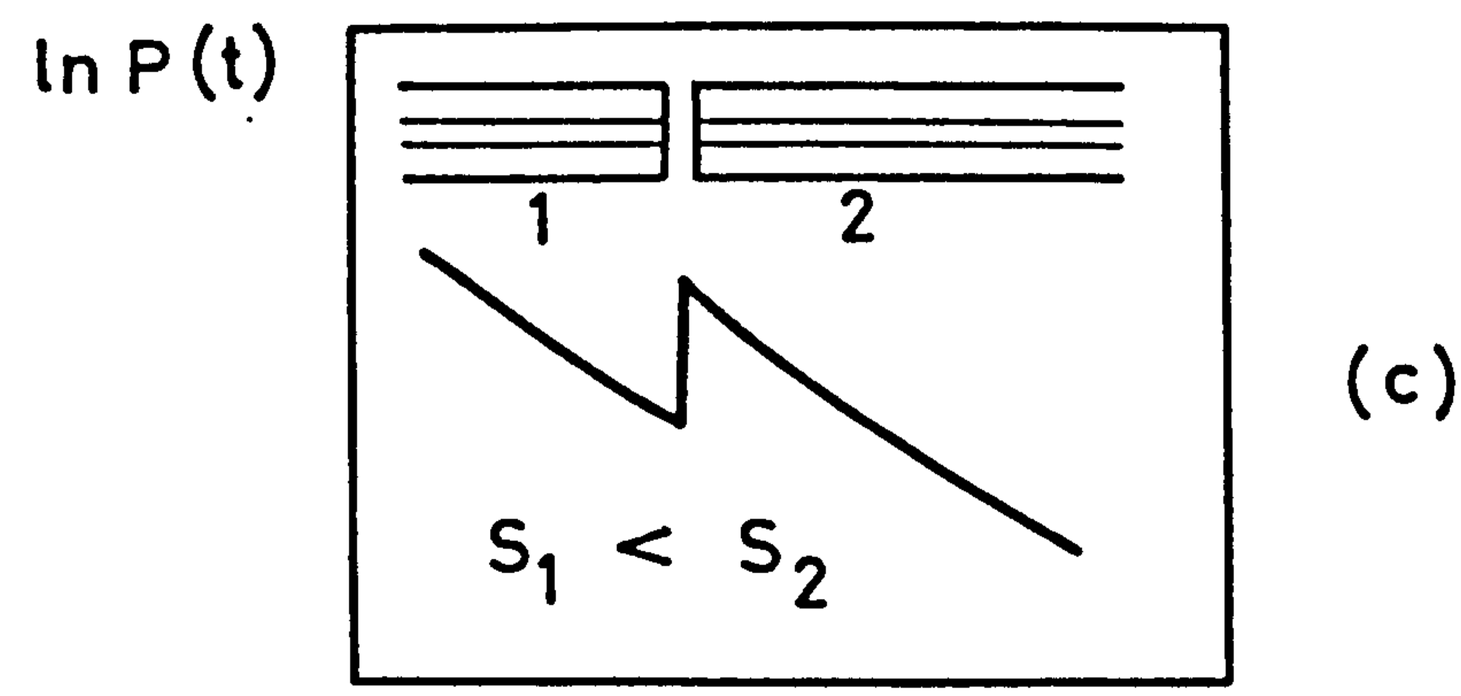

(c)

Calculation of attenuation for (a) uniform fibre loss section, (b) point defect or fault.
In addition (c) shows an anomalous effect which sometimes occurs at a joint if the scattering level in the second fibre is greater than in the first.

Figure 2.3

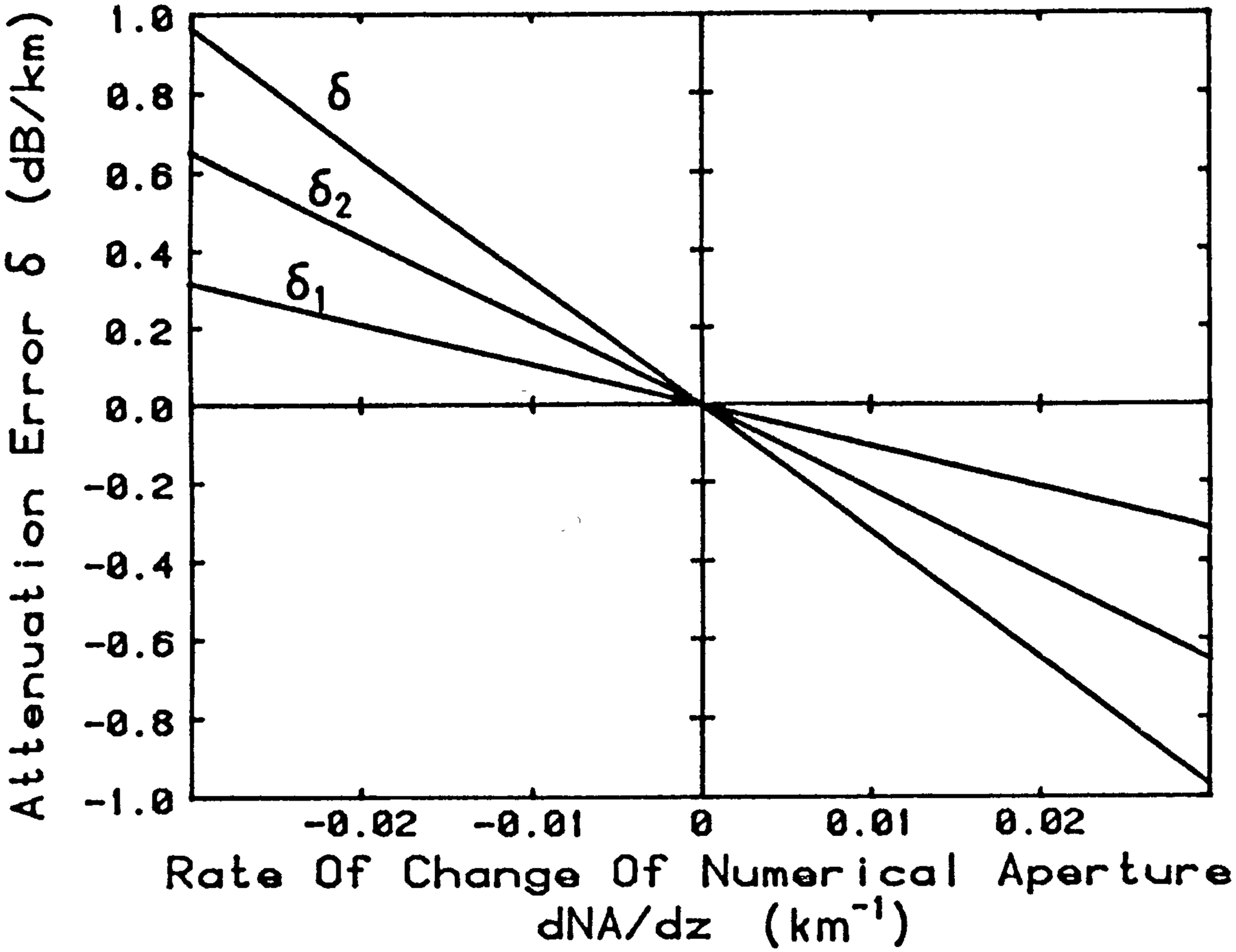

Variation of NA along the length of a fibre results in an error in backscatter measurements. For a germano-silicate glass δ_1 represents the contribution due to the change in intrinsic scattering associated with the NA change. δ_2 is due to to the change in capture cross-section. Neglecting the small contributions to error caused by variation in profile or core index n_1 then δ represents the total error in measurement.

Figure 2.4

CHAPTER 3

THEORY OF MEASUREMENT LIMITATIONS AND THE ULTIMATE RANGE

The accuracy of a backscatter local attenuation measurement depends not only on the constancy of the backscatter factor; the resolution of the measurement apparatus must also be taken into account. The analysis presented in this chapter indicates that an optimum operating strategy exists in terms of choice of system parameters such that measurement errors are minimized.[93] Linearity, offsets, timing jitter and noise are but some of the factors to be considered.

The maximum fibre length over which measurement can be performed to a desired accuracy, 'the range', is calculated. It is inevitable that when near maximum range, the signal-to-noise ratio is low and measurements must be averaged in order to attain the desired accuracy. The availability of inexpensive microprocessors suggests numerical averaging as a better alternative to the analogue techniques used in the past[2-4,99]. Accordingly, parameters pertaining to digital data aquisition are taken into account.

A new 2-channel approach to backscatter waveform analysis is proposed[93] which does not require a rigidly-controlled and stable optical source and detector. In addition, the amplifier gain can be adjusted to avoid compromising instrument accuracy due to the small signal amplitudes when near maximum range. An extension to m-channels is also considered at the end of the chapter. Firstly, however, the single-channel method for backscatter analysis is described.

3.1 Single-channel Sampling, Boxcar Integration and Numerical Averaging

The configuration of a single-channel backscatter instrument is shown in figure 3.1. A short optical pulse, typically of width 10-200 ns, is launched into a fibre and the backscattered return is directed by a beam splitter to an optical receiver/amplifier. With the standard point-by-point approach to attenuation measurement[2-4,99] an estimate of p(t),

denoted $\hat{p}(t)$, is extracted from the receiver noise, usually by a boxcar averager (also called a 'Linear Gate'), which progressively samples and averages each point on the waveform. An average attenuation $\hat{\alpha}(L)$, is then derived from the slope of $\ln \hat{p}(t)$.

The boxcar integrator is an analogue averager[100-109] which operates on the principle shown in figure 3.2. The gating of a switch is synchronized to the waveform and the signal level is sampled for a short period on consecutive cycles. Within each gating period, a capacitor charges at a rate RC towards the signal level and then provides a memory from one sample to the next. Boxcar averaging results in signal-to-noise ratio improvement (SNRI), since uncorrelated noise averages to zero over a long time interval. If the signal-to-noise ratio is defined as the ratio of the peak signal voltage to the rms value of the noise voltage, it can be shown[107] that

$$\text{SNRI} = \sqrt{2 * \text{ITC/AD}} \qquad \ldots (3.1)$$

where ITC = internal time constant (RC)

AD = aperture duration or gate trigger period

and where the noise is assumed to be white and Gaussian with frequency components up to 1/2AD Hz[107].

After a sufficiently large number of samples the capacitor reaches full charge and the time constant for the process, termed the 'observed time constant' (OTC), is given by

$$\text{OTC} = \text{ITC} * \frac{\text{RP}}{\text{AD}} \qquad \ldots (3.2)$$

where RP = sampling repetition period.

The boxcar output is within 99% of the input signal amplitude after 5 observed time constants. Additional signal-to-noise improvement can be achieved by using a low pass filter at the boxcar output, but this results in a further increase in the integration time[108,109].

An alternative to analogue averaging is numerical averaging, where the output from a fast sample and hold is digitized and loaded into a computer for processing. Signal-to-noise ratio improvement for the case of numerical averaging is[102]

$$SNRI = \sqrt{N} \qquad \ldots (3.3)$$

where N is the number of samples.

For application to a backscatter instrument, when near maximum range, the receiver signal-to-noise ratio is low and the scan time must be long to obtain adequate noise averaging, whether it be by boxcar or numerical methods. This imposes rigid limits on the stability of the optical source,detector and integrator if the measurement accuracy in α is to be maintained. In addition, when far from the fibre input, the signal amplitude is small, and measurement accuracy becomes extremely sensitive to sampling errors caused by leakage (or droop), drift and offsets, etc[108,109]. These are major disadvantages of the single-channel scanning approach and prompted the proposal[93] for an implementation of 2-channel sampling in backscatter measurements.

3.2 Two-channel Sampling

The configuration for the proposed 2-channel technique is shown on figure 3.3. An optical pulse obtained from a laser is launched into a fibre and the resulting backscattered power is detected on an avalanche photodiode and amplified for analysis. A small fraction of the launched pulse is reflected from the beam-splitter and detected to provide a timing reference for a programmable time delay generator. The latter provides timing pulses to enable two Sample and Holds , S-H 1 and 2, to sample the amplified backscatter waveform at times t_1 and t_2 respectively. Note that since the time delay generator is synchronized to the optical pulse, jitter in the laser does not result in uncertainty in the time position of the sampling windows. The analogue samples, denoted $\hat{p}(t_1)$ and $\hat{p}(t_2)$ are then converted in to digital form (A-D converted) for processing. The results of many such samples may be numerically averaged and provide an estimate of the fibre attenuation.

$$\hat{\alpha}(t_1,t_2) = \frac{\ln\left[\hat{p}(t_1)/\hat{p}(t_2)\right]}{v_g(t_2 - t_1)} \qquad \ldots (3.4)$$

where $\hat{\alpha}(t_1,t_2)$ represents the measured attenuation over the section of fibre in the region $t_1\ v_g/2 < \ell < t_2\ v_g/2$.

To obtain the attenuation characteristic of the whole fibre, the sampling pair is scanned across p(t) and further application of equation (3.4) yields $\hat{\alpha}(t,t + \Delta T)$, where ΔT is the time separation of the samples, given by

$$\Delta T = t_2 - t_1 \qquad \ldots (3.5)$$

An advantage of the above scheme is that variations in level of the backscatter signal from pulse to pulse does not affect the accuracy of the calculation since the two sample sets, $\hat{p}(t_1)$ and $\hat{p}(t_2)$, are averaged over the same group of laser pulses. Accordingly, the stability of the laser, avalanche photodiode and amplifier is not critical and simple, economic circuits may be employed.

Furthermore, the amplifier gain may be adjusted such that the signal at $p(t_1)$ spans the full dynamic range of the sampling system and thereby enables a high measurement accuracy to be achieved. The attenuation is determined from the ratio of the two averaged sample sets and therefore no error is introduced to the measurement due to the change in gain. Thus, for sections of fibre remote from the input, sampling accuracy need not be compromised as a result of the signal amplitudes being small, as is usually the case with single-channel sampling[3,4,99].

It should be noted that the implementation of a 2-channel processing system does not prevent the instrument being used in single-channel mode. In fact, it is believed that the incorporation of both facilities into an instrument would be a further aid to the interpretation and diagnosis of loss features in the backscatter waveform.

One potential problem with a 2-channel system is that a difference in gain in the two channels can result in a measurement error. However, this error can be eliminated by operating the gates alternately at times t_1 and t_2 and then at times t_2 and t_1. The effects of offsets in the sampling and A-D conversion can also be removed by a signal baseline measurement.

An extension of 2-channel processing is m-channel processing (where $m > 2$). Recent advances in fast sequential digitizers, memories and microprocessors make this method attractive for future development. An instrument based on this technique is

described in section 3.11 and is implemented in Chapter 8 to analyse the effect of fibre diameter variation on the back-scatter loss signature.

3.3 The Optimum Operating Strategy and Measurement Accuracy Requirements

The sampling accuracy required to determine the local fibre attenuation is now considered. The analysis assumes that the waveform consists of a pure exponential defined by

$$P(t) = \tfrac{1}{2}P_o WSv_g \exp(-\alpha v_g t) \qquad \ldots (3.6)$$

where from equation (2.33), α is the average of the fibre forward and backward losses and the other terms are defined in section 2.4.

The possibility for S to vary along the length of the fibre is ignored in this chapter, since the primary concern is the specification of the instrumentation. The development, although emphasising the 2-channel processing method, is general in that results can be applied to single-channel and m-channel systems with only slight modification.

3.3.1 The attenuation measurement error

If ε represents the worst case error in the estimate of $p(t_1)$ and $p(t_2)$, the maximum error in measured attenuation $\hat{\alpha}(t_1,t_2)$, occurs when

$$\frac{\hat{p}(t_1)}{\hat{p}(t_2)} = \frac{p(t_1) + \varepsilon}{p(t_2) - \varepsilon} \qquad \ldots (3.7)$$

Defining δ as the maximum error in $\hat{\alpha}(t_1,t_2)$,

i.e.

$$\delta = \left[\hat{\alpha}(t_1,t_2) - \alpha(t_1,t_2)\right]_{max} \qquad \ldots (3.8)$$

it follows from equations (3.4), (3.6) and (3.7) that

$$\delta = \frac{1}{v_g \Delta T} \ln\left[\frac{1 + \varepsilon/p(t_1)}{1 - \varepsilon/p(t_2)}\right] \qquad \ldots (3.9)$$

If the error, ε, is small in comparison to the samples $p(t_1)$ and $p(t_2)$, then equation (3.9) reduces to

$$\delta \simeq \frac{1}{v_g \Delta T}\left[\frac{\varepsilon}{p(t_1)} + \frac{\varepsilon}{p(t_2)}\right] \qquad \ldots (3.10)$$

It can be seen from equation (3.10) that the error in $p(t_2)$ dominates when $p(t_1) >> p(t_2)$, whereas if $p(t_1) \approx p(t_2)$, each sample contributes roughly equally to the attenuation error. In practice, this corresponds to operation with large and small gate spacings, respectively, since from equations (3.4) and (3.5),

$$\Delta T = \frac{1}{\alpha v_g} \ln \frac{p(t_1)}{p(t_2)} \qquad \ldots (3.11)$$

Substituting for ΔT in equation (3.10) results in

$$\delta \simeq \frac{\alpha\left[\frac{\varepsilon}{p(t_1)}\right]}{\ln\left[\frac{p(t_1)}{p(t_2)}\right]}\left[1 + \frac{p(t_1)}{p(t_2)}\right] \qquad \ldots (3.12)$$

If, on the other hand, ε is large then equation (3.10) breaks down. Using equation (3.11) to express $p(t_2)$ in terms of $p(t_1)$ and ΔT, equation (3.9) becomes

$$\delta = \frac{1}{v_g \Delta T} \ln\left[\frac{1 + \left|\frac{\varepsilon}{p(t_1)}\right|}{1 - \left|\frac{\varepsilon}{p(t_1)}\right| \exp(\alpha v_g \Delta T)}\right] \qquad \ldots (3.13)$$

3.3.2 The optimum sample separation

From an instrumentation point of view, the larger the sample error can be, the less stringent are the circuit requirements on such parameters as linearity, offsets and quantization error. The value of ε which is tolerable in order to obtain a measurement result to within δ of its true value α is calculated from equation (3.13). The normalized error $\left|\frac{\varepsilon}{p(t_1)}\right|$ is shown in figure 3.4 as a function of sample separation ΔT, for fibres having attenuations of 3 dB km^{-1} and 15 dB km^{-1}. Consider, for example, the curve for the 3 dB km^{-1} fibre ($\alpha = 6.9 \times 10^{-4}$ np m^{-1}); if the attenuation is to be measured to within 0.1 dB km^{-1} ($\delta = 2.3 \times 10^{-5}$ np m^{-1}), then for sample separations ΔT, of 0.1μs, 10 μs and 30 μs, the tolerable error is 0.02%, 1% and 0.22%, respectively, of the signal level $p(t_1)$.

It is clear from the curve that there is an optimum sample separation ΔT_{opt}, which maximizes the allowable ε and thereby minimizes the accuracy requirements of the instrumentation

system. Thus, for a fibre having an attenuation of 3 dB km^{-1}, the sample separation which maximizes attenuation accuracy is approximately 10 μs, corresponding to a 1 km length of fibre between the two sampling points; the use of other gate separations will necessarily invoke a penalty in measurement accuracy.

The ratio $p(t_1)/p(t_2)$ which maximizes attenuation accuracy can be found by differentiating equation (3.12). It is found that the optimum is independent of fibre attenuation and has a value ∿5.6 dB. Substituting this value into equation (3.11) results in the optimum sample separation

$$\Delta T_{opt} \simeq \frac{1.28}{\alpha v_g} \qquad \ldots (3.14)$$

Therefore, test equipment which is able to adjust the value of ΔT until the ratio of the samples is 5.6 dB will automatically maximize attenuation measurement accuracy. The optimum sample separation is plotted as a function of fibre attenuation on figure 3.5.

It should be noted that the existence of an optimum sample separation for a local attenuation measurement is a property of the backscatter waveform and is not unique to 2-channel sampling. Thus single-channel and m-channel systems possess the same characteristics or limitations in this regard.

The tolerable sampling error at optimum $\left|\frac{\varepsilon}{p(t_1)}\right|_{opt}$ can be found by solving equation (3.13) and is plotted in figure 3.6 with fibre attenuation α, and required measurement accuracy δ, as parameters. An approximation can also be found by substituting 5.6 dB for $p(t_1)/p(t_2)$ in equation (3.12). Thus,

$$\left|\frac{\varepsilon}{p(t_1)}\right|_{opt} \simeq 0.28\ \frac{\delta}{\alpha} \qquad \ldots (3.15)$$

For a given resolution in δ, $\left|\frac{\varepsilon}{p(t_1)}\right|_{opt}$ represents a minimum requirement on any sampling system.

3.3.3 Dynamic range utilization

In order to minimize the sampling error due to quantization noise from the digitizer, the signal level $p(t_1)$ should be maximized within the receiver dynamic range. Let the latter be defined by the limits ±K. If $p(t_1) < K$, then the ε required

expressed as a fraction of K is decreased proportionately,

$$\text{i.e.} \quad \left|\frac{\varepsilon}{K}\right| = \left|\frac{\varepsilon}{p(t_1)}\right| \cdot \left|\frac{p(t_1)}{K}\right| \qquad \ldots (3.16)$$

The ratio $\left|\frac{\varepsilon}{K}\right|$, which is called here 'the absolute accuracy' determines, amongst other things, the resolution requirements of the A-D converter (i.e. number of bits), the tolerable offsets and non-linearities and thus ultimately the performance of the instrument.

A major advantage of 2-channel sampling is immunity to drift and gain changes. Thus, automatic gain control can be used to maintain $p(t_1)$ close to the maximum level K, acceptable by the sampling system; the requirements on the ratio $\left|\frac{\varepsilon}{K}\right|$ are thereby minimized. This subject is discussed further in section 3.7.

3.3.4 Penalties for non-optimal operation

In some cases, the optimum sample separation is difficult to achieve; for example, it is inadvisable to site the two samples within different sections of a jointed fibre link, owing to the possible variation of the backscatter factor S, between the sections[79,80]. In addition, the resolution of short-length attenuation variations requires a small gate separation. For non-optimal gate spacings the penalty P, to be paid in the tolerable sample error ε , in order to achieve a given attenuation accuracy is defined as

$$P = 10 \log_{10}\left[\varepsilon_{opt}/\varepsilon\right] \qquad \ldots (3.17)$$

where ε_{opt} is the sample accuracy required at the optimal gate separation. Curves giving the penalty P as a function of attenuation and ΔT are shown in figure 3.7. Note that the curve P=0 corresponds to that for optimal sample separation as given by equation (3.14). As an example, let us take a fibre having an attenuation of 3 dB km^{-1} for which the optimum sample separation ΔT_{opt} is 10 μs. Assume, also for the moment, that $p(t_1) = K = 1$. The sample accuracy required for an attenuation accuracy of $\delta = \pm 0.1$ dB km^{-1} is $\varepsilon_{opt} = 1\%$ (figure 3.6). Suppose, however, that we require to inspect the fibre over a 250 m section (ΔT = 2.5 μs). Figure 3.7 shows that for the same

error in attenuation we now require a 3 dB greater sample accuracy, i.e. $\varepsilon = 0.5\%$.

The implication of the foregoing is that a compromise is necessary between the achievement of overall attenuation accuracy and the resolution of short-length fluctuations, since the latter requires small gate separations. This results from the difficulty in determining the slow decay in the back-scatter signal when the difference between the power levels $p(t_1)$ and $p(t_2)$ is small. On the other hand, relatively large localized power variations are found at fault points and imperfections[2-4,99], leading to significant differences in signal levels if gates are positioned immediately before and after the point of interest. Thus, relatively small gate separations are permitted and accurate loss measurement of such discontinuities is not precluded.

A further consequence of the existence of an optimum gate separation is that greatest accuracy in the determination of overall link attenuation is obtained by summing the attenuation of individual fibre sections having lengths corresponding to ΔT_{opt}. This approach may well have a further advantage in that it should allow both sample points to be sited within the same fibre section in a jointed link, thus avoiding the problems which can result from variations in the backscatter factor S, between fibre sections[79,80]. The latter may be caused by both material and geometrical changes in the fibre (see section 2.8).

3.4 Timing Sensitivity

Sample-and-hold circuits exhibit an aperture delay, i.e. a delay between the trigger pulse and capturing of the sample. In addition, there is an aperture uncertainty or timing jitter which usually comprises a small fraction of the total delay[110,111].

Sample-and-hold aperture uncertainty, U, produces an amplitude error when sampling fast slewing signals. For the sampling of $p(t_1)$, the error ε_a, is equal to

$$\left|\frac{\varepsilon_a}{p(t_1)}\right| = U \alpha v_g \qquad \ldots (3.18)$$

where from equation (3.6), $1/\alpha v_g$ is the time constant of $p(t)$.

It should be noted that aperture uncertainty causes the same percentage error in the sampling of $p(t_2)$. Therefore, according to equation (3.10), the attenuation error resulting from aperture uncertainty is equally critical for both $p(t_1)$ and $p(t_2)$ samples.

Figure 3.8 plots $|\frac{\varepsilon_a}{p(t)}|$ against U. From these curves and those of figure 3.6, it can be seen that if the aperture uncertainty is not to be limiting, an uncertainty time of some 100 ps is required. This fortunately is possible with current technology.

3.5 Bandwidth Requirements and Distance Resolution

For OTDR, the bandwidth requirements can be divided into the two application categories, namely fibre attenuation measurement and fault location.

3.5.1 Bandwidth for local attenuation measurement

The amplifier bandwidth need only be sufficient to acquire the fastest expected backscatter exponential, without dispersion. The time constants and corresponding spectral bandwidths can be calculated from equation (3.6); fibres with attenuations of 15 dB km^{-1} and 3 dB km^{-1} possess backscatter time constants (bandwidths) of 1.4 μs (113 kHz) and 7.2 μs(22 kHz) respectively. Therefore, an amplifier bandwidth of 5-10 MHz is sufficient for high resolution of smooth fibre loss sections. The use of higher bandwidths is undesirable since it gives rise to a noise penalty which restricts the range of the instrument (see section 3.9).

3.5.2 Bandwidth for fault location

For fault location and local attenuation measurement, the smallest distance that can be resolved is determined by the width of the forward propagating optical pulse ($\pm v_g$ W metres). The impulse response of any amplification and detection circuitry should be at least as fast as the equivalent time (W seconds), to be resolved.

Excessive amplifier bandwidth is , however, undesirable since the penalty is higher noise, which causes a restriction

in instrument range. In addition, the lower pulse energy $\bar{P}_o W$, associated with short input pulses also results in a restricted range (see section 3.9). Thus, there is no advantage in using pulse widths which are shorter, or amplifier bandwidths which are larger than required. The best compromise between instrument range and distance resolution is achieved when the optical pulse width and amplifier dispersion contribute equally to the distance uncertainty. Under these circumstances, the effective distance resolution is approximately $\sqrt{2} v_g W$ metres.

Pulse widths of 10-50 ns (i.e. 2-10 m eqivalent) achieve a high resolution in fault location. However, when an extension of instrument range is desired, a pulse of typically 100-300 ns is chosen. In some situations, a variable pulse width may be advantageous. A wide optical pulse can be used for fast initial location of the fault, and then a narrow pulse can be used, along with signal averaging, to provide a more precise location. The trade-off between range and distance resolution is discussed further in section 3.9 and 3.12.

3.5.3 The minimum distance resolution

The distance resolution is determined by the convolution of the optical pulse width and the amplifier response (see section 3.5.2). The minimum pulse width is that determined by the pulse dispersion[82]. For measurements on sections which are far from the fibre input, pulse dispersion causes a spreading or blurring of features in the backscattered power. The effect is particularly severe for step-index fibres with dispersions of a few tens of ns.km. Typical values for near-to-parabolic graded-index fibres are in the range 0.5-2 ns.km. As mentioned in subsection 3.5.2, improved distance resolution is usually achieved at the expense of instrument range. It is therefore inadvisable to use pulse widths which are shorter than the fibre dispersion.

A second limitation to resolution for local loss measurement results from the small gate separations required, which leads to a very stringent tolerance on sample accuracy. However, this applies only to uniform fibre loss sections and

therefore does not preclude the accurate measurement and location of discontinuities and faults (see sections 3.9-3.12).

A final limitation on the accuracy of fault location is that determined by the uncertainty in the average group velocity v_g. In general v_g can vary from fibre to fibre since it depends on the glass composition. For the location of faults cumulative error which results from the uncertainty of v_g may be reduced by taking a reference from the nearest joint or from the far end of the fibre. Often, however, these features may be difficult to resolve since, in the former case the losses may be small [77,78] or, in the latter case, the fibre may be broken.

Typically, multimode fibres are fabricated with core-cladding index differences of 1-1.5% and can be accurately controlled in mass production to approximately 0.1-0.2%[86]. A 0.2% uncertainty in v_g results in a 40 m error in position at the far end of a 20 km link. This figure perhaps sets a limit to uncertainty in length determination when the fibre input is used as a reference, however, in practice a further contribution may also result from measurement error.

A technique which enables accurate measurement of the fibre group delay is described in Chapter 9; the method is used to analyse fibre delay-stability as a function of temperature and externally-applied longitudinal stress.

3.6 Noise Averaging

When the predominant source of noise on the signal at the processor input is due to quantization, ε is governed by the accuracy of the A-D converter. Accordingly, for an n-bit converter spanning a range $\pm K$, the signal can be resolved to within $\pm\frac{1}{2}$ bit, or

$$\varepsilon = \frac{K}{2^n} \qquad \ldots (3.19)$$

When the amplifier noise predominates, numerical sample averaging can be used to reduce ε to the level required. The accuracy is no longer limited to that determined by the smallest quantization level, and the effective resolution of the A-D converter can be improved. This effect is called 'dithering' (i.e. digital averaging in the presence of noise)

and results from the 'masking' of the individual quantization levels by the noise. If the noise is assumed to be Gaussian with variance of σ^2, then averaging N samples reduces the variance to σ^2/N.[102] Taking ε as the error in $p(t_1)$ or $p(t_2)$ which is exceeded with a probability of 5%, it follows from the Gaussian distribution that

$$\frac{\varepsilon}{\sigma/\sqrt{N}} = 1.96 \qquad \ldots (3.20)$$

It should be noted that the sampling accuracy cannot be improved indefinitely by dithering. In practice, other factors such as non-linearities, offsets and timing jitter determine the ultimate resolution limits (see section 3.8).

Defining the signal-to-noise ratio before averaging as

$$SNR = \left[\frac{p(t_1)}{\sigma}\right]^2 \qquad \ldots (3.21)$$

it follows from equations (3.20) and (3.21) that

$$\left|\frac{\varepsilon}{p(t_1)}\right| = \frac{1.96}{\sqrt{N(SNR)}} \qquad \ldots (3.22)$$

This equation is plotted on figure 3.9. Figures 3.6 and 3.7 give the value of $\left|\frac{\varepsilon}{p(t_1)}\right|$ required to obtain a given measurement accuracy in local fibre attenuation. In combination with figure 3.9, the number of samples which must be averaged to obtain $\left|\frac{\varepsilon}{p(t_1)}\right|$ can be found. A design example in section 3.9 will serve to clarify the procedure.

It is noted here that in a recent publication, the sources of noise in backscatter measurements have been quantified[112]. The 2-channel technique is shown to be superior to single-channel sampling, particularly when measuring fibre sections close to the input, where the noise from the laser pulse-to-pulse variation is dominant.

3.7 Effects of Noise Clipping

It is shown in section 3.2.3 that the use of gain control to maximize $p(t_1)$ within the A-D converter dynamic range eases the requirements on sampling resolution for sections of fibre far from the input. However, the amplifier gain must not be so large that $p(t_1)$ is clipped by the measurement system.

Furthermore, $p(t_1)$ should not be so close to the dynamic range limit that the noise is truncated, otherwise a bias appears in the mean, since the noise cannot average to zero, even after an infinite number of samples. In practice, this means that when operating with a low SNR the dynamic range utilization, defined as $|\frac{p(t_1)}{K}|$ (where $\pm K$ represents the range limits of the A-D converter), must be reduced.

Let σ^2 be the variance of the noise $n(t_1)$, at the amplifier output. It is shown in Appendix I that the bias produced in the mean of $p(t_1) + n(t_1)$ by truncation is given by

$$|\frac{\varepsilon}{p(t_1)}| = \frac{1}{2}\left[|\frac{K}{p(t_1)}| - 1\right] \operatorname{erfc}\left[-J_1\right] - \frac{1}{2}\left[|\frac{K}{p(t_1)}| + 1\right] \operatorname{erfc}\left[-J_2\right]$$

$$- \frac{1}{\sqrt{2\pi(SNR)}}\left[\exp\left[-J_1{}^2\right] - \exp\left[-J_2{}^2\right]\right] \quad \ldots (3.23)$$

where

$$J_1 = \left[|\frac{K}{p(t_1)}| - 1\right]\sqrt{\frac{SNR}{2}} \quad \ldots (3.24)$$

$$J_2 = \left[|\frac{K}{p(t_1)}| + 1\right]\sqrt{\frac{SNR}{2}} \quad \ldots (3.25)$$

The bias $|\frac{\varepsilon}{p(t_1)}|$, can be determined by substituting values for SNR and the dynamic range utilization $|\frac{p(t_1)}{K}|$, into equation (3.23).

Conversely, for a given $|\frac{\varepsilon}{p(t_1)}|$ and SNR, the maximum allowable $|\frac{p(t_1)}{K}|$ can be evaluated using a rational expansion of the error function[138] and by iterative calculation on a digital computer. The result is shown on figure 3.10. It can be seen that when the SNR is low, as is the case when measuring backscatter signal levels from sections of fibre remote from the launch point, the permitted utilization of the full A-D converter range is necessarily reduced. Thus, the amplifier gain cannot be increased if further noise clipping is to be avoided.

The magnitude of ε expressed as a fraction of the A-D converter range $\pm K$, is a quantity which is useful in describing the resolution requirements of a backscatter instrument. $|\frac{\varepsilon}{K}|$, described here as the absolute accuracy, can be derived from figure 3.10 using equation (3.16). Figure 3.11 plots $|\frac{\varepsilon}{K}|$

as a function of SNR with the parameter $|\frac{\varepsilon}{p(t_1)}|$.

It is shown in section 3.3 that the fraction $|\frac{\varepsilon}{p(t_1)}|$, determines the attenuation measurement accuracy. Thus for high SNR, figure 3.11 shows that $|\frac{\varepsilon}{p(t_1)}| \simeq |\frac{\varepsilon}{K}|$. However, for an SNR less than about 10 dB, the absolute accuracy required, $|\frac{\varepsilon}{K}|$, decreases rapidly due to the smaller range utilization, since the sampling accuracy $|\frac{\varepsilon}{p(t_1)}|$must be maintained. Eventually the $|\frac{\varepsilon}{K}|$ required becomes so small as to render an accurate attenuation measurement impossible. It is this effect that determines the ultimate range of a backscatter instrument (see section 3.9).

3.8 Limits to Measurement Accuracy

The smallest value of the absolute accuracy which can be achieved, designated as $|\frac{\varepsilon}{K}|_{min}$, is a measure of instrument performance; high sampling accuracy is a property of an instrument with a small $|\frac{\varepsilon}{K}|_{min}$. The factors which determine $|\frac{\varepsilon}{K}|_{min}$ are the sampling bit-resolution and errors due to offsets, timing - jitter and non-linearity.

There are a number of approaches to sampling in backscatter measurements and each must be considered from both technical and economic viewpoints. Present day, the most common analogue-to-digital converters are of successive-approximation type[113] and combined with high speeds sample-and-hold circuits[111] can acquire repetitive signals of video bandwidth (i.e.$\sim$5 MHz) with 12-bit accuracy. Typical acquisition times for the 12-bit A-D converters,however,are in the range 1-20 μs.

Recent advances in semiconductor technology have resulted in the development of fast sequential n-bit digitizers called video or 'flash' converters[114-116]. Each device comprises 2^n-1 individual comparitors to sense the signal level. These devices can acquire waveforms with 9-bit accuracy at sampling rates up to 20 MBit/s and bandwidths of 5 MHz, without the need for a sample and hold. 8 and 9 bit converters are now commercially available[116] and will find a wide range of applications, especially in the video industry. Flash converters of 10-bit resolution can be fabricated but will be expensive due to the large number of comparitors required on each chip. Higher bit resolutions at these speeds are yet to be achieved.

An alternative sampling method based on a fast sample-hold and charge-coupled devices (CCD) may also be used for the recording of fast transient waveforms[118]. This technique, however, is still in the development stages.

Finally, a more expensive technique for digitizing is the EBS (electron bombardment semiconductor) technique[119] used by Tektronix Ltd in their new range of digital processing oscilloscopes[120]. Signals with bandwidths of 400 MHz can be acquired with 10-bit resolution. A Tektronix 7912 AD with a bandwidth of 500 MHz and a 9-bit resolution (single shot) is used in measurements of backscatter loss signatures in Chapter 8.

From equation (3.19), the absolute accuracy before averaging for 8, 10 and 12-bit A-D converters is $|\frac{\varepsilon}{K}| = 0.4\%$, 0.1% and 0.02% respectively. These may be improved by averaging in the presence of noise (see section 3.6), however, the ultimate absolute accuracy $|\frac{\varepsilon}{K}|_{min}$, for each converter, depends on the combined effects of offsets, timing-jitter and non-linearity.

Offsets in sampling may occur in the S-H and the A-D circuits but can generally be trimmed to less than $\pm \frac{1}{2}$ of a least significant bit (LSB). Timing jitter also results in an offset or uncertainty in the S-H measurement and must be within the limits specified in section 3.4. Fortunately, this is possible with current technology.

It should be noted that in a practical backscatter instrument, both the signal and baseline must be measured in order to determine p(t); offsets which are common to both measurements do not affect the sampling accuracy.

Non-linearities can be split basically into two categories, digital non-linearity and analogue non-linearity. The former occurs in A-D converters and results from a deviation of the actual bit-decision levels from the ideal straight line characteristic[113,120,121]. Digital or differential non-linearity is limited to <1 LSB for monotonic operation. In general, however, $\pm \frac{1}{2}$ LSB is usually guaranteed over the full conversion range.

The effect of differential non-linearity has been analysed by computer calculation. An 8-bit A-D converter was simulated with a non-linearity such that each decision level fell randomly within $\pm \frac{1}{2}$ LSB from the ideal value. Noise with a Gaussian amplitude characteristic was inputed to the program and the mean and variance of the A-D converter output were determined after many thousands of samples. The bias in the mean of the noise is found to be a maximum at high SNR and is limited to $\pm \frac{1}{2}$ LSB, whereas at low SNR the randomness of the individual bit levels is averaged. In the latter case, an equivalent accuracy of 12-bits can be achieved after sufficient averaging, even with an 8-bit converter.

Thus, digital non-linearity is not a limiting factor with a backscatter instrument operating near the end of its range, since here the SNR is low. In contrast, at high SNR digital non-linearity is important, especially with an 8-bit converter, in view of the resolution required (see figures 3.6 and 3.7). One method of improving converter resolution at high SNR is to artifically add noise to the signal, and remove it again when the SNR is low. However, this increases the complexity and cost of both the receiver and sampling circuitry.

The origin of analogue non-linearity is in the transfer characteristics of the S-H circuit, the A-D converter and the optical receiver/amplifier, the latter which also includes the photodiode response. In contrast to the digital non-linearity described above, analogue non-linearity results in maximum error at low SNR, due to a bias resulting from distortion of the Gaussian noise envelope.

Non-linearity error, in combination with offset error, is expected to determine a limit to absolute accuracy of $|\frac{\varepsilon}{K}|_{min}$ $\simeq$ 0.01% for a 12-bit A-D converter. An 8-bit converter is believed to be inferior, even with digital averaging in the presence of noise, due to the larger non-linearity in its transfer characteristic.

In the next section it is shown that $|\frac{\varepsilon}{K}|_{min}$ should be as small as possible in order to achieve large instrument range. Thus, it is concluded here, that for the best performance, present-day technology dictates that 12-bit A-D

converters of successive-approximation type be incorporated into the instrument design. In the future, however, the natural development will likely be towards sequential digitizing, provided that lower cost and higher resolution methods, based on either the flash converter , the CCD, or EBS principle, can be realised.

3.9 Range Performance

The backscatter range can be defined in general as the maximum fibre attenuation over which measurements can be performed to a desired accuracy. Previously, it was indicated that there exists trade-offs between range, distance resolution, attenuation accuracy and measurement time. Strictly, the user must specify all requirements before the instrument range can be determined.

The calculation of range can once again be split broadly into two instrument applications, namely local attenuation measurement and fault location. In the former, high resolution of backscattered power level is required for an accurate attenuation calculation. In the latter, accurate fault location is the priority and therefore a considerable sacrifice in power level resolution is allowable.

3.9.1 The decay in signal-to-noise ratio

The backscattered power has been derived previously and given in equation (3.6). Taking into account the 3 dB loss in the beam-splitter, shown in figure 3.3, the signal current at the amplifier input is

$$i_{p(t)} = \frac{1}{4} R\ G\ P_o W\ S\ v_g \exp(-\alpha v_g t) \qquad \ldots (3.26)$$

where R is the primary responsivity of the photodiode and G is the avalanche gain. This equation can be expressed in spatial terms using the variable transformation $t = 2\ell/v_g$ (where $\ell = z$), as

$$i_{p(t)} = \frac{1}{4} R\ G\ P_o W\ S\ v_g \exp(-2\alpha\ell) \qquad \ldots (3.27)$$

The variance of the noise is given by

$$\sigma^2 = i_n{}^2 B \qquad \ldots (3.28)$$

where i_n is the rms noise current referred to the amplifier input (amp-Hz$^{-\frac{1}{2}}$) and B is the equivalent noise bandwidth.

For a sample at $t_1 = \frac{2\ell}{v_g}$ the signal-to-noise ratio from equations (3.19), (3.27) and (3.28) is

$$SNR = \frac{(R\ G\ P_o\ W\ S\ v_g)^2}{16 i_n^2\ B} \exp(-4\alpha\ell) \qquad \ldots (3.29)$$

The decay of SNR with length determines the maximum fibre attenuation after which local attenuation measurements can be made to a desired accuracy ('the range'). From figures 3.6 and 3.7 the tolerable sample accuracy, $|\frac{\varepsilon}{p(t_1)}|$, can be determined for a measurement resolution δ in a fibre having a nominal attenuation α. For this value of $|\frac{\varepsilon}{p(t_1)}|$ and a chosen value of N, figure 3.9 yields the minimum allowable signal-to-noise ratio, SNR_{min}. Figure 3.11 then gives the value of $|\frac{\varepsilon}{K}|$ corresponding to SNR_{min} and $|\frac{\varepsilon}{p(t_1)}|$. Provided that the value $|\frac{\varepsilon}{K}|$ exceeds the ultimate resolution of the instrument given by $|\frac{\varepsilon}{K}|_{min}$, equation (3.29) can be solved with SNR_{min} to give ℓ_{max} from which the range ℓ_T, is

$$\ell_T = \ell_{max} + \tfrac{1}{2} v_g \Delta T \qquad \ldots (3.30)$$

The range can be expressed in terms of the maximum allowable one-way fibre loss by multiplying by the fibre attenuation α. Thus equation (3.30) becomes

$$R_T = R_1 + R_2 \qquad \ldots (3.31)$$

where

$$R_T = \ell_T . \alpha \qquad \ldots (3.32)$$

$$R_1 = \ell_{max} . \alpha \qquad \ldots (3.33)$$

$$R_2 = \tfrac{1}{2} v_g \Delta T . \alpha \qquad \ldots (3.34)$$

3.9.2 Design example

To demonstrate the utility of the analysis reported here, the range is now calculated using typical fibre and instrument parameters.

Consider an optical pulse of width 100 ns and of peak power 1 W launched into a multimode fibre with a parabolic index-profile and a numerical aperture of 0.2. The refractive index

n_1, is assumed to be approximately equal to the average group index N_1, and is given a value of 1.5. Thus, the average group velocity $v_g = c/N_1 = 2 \times 10^8$ ms^{-1}. The backscatter factor, from equation (2.54) is

$$S = (4.4 \times 10^{-5})\alpha_S \qquad \ldots (3.35)$$

A suitable avalanche photodiode for backscatter measurements is an RCA 30817 with a primary responsivity of R = 0.87 AW^{-1} at 0.9 μm. It is a Si-device, sensitive over the wavelength range 0.6-1.06 μm and can be operated with an avalanche gain G = 80 (RG ≃ 70 AW^{-1}). The optical receiver is assumed to have an input rms noise current of 1 pA Hz$^{-½}$ [122-124] and an equivalent noise bandwidth of 10 MHz. Thus, for the typical parameter values, equation (3.29) becomes

$$SNR = (1.56)^2 \alpha_s^2 \, 10^{17} \exp(-4\alpha\ell) \qquad \ldots (3.36)$$

3.9.2.1 Limits to range

Using equation (3.22), SNR can be expressed in terms of N and $|\frac{\varepsilon}{p(t_1)}|$. Substituting into equation (3.36) and using equation (3.35) gives

$$R_1 = \frac{1}{4} \ln\left[\left(\frac{1.56}{1.96}\right)^2 10^{17} \alpha_s^2 \, N \, |\frac{\varepsilon}{p(t_1)}|^2\right] \qquad \ldots (3.37)$$

This relation is shown on figure 3.12 (thin lines) for α_s = 3 dB km^{-1}, a typical value at a wavelength of 0.85 μm. If the instrument operates at a pulse repetition rate of 1 kHz and the time allowed for each attenuation measurement is 1 second, then N = 1000. Thus if the sampling accuracy required $|\frac{\varepsilon}{p(t_1)}|$ is 1%, the range R_1 is 24 dB (indicated by the circle on figure 3.12).

Greater range, in terms of fibre attenuation, can be achieved by taking further samples or by relaxing the requirements on sampling accuracy. However, the range cannot be increased indefinitely owing to the degradation in SNR, and the requirement that $|\frac{p(t_1)}{K}|$ be reduced in order to avoid noise truncation (see section 3.7 and figures 3.10 and 3.11).

The ultimate instrument range for the chosen parameters is also shown on figure 3.12. Each thick line defines a value of $|\frac{\varepsilon}{K}|_{min}$ derived from equation (3.23). Suppose, for example, that the ultimate resolution of the instrument is $|\frac{\varepsilon}{K}|_{min}$ = 0.1%.

Then the instrument operation is limited to the shaded region. In order to achieve the maximum range, the operator will increase the gain until the sampling error due to truncation of the noise is at least equal to all other sources of error (i.e. those due to offsets and non-linearities etc.). At this point, no further range increase can be achieved unless the requirement on $|\frac{\varepsilon}{p(t_1)}|$ is relaxed.

Thus, for $|\frac{\varepsilon}{p(t_1)}| = 1\%$ and $|\frac{\varepsilon}{K}|_{min} = 0.1\%$, the maximum range, shown by the cross in figure 3.12, is $R_1 = 31$dB; further averaging results in no improvement.

In other applications, the requirements on $|\frac{\varepsilon}{p(t_1)}|$ may not be so stringent. For example, if $|\frac{\varepsilon}{p(t_1)}| = 10\%$ and $|\frac{\varepsilon}{K}|_{min} = 0.1\%$, then R_1 is increased to 37 dB.

3.9.2.2 Range at optimum sample separation

In the previous sub-section, range is calculated on the basis of required sample resolution for a single-point measurement of the backscattered power. However, in order to determine the attenuation of a fibre section a 2-point measurement must be performed. It is shown in section 3.3.2 that in the determination of overall link attenuation, greatest accuracy can be obtained by summing the attenuation of individual fibre sections having lengths corresponding to ΔT_{opt}. Table 3.1 gives the range R_T, defined by equation (3.31) for measurement accuracies of $\delta = \pm 0.01$, ± 0.1 and ± 1 dB km^{-1}, assuming that the total number of samples is limited to 1000. In addition, it is assumed that $\alpha = \alpha_s$ (i.e. that the fibre attenuation results predominantly from Rayleigh scattering), and the instrument parameters are as defined previously. It can be seen that for a measurement accuracy of $\delta = \pm 0.1$ dB km^{-1}, the maximum fibre attenuation, after which a 2-point measurement with optimum gate spacing (5.6 dB) could be made, is 27 dB. The realization of this figure of merit would permit the determination of the attenuation of long fibre links with high accuracy[93].

The calculations of the range in table 3.1 are based on the assumption that the absolute accuracy of the instrument $|\frac{\varepsilon}{K}|_{min}$ is not compromised. However, this may be an optimistic assumption in the case of $\delta = \pm 0.01$ dB km^{-1} since the

resolution requirements on $|\frac{\varepsilon}{p(t_1)}|$ and $|\frac{\varepsilon}{K}|$, shown in figures 3.6 and 3.11, are quite harsh. In the cases $\delta = \pm 0.1$ and ± 1.0 dB km^{-1}, increasing the number of samples can improve the range, but the limits are again defined by $|\frac{\varepsilon}{K}|_{min}$ as shown on figure 3.12.

Operation at non-optimal gate spacings requires that $|\frac{\varepsilon}{p(t_1)}|$ be reduced (see section 3.3.4). The value of $|\frac{\varepsilon}{p(t_1)}|$ required may be determined from figures 3.6 and 3.7, and for the case $\alpha_s = 3$ dB km^{-1}, R_1 can be found from figure 3.12 as before. The total range R_T is found from equation (3.31).

3.9.2.3 Extension of range

It should be noted that the calculations of range here, apply only to the chosen optical and instrument parameters. Although these parameters are typical, further signal-to-noise ratio improvement and therefore range extension can, in principle, be achieved by increasing P_o, W or decreasing i_n, B as shown in equation (3.29). Recently reported[125] was the achievement of a range of 17 dB in a single-mode fibre where the receiver bandwidth was reduced and a pulse of 1 μs width was used (equivalent to 100 m resolution). It is therefore very much up to the operator to decide the sacrifices he is prepared to make for the achievement of further range.

In addition, range can be increased further by a decrease in $|\frac{\varepsilon}{K}|_{min}$ of the instrument or by relaxing the sample accuracy requirements in terms of $|\frac{\varepsilon}{p(t_1)}|$. As an example, a value of $|\frac{\varepsilon}{K}|_{min}$ of 0.1% is chosen in section 3.9.2.1; however, in practice it is believed that with current technology an absolute accuracy approaching 0.01% can be achieved. Since the typical power budgets for present day multimode optical fibre communication links is ∿40 dB[126], it seems likely that an OTDR can be developed with sufficient range to cover the maximum repeater span.

3.10 Measurement Time

The previous sections identified $|\frac{\varepsilon}{K}|_{min}$ as the parameter which determines ultimately the instrument performance and range. In practice, however, measurement time is also a major consideration since it often determines the economics of

performing a measurement; production facilities require fast measurement for economic quality control and in the telecommunications environment faults must be located and rectified quickly to avoid excessive loss of revenue.

If the optical pulse repetition rate is 1 kHz then N = 10^3, 10^5 and 10^7 corresponds to times of 1 second, 1.40 minutes and 2.47 hours respectively. Pulse repetition rate is determined by two factors. Firstly, if the fibre link is 20 km in length, then the round trip time for the backscattered power is 200 μs. Thus, if ambiguities are to be avoided, another pulse should not be launched until after this time has elapsed. Secondly, single-heterojunction lasers, which are attractive for backscatter applications, have output powers and also lifetimes that depend on duty factor[127]. In general, duty factor is limited to about 0.1%. For an RCA SG-2002 maximum repetition rates are only ∿2 kHz for 100 ns optical pulses, before a power reduction and deterioration in backscatter SNR and range is observed. The number of samples required for an accurate 2-point measurement of a particular fibre section depends on SNR. Therefore, not nearly so many samples need be taken for measurement near the fibre input as when near maximum range. In practice, measurement time may be minimized since the standard deviation of consecutive samples can be calculated by a processor and N varied according to the SNR and the required accuracy.

3.11 Multi-channel Sampling

An extension of the 2-channel method is multi-channel or m-channel processing. It retains all the advantages of the 2-channel technique, but in addition reduces the measurement time. The technique is used in Chapter 8, in conjunction with the 2-channel method to analyse the effect of variations in the backscatter factor on the returned power.

The proposed arrangement is shown in figure 3.13. A fast sequential A-D converter of the type described in section 3.8 (i.e. a flash converter, CCD or EBS device) is used to sample the backscatter waveform. The triggering is derived from a crystal oscillator which pulses 'm' times within a 'window' of width T seconds. The timing of the first sample at t = t_1,

and the width of the window are determined by the output of a time delay generator synchronized to the launched optical pulse. Measurement results are loaded into memory (RAM) where they await processing; 2-point or multi-point curve fitting can be used to determine the attenuation of the sampled sections.

The implementation using a flash-converter appears to simplify the arrangement shown in figure 3.3 where two S-H circuits and two A-D converters are used. However, severe requirements are placed on the technology of both A-D conversion and data processing in view of the speed and the quantity of data which must be handled. In addition, the absolute accuracy of present day sequential digitizers is inferior to that of the A-D devices of successive approximation type (see section 3.8), and this may result in a smaller instrument range. In the future, however, provided that lower cost and higher resolution devices can be realized, then the development will likely be towards sequential digitizing in backscatter measurements.

Figure 4.4 shows a multi-channel record of a backscatter waveform taken on a Tektronix 7912 AD transient digitizer. The 7912 AD has a 9 bit resolution, single shot, which may be improved by digital averaging in the presence of noise (see section 3.6). The figure displays the result of a single shot measurement (i.e. no averaging) and the individual quantization levels are just discernable at the far end of the fibre. Recently, an example of m-channel processing using a flash converter has also appeared in the literature[129].

It is the intention in the following sub-sections, not to design an m-channel system, but to describe briefly the factors which limit its range performance.

3.11.1 Maximum span (T_{max})

Let the gain of the optical receiver be such that the backscattered power utilizes the full dynamic range of the A-D converter (i.e. $p(t=0) = K$). The waveform is then sampled 'm' times within a section of length T. A total of (m-1) two-point calculations can be performed to give the attenuation characteristic of the fibre over the span T. Each 2-point

calculation requires that an accuracy $|\frac{\varepsilon}{p(t_1)}|$ be achieved in the sampling as described previously (see figures 3.6 and 3.7).

Consider the section of fibre between the k^{th} and the $(k+1)^{th}$ sample. The value at $p(t = t_k)$ is considerably less than the full dynamic range of the A-D converter,i.e. $|\frac{p(t)}{K}| << 1$ Therefore, if the accuracy $|\frac{\varepsilon}{p(t_1)}|$, required for a 2-point calculation in the k^{th} section is to be achieved, the absolute accuracy of the instrument, $|\frac{\varepsilon}{K}|_{min}$, must be extremely small (see equation (3.16)). The limitation imposed by $|\frac{\varepsilon}{K}|_{min}$ defines a maximum value T_{max} given by

$$|\frac{K}{p(t_1)}|_{min} = \frac{K}{K \exp(-\alpha v_g T_{max})} = \frac{|\frac{\varepsilon}{p(t_1)}|_{required}}{|\frac{\varepsilon}{K}|_{min}} \quad \ldots (3.38)$$

therefore

$$T_{max} = \frac{1}{\alpha v_g} \left[\ln|\frac{\varepsilon}{p(t_1)}|_{required} - \ln|\frac{\varepsilon}{K}|_{min} \right] \quad \ldots (3.39)$$

Thus, even in an m-channel sampling system, the local attenuation characteristic must be put together in a piece-wise fashion with section lengths of equivalent time T_{max}. Note that the value T_{max}, also defines the maximum scan width of a single-channel system, after which the amplifier gain must be changed in order to maintain sampling accuracy.

3.11.2 Range for m-channel sampling

In order to achieve the highest accuracy in each span T, the backscatter waveform should be amplified until the first sample utilizes the full A-D dynamic range. Note, however, that equation (3.39) applies only when the SNR is high. If the SNR is low, the first sample in any section must be reduced relative to the full A-D dynamic range in order to avoid noise clipping (see section 3.7). The effect of reduced dynamic range utilization on the absolute accuracy required is shown in figures 3.10 and 3.11. If the required $|\frac{\varepsilon}{K}|$ is reduced for the first sample in the span T_{max}, then accurate measurement of the m^{th} sample is beyond the capabilities of the instrument. Thus, when the SNR is low, T must be reduced so that the accuracy in the last sample is not compromised.

Therefore, the range for a m-channel system is determined in the same way as for a 2-channel system; that is, when the dynamic range utilization of the 1st sample $|\frac{p(t_1)}{K}|$, is reduced so far that the tolerable $|\frac{\varepsilon}{K}|$ is less than the $|\frac{\varepsilon}{K}|_{min}$ of the instrument.

A major attraction of the multi-channel technique is decreased measurement time. However, it is clear from the above analysis that this advantage is only realized for sections close to the fibre input where the SNR is high, since for sections far from the fibre input where the SNR is low, the span T must be reduced.

3.12 Fault Location

Although the characterization and location of faults is not a primary objective in this thesis, it is an area of considerable importance and therefore some discussion is warranted.

Faults can be separated generally into two categories; those of distributed nature where a loss increase occurs over a large section of fibre and those where the loss occurs at a particular point.

Distributed loss increases may be caused by an increase in microbending resulting either from residual stress or a contraction of cable sheath due to temperature or creep[34,130]. These increases are perhaps best detected by performing 2-point scans of the local fibre loss and comparing with previously measured results.

In the case of point defects, four general types can be identified:-

a) reflecting, complete break
b) non-relfecting, complete break
c) reflecting, partial break
d) non-reflecting, partial break

and the backscatter signatures are shown in figure 3.14. The term partial break is used here to apply to all situations where the fibre cable is not completely severed, i.e. some light does pass across the faulty section. This includes cases where the fibre is shattered, but still held intact by the secondary plastic jacketing and cases where a microbend

or kink causes loss of optical power at a particular point. In addition, lossey joints may also fall into this category.

A reflecting break is detected most easily since the reflection is normally well above the backscatter level at that point. Partial breaks, especially those of non-reflecting type are the most difficult, since the change in backscatter power level may only be small.

Instrumentation requirements for the location of point defects differs markedly to those for local attenuation measurement. The differences in regard to optical pulse width and amplifier bandwidth are described in section 3.5. Another major difference is that accurate fault location is the main priority, and accurate measurement of the level of the backscattered power is of secondary importance.

When near maximum range, the bias due to noise clipping does not immediately affect the basic monotonic decreasing character of the backscatter waveform. Thus, for fault location, the amplifier gain need not be restricted in as harsh a manner as described in section 3.7 and 3.9. Sudden drops in backscattered power due to the presence of a fault, results in a sudden change in the level of the sampled signal, whether it is biased or not. Thus, in principle, the bias due to noise clipping can be a large percentage of the signal level and the instrument range can be extended beyond that of the local attenuation measurement. Ultimately, however, the bias will be so large as to hide any variations in the back-scattered power and this defines the end of range for fault location.

3.13 Extension to Long Wavelengths

The instrument parameters chosen in the range calculations of section 3.9 apply strictly only to operation in the wave-length region 0.8-0.9 μm. Operation in the long wavelength region, 1.3-1.55 μm, requires the use of different optical source and detector materials.

Commercially available Ge-avalanche photodiodes are suited but are inferior to the shorter wavelength Si-devices due to excess multiplication noise and higher leakage current. The

effect on backscatter measurements is a decrease in SNR, and therefore a smaller instrument range is expected. Currently, development of lower noise, long wavelength devices, is focussed on the very low capacitance PIN-FET hybrid detectors using GaInAs and GaInAsP diodes on GaAs or InP substrates, and a GaAs MESFET[132-134].

Development of optical sources for long wavelengths again centres on the GaInAs/InP and GaInAsP/InP materials[135,136] and recently some very low threshold lasers have been developed[137]. It is hoped that in the future, high power pulse lasers will also be commercially available.

In addition to the source and detector considerations, the existence of an optimum sample separation[93] also has implications in the long wavelength region where the losses may be extremely small[9]. The optimum gate separation, from equation (3.14), is large due to the low fibre loss and therefore the measurement of local variations in loss, especially over small fibre sections, is extremely difficult because of the increased accuracy required (see section 3.3.4). Furthermore, it is shown in section 2.8.2 that variations in the backscatter factor along the length of the fibre are expected to be almost independent of wavelength. Therefore, due to the low losses in the long wavelength region, significant errors in local backscatter loss measurements can be expected. This is in contrast to measurements in the 0.8-0.9 μm region where the attenuation is larger.

Thus, the measurement of local fibre attenuation by the backscattering technique is more difficult at long wavelengths due to the small fibre losses and the expected variations in the backscatter factor. However, the measurement and location of faults is not precluded and it seems likely that an instrument possessing this limited, but important facility can be developed[125].

3.14 Summary

The resolution requirements of instrumentation to measure the scattered return in optical fibres is considered in this chapter. A 2-channel technique, insensitive to instability

and drift in the optical source and detector, is proposed for the measurement[93]. Results are plotted directly as attenuation versus position in the fibre, a generally more useful form than the more standard exponential or logarithmic plots[2-4,99]. Furthermore, when near maximum range, the receiver gain can be adjusted to increase signal amplitude and this minimizes the required instrument resolution and maximizes measurement accuracy. Single-channel and multi-channel operation are also considered.

In the measurement of local fibre attenuation it is shown that there is an optimum operating condition in terms of the time interval between samples. Optimum operation provides for maximum accuracy in the estimated attenuation with least sensitivity to measurement error.

The necessary sample resolution, denoted by $|\frac{\varepsilon}{p(t_1)}|$, is normalized relative to the signal amplitude at t_1 and depends on both the desired accuracy in measured attenuation and the 'distance' from optimum. An error in local attenuation measurement of 0.1 dB km^{-1} appears to be an appropriate design objective for an instrument operating in the wavelength range 0.8-0.9 μm, in view of both the sample resolution required and the errors predicted in section 2.7 due to scattering variations.

The absolute resolution of measurement, denoted by $|\frac{\varepsilon}{K}|_{min}$, is shown to determine instrument performance in terms of both range and ultimate accuracy; a value approaching 0.01% is desirable. Note that the range limitation defined by $|\frac{\varepsilon}{K}|_{min}$ is identical for 1, 2 and m-channel systems.

It is shown in section 3.9 that for the instrument parameters chosen and averaging 1000 samples at optimum gate separation, a range corresponding to 27 dB of one-way fibre loss can be achieved with a measurement confidence of ±0.1 dB km^{-1}.

Chapters 4 and 5 describe the implementation of 2-channel backscatter systems, based on considerations described in this and the previous chapter. Following, Chapter 6 details an alternative method for fibre attenuation measurement, 'the cutback method', and in Chapters 7 and 8 the experimental results are presented.

Required attenuation accuracy dB/km	Measured insertion loss dB
0.01	22
0.1	27
1	31

Maximum fibre loss after which localised attenuation measurements can be made to the accuracy stated

Table 3.I

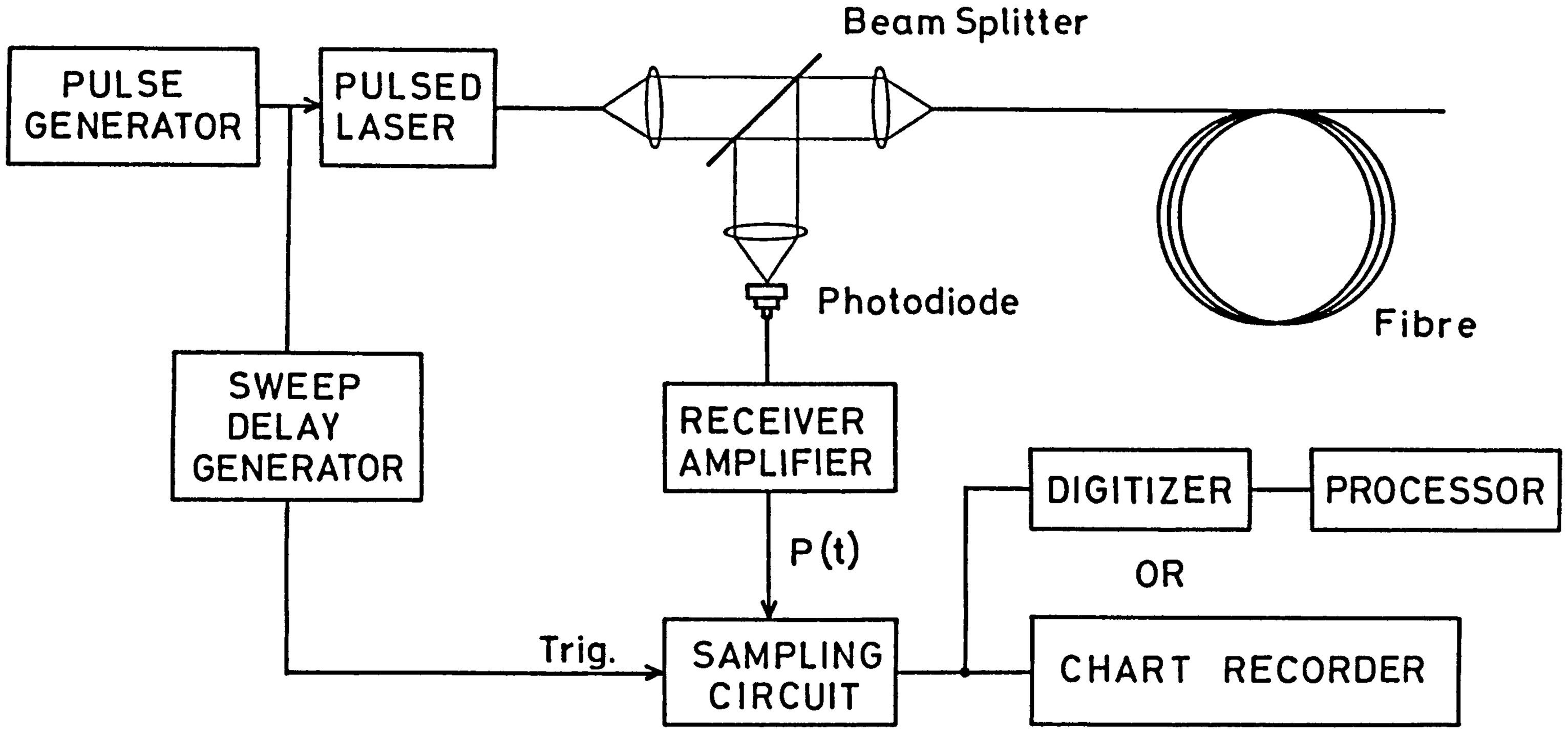

Fig. 3.1 A Single-Channel Sampling System

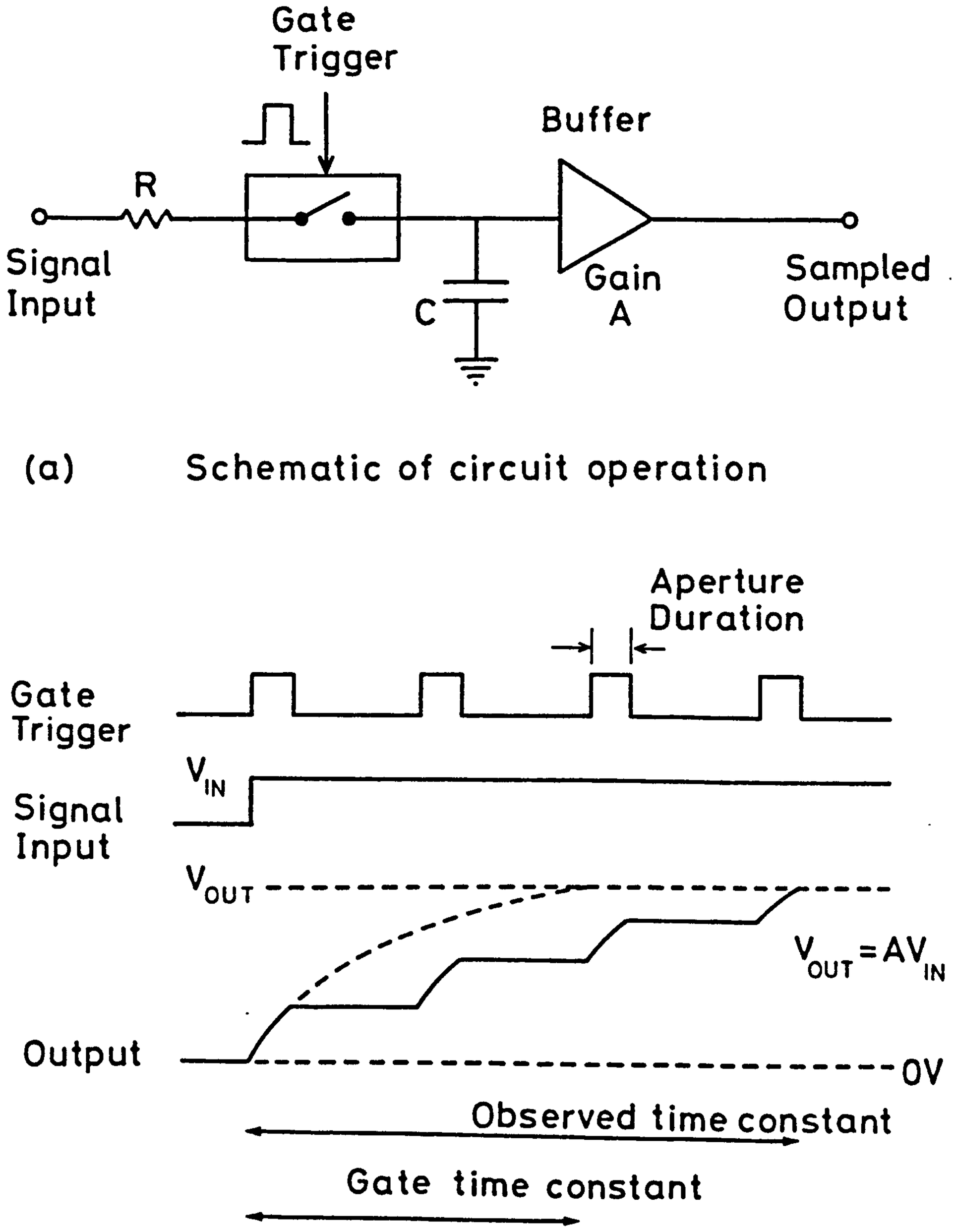

Boxcar Integrator: A gate trigger causes sampling of the signal on consecutive cycles. Within each sampling window a capacitor charges exponentially and after a period of approximately 5 'observed' time constants the boxcar output is within 1% of its final value

Figure 3.2

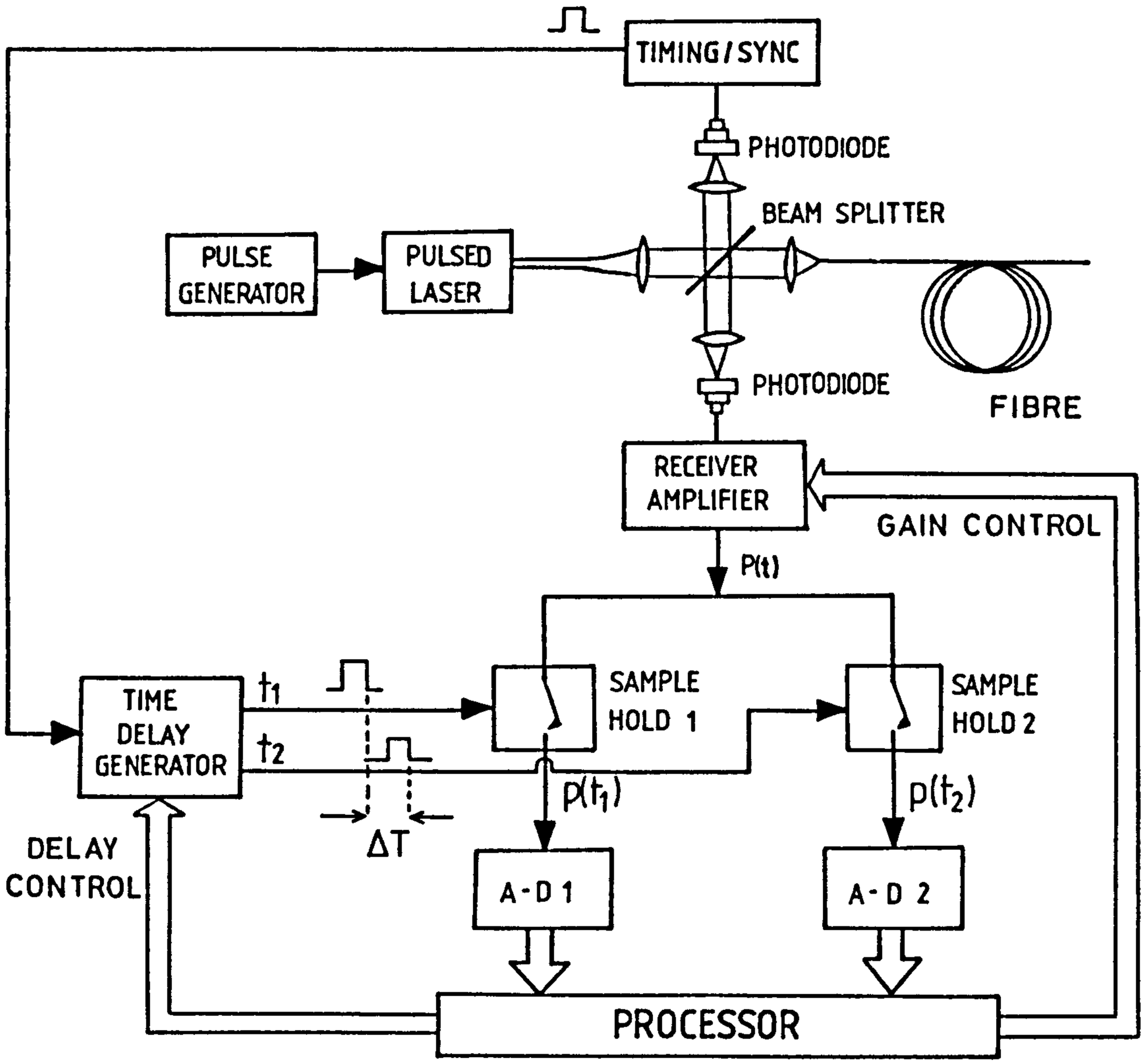

Schematic of a 2-Channel Backscatter Samping System

Figure 3.3

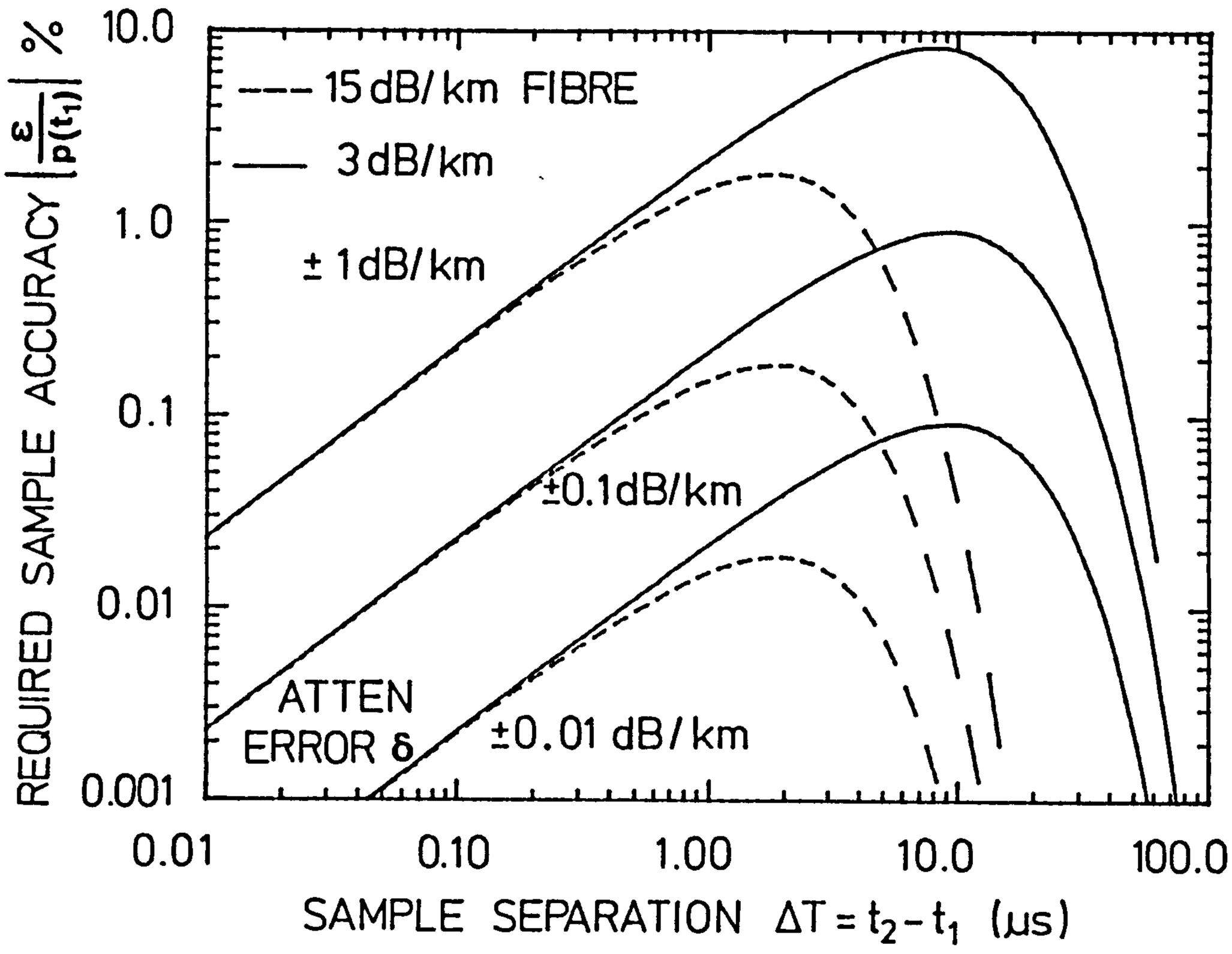

Required sample accuracy, $\left|\frac{\varepsilon}{p(t_1)}\right|$%, versus sample separation for fibres having attenuations of 3 dB km^{-1} and 15 dB km^{-1}. The turning points in the curves represent an optimum operating condition with respect to sample separation. The curves are drawn for attenuation measurement errors of 0.01, 0.1 and 1.0 dB km^{-1}.

Figure 3.4

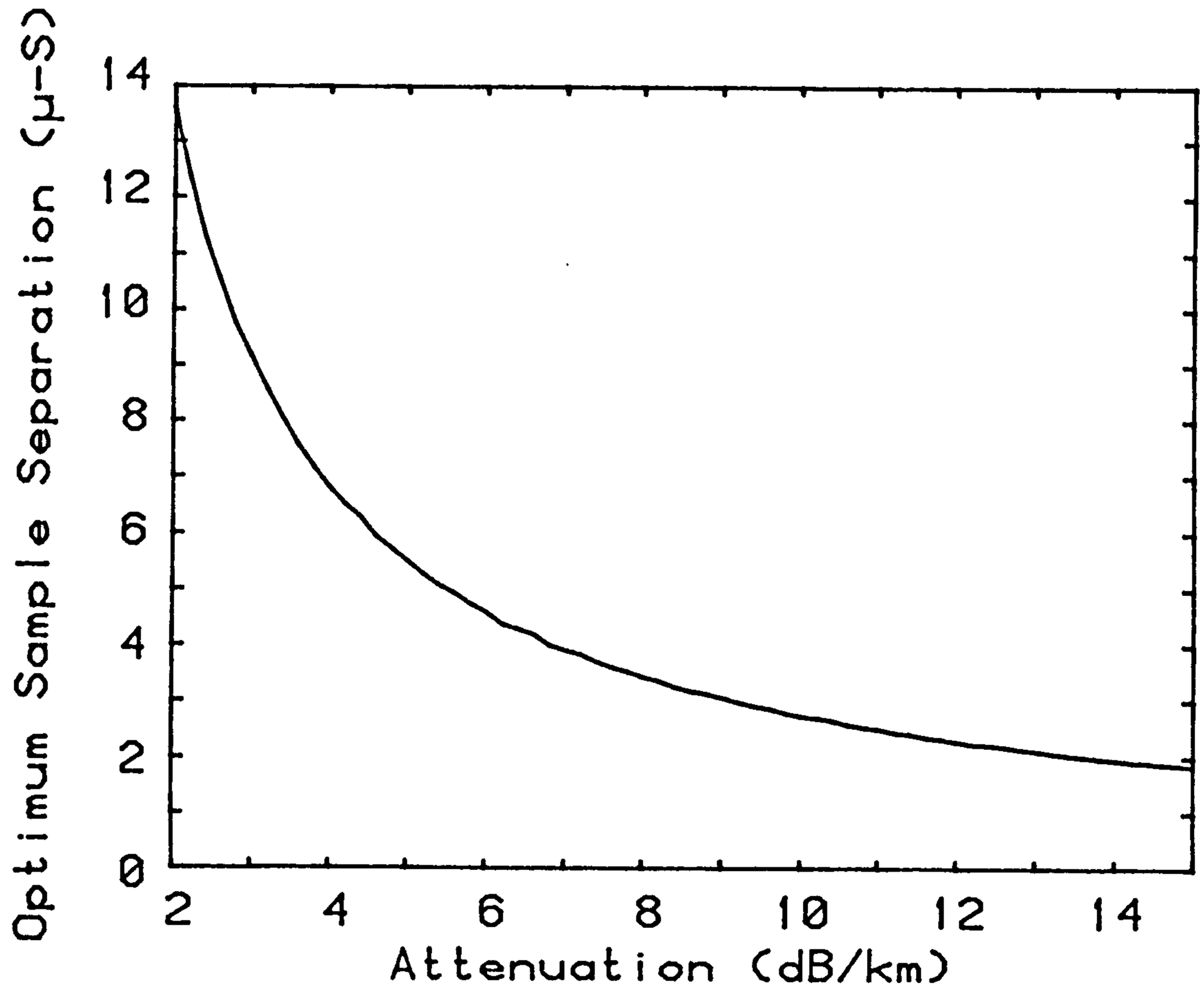

Optimum Sample Separation versus Fibre Attenuation

Figure 3.5

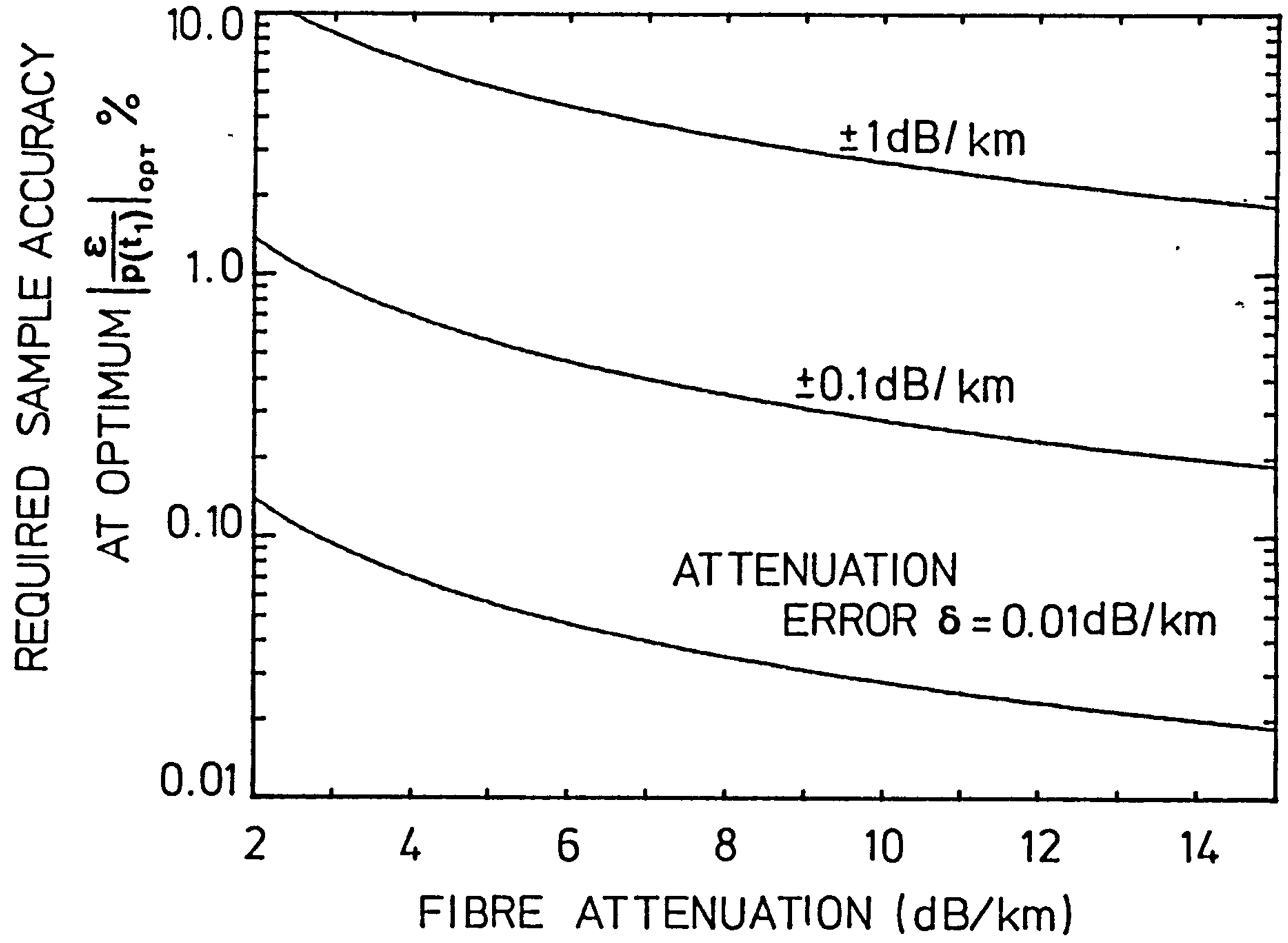

Sampling accuracy, $\left|\frac{\varepsilon}{p(t_1)}\right|_{opt}$ %, required at optimum sample separation, ΔT_{opt}, for attenuation measurement errors of 0.01, 0.1 and 1.0 db km^{-1}.

Figure 3.6

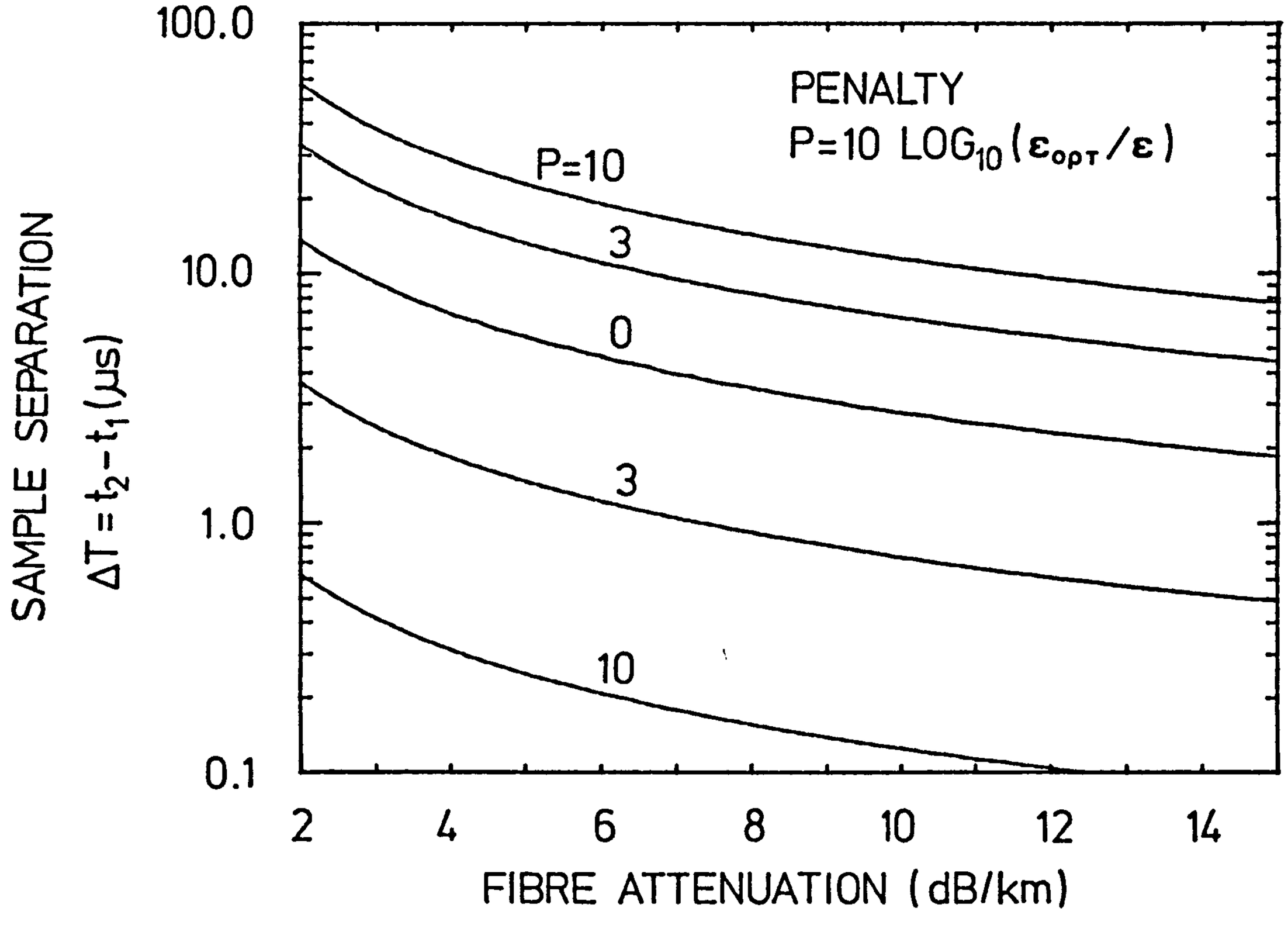

Increased sample accuracy requirements, P(dB), relative to the accuracy required at optimum spacing, ΔT_{opt}, as a function of sample separation and fibre attenuation

Figure 3.7

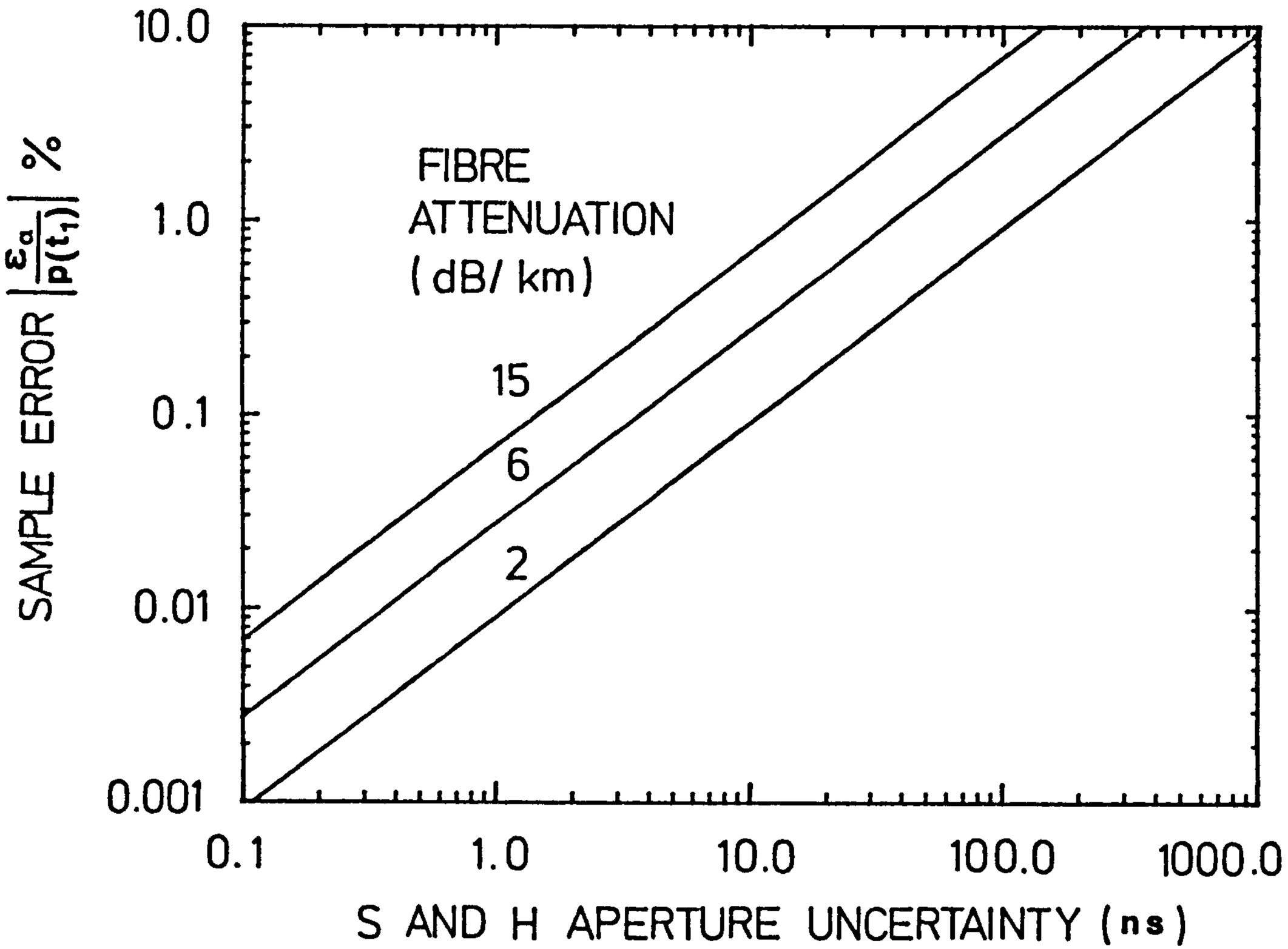

Sample error, $\left|\frac{\varepsilon}{p(t)}\right|$%, as a function of aperture-timing uncertainty for fibre attenuations 2, 6 and 15 dB km^{-1}.

Figure 3.8

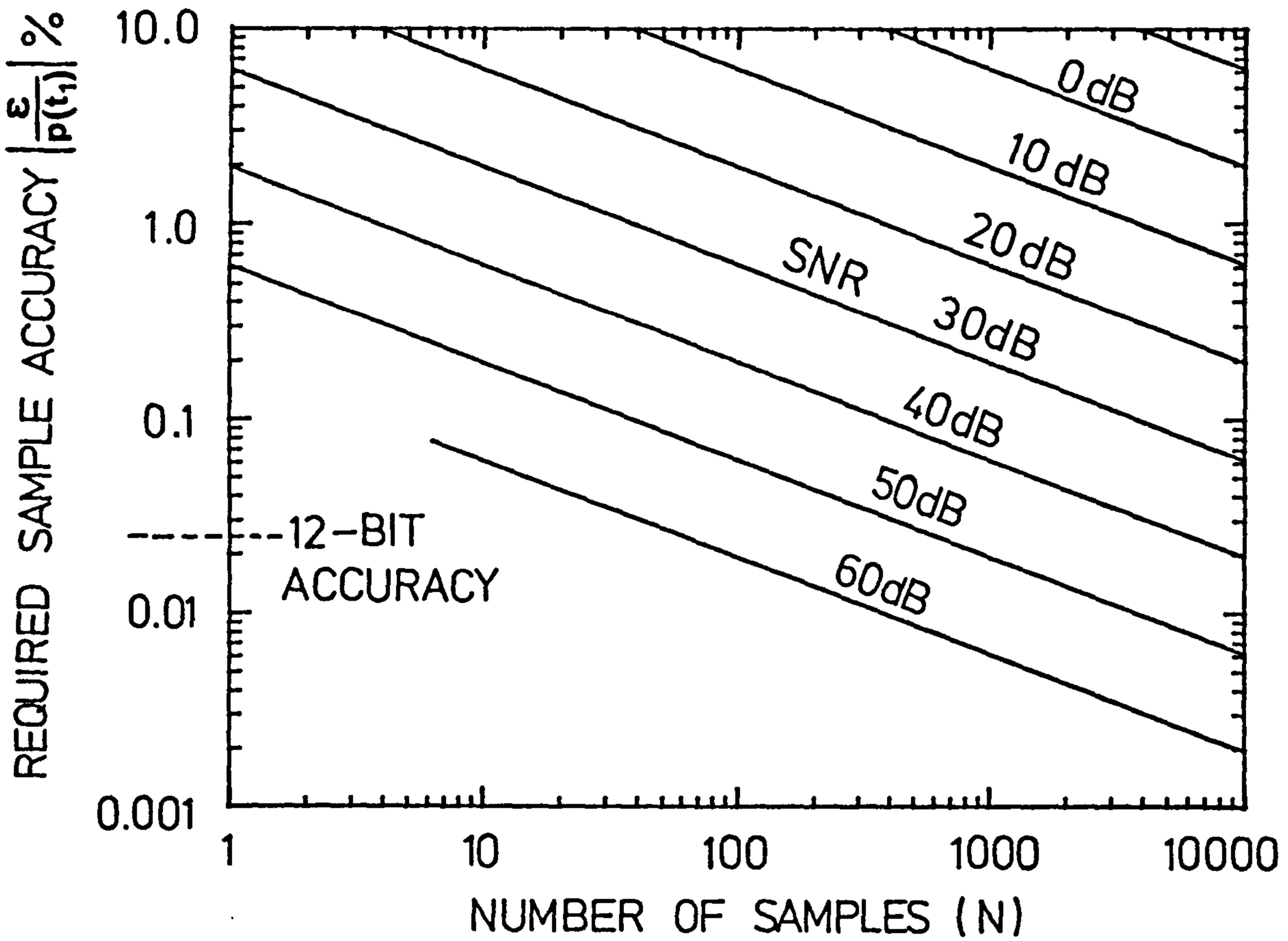

Number of samples, N, required to reduce the sampling error to $|\frac{\varepsilon}{p(t_1)}|$% for various signal-to-noise ratios (SNR)

Figure 3.9

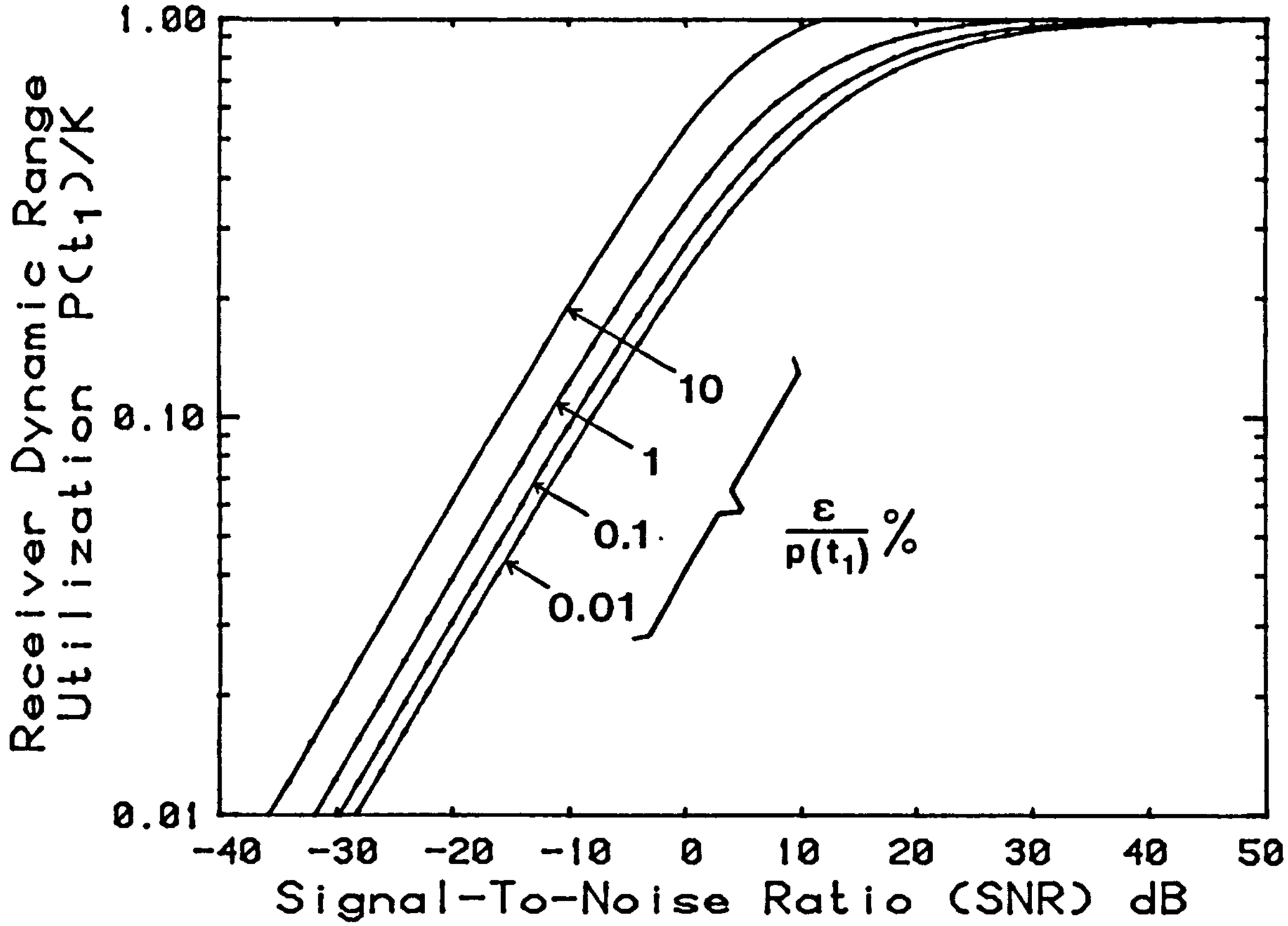

Receiver dynamic range utilization, $|\frac{P(t_1)}{K}|$, versus signal-to-noise ratio with sampling accuracy, $|\frac{\varepsilon}{p(t_1)}|$, as a parameter. When the SNR is small the dynamic range utilization must be reduced to avoid noise clipping.

Figure 3.10

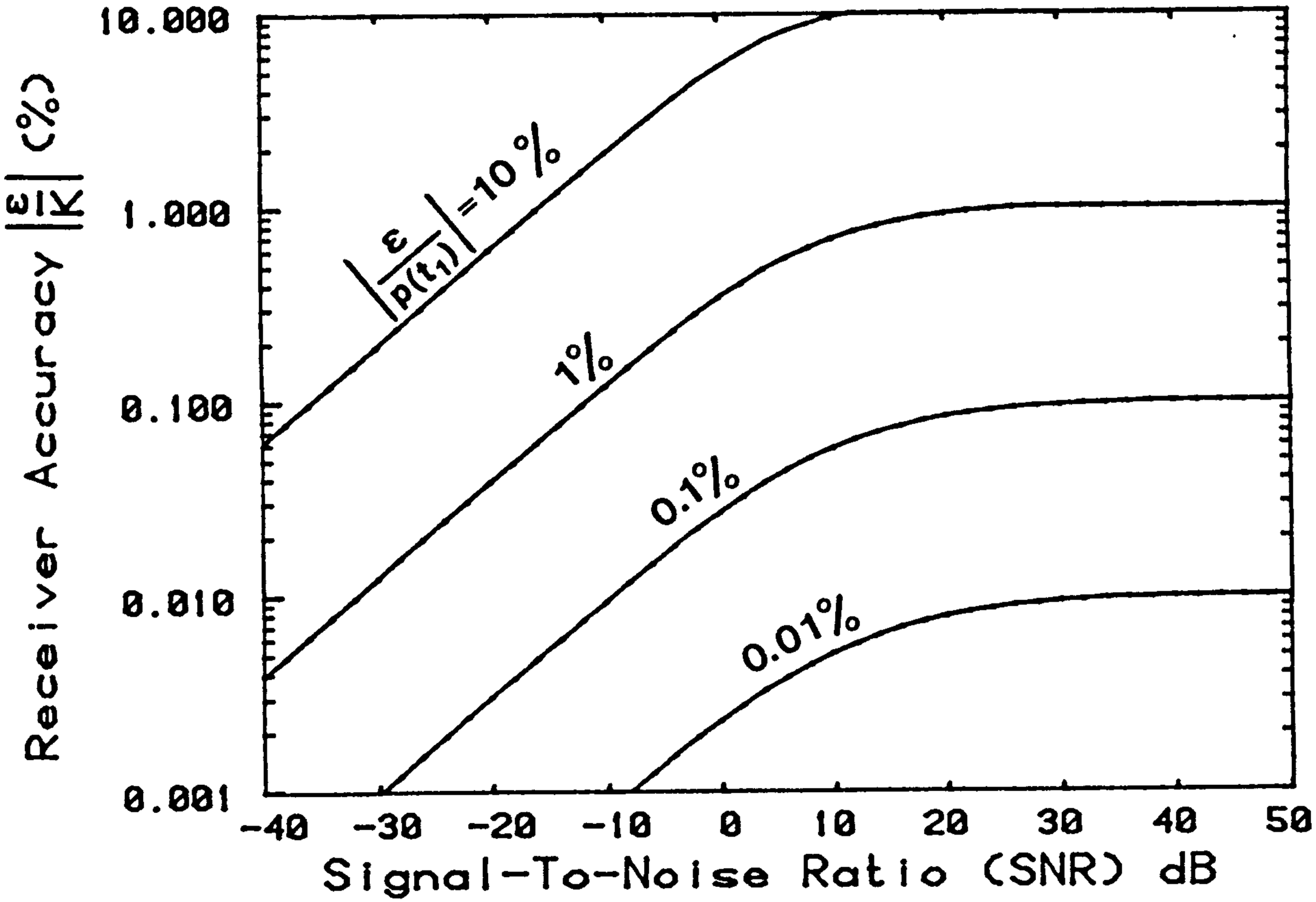

Receiver absolute accuracy, $|\frac{\varepsilon}{K}|$, required as a function of signal-to-noise ratio with sampling accuracy, $|\frac{\varepsilon}{p(t_1)}|$, as a parameter. When the SNR is small the receiver accuracy requirements are more stringent due to the necessary reduction in dynamic range utilization.

Figure 3.11

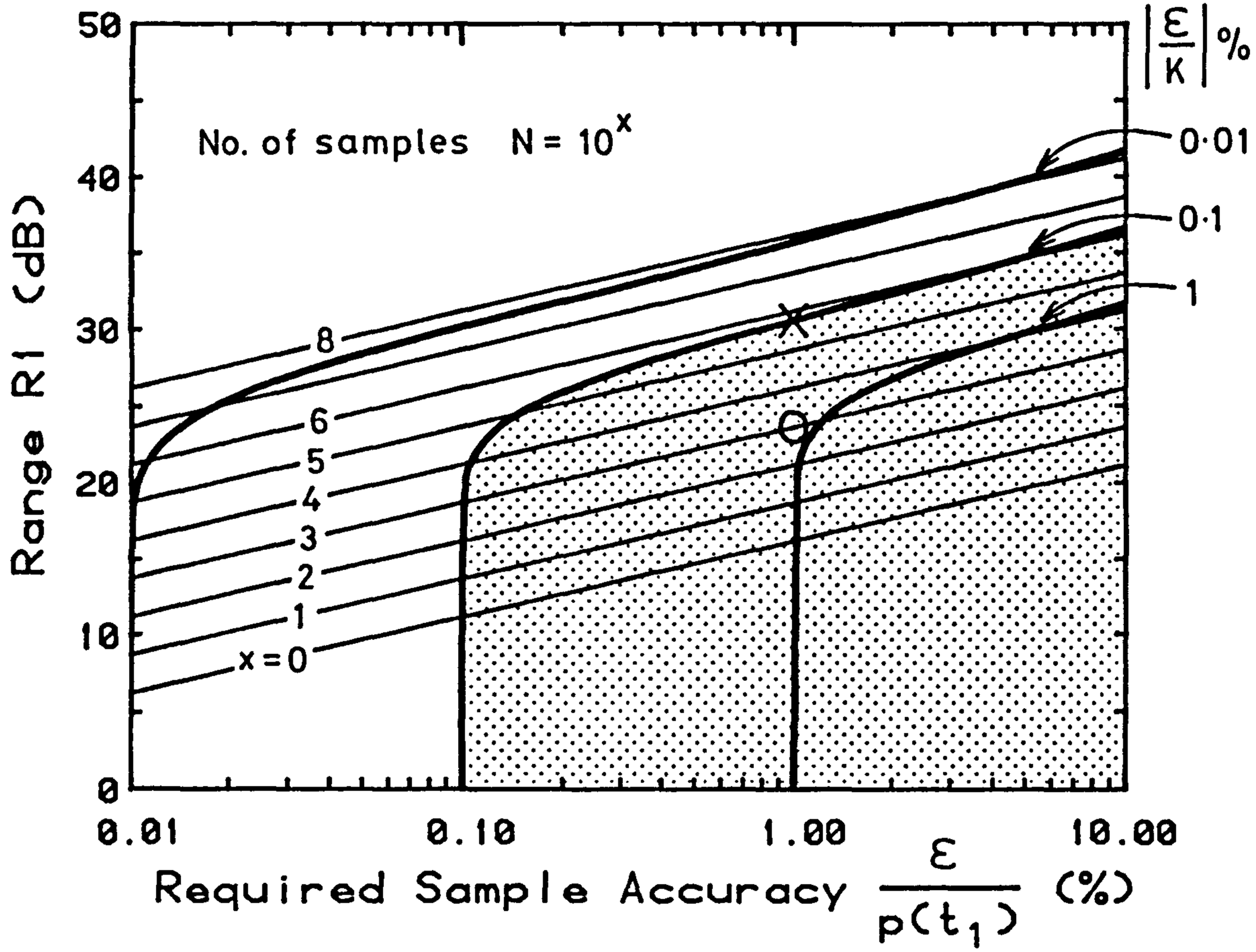

The thin lines show the range, R1, of a backscatter system versus the required sample accuracy, $|\frac{\varepsilon}{p(t_1)}|$, with the number of samples, N, as a parameter. The thick lines represent the limits to range imposed by receiver accuracy considerations. The shaded region represents the operating regime for an instrument of accuracy $|\frac{\varepsilon}{K}| = 0.1\%$.

Figure 3.12

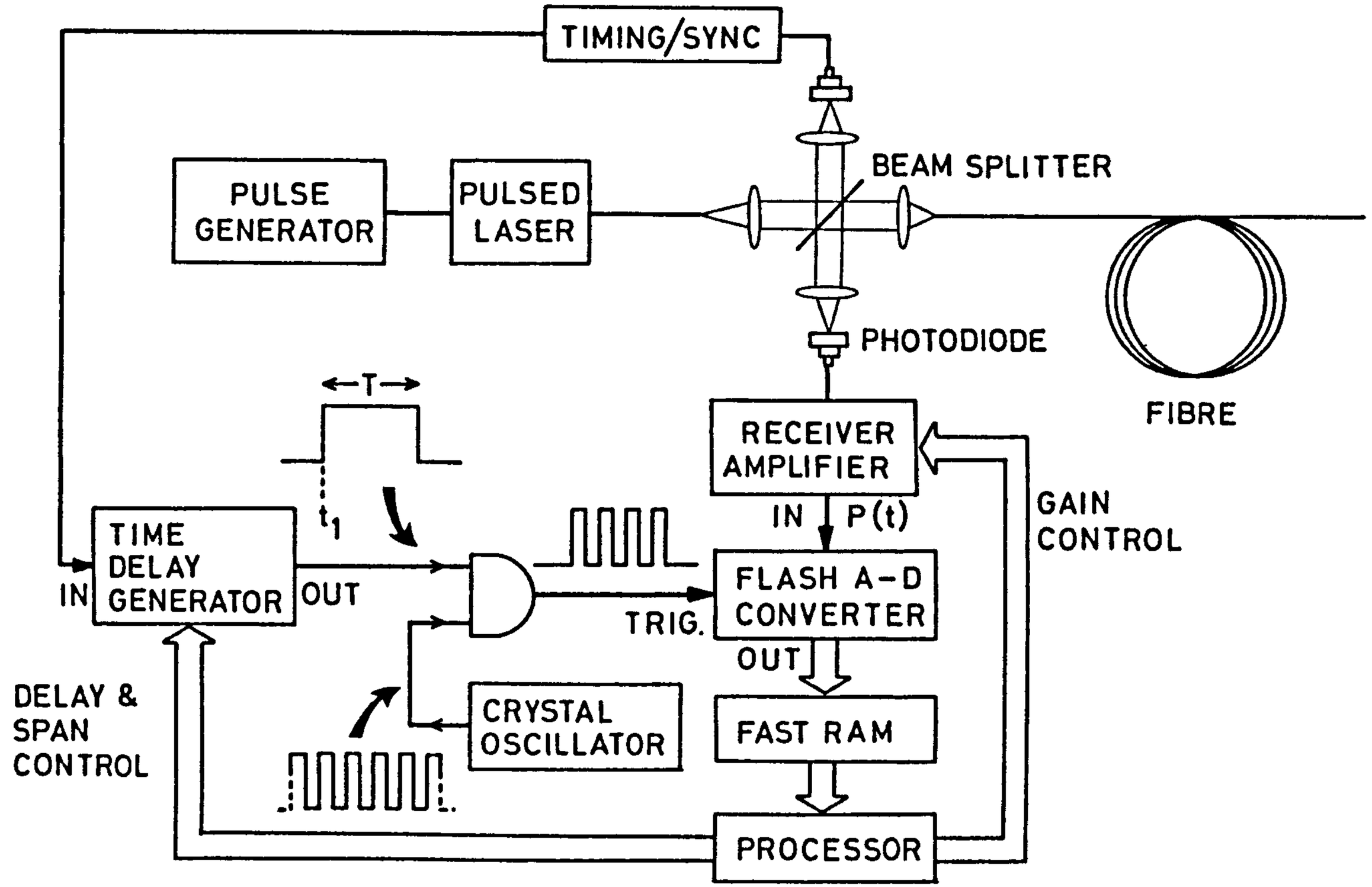

Fig. 3.13 A Multi-channel Backscatter Sampling System

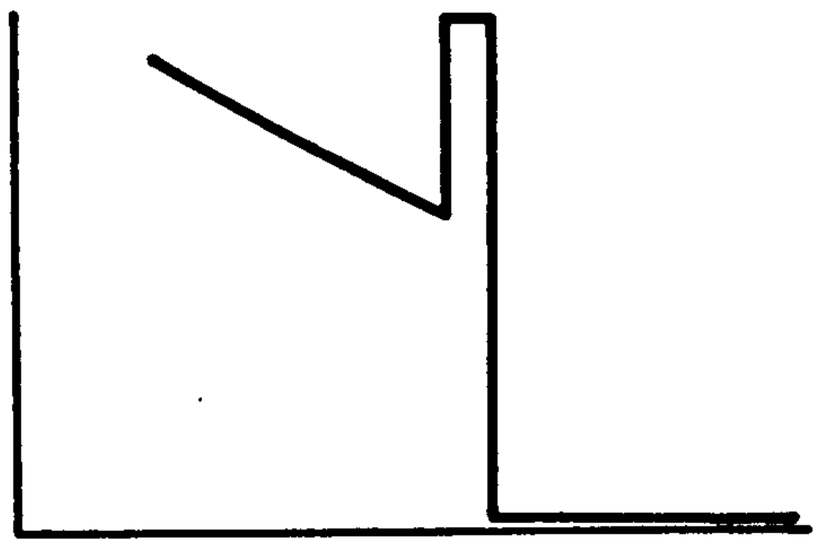

(a) reflecting complete break

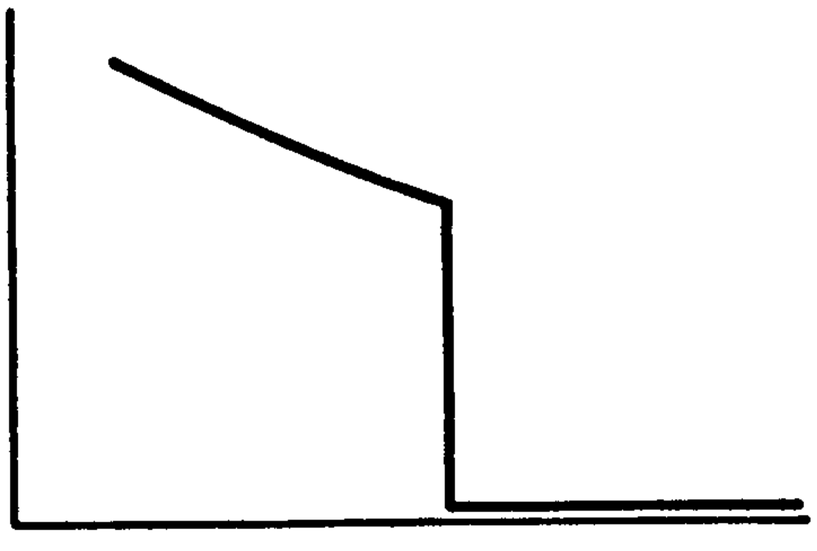

(b) non-reflecting complete break

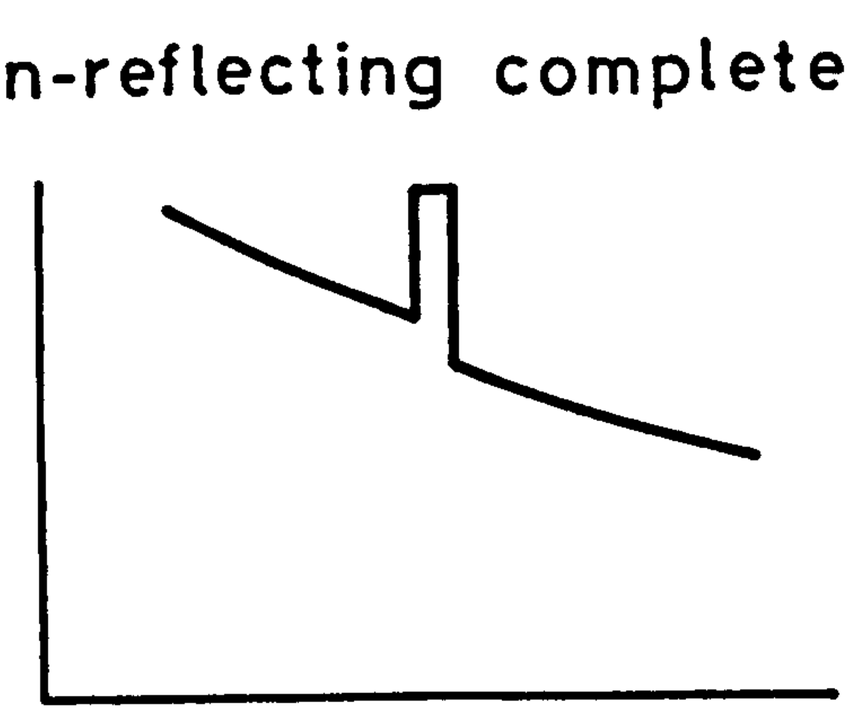

(c) reflecting partial break

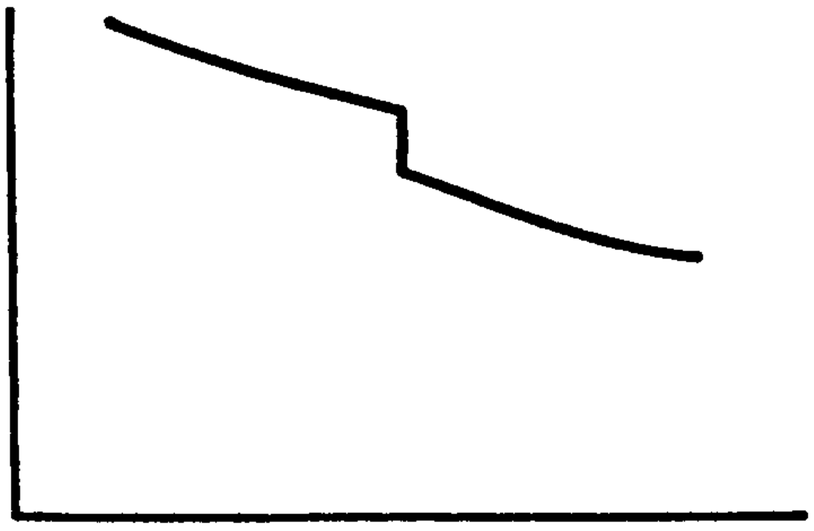

(d) non-reflecting partial break

Fig. 3.14 Classification of fault types

A 2-CHANNEL IMPLEMENTATION WITH BOXCAR AVERAGING AND A DYE LASER

An instrument developed for field applications will probably comprise fast S-H circuits, A-D converters and a semiconductor laser operating at a single wavelength (see Chapter 5). The measurements of fibre spectral attenuation presented in Chapter 7, however, required the use of a tunable source, and a dye-laser with an optical-parametric-oscillator (OPO) was chosen for this purpose. Furthermore, two boxcar integrators were used in this, the first implementation of 2-channel sampling, in order to postpone investment in expensive S-H and A-D electronics until after the technique had been proven. This chapter describes the development of the instrumentation for the spectral loss measurement.

4.1 Basic Experimental Arrangement

The dye-laser and OPO offered advantages of wavelength tunability and high power output. However, a number of measurement problems caused by characteristics peculiar to the dye-laser and OPO required solution. In particular, the laser suffers from very poor pulse-to-pulse stability (10-20% variation) and an overall drift in output power of $\pm$10% over a few minutes. The amplitude of these fluctuations depends very much on the laser-cavity alignment, the age of the dye, the condition of the flash-lamp and spark-gaps and the temperature and alignment of the OPO. In addition, a low laser repetition rate of 12.5pps compounded signal acquisition problems.

It has been emphasised previously that the 2-channel technique is insensitive to source power fluctuations and drift, since the two sample sets are averaged over the same group of laser pulses. In fact, the need to perform measurements with a relatively unstable dye-laser first prompted the development. Since then, however, the 2-channel approach has proved useful with other lasers because of both immunity to source noise and drift, and due to its proven accuracy in resolving the local fibre attenuation.

The basic experimental arrangement for the 2-channel method with the dye laser and boxcar integrators is shown in

figure 4.1. Optical pulses of 1 μs duration, tunable over the wavelength range 580 nm to 2.6 μm, emanate at a rate of 12.5 pps from the dye-laser and OPO system. An optical shutter, designated 'the Pockels cell modulator' allows an 80 ns slice of the optical pulse to pass,the latter which is then launched via a set of lenses into the fibre. The backscattered light from the fibre, travelling in the opposite direction to the original optical pulse, is directed by a 50% beam-splitter to a silicon avalanche photodiode (APD) for detection and amplification. The output of the amplifier is connected to two linear gates (or boxcar integrators) which perform waveform sampling. Samples are taken at times t_1 and t_2 determined by a time delay generator which is triggered by a pulse from the optical modulator. The two samples are measured by a DVM whose input is switched rapidly from one gate to the other, and the result is loaded into a computer for further averaging and calculation. The experiment is automated and the computer controls the delays t_1 and t_2 and other circuit switching operations.

The finer details of the optics and data acquisition system are shown on figures 4.2 and 4.3 respectively, and these are described in the following sections.

4.2 Dye-laser and Optical-Parametric-Oscillator (OPO)

4.2.1 Dye-laser

The dye laser[139] used for backscatter spectral attenuation measurements is a flash lamp pumped Chromatix CMX-4 laser. By changing the dyes and adjusting a Fabry-Perot etalon in the cavity, the laser may be tuned from 0.4 to 0.8 μm. For the dyes Rhodamin 6G in 1:1 water/methanol and 4% Amonyx in water, the power output and tuning ranges are respectively 10kW, 580-620 nm and 6 kW, 595-635 nm, in approximately 1 μs width pulses.

Dye lifetimes and pulse-to-pulse stability are important considerations when choosing a dye for backscatter measurements. Although the former dye is slightly inferior from a stability viewpoint, its long lifetime was found to be useful in these experiments.

The laser may operate at up to 25 pps, although much improved stability is achieved for slower repititions. For the present application, however, the rate is limited to ∿15 pps by the parametric oscillator and a figure of 12.5 pps was chosen as a compromise between stability and measurement time.

4.2.2 Optical-Parametric-Oscillator (OPO)

The majority of wavelength tuning is achieved by a $LiNbO_3$ parametric oscillator pumped at about 0.6 μm by the dye-laser. The output-signal and idler wavelengths, λ_s and λ_i respectively, are determined by both the crystal temperature and the pump wavelength λ_p,

$$\frac{1}{\lambda_p} = \frac{1}{\lambda_s} + \frac{1}{\lambda_i} \quad \ldots (4.1)$$

Variation of the pump wavelength produces fine tuning of the final output wavelength, while major changes are produced by adjustment of the oven temperature and changes of the OPO-cavity mirrors. The OPO may be tuned from 0.76 to 2.6 μm, although four mirror changes are required. The present backscatter measurements over the wavelength range 0.77-1.06 μm require that three mirror changes be made. The OPO output is linearly polarized and orthogonal to the dye-laser pump and typical output powers are 200-500 W.

4.3 Pulse slicing

The ∿1 μs-width pulses from the dye-laser and OPO system must be shortened for backscatter applications (see equation (2.30)). The technique used here, shown in figure 4.2, is similar to the arrangement developed by A. H. Hartog[42,140] for experiments on material dispersion in optical fibres. The linear-polarized, wavelength-converted pulse from the OPO passes through a Pockels cell and to a prism-polarizer which is orientated to extinguish the incident beam. A beam-splitter placed between the OPO and the polarizer, directs a small fraction of the optical power onto a pin-photodetector. This generates an electrical pulse which triggers a spark-gap[140,141] via a high-tension (H.T.) power supply. The spark in the gap is sustained for a period determined by the length of a transmission line, the latter charged through a resistor from

the H.T. supply (the period is 80 ns ≡ 8 m of RG 8A/U in these experiments). During spark-gap breakdown, a high voltage (∿5 kV) is placed across the Pockels cell and causes rotation of the polarization. In this way an 80 ns slice of the original 1 μs optical pulse passes through the polarizer and is launched into the fibre for the backscatter measurement. Note that only the infra-red is allowed to pass to the fibre. Any visible light from the dye laser pump which is not wavelength converted in the OPO is blocked by the filter shown in figure 4.2.

4.4 Optical Pedestal

During the pulse slicing process, it is unavoidable that a small fraction of the infra-red 1 μs pulse, designated the 'pedestal' passes through the polarizer and into the fibre. The ratio of the energy in the 80 ns sliced pulse (which 'sits' on the 'pedestal') to the energy of the pedestal is a measure of slicing efficiency. For backscatter measurements this efficiency must be maximized in order to prevent distortion of the backscatter waveform and dispersion in the local attenuation characteristic (see equation (2.30)). In practice, it is found that with a good polarizer, a rejection ratio of 80:1 can be achieved. At this level the pedestal causes negligible distortion of the backscatter waveform.

4.5 Anti-reflection Cell

The backscatter waveform, shown in figure 4.4, consists of three distinct parts:

i) an initial pulse resulting mainly from the 4% air-glass Fresnel reflection at the fibre input;

ii) an exponential 'tail' caused by the Rayleigh (assumed mechanism) backscattered light;

iii) a final pulse from the 4% glass-air Fresnel reflection at the far end of the fibre.

The Rayleigh scattered signal obtained for a 0.2 NA graded index fibre having an attenuation of 3 dB km^{-1} and with a 100 ns pulse is approximately 45 dB below the incident power level (see section 2.4). Thus a considerable amplification is

necessary. The presence of relatively large initial and final Fresnel reflection pulses, however, may cause problems of system overload and any interference with the exponential backscatter signal must be avoided.

In a good backscatter system, proper amplifier design limits overload to a time corresponding to the width of the input optical pulse. Unfortunately, in the present instance, this corresponds to ∿1 μs due to the optical pedestal described in the previous section. Thus, measurements of local attenuation could not be made in the first ∿100 m from the fibre input.

Aside from using an amplifier with fast overload recovery, good optical design may also minimize reflections. The method used here is based on a concept invented by A.H.Hartog and independently by the British Post Office[142]. The optical fibre is mounted in a cell filled with an index-matching liquid, as shown in figures 4.2 and 4.5. The angle of the fibre is such that the refraction at the cell front-face causes light to be directed along the fibre axis. Because the fibre is immersed in an index-matching medium there is no Fresnel reflection at the fibre input. A Fresnel reflection does occur, however, at the air-glass interface at the front of the cell, but this face is cut at an angle, and therefore reflected light is directed out of the line of the on-coming beam and is not detected. The backscattered light which returns to the fibre input suffers a reverse refraction and is directed by a beam-splitter to the receiver. The method is extremely efficient and can achieve a front-face reflection of magnitude less than the backscattered power at that point (see figure 4.4).

The Fresnel reflection from the far end of the fibre is not usually a problem since it occurs after the 'Rayleigh tail'. However, it can be eliminated, if desired, by placing the far end of the fibre in an index-matching medium.

There are also other methods which may be used to minimize front-face reflection[2,4,99,143]. One of these is utilized in Chapter 5.

4.6 Mode-scrambler

It is shown in section 2.7 that the backscattered power depends on the mode energy distribution of the forward travelling pulse. In particular, variations in the mode pattern along the fibre results in a variation in the back-scatter factor and an error in measured fibre loss. This error is expected to reduce when far from the fibre input due to the stabilization of modes into an equilibrium distribution (see section 2.3). The distance over which an equilibrium is obtained may be from tens of metres to a few kilometres.

When using the dye-laser, the fibre in general is under excited and the distance over which an equilibrium is achieved is expected to be larger. Mode-scrambling[65,144,145] is a commonly used technique which assists the equilibrium.

The method used in Chapter 7 is shown schematically in figures 4.1 and 4.2. The fibre is sandwiched longitudinally between two mating linear gears of pitch 1 mm and an overall length of 5 cm. The gear material is a plastic (PVC) and does not damage the silicone primary fibre protection. Compression of the sandwich causes microbending and a re-distribution of power in the guide. Low-order modes are converted to high-order and vice-versa. In addition, some power is also converted beyond cut-off and is radiated from the guide.

Unfortunately, the distribution of modes at the scrambler output is not certain due to the ill-defined nature of the excitation and mode mixing[65,144]. However, in many cases (e.g. if the guide is under-excited) the re-distribution of power does assist equilibrium and the effective coupling length is reduced. The effect of the mode-scrambler on the backscattered power is considered in section 7.3.

4.7 Amplifier

The amplifier designed for measurements with the dye-laser is shown in figure 4.6. The salient features of this amplifier only shall be mentioned here. A more detailed discussion of optical receiver design is included in reference 146.

The amplifier has a J-FET input with 3-stages and an overall feedback transimpedance of 56 kΩ and operates over a frequency range dc-15 MHz. The biassing of each stage is provided by the previous stage and by dc-continuity of the closed feedback loop. The high frequency cut-off satisfies requirements for a backscatter measurement as detailed in section 3.5. The requirements on low frequency cut-off are that it must be less than the pulse repetition rate in order to prevent distortion caused by signal integration. In the case of backscatter measurements with the dye-laser, the repitition rate was only 12.5 Hz and therefore the amplifier must operate almost down to dc.

Fast overload recovery is desirable in order to prevent interference of the large front-face Fresnel reflection with the exponential Rayleigh tail (see section 4.1.4). The amplifier was designed with no biassing capacitors to aid in this regard[147].

The noise current of the amplifier measured with an rms voltmeter and referred to the input was 1.4 pA $Hz^{-\frac{1}{2}}$ and the corresponding output noise voltage was 0.3 mV rms. In view of the large optical power available from the dye-laser and OPO system (see section 4.2), further amplification or noise improvement was not required. A modification of the amplifier design described in Chapter 5 results in an improved noise performance, although at the expense of increasing the low frequency cutoff.

The dc offset at the pre-amplifier output and a need to drive a 50 Ω load required that a voltage translation interface be developed (see figure 4.6). The special characteristics of this circuit are that it translates the signal with negligible attenuation and the output voltage can be finely adjusted to zero by a resistance external to the signal path. The latter facility enabled a compensation to be made for drift which was found to be a few hundred millivolts over a period of 5 minutes.

The Si-APD can be direct coupled to the amplifier input, however, in practice it was found useful from the viewpoint of drift that it be capacitively coupled and this resulted in an increased low frequency cutoff of less than 0.1 Hz.

For a further discussion of amplifier design and requirements, refer to reference 146.

4.8 2-Channel Sampling with Boxcar Integrators

Boxcar integrators (or linear gates) operate by integrating the signal over a number of cycles in order to achieve the desired sample accuracy (see section 3.1). For the present application, however, the SNR is high due to the large laser power. Thus, an implementation employing fast sample-hold circuits is superior since in principle the attenuation may be calculated from 2-channel sampling of a single backscatter pulse. Furthermore, when the SNR is low, digital averaging can be used to achieve the desired accuracy (see section 3.6).

It is stated at the beginning of the chapter that boxcar integrators are used in this, the first implementation of 2-channel sampling, in order to postpone investment in expensive S-H and A-D circuits until after the technique had been proven. The implementation was useful, however, in that it showed that standard equipment used by other researchers[2-4], could be adapted to 2-channel processing, provided that sufficient care and attention is given to experimental detail.

The configuration of the two linear gates, designated 1 and 2, is shown in figure 4.3. The gates[108] possess a common signal input and are independently triggered. The trigger signals, designated 't_1' for gate 1 and 't_2' for gate 2, cause sampling of the backscatter waveform at the respective times and are derived from a gate-separation-generator which determines the time difference $\Delta T = t_2 - t_1$. The gate-separation-generator is triggered from a Hewlett-Packard HP 5359A time-delay-generator (TDG) which in turn is synchronized to the dye-laser via switch S2 and the spark-gap-logic (refer also to figure 4.2). The function of the latter is described in section 4.10. The initial delay t_1, to the first sample is determined mainly by the HP 5359A which is programmed from a minicomputer via an IEEE-488 data interface. There is also a small contribution to t_1 due to propagation delays in cables and electronics which is not explicitly shown on figure 4.3, but is accounted in

experimental results.

4.8.1 Aperture duration

The aperture duration or 'window' for each sample is determined by the width of the trigger pulse and is 200 ns, a compromise between distance resolution and the droop performance of the linear gates, the latter being degraded at low repitition rates[108,109].

The sampled values are the averaged signal in each sampling window. Therefore, the variation of power across the windows due to the decaying nature of the backscatter signal must be considered. However, it can be shown that for an exponential waveform the shift in the 'centre of gravity' of the power, from the centre of the gate window, is identical for both gates. Thus, the difference $\Delta T = t_2 - t_1$, is not altered. For a fibre having an attenuation of 15 dB km^{-1} the shift is only 2 ns and therefore aperture uncertainty (see section 3.4) is not degraded, even if the signal deviates slightly from an exponential character.

4.8.2 Analogue averaging

The gate duty factor (repitition period/aperture duration) with a 200 ns aperture and a repitition rate of 12.5 pps is 4×10^5. The internal time-constant of the boxcar is 1 μs[108] and the observed time-constant, from equation (3.2) is 0.4 seconds. Thus, samples taken on consecutive laser pulses by each gate are within 1/e of their final values, $p(t_1)$ and $p(t_2)$, after a period of 0.4 seconds.

Further smoothing of gate samples are provided by low-pass filters shown in figure 4.3, and these were necessary to avoid excessive variations in output due to dye-laser pulse-to pulse instability. The time-constant of these filters, called the 'external' time constant, was between 3 and 10 seconds.

4.8.3 Digital averaging

The smoothed samples, $p(t_1)$ and $p(t_2)$, at the low-pass filter outputs are measured by a Hewlett-Packard HP 3455A digital voltmeter (DVM). The DVM is switched rapidly via switch S3 and the results of many such operations are loaded into the computer for the calculation of fibre attenuation.

It should be noted that the DVM measurement cannot begin until the low-pass filter outputs have stabilized. Normally a time equivalent to five external time constants is required. In the present instance, however, waiting time is reduced by adjusting the external time constant under computer control. This facility is indicated by the dashed-line which connects the low-pass filters to the controller interface on figure 4.3. Initially, the low-pass filters are given a short 0.3 s time-constant and therefore storage capacitors charge quickly. When the capacitors are fully charged the computer switches the time-constant to 6 s and thereby provides smoothing against the laser pulse-to-pulse variation. The DVM measurement begins 1 or 2 time-constants later, after which no further improvement in analogue sample stability is normally observed.

The computer provides further noise improvement, by averaging some 75 consecutive 2-channel DVM measurements, before performing the attenuation calculation.

4.9 Alignment of a 2-Channel Boxcar System

The results in Chapter 3 indicate that an absolute sampling accuracy approaching 0.01% is desirable. Non-linearities, sample-to-hold error, offsets, droop, etc. must not degrade this specification. In the case of a 2-channel boxcar implementation, a number of problems arise due to individual gate characteristics and due to differences between the gates.

4.9.1 Gain correction

Different linear gates have different gains[108,109] and therefore a calibration is necessary. This is achieved by performing a 'gain correction measurement' (GCM) where the signal level $p(t_1)$ is measured on both gates simultaneously. It provides the correction factor for the 'signal attenuation measurement' (SAM), which is then performed by sampling $p(t_1)$

and $p(t_2)$ on the separate gates.

The gate-separation generator, shown in figure 4.3, controls the sampling times for GCM and SAM measurements. It receives an initial trigger from the laser via the spark-gap logic and HP 5359A time-delay generator, the latter which sets the time t_1. In response to a command from the computer-controller the time delay ΔT, can be set to zero (i.e. $t_1 = t_2$) for the GCM cycle, or to a finite value ΔT_{opt}, for example, for the SAM measurement. (The computer control path is shown schematically by the dashed-line joining the controller interface and the gate-separation generator.) The gain correction determined in the GCM measurement is then used to compensate for the error in the SAM result.

4.9.2 Offset compensation

Gate output offsets and drift are important when measuring voltage levels in the 6-10 volt range to an accuracy of 0.01%. Gate offsets are measured by the DVM and loaded into the computer, where they are then accounted in the attenuation calculation. It can be shown that

$$\frac{V_1}{V_2} = \frac{V_{1m}}{V_{2m}} \left[\frac{1 + \dfrac{off_2}{V_{2m} - off_2}}{1 + \dfrac{off_1}{V_{1m} - off_1}} \right] \qquad \ldots (4.2)$$

where V_1 = actual signal level into gate 1
V_2 = actual signal level into gate 2
V_{1m} = measurement value on gate 1
V_{2m} = measurement value on gate 2
off_1 = voltage offset on gate 1
off_2 = voltage offset on gate 2

The validity of the offset compensation has been tested by experiment. Typically for a 10 mV offset on both gates and for a known signal input, the ratio V_{1m}/V_{2m} was found to be in error by 1.8 in 10^3, whereas V_1/V_2 was in error by 1.6 in 10^4. This represents an order of magnitude improvement and is close to the required 0.01% resolution. Offset correction is used to amend both the GCM and the SAM results.

4.9.3 Gate triggering

A property of the linear gates[108,109] is that at low duty factors slight variations in the shape and repetition rate of trigger pulses causes considerable changes in gate offsets. Minimization of offsets is desirable, even though compensation is provided in the attenuation calculation.Thus, the gate-separation generator, shown in figure 4.3, is designed so that nearly identical 200 ns pulses trigger the gates in both the GCM and SAM cycles.

4.9.4 Gate non-linearity

The non-linearity is found to be approximately 0.02% for both gates over their full dynamic range. However,measurements are performed only over about 30% of this range and therefore the gates are within the required specification of 0.01%.

4.10 Spark-gap Instabilities and Electrical Interference

The data acquisition system described in sections 4.8 and 4.9 is triggered by pulses originating from the spark-gap breakdown, which occurs at the same time the 80 ns sliced optical pulse is allowed pass through the polarizer and into the fibre (see section 4.3 and figure 4.2). This provides the timing reference t = 0.

Instabilities in the spark-gap may cause

i) the occurrence of a missed-pulse if the spark-gap fails to breakdown in response to the H.T. trigger; the effect on the boxcar output is small provided that missed-firing is infrequent;

ii) the occurrence of spontaneous or multiple firing of the spark gap. This is a serious problem, especially if the data acquisition equipment takes a sample when the backscattered pulse is not present; the result is a rapid reduction in linear-gate output. The problem may be overcome, however, by logic electronics in the triggering line. The function performed by the spark-gap logic shown schematically in figure 4.2 is 'AND'. The data acquisition system is triggered only if the dye-laser and spark-gap operate simultaneously. Thus, multiple or spontaneous firing no longer affects the

boxcar outputs. It should be noted that the interfacing of the spark-gap logic to the high voltage and photodiode circuits is not shown in figure 4.2.

As a further precaution, cables and electronics are shielded and proper earthing is used to minimize both distortion of the analogue signal, and false triggering due to electrical interference from the flash lamp, spark-gaps and the dye and water pump motors.

4.11 Computer Control

Signal and offset measurements were originally made with the DVM switched manually between the two gates. However, due to instability in the dye-laser[139] the intervening period between the measurement of one gate and the next, was sufficient to produce large standard deviations in results. It was necessary to reduce switching and measurement time to an interval sufficiently short that the effect of optical power fluctuations was negligible. A computer-controller provided the solution.

The implementation shown in figures 4.3 and 4.2 uses a Tektronic 4051 controller with an 8 K memory. A Hewlett-Packard HP 3355A DVM performs the A-D conversion and a HP 5359A time-delay generator sets the time of the first sample at $t = t_1$. Both instruments are programmable and operate in response to controller commands which are conveyed over an IEEE-488 general purpose interface bus (GPIB).

In addition, a multi-purpose controller interface, shown on figure 4.3 and also compatible with the IEEE-488 standard, enables the computer

i) to switch the DVM to read gate 1, gate 2 or the amplifier output (S3);
ii) to change the low-pass filter from a short 0.3 second time-constant, which allows fast integration when the laser is initially turned on, to a longer 6 second time-constant prior to the DVM measurement, so that the laser power fluctuations are sufficiently smoothed;
iii) to initiate or terminate laser operation by connecting it to a 12.5 Hz mains-synchronized clock via switch S1;
iv) to ensure that, when the laser is turned off, the linear

gates continue to receive trigger pulses from the same 12.5 Hz clock via S2, so that gate outputs do not drift and are correctly set to zero at the beginning and completion of each measurement. This enables the computer, via the DVM, to perform the gate offset measurements required for offset correction in the attenuation calculation;

v) to switch S2 so that when the laser is operating the data acquisition system is synchronized to the optical signal via the spark-gap logic;

vi) to cause the gate-separation generator to switch from GCM (coincident trigger) to SAM (delayed trigger) operations (see section 4.9).

Under computer control the total measurement time for an attenuation calculation on a single fibre section is approximately 2 minutes. This includes the time for both GCM and SAM cycles and two offset compensations.

Measurement results are loaded directly into the computer and stored on magnetic tape. The GCM and SAM cycles each comprise the average of 75 DVM samples of the two gate outputs. In addition, offsets are measured prior-to and at the completion of each cycle. Thus, the method utilizes both hardware averaging in the form of low-pass filtering and software averaging in the computer, to smooth optical power fluctuations.

Three factors are not under computer control.

i) The backscattered power level is manually adjusted using a variable optical attenuator in the signal path (figure 4.2) and by control of the APD gain. In a field-instrument, an automatic gain-controlled amplifier is a better alternative (see Chapter 5).

ii) The boxcar and amplifier offsets are periodically nulled, even though compensation is provided in the computer program. This is to prevent them becoming excessive in the event of a large environmental temperature change.

iii) The wavelength of the dye-laser and OPO system must be adjusted manually (see section 4.2).

Further automation of the 2-channel experiment with the dye-laser was thought to be unwarranted.

4.12 Summary

The instrumentation described in this chapter is primarily intended for backscatter spectral loss measurements in optical fibres. The experimental results are presented in Chapter 7, where the backscatter method is compared to the more-standard cutback technique.

Two types of measurements can be performed with the 2-channel boxcar system and dye-laser. Firstly, the spectral attenuation characteristic of a fibre may be determined by positioning t_1 and t_2 at the beginning and end, respectively, of the section under test, and then tuning the optical wavelength. Secondly, the length variation of loss at a particular wavelength (i.e. the local attenuation), may be determined by using a small sample separation (e.g. $t_2 - t_1$ = 500 ns ≡ 50 m) and stepping t_1 along the length of the fibre.

Highest accuracy in measured attenuation is achieved if the sample $p(t_1)$ is maximized within the dynamic range of the boxcar integrators; for both spectral- and length-dependent measurements the sample magnitude is adjusted to fall between 6 and 10 volts. Offsets are checked to ensure that they remain within ±3 mV at the gate outputs. In the case of the spectral measurement the dye-laser and OPO wavelength is adjusted manually and set with the aid of a monochrometer. In the case of the length measurement, the time-delay t_1 is automatically set by the computer.

The Execute Key on the computer initiates the measurement. Readings of gate 1 and 2 are taken for both the gain-correction (GCM) and signal-attenuation measurements (SAM). After a 2 minute period, the program terminates and the calculated fibre attenuation is displayed on the VDU. A complete spectral or length measurement of a fibre takes a few hours, depending on the number of points; minor adjustments to signal levels and offsets are required throughout. The long measurement time is due mainly to the low repitition rate of the dye-laser and the need to average pulse-to-pulse amplitude variations.

Typically, for a fibre with an average measured loss of 3 dB km^{-1} over a 50 m section (i.e. ΔT = 500 ns), the standard deviation of the measurement technique was found to be better than 0.05 dB km^{-1}. This small figure is adequate to enable a comparison in Chapter 7 with the more-standard cutback method. (The experimental development of the cutback measurement technique is described in Chapter 6).

Firstly, however, in Chapter 5, a 2-channel backscatter system based on fast S-H circuits and A-D converters, and using a semiconductor laser is described. The system which is portable and more suited to a field environment is used in Chapter 8 for the probing of fibre local attenuation.

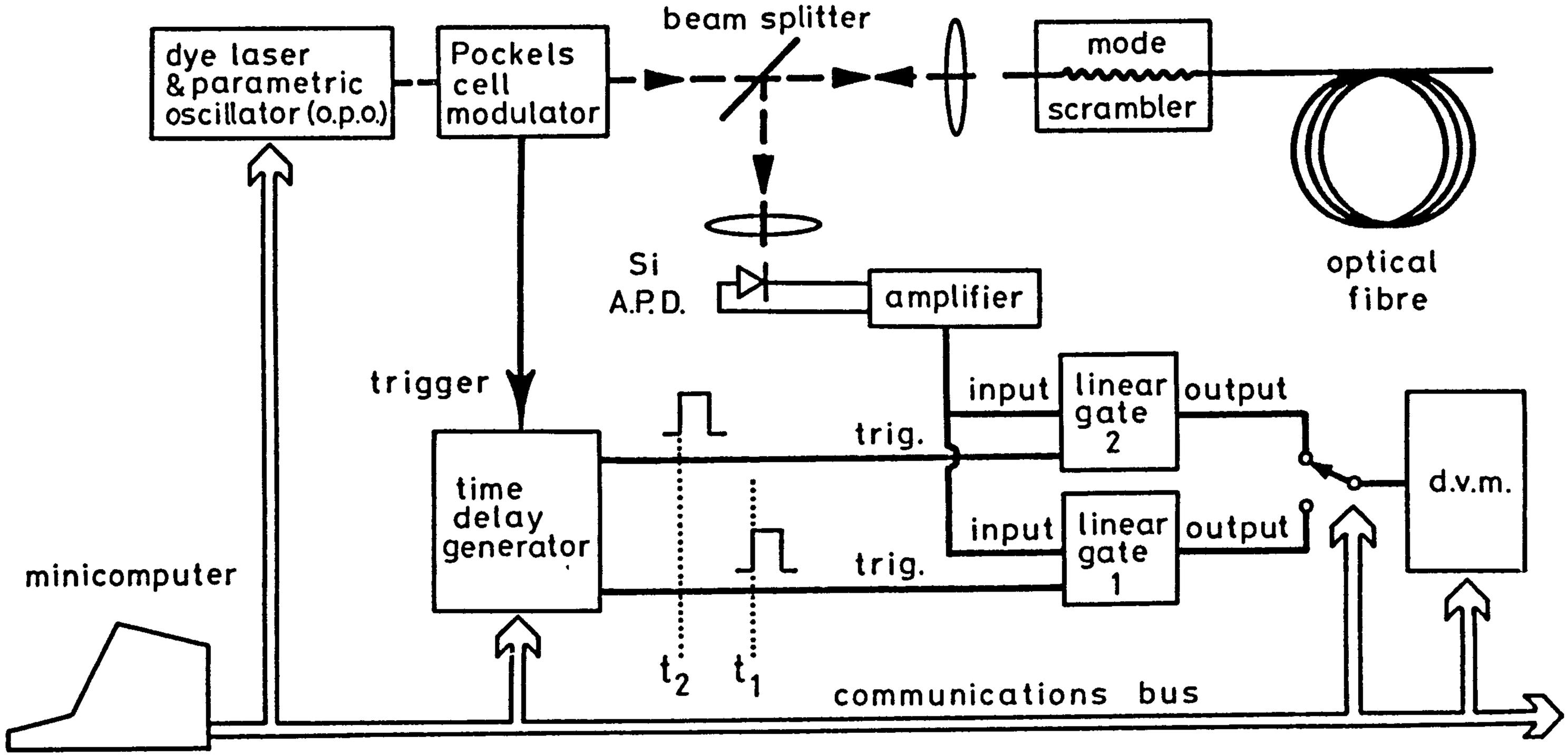

Basic experimental arrangement for Spectral-Backscatter Measurements
(Refer to Figures 4.2 and 4.3 for further details)

Figure 4.1

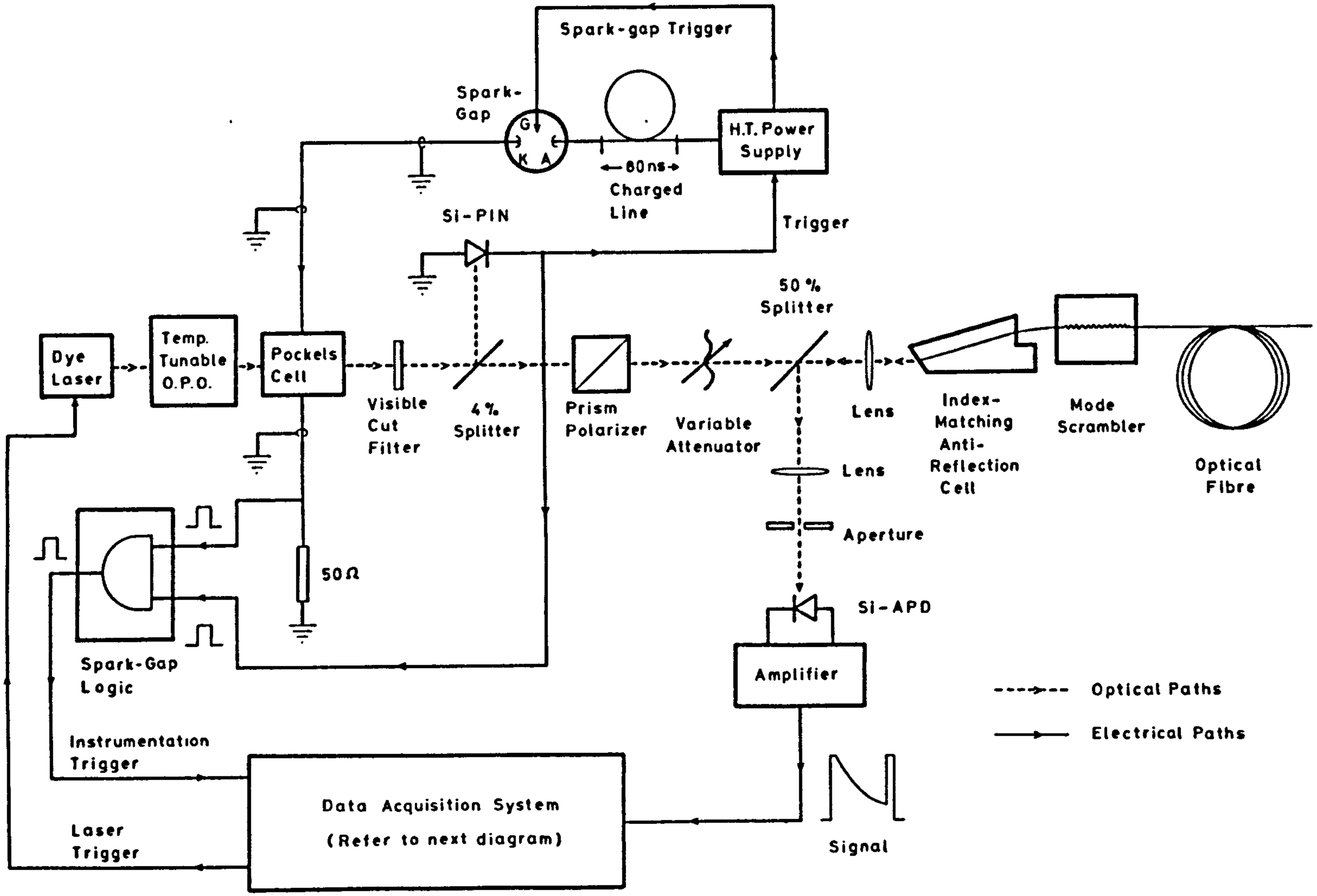

Fig. 4.2 Optical Apparatus for Spectral Backscatter Measurements

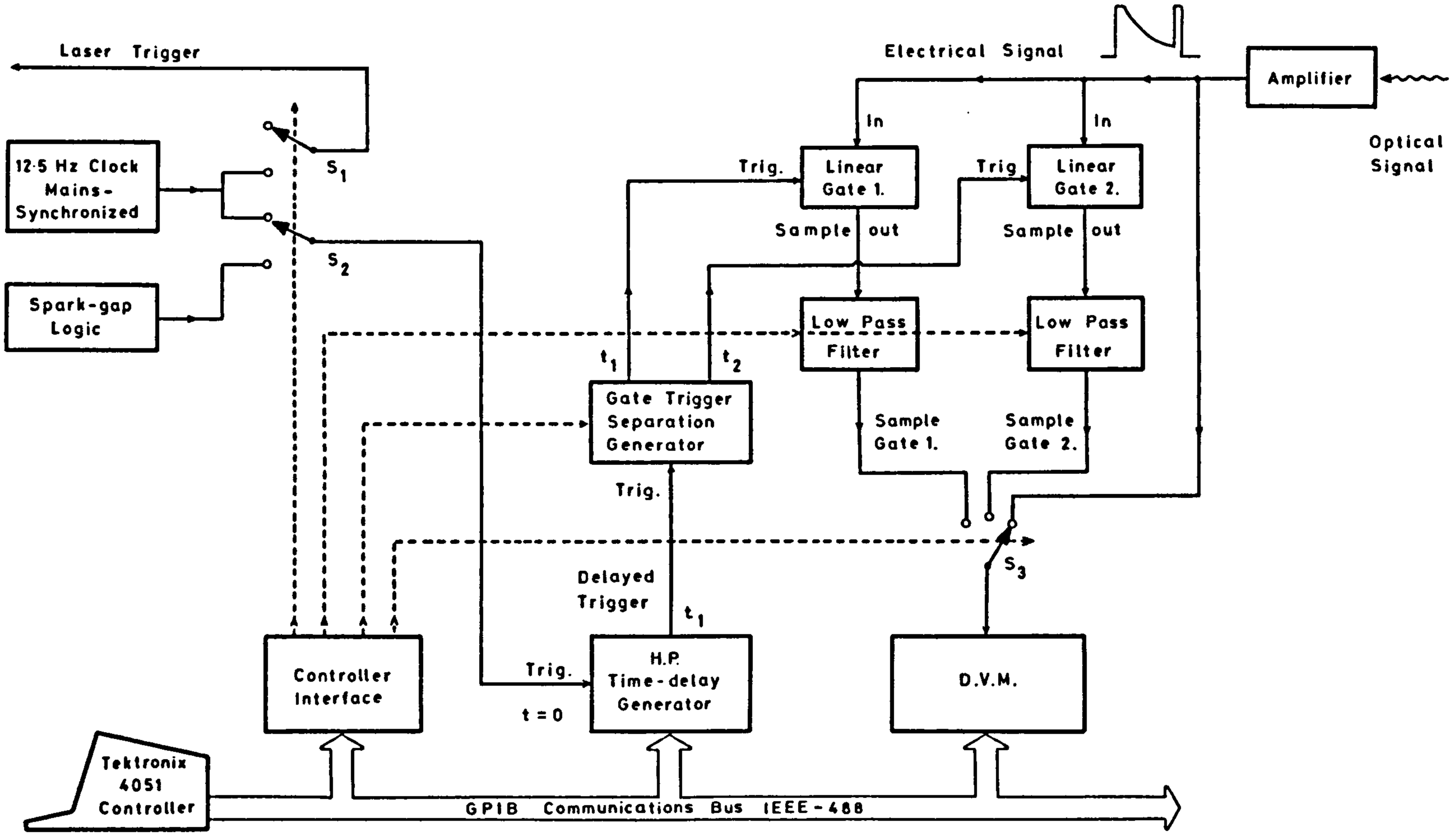

Fig. 4.3 Data Acquisition System for Spectral Attenuation Measurements

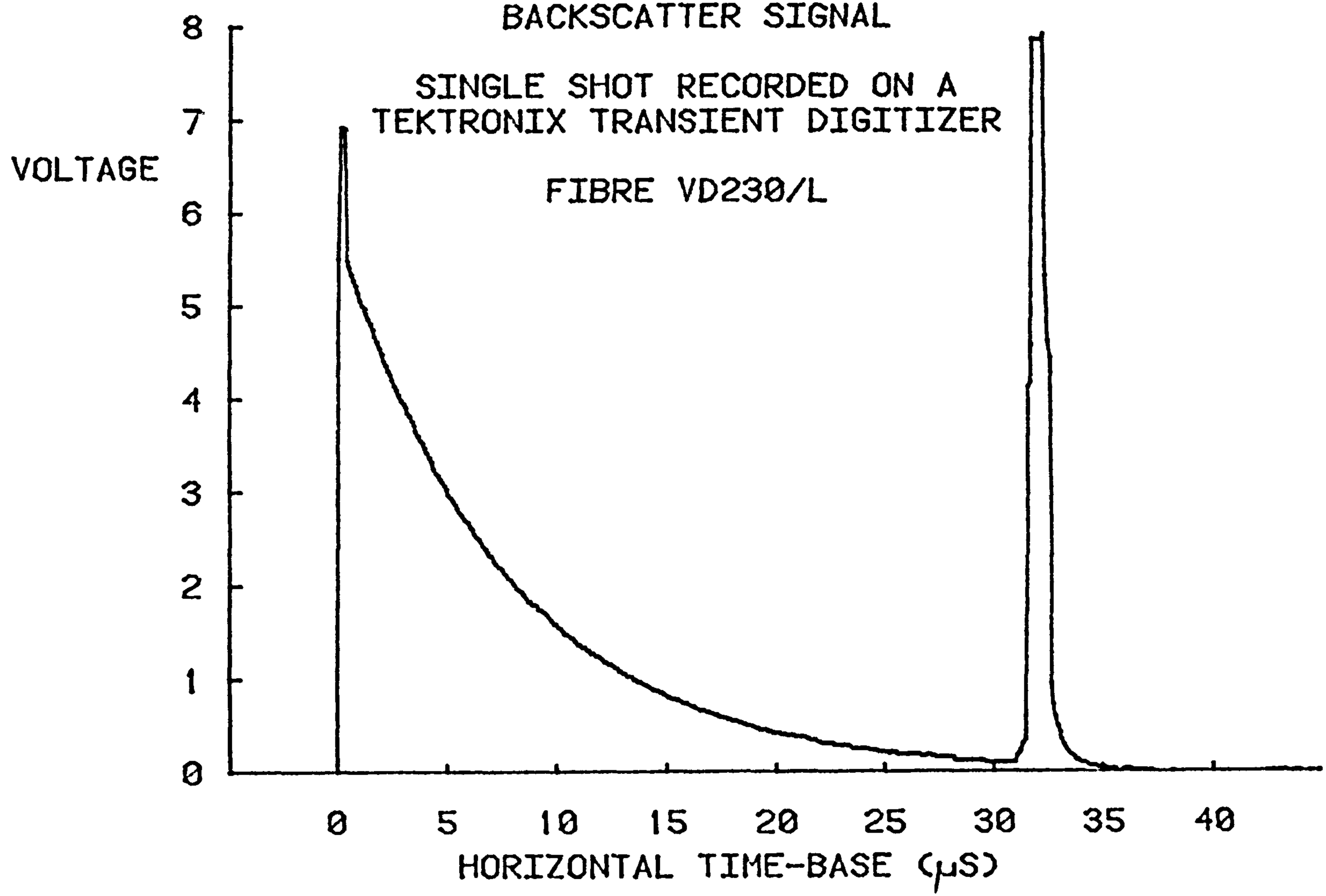

A typical backscatter waveform showing front-face and far-end reflections and the Rayleigh 'exponential tail'.

Figure 4.4

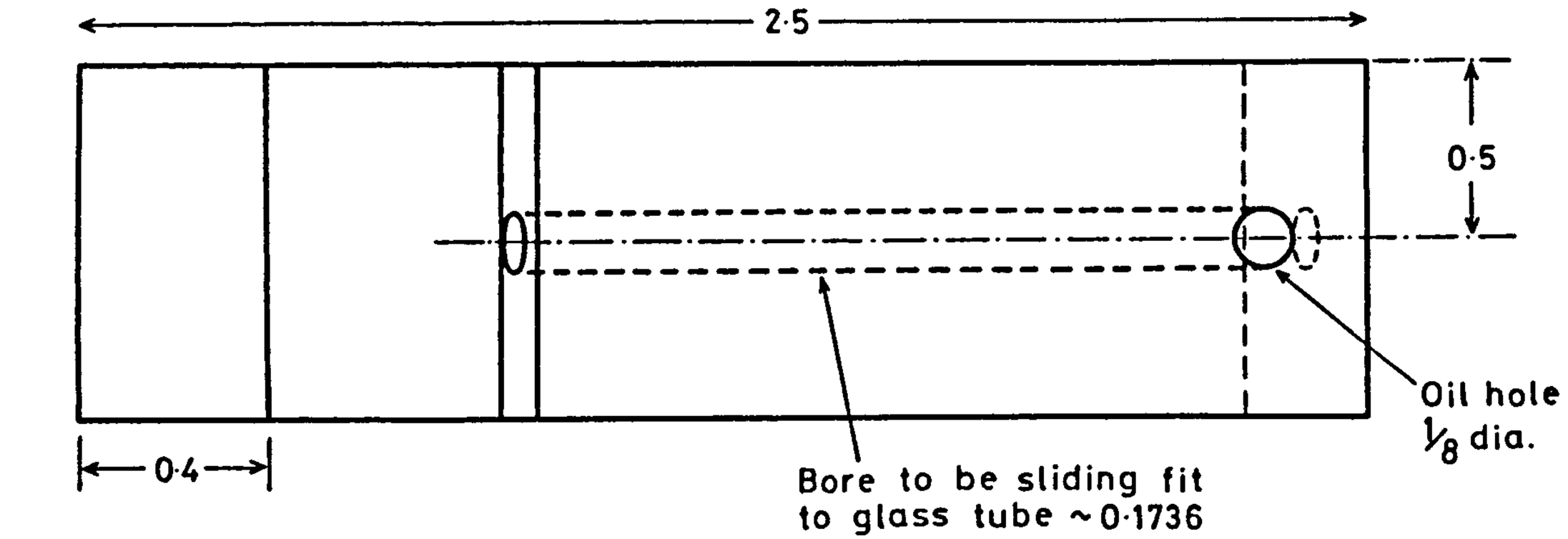

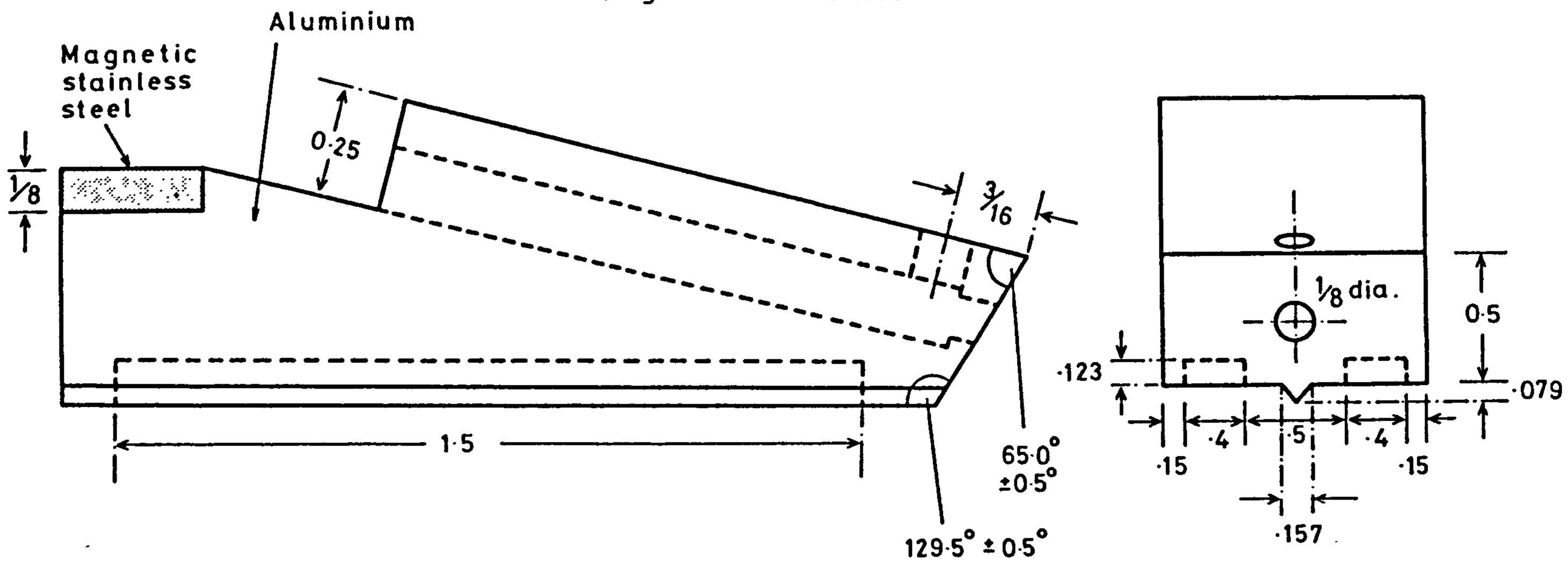

Dimensions : Inches

Fig. 4.5 Index matching cell

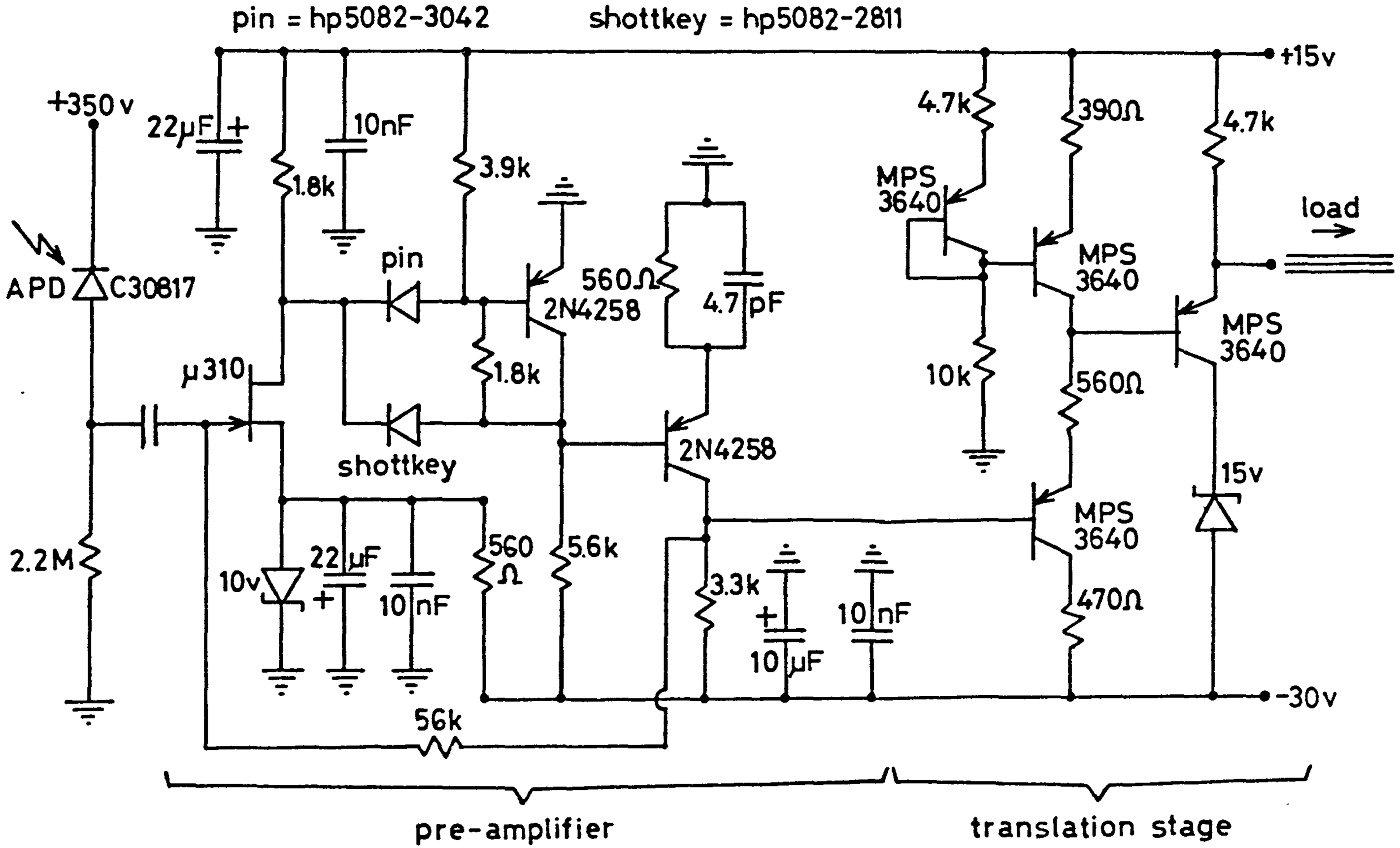

Figure 4.6 : Optical Receiver (dc-15 MHz)

CHAPTER 5

A 2-CHANNEL IMPLEMENTATION WITH FAST SAMPLE-HOLDS, FAST ANALOGUE-DIGITAL CONVERTERS AND A SEMICONDUCTOR LASER

The dye laser and instrumentation described in Chapter 4 were used for spectral backscatter measurements in the laboratory. For the field environment, however, this system is not suitable due to its bulk, expense and the need for regular calibration and alignment. A more suitable equipment which is now described is based on a semiconductor laser operating at a single wavelength and fast S-H circuits and fast A-D converters. Single wavelength measurements are believed to be adequate for field testing and are used extensively in Chapter 8 for probing the local fibre loss.

The backscatter instrument detailed in this chapter was demonstrated as part of a contribution by Southampton University to the British Telecom Exhibition of Optical Fibre Technology[176].

5.1 Basic Experimental Arrangement

Figure 5.1 is a schematic of the equipment arrangement. Optical pulses from a semiconductor laser are launched into the fibre at a rate of ∿5000 pps and the backscattered light travelling in the opposite direction is sensed by a silicon avalanche photodiode and amplifier. The amplifier gain is varied to set the signal amplitude at the desired level before inputing to the sampling system. (Gain adjustment is achieved by varying the output of a D-A converter which responds to computer commands.) The sampling system comprises fast sample-holds, A-D converters and a computer interface. Results of waveform sampling are transferred to the computer for digital averaging and fibre loss calculations. The sampling times t_1 and t_2 are set by a commercial time delay generator also operating under the computer control. The computer, a Tektronix 4052 with a 32K memory, issues commands over an IEEE-488 communications bus.

Further details of the equipment design and computer control are given in the following sections.

5.2 Pulse Laser

The optical source (see figure 5.1) is a single hetero-junction semiconductor laser (RCA SG-2002) operating at a wavelength of 0.904 μm with a repetition rate of 5 kHz and an output pulse power of ∿2 watts. A threshold drive current of ∿3 A is required to initiate lasing and may be achieved using well-known avalanche transistor, thyristor and VMOS-circuit techniques[181,182]. Although not as fast as avalanche transistors, VMOS circuits are useful in backscatter measurements since a high voltage power supply is not required and both the pulse amplitude and width can be easily varied.

5.3 Launching and Reception Optics

Two different optical arrangements were developed for use with the semiconductor laser system.

i) Laboratory measurements were performed with lenses and a beam-splitter arrangement similar to that shown on figure 5.1. An anti-reflection cell (see section 4.5) reduced front face reflections from the fibre input,and the beam characteristics of the launched and backscattered light could be adjusted using apertures in the optical paths.

ii) An optical arrangement was also developed for the British Telecom Exhibition of Optical Fibre Technology[176]. A photograph of this compact and easily portable apparatus is shown in figure 5.9. The pulse laser, launching and reception optics and the optical receiver are mounted on a 35cm x 35cm aluminium base-plate.

The optical system utilizes a 4-port biconical fibre coupler[183,184] instead of the more standard beam-splitter arrangement. Light from the semiconductor laser is focussed through two lenses and into port 1 of the coupler where it then divides between ports 2 and 3. The actual splitting ratios are approximately 48% and 43% respectively, with a 9% loss and a reflection coefficient of ∿ -40dB. Ports 3 and 4 are index-matched and the former is butted to the fibre under test. The backscattered light travelling in the opposite direction in the test fibre re-enters port 3 of the coupler and divides between ports 1 and 2. The output of port 2 is focussed through

two lenses and onto an avalanche photodiode.

The technique is ideal for field applications, due to its simplicity and the need for only infrequent re-alignment. However, the optical apparatus was not used for the laboratory measurements described in Chapter 8 since a control of launching and reception conditions was also desired.

5.4 Amplifier

The power output of the semiconductor laser is approximately 100 times less than the dye laser system described in Chapter 4 and therefore a greater amplification is required.

5.4.1 Pre-amplifier

The pre-amplifier designed for measurements with the semiconductor laser is shown in figure 5.2. The configuration is similar to that described in section 4.7 and shown in figure 4.6, except for the biassing arrangement in the first stage. The repetition rate of the semiconductor laser is ∿5000 pps and ac-coupling may be used for both biassing and connection to further amplification stages. The noise current was found to be only 0.64 pA $Hz^{-\frac{1}{2}}$ when referred to the amplifier input.

For a further discussion of the pre-amplifier characteristics refer to section 4.7 and reference 146.

5.4.2 Automatic gain control

Figure 5.3 shows the overall amplifier configuration. The pre-amplifier is connected to an 18dB fixed gain amplifier (EMI C502), a 20 dB gain-controlled amplifier (Fairchild μA757) and an 18 dB operational amplifier stage (Teledyne Philbrick 1435 and 2035). The overall bandwidth is approximately 5 MHz.

The gain control input of the μA757 is connected to the output of a D-A converter (see figures 5.1, 5.3 and 5.10) which in turn is connected to the computer. Thus, the signal level may be adjusted automatically under computer control,and thereby is realized one of the major attractions of the 2-channel technique. The procedure is described further in section 5.7.2.

5.5 Computer Interfacing

A general purpose listen/talk interface was designed and constructed to the IEEE-488 standard (GPIB). A schematic of the circuit design is shown in figure 5.4. It possesses eight bi-directional data lines and 4 control or handshake lines. Data can be passed from the computer and to a peripheral device or vice-versa. The circuit was used frequently to interface many different types of equipment to the computer. In particular, the sampling system (see figure 5.9) and the D-A converter (see figure 5.10) incorporate the interface card.

5.6 Sampling System

Figures 5.1 and 5.9 show a schematic and a photograph respectively, of the backscatter sampling system used with the semiconductor laser. It may also be used with other lasers but had not been developed at the time of the dye laser spectral measurements described in Chapters 4 and 7. The sampling system possesses three separate channels incorporating fast sample-holds, fast A-D converters and a computer interface. Two channels are used to measure the waveform at times t_1 and t_2 and the third measures the baseline level prior to the backscatter pulse. The latter measurement, designated as the t_{-1} sample, is important in backscatter systems with ac-coupled amplifiers since for high duty factors the baseline is significantly offset from zero. Subtraction of the baseline from measurements on the other channels gives the signal levels $p(t_1)$ and $p(t_2)$.

Each sampling channel is identical and comprises a fast sample-hold (Teledyne Philbrick 4855), and a successive approximation A-D converter (Analog Devices AD-572) as shown on figure 5.5. The required specifications for this circuit are described in Chapter 3 and various electronic design rules may be found in the literature[111,113]. The sample-hold has an accuracy of 0.01% with a 250 ns acquisition time and a ±0.2 ns aperture uncertainty. The A-D converter resolution is 12-bits and a conversion time of <25 μs is chosen to suit the sample-hold droop performance.

Results from sampling are latched on the sample boards and await transfer to the computer. Each sample of 12-bits is separated into two 8-bit words for transfer over the IEEE-488 communications bus and is later recombined in the computer. The necessary protocol for data transfer is controlled by the interface circuitry shown on figure 5.4.

An absolute sampling accuracy approaching 0.01% is required (see Chapter 3). Non-linearities, sample-to-hold errors, offsets, droop, etc. should not compromise this specification. In addition, the channels should possess identical transfer characteristics, otherwise offset and gain corrections are required (see section 4.9). Adjustment of the offset- and gain-pots shown on figure 5.5 enabled the separate channels to be aligned. The performance of the sampling system under static and dynamic conditions is now described.

5.6.1 Linearity of sampling system

Under computer control the output of the D-A converter (see figure 5.10) was varied between -5 and +5 volts in 256 steps and inputed to the sampling system (see figure 5.9). One hundred samples taken by each sampling channel were acquired and averaged by the computer at each voltage step. Results for channel 1 and 2 are shown in figure 5.6(a) and (b) respectively. The gate linearity was determined by least-squares fitting to a 3rd order polynomial and is found to be within the 0.01% specification. Furthermore, the difference between the two channels (see figure 5.6(c)) is less than 1 LSB (1 least significant bit), i.e. 1 part in 4096, over the full dynamic range.

5.6.2 Dynamic performance of sampling system

The dynamic performance is an important consideration when measuring fast-slewing signals (e.g. backscatter wave-forms). Small differences in the aperture times of separate channels may result in sampling errors which are only apparent at high frequencies (see section 3.4).

Figures 5.7(a) and (b) show the tracking performances of channels 1 and 2 for two triangular wave inputs. The

frequencies and amplitude of the triangular signals are chosen such that the slew rate approximately corresponds to the time constant of a 3 dB km^{-1} (figure 5.7(a)) and a 15 dB km^{-1} (figure 5.7(b)) backscatter waveform. It is clear that the error due to differences in aperture delays is greatest at high frequencies but is less than 1 LSB (1 part in 4096) over the full dynamic range (except at the waveform turning points).

It should be noted that the performance of the 3rd sampling channel which is used for the backscatter baseline measurement is not shown in figures 5.6 and 5.7 but is not significantly different from the channels 1 and 2.

Thus, the linearity and dynamic tracking capabilities of the sampling system would appear to be sufficient to enable backscatter waveforms to be acquired with high accuracy.

5.7 Computer Control

Backscatter measurements with the 2-channel system and semiconductor laser are completely automated. A Tektronix 4052 computer (see figure 5.1) offers an improved speed relative to the 4051 computer described in Chapter 4 and can acquire and average ∿200 attenuation measurements per second. A microprocessor controller with a fixed program would be faster, however, the software flexibility of the 4052 was found to be a significant advantage in laboratory prototype design. Additional advantages of the desktop computer are internal magnetic storage, graphics display and compatibility with a wide range of commercial peripherals.

Synchronization of the sampling system to the laser pulse is provided by a programmable time delay generator which sets the times t_1 and t_2 (see figure 5.1). Typical gate separations are $\Delta T = t_2 - t_1$ equivalent to 50 m and measurements are performed at each 25 m intervals along the fibre. The waveform is sampled in response to a controller-command and results are plotted on a graphics display and stored on magnetic tape.

5.7.1 Number of samples

The computational speed of the computer could be enhanced by using the matrix handling capabilities of the 4052. Data is transferred in basic blocks of 200 measurements from the 3 sampling channels and the computer calculates the mean and variance of $p(t_1)$, $p(t_2)$ and $\alpha(t_1,t_2)$.

The number of data blocks for a 2-point calculation in each fibre section is adjusted automatically according to the desired accuracy and the measured SNR (see sections 3.6). Thus, for fibre sections close to the input only one data block of 200 is required since the SNR is high, whereas for sections remote from the input the number of samples is increased to compensate for a lower SNR.

5.7.2 Dynamic range utilization

It is shown in section 3.2.3 that $p(t_1)$ should be maximized within the A-D converter dynamic range to ease the requirements on sampling resolution. However, $p(t_1)$ should not be so close to the dynamic range limit of the A-D converter as to cause noise truncation (see section 3.7). In the present set-up, the mean and variance of signal and noise respectively may be calculated from a small number of waveform samples. (Usually, one data block comprising 200 measurements is sufficient.) The computer controls the amplifier gain via the D-A converter (see figure 5.1) and adjusts the dynamic range utilization of the signal, $|\frac{p(t_1)}{K}|$, to a level which maximizes sampling accuracy and yet avoids noise clipping. Further sampling is then performed to calculate the loss $\alpha(t_1,t_2)$ over the section.

5.8 Summary

This chapter describes the design of an automated back-scatter instrument based on the 2-channel principle and using fast sample-holds, A-D converters and a semiconductor laser. The instrument, which is portable and more suited to field applications than the equipment described in Chapter 4, may be used to probe the length dependence of fibre loss at a single wavelength (0.9 μm). Experimental results are presented in Chapter 8.

Typically, a sample gate separation of 50 m is used and the sample pair are stepped along the fibre. For each 2-point attenuation calculation the computer firstly determines the signal and noise levels from a small number of samples and adjusts the amplifier gain to maintain the dynamic range utilization $|\frac{P(t_1)}{K}|$ close to the limits defined by noise truncation (see section 3.7). Thus, the resolution requirements are minimized even for sections remote from the input and one of the major advantages of 2-channel sampling is realized. After setting the amplifier gain the computer averages further samples and calculates the section loss $\alpha(t_1,t_2)$. The number of averaged samples is adjusted according to the desired accuracy and the measured SNR. In practice, for a fibre having an attenuation of 3 dB km^{-1} over a 50 m section, a measurement uncertainty of better than δ = 0.05 dB km^{-1} can be achieved (see results in Chapter 8).

The measurement is completely automated and results of local attenuation versus length are plotted on the VDU. The program terminates when the far end of the fibre is detected.

The description of instrumentation for backscatter measurements is now terminated. The next chapter describes the cutback method for attenuation measurement and Chapters 7 and 8 give the experimental results.

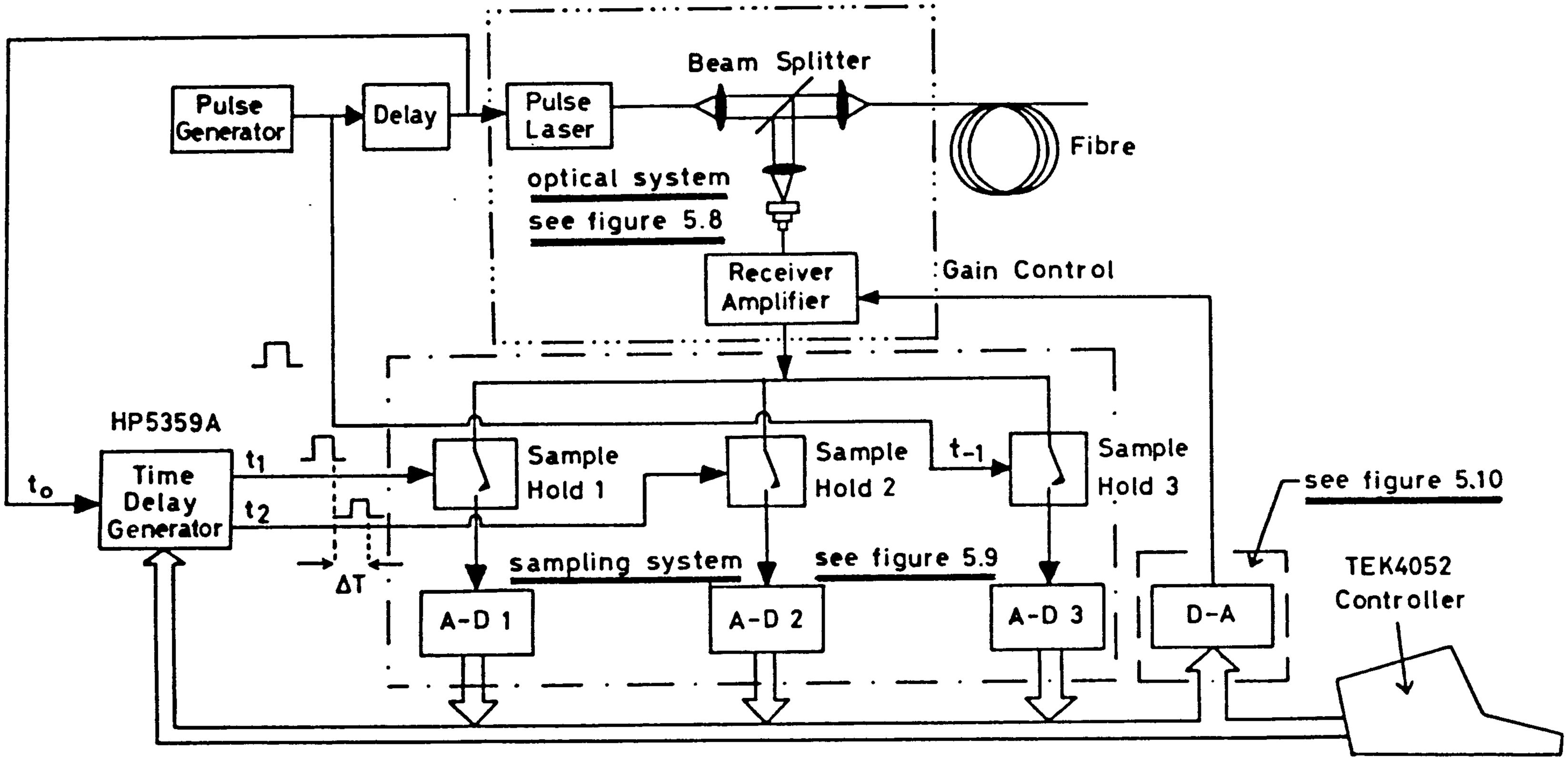

Schematic of the complete backscatter measurement system using the semiconductor laser, sample-holds and analogue-digital converters. The apparatus is controlled by a Tektronix 4052 computer over an IEEE-488 communications interface.

Figure 5.1

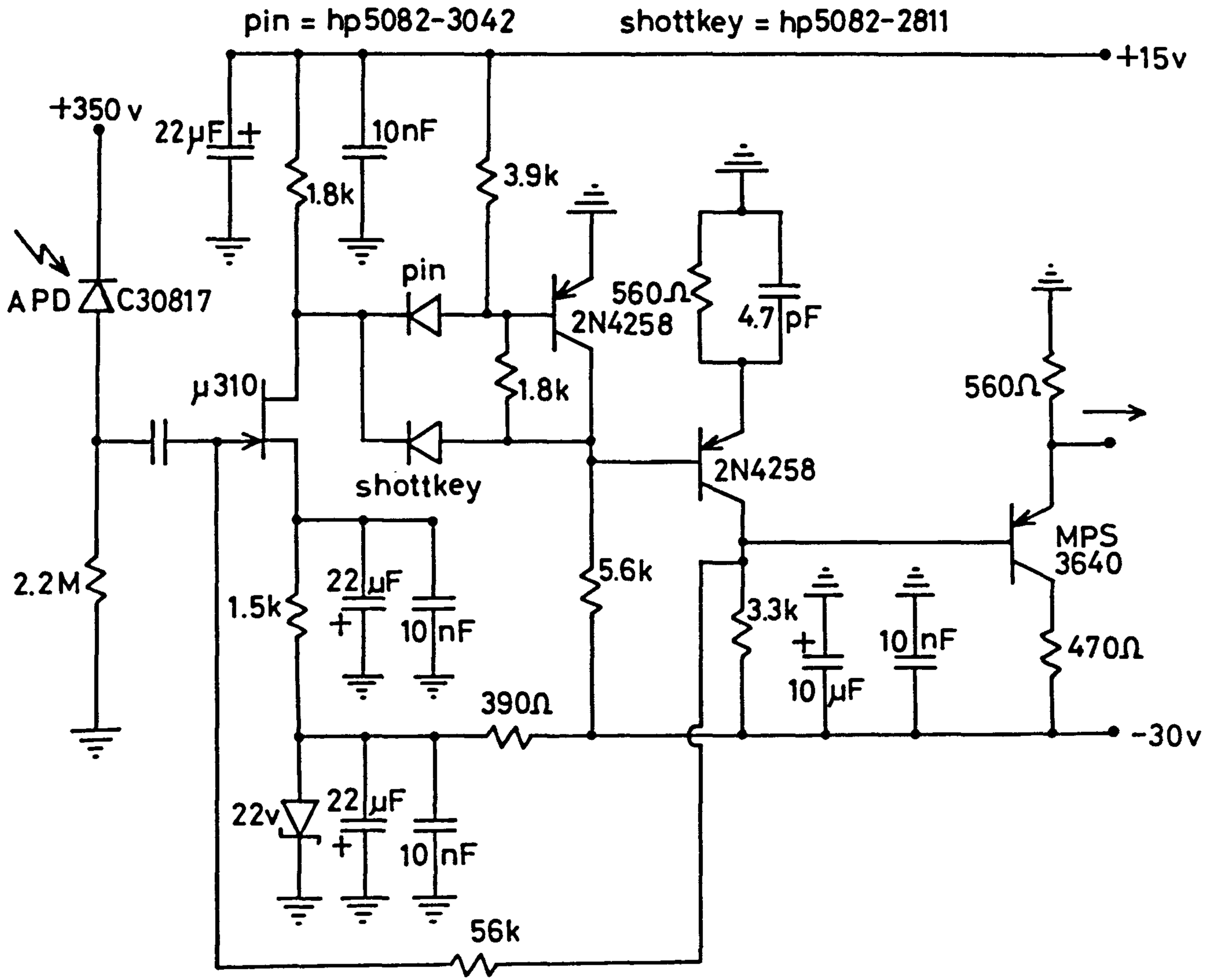

Figure 5.2 : Optical Receiver

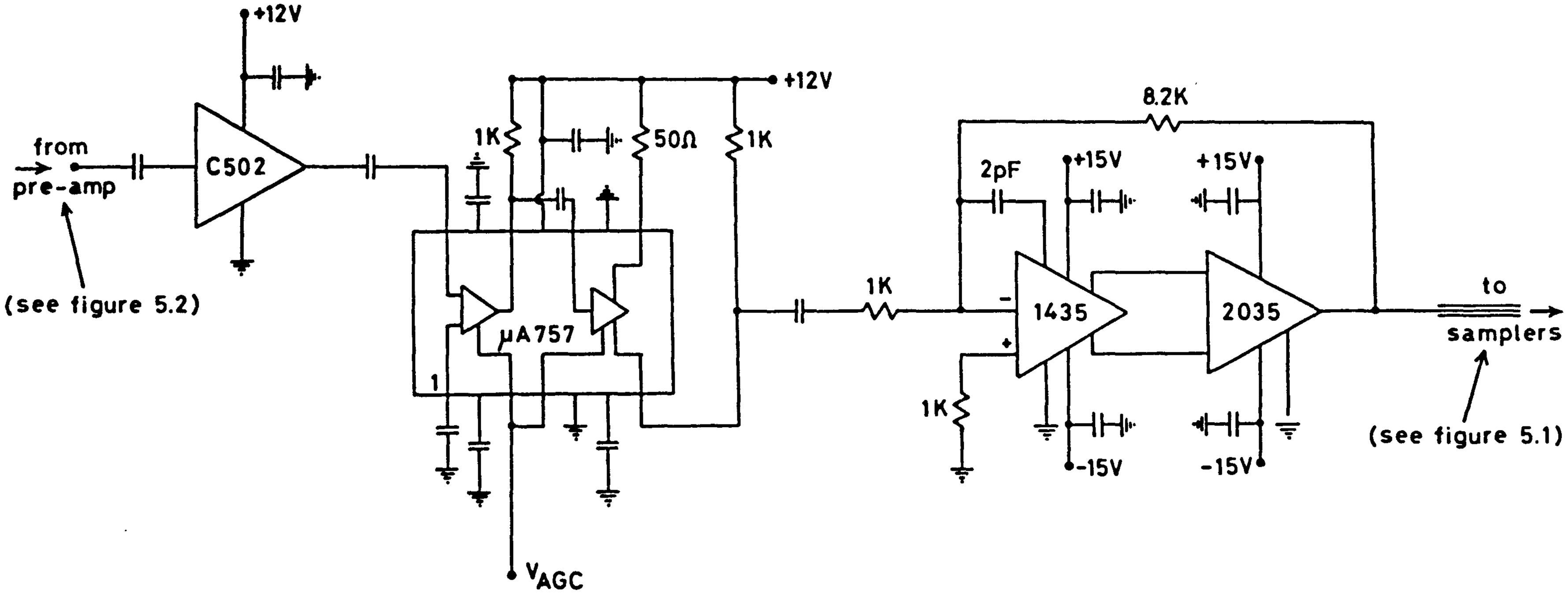

Amplifier configuration for use with the semiconductor laser backscatter measurement system. The pre-amplifier is connected to an 18 dB fixed gain amplifier (EMI C502) followed by a 20 dB gain controlled amplifier (Fairchild μA757) and a final 18 dB operational amplifier/line driver stage (Teledyne Philbrick 1435 and 2035).

Figure 5.3

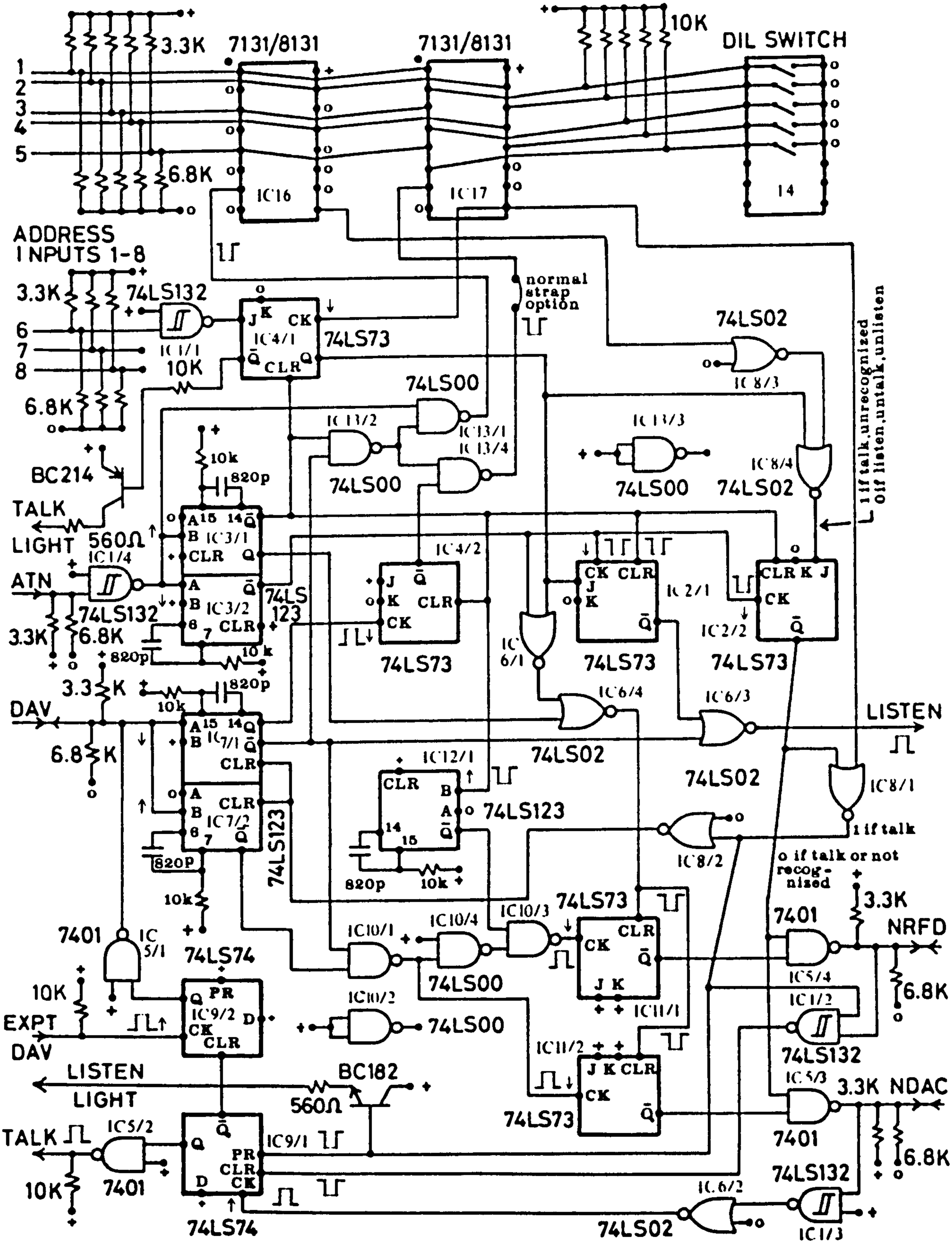

Schematic of a general purpose listen/talk computer interface designed to the IEEE-488 standard (GPlB). The circuit may be used to interface many different types of equipment to the computer.

Figure 5.4

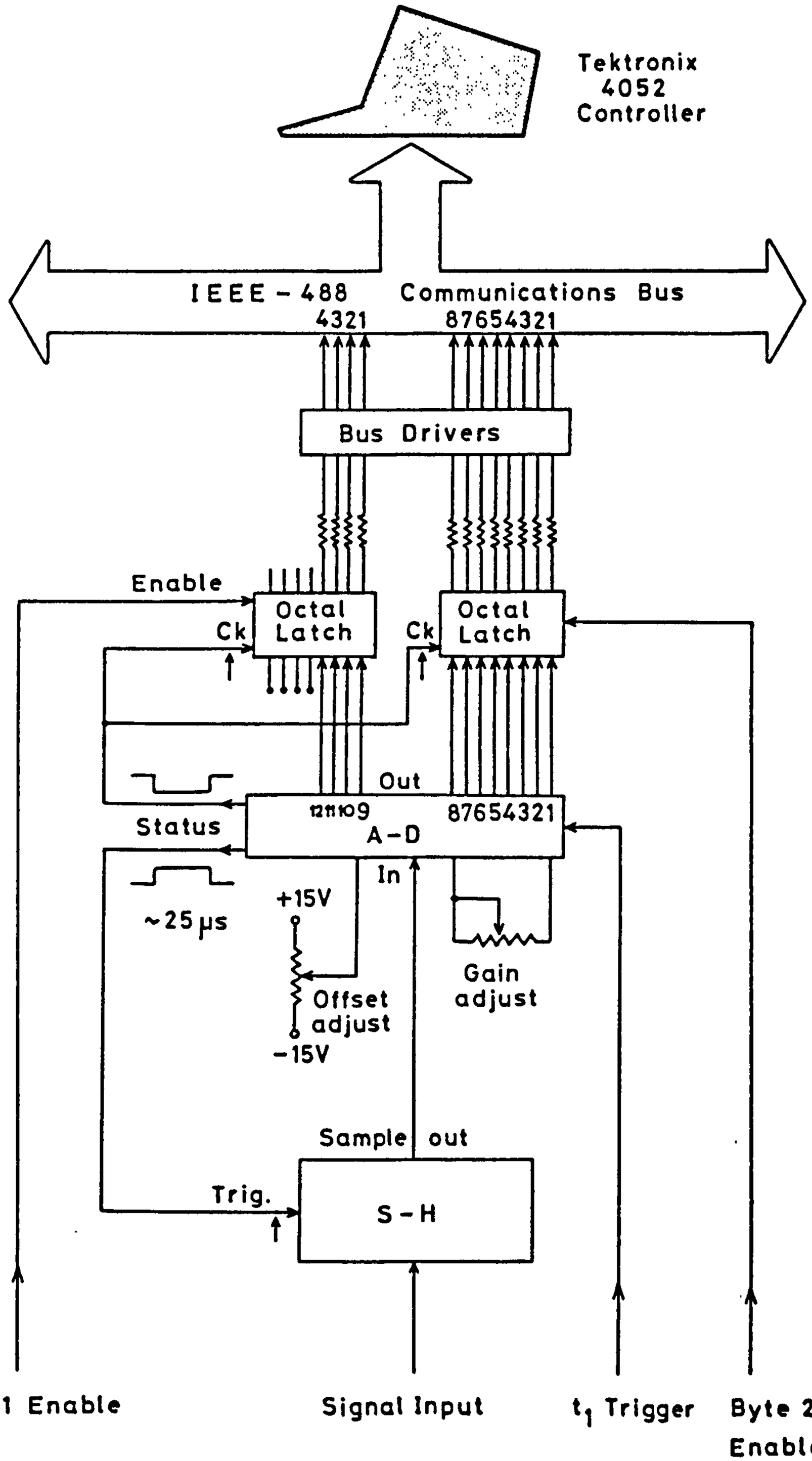

Schematic of the sampling circuit board: In response to a trigger the signal level is sampled, digitized and stored in an octal latch. The 12-bit sample is split into two 8-bit words and the Byte 1 and Byte 2 Enables control the separate transfer of each word to the computer. The two bytes are then recombined and along with the samples from parallel sampling boards, the attenuation calculation is performed.

Figure 5.5

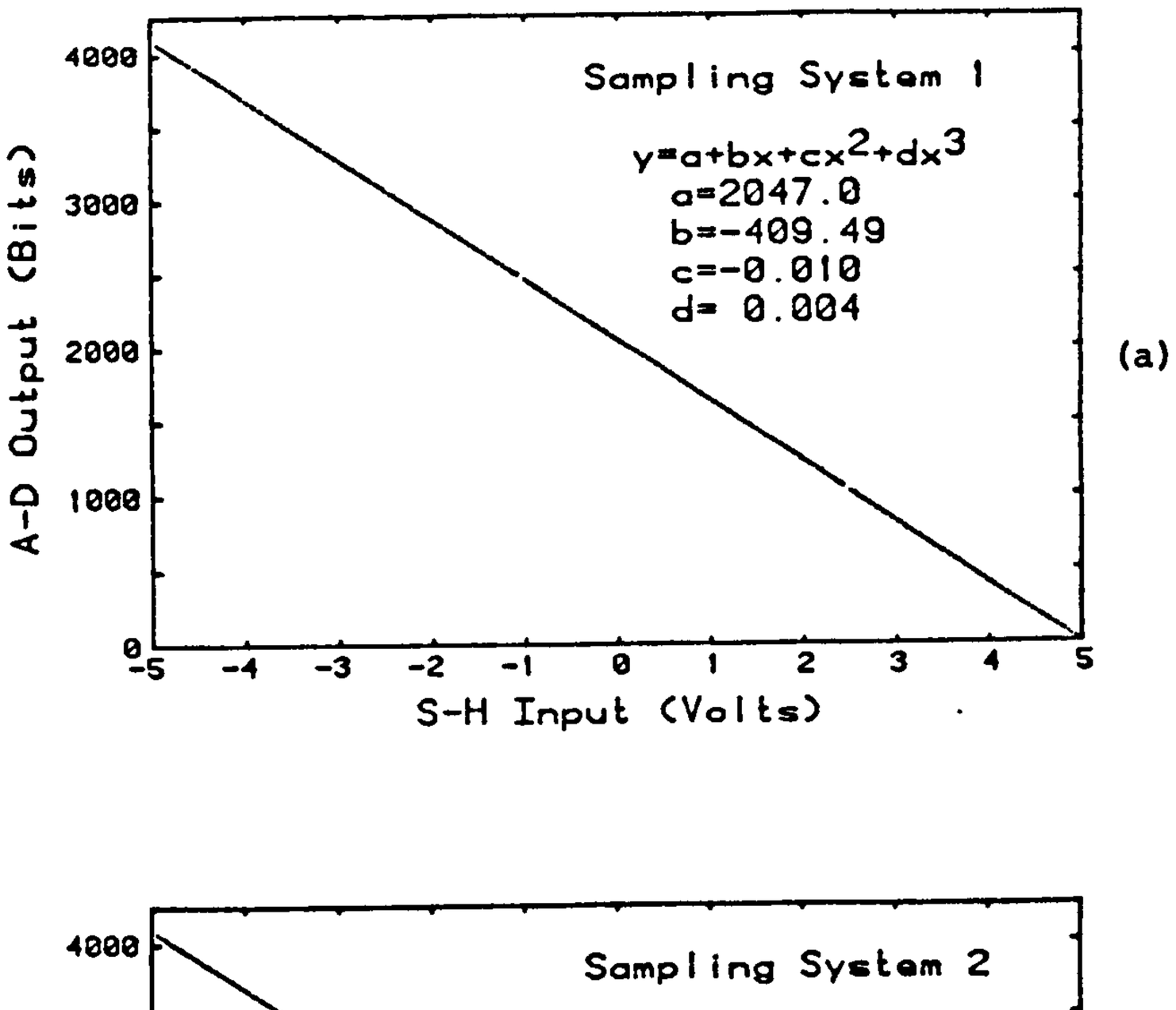

Linearity Test for (a) Sampling System 1 and (b) Sampling System 2. Figure (c) shows the difference between the two sampling channels over the full dynamic range. Each point represents the average of 100 samples at each input voltage level.

Figure 5.6

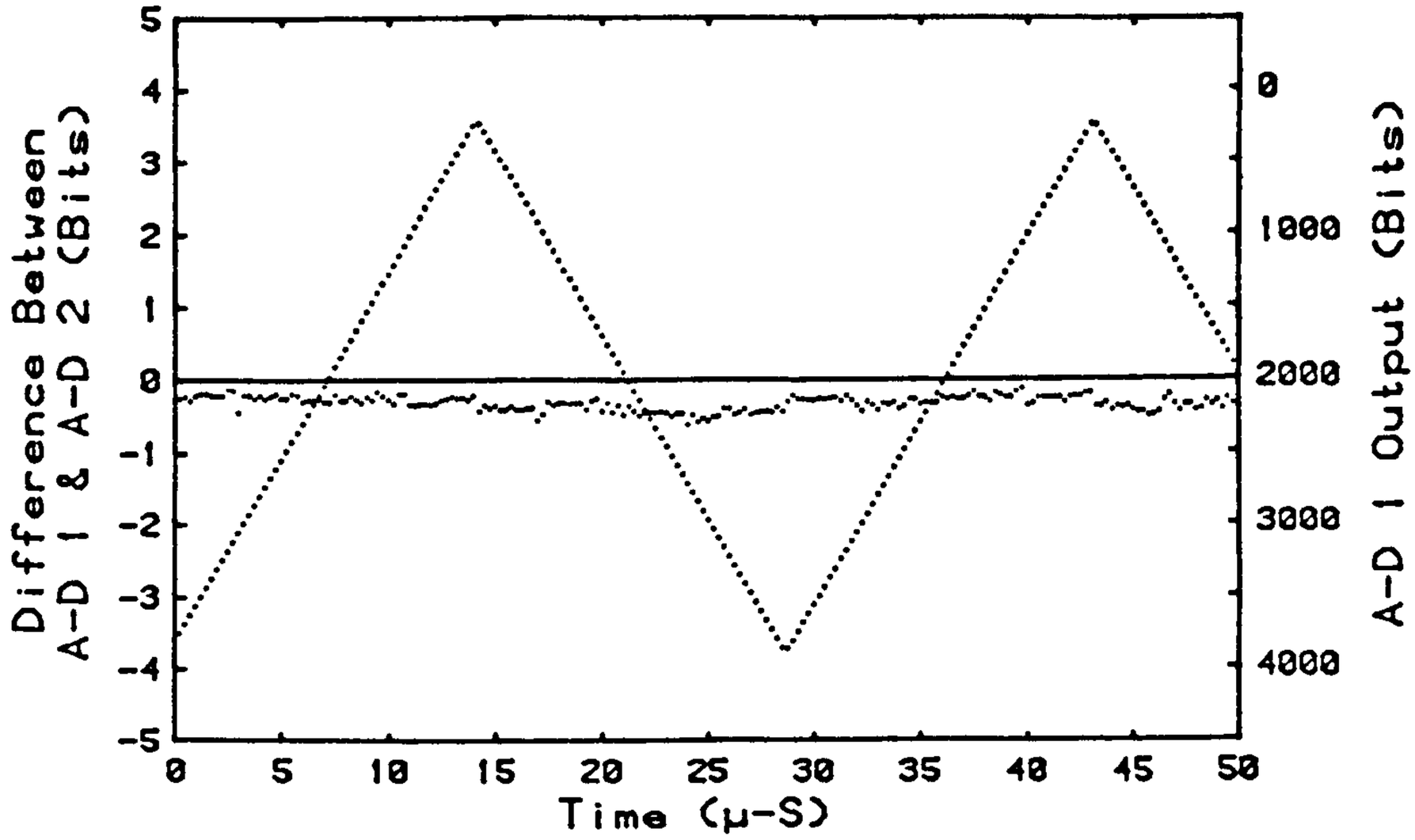

(a)

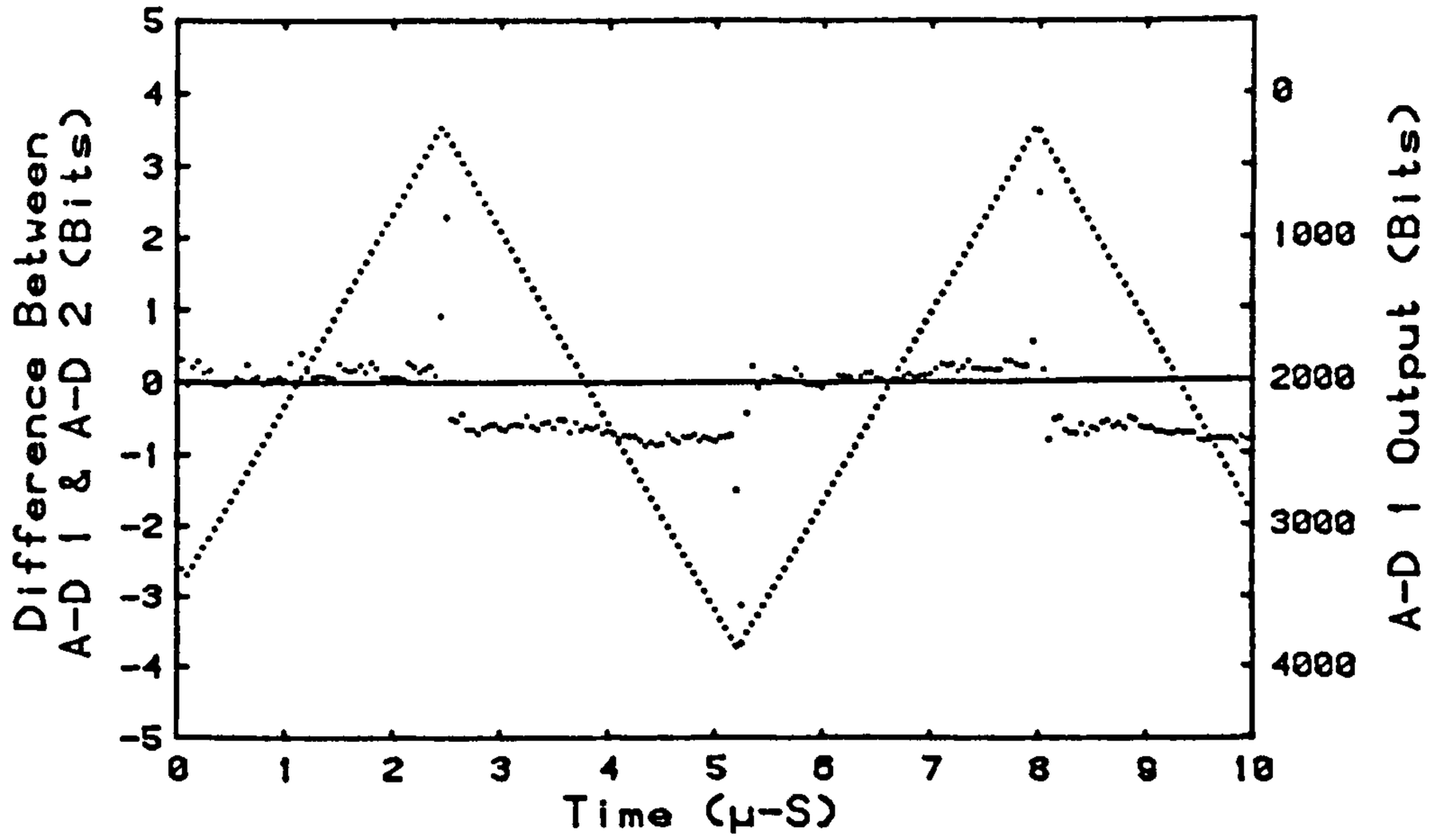

(b)

Dynamic performance of sampling systems for triangular input waveforms: The frequencies and amplitudes of the input signals are chosen such that the slew rate approximately corresponds to the time constant of a 3dB km^{-1} (figure (a)) and a 15 dB km^{-1} (figure (b)) backscatter waveform. The difference between the channels 1 and 2 are shown.

Figure 5.7

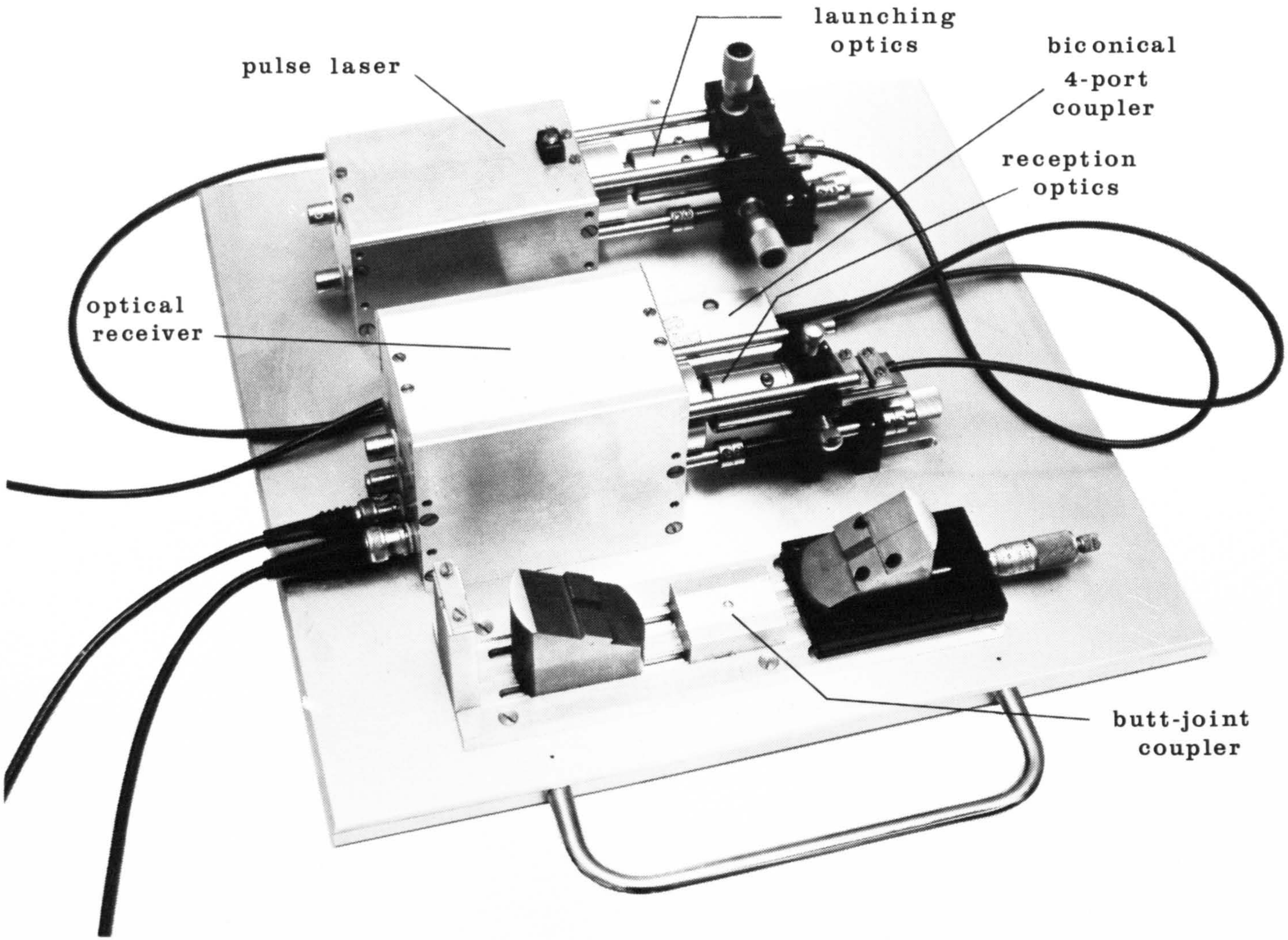

Photograph of a compact and easily portable optical apparatus for backscatter measurements. The system was demonstrated as part of a contribution by Southampton University to the British Telecom Exhibition of Optical Fibre Technology (see Reference 176)

FIGURE 5.8

Photograph of the 12-Bit sampling system designed for backscatter measurements of local fibre attenuation. The system comprises fast sample holds, fast A-D converters and an IEEE-488 computer interface.

FIGURE 5.9

Photograph of the 8-bit Digital-Analogue converter. The instrument is controlled by a computer over an IEEE-488 communications interface.

FIGURE 5.10

CHAPTER 6

CUTBACK METHOD FOR SPECTRAL LOSS MEASUREMENTS

This chapter describes the more-standard 'cutback' attenuation measurement[148-150] and demonstrates experimentally its accuracy and limitations. The technique is used in Chapter 7 for a comparison with backscatter attenuation results.

The effects of different launching conditions, microbending, differential mode attenuation (DMA) and the equilibrium mode distribution (EMD) are also considered and results are found to be in general agreement with measurements reported by other researchers[48,64,65,72,151].

6.1 Experimental Arrangement

A schematic of the cutback method is shown in figure 6.1. The apparatus was developed by F. M. E. Sladen and D. N. Payne and has been a standard laboratory tool at Southampton for some years. White light from a tungsten-halogen lamp (projector bulb) passes into a monochrometer which selects the wavelength for the attenuation measurement. The output of the monochrometer is focussed through a lens and launched into the fibre under test. The light is modulated by a chopper operating at about 75 Hz and a variable iris at the fibre input facilitates control of launch numerical aperture. The far end of the fibre is index-matched and butted to a large area silicon pin-photodiode for detection. The received power is then amplified in a low noise receiver (LNA) and inputed to a phase-sensitive detector (PSD). The PSD also obtains a reference-signal from a chopper and has a 1 second time-constant. Measurements of its output are taken by a DVM, stored and later transferred to a desktop computer.

In order to calculate the fibre attenuation, the power launched at the input must also be determined (i.e. source compensation). This is accomplished by measuring the output power from the short length remaining when the fibre is cut at a point normally 2-3 metres from the fibre input (hence 'cutback'). The ratio of the 'short-length' and 'long-length' results give fibre attenuation.

Power propagating in the cladding due to over-excitation at the fibre input may produce an error, particularly in the 'short-length' measurement, and lead to an over-estimate of the fibre loss. However, this error can be reduced by using a cladding mode stripper close to the fibre input as shown in figure 6.1.

It should be noted that the cutback technique gives only the overall fibre loss, in contrast to the backscatter method where the loss as a function of length may also be determined. The cutback method is not attractive as a field test in telecommunications since a short length of fibre must be cut for each measurement. Furthermore,access to both fibre ends is required and may be inconvenient or impossible in a field environment, where the fibre spans many kilometres.

The spectral loss characteristic of a fibre may be determined by scanning the monochrometer over a range of wavelengths for both the 'long- and short-length' results. In the present instance, the monochrometer is under motor control (see figure 6.1) and the DVM is triggered for a measurement at every 10 nm of the scan. The measurements described in this chapter are restricted to the wavelength range 500-1100nm, however they could be extended to longer wavelengths by using either a germanium or lead-sulphide detector.

6.2 Confidence of Measurement

The repeatability of attenuation measurements by the cutback technique may be better than 0.1 dB km^{-1}, however, this depends to a large extent on the skill of the operator. For example, the fibre ends should be well-cleaved and clean, cladding modes should be stripped and all the light from the fibre core must be collected by the detector. In addition, the fibre launching conditions and the lamp brightness must not vary during the procedure of both 'long- and short-length' results.

6.3 Measurement on a Plastic-clad Silica Fibre (PCS)

A series of measurements on a PCS fibre[64,152] manufactured by Quartz and Silica Products Ltd provides a practical example to demonstrate the implementation of the cutback method. The effect of launching conditions and microbending on the fibre loss is also described.

The fibre, 1 km in length and wound on a 38 cm diameter drum, consisted of a silica core of 200 μm diameter surrounded by a 500 μm diameter silicone-rubber cladding and a nylon protective over-jacket increased the overall dimensions to 1 mm.

Significant mechanical losses may be caused by microbending if the fibre is laid in an uneven fashion on the drum or if pressure is applied to the fibre. In the present experiment microbends were deliberately introduced as shown in figure 6.2(a).The fibres were lain tightly over an obstacle in as smooth layers as was possible with the winding equipment available. This winding condition is hereafter designated the 'tight-winding' condition. The obstacle consisted of a 6 mm diameter multiple-core electric cable and could be removed simply by pulling the inner conductors from the sheath and subsequently removing the sheath. The robustness of the fibre ensured there was no damage during the operation. The fibres were then loose on the drum, in the state now designated as the 'loose-winding' condition (see figure 6.2(b)).

The results of attenuation measurements on the fibre under both tight- and loose-winding conditions and for a number of different launching numerical apertures are shown on figure 6.3.

The curves exhibit a number of peaks which are caused by overtones of CH absorptions in the polymer and by OH^- impurities in the glass[152]. It is clear that the best operating wavelength for a transmission system lies in the range 0.77-0.85 μm.

6.3.1 Microbending losses

The effect of the obstacle is to increase the microbending loss of the tight-winding relative to the loose-winding condition (see figure 6.3); for best transmission performance

the drum should exert minimal external force to the fibre.

Thus, all comparitive measurements of attenuation presented in the following sections were performed with the fibres loosely-wound and in a stress-free state. This was accomplished by winding fibres on polystyrene drums at room temperature and then transferring them to a refrigerator operating at $\sim 0^{o}C$. The reduction in temperature and the difference in expansion coefficients ensured a contraction of the drums relative to the fibre and therefore minimized drum-induced microbending loss. This also provided a stable environment for comparitive measurements since fibre losses were independent of room temperature variations.

6.3.2 Launch-dependent losses

The effect of launching conditions on the fibre loss is shown in figure 6.3. It can be seen that a high numerical aperture launch results in a higher loss for the 1 km section of fibre. The equilibrium numerical aperture of the PCS fibre is ~ 0.3 and this curve is expected to be indicative of the fibre attenuation when measured in long lengths. Launching with larger numerical apertures is wasteful of power since the higher-order modes are preferentially attenuated[48,64]. The majority of the excess loss occurs in the first few hundred metres, but depends critically on the degree of microbending and mode conversion (see section 2.3).

It is clear from the above that fibre attenuation is sensitive to launching conditions and the degree of microbending. This observation is important and must be taken into account in any comparitive attenuation measurements. In particular, for the comparison between the backscatter and cutback techniques presented in Chapter 7, the experiment was designed so that in each case the excitation of the fibre section was approximately equal. Only under these circumstances could a proper comparison be made.

6.4 Measurements on a MCVD Fibre

The results presented in this section demonstrate the effect of the 'short-length' on the cutback technique. A 1.5 km section of the 0.2 NA graded-index MCVD fibre, number

VD277/L, is used in these tests. The fibre consisted of a 60 μm $GeO_2/P_2O_5/SiO_2$ core, a thin B_2O_3/SiO_2 buffer-cladding and a SiO_2 cladding of 125 μm diameter. Further details of the fibre construction are in section 7.1.

6.4.1 Effect of the 'short-length'

It is noted in section 6.1 that the presence of cladding modes may produce an error in the 'short-length' measurement. However, the error can be made insignificant by using a cladding-mode stripper close to the fibre input and a 'short-length' of ∿3-10 m, as shown in figure 6.1. An additional measurement consideration is the distribution of modes excited at the input and the rate at which an equilibrium is approached (see section 2.3).

Figure 6.4 displays the attenuation of the final 1 km of the 1.5km fibre VD277/L measured under varying cutback conditions. For curve 1, the fibre was fully excited at position z = 0 and the power outputs of the 'long- and short-lengths' measured at z = 1500 m and z = 500 m respectively. That is, the 'short-length' for this measurement was 500 m.

Curves 2 and 3 show the results of measurements performed on the final 1 km section, however, here 'short-lengths' of only 10 m are used. In the case of curve 2, the fibre is fully excited and for curve 3, the launch numerical aperture is 0.1.

The fibre exhibits the typical spectral loss dependence of MCVD fibres except that the loss peak at 0.95 μm due to OH^- absorption is high[9,14] (see section 7.1.1).

The differences between the curves on figure 6.4 are quite significant, even though all measurements are on the same fibre section. In the case of curve 1, the mode distribution entering the final 1 km of fibre was almost at equilibrium, the lossy higher-order modes having been preferentially attenuated in the first 500 m 'short-length'. In contrast, the 10 m 'short-length' in the curve 2 measurement was insufficient to ensure the mode equilibrium. Thus, the loss of curve 2 is greater than that of curve 1. This is particularly evident at 0.95 μm where the higher concentration of OH^- ions towards the edge of the core[153,154] causes a

further attenuation of the high order modes (see section 7.1.1).

The difference between curves 1 and 2 may be considered as a 'transition loss' caused by a deviation of the mode distribution from equilibrium. In the present instance, the transition loss was caused by over-excitation at the launch point (curve 2), however, in general such losses may also result from mode disturbances at joints and other discontinuities.

The result on curve 3 shows the effect of under-excitation when the 'short-length' is only 10 m. Comparison with curve 1 shows that a small negative transition loss has occurred and this is preserved even at the water peak at 0.95 μm. The effect is not surprising since low-order modes are predominantly excited by the 0.1 NA launch and these exhibit a lower loss.

6.4.2 Effect of drift

It is clear from figure 6.4 that there is a small 'tilt' on curve 3 and this may be attributed to a drift in either lamp output or launching conditions during the course of the short-length measurement. The deviation is only small, ~0.1 dB km^{-1} over the full wavelength range, but can be a significant source of error in cutback measurements. Unfortunately, such effects occur on a statistical basis and are often beyond the control of the operator. Some precautions, however, may be taken:-

i) allow sufficient time for the lamp to stabilize before commencing measurement and eliminate draughts in the room which may cause lamp cooling;

ii) use sufficiently rigid and stable optical equipment.

6.5 Summary

Measurements of attenuation by the cutback technique may achieve an accuracy of better than 0.1 dB over kilometre fibre sections, however, careful consideration must be given to the experimental detail. Launching conditions, cladding mode stripping, microbending and the equilibrium mode distribution are but some of the important factors.

The dependence of fibre attenuation on all these variables presents somewhat of a dilemma to fibre and system designers who need reliable data for performance calculations. In section 6.4, it is shown that over-excitation of the fibre results in an over-estimate in the fibre loss, and under-excitation, the reverse. These results are in general agreement with measurements reported by a number of other researchers[48,64,65,72,151]. It is interesting to note that mode conversion and differential mode attenuation cause a re-distribution and then, over a distance, an equilibration of the optical energy almost independent of the excitation at the fibre input. It is also shown in section 6.4 that if the 'short-length' in the cutback measurement is sufficiently long, the measured attenuation is almost independent of the launching conditions. The recognition of this important point forms the basis for a comparison with backscatter attenuation measurements described in Chapter 7.

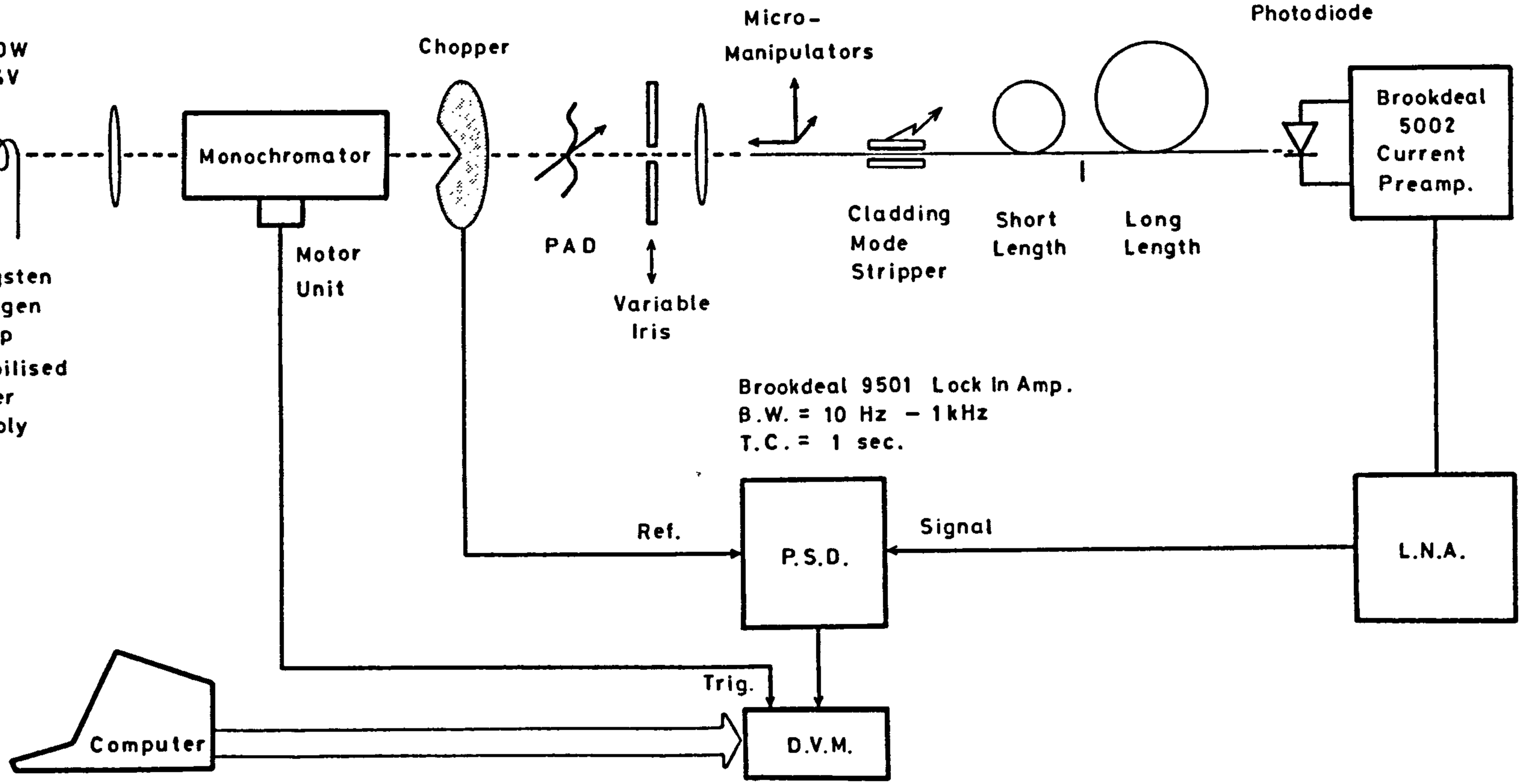

Fig. 6.1 Experimental Arrangement for Cutback Attenuation Measurement

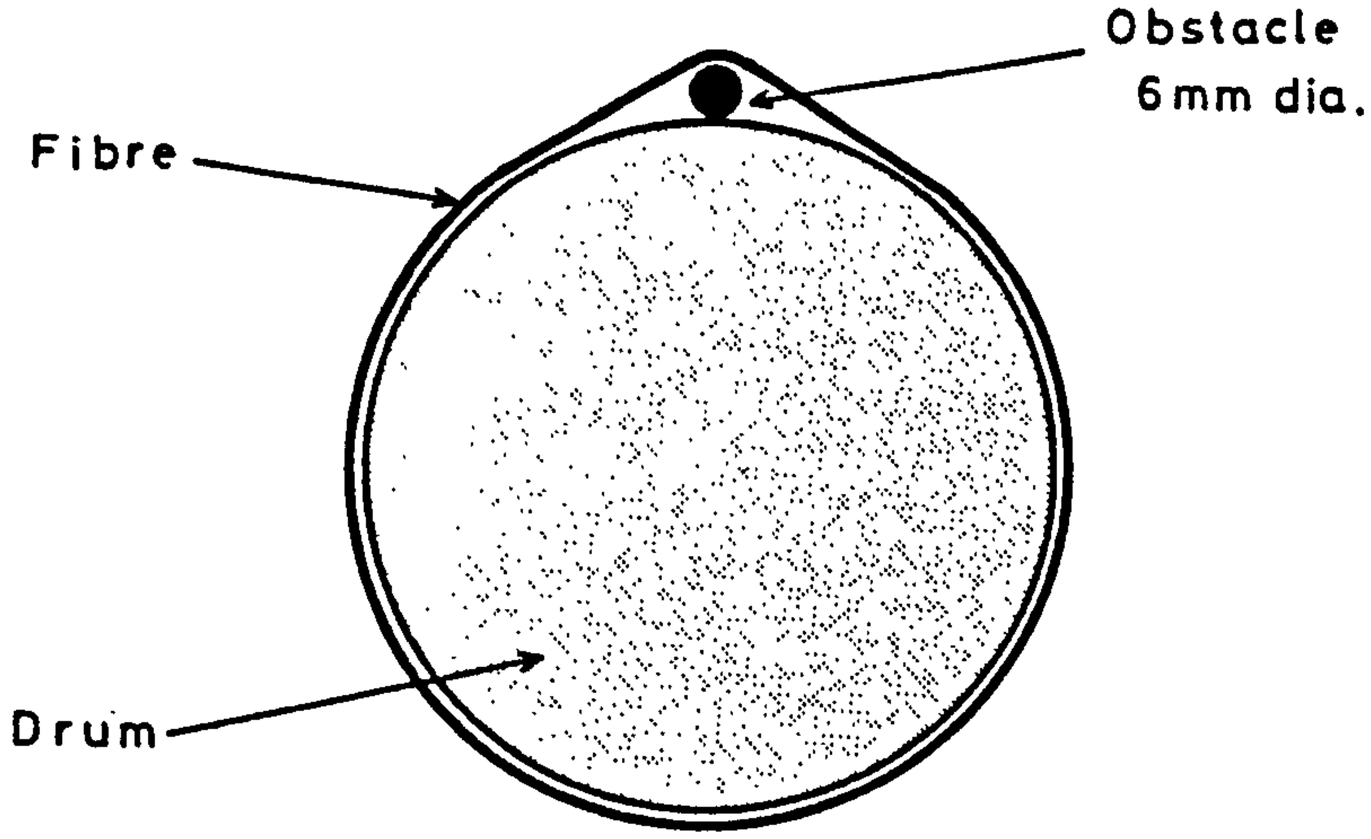

(a)

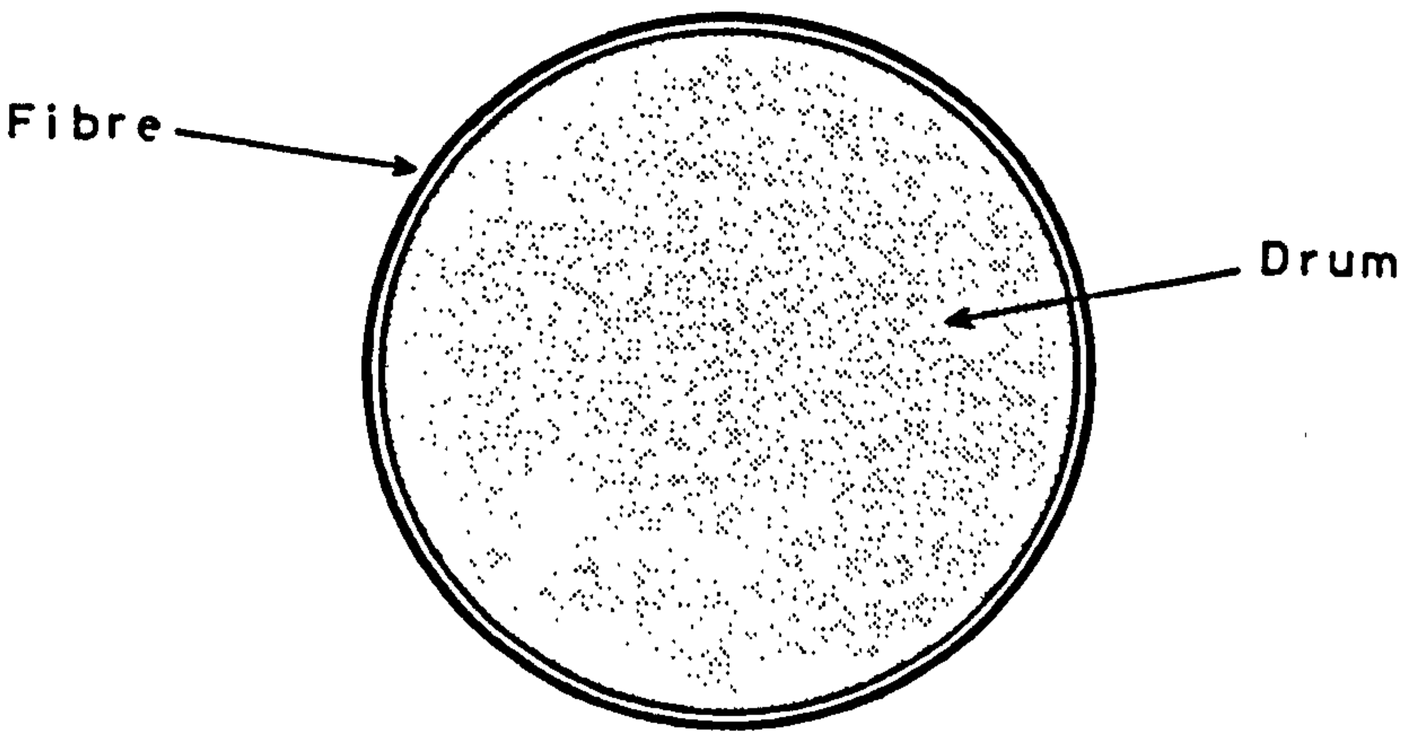

(b)

The methods designated in text as (a) 'Tight Winding' and (b)'Loose Winding' conditions. Under the 'Tight Winding' condition an obstacle placed under the fibre wound on a nominally 38cm-diameter drum induced an additional loss due to microbending. The fibre was a 200 μm-diameter core, PCS fibre manufactured by Quartz and Silica Products Ltd.

Figure 6.2

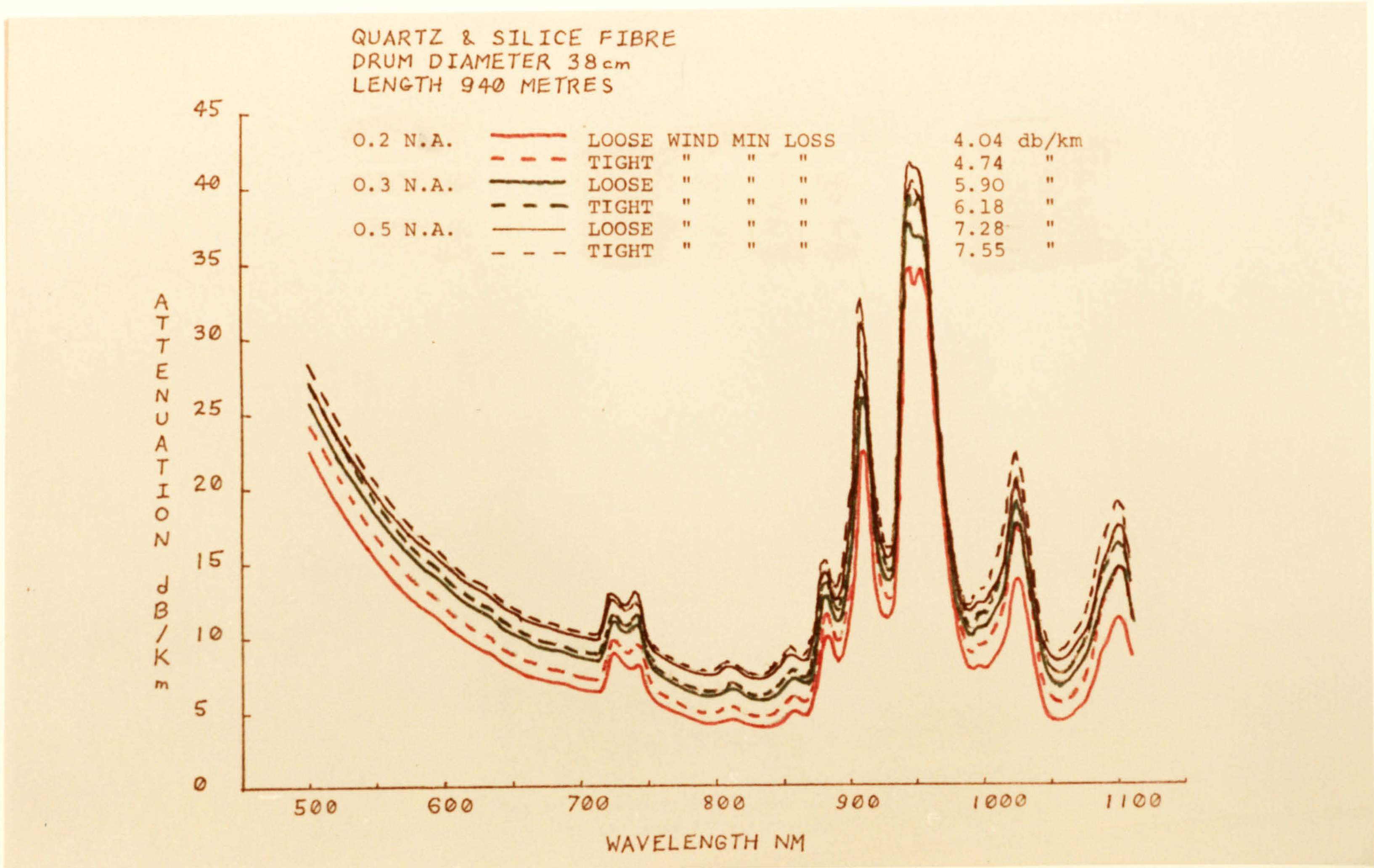
QUARTZ & SILICE FIBRE
DRUM DIAMETER 38cm
LENGTH 940 METRES
0.2 N.A. LOOSE WIND MIN LOSS 4.04 db/km
TIGHT " " " 4.74 "
0.3 N.A. LOOSE " " " 5.90 "
TIGHT " " " 6.18 "
0.5 N.A. LOOSE " " " 7.28 "
TIGHT " " " 7.55 "
ATTENUATION dB/Km
45
40
35
30
25
20
15
10
5
0
500
600
700
800
900
1000
1100
WAVELENGTH NM

Figure 6.3

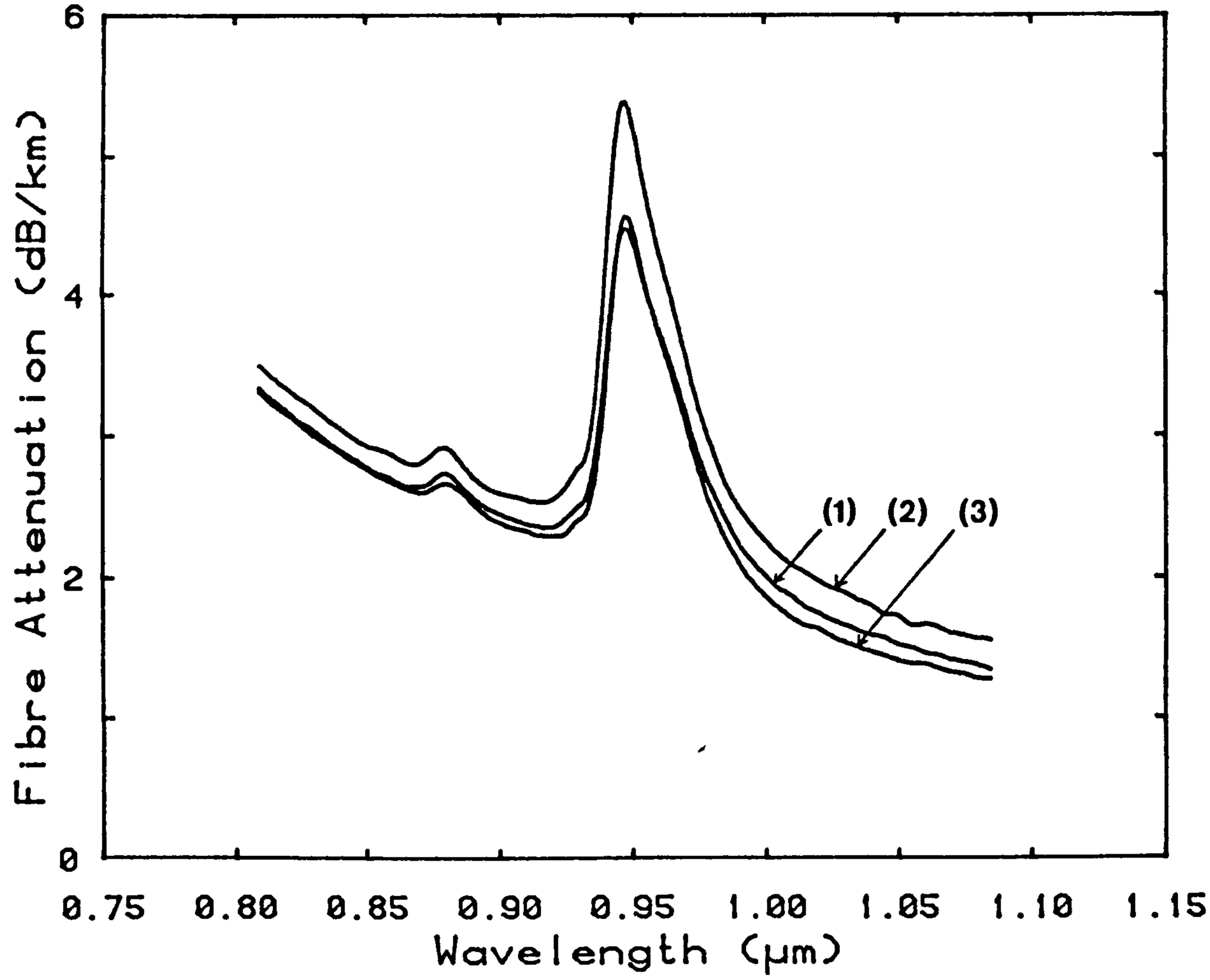

Attenuation of fibre VD277/L measured by the cutback-method; Curve 1, 'short length' = 500 m and full excitation; Curve 2, 'short length' = 10 m and full excitation; Curve 3, 'short length' = 10 m and 0.1 NA excitation.

Figure 6.4

CHAPTER 7

SPECTRAL BACKSCATTER ATTENUATION MEASUREMENTS AND A COMPARISON WITH THE MORE STANDARD CUTBACK METHOD

The theory of the backscatter technique and the instrument limitations are described in Chapter 2 and 3. Variation in the backscatter factor along the length of a fibre is identified as a potential source of error in local attenuation measurements. A calculation in section 2.8 based on a simplified model predicted the accuracy of the method to be approximately 0.2-0.3 dB km^{-1}. The objective of the present chapter is to determine experimentally the accuracy of the backscatter loss measurement. The technique is based on a comparison of the backscatter and cutback methods over a wide spectral range.

The development of instrumentation for backscatter spectral attenuation measurements using a dye-laser and parametric oscillator system is described in Chapter 4. The laser system offered the advantages of wavelength-tunability and high power output, but other performance features produced a number of problems with respect to data acquisition. These were overcome by the implementation of the 2-channel approach and a computer control.

The cutback technique is described in Chapter 6 and the accuracy and limitations of the method are demonstrated by a number of practical examples. Cutback measurements are repeatable to approximately 0.1 dB km^{-1} over kilometre fibre sections but this depends critically on launching conditions, micro-bending, mode-conversion, differential mode attenuation and the 'short-length'. These considerations are of particular importance in the sections to follow.

7.1 Fabrication Details of Fibre VD277/L

The fibre VD277/L used extensively in the following sections was designed specifically to test the accuracy of the backscatter method. It was a graded-index multimode fibre, 3.2km in length and was manufactured at Southampton University by the MCVD process[11,14,155,156].

7.1.1 Refractive index profile

The refractive index profile of VD277/L, measured in the preform stage by Mr. I. Sasaki using a new spatial filtering technique[157,158], is shown in figure 7.1. The fibre consisted of a 0.2 NA graded-index core comprising 42 layers of deposited glass, $GeO_2/P_2O_5/SiO_2$. A buffer of 4 layers of B_2O_3/SiO_2 separated the core from a cladding-substrate of SiO_2 (Heralux-WG). The latter was relatively impure compared to the core materials and possessed a high OH^- ion concentration ($\sim$170 ppm)[153,154].

The function of the B_2O_3/SiO_2 buffer-layer is that during high temperature deposition it slows the diffusion of OH^- ions into the core region[14]. This has proved successful in almost eliminating the loss at 0.95 μm due to OH^- absorption[9,11].

In the present instance, however, the buffer-layer was made relatively thin in order to allow some diffusion of OH^- from the cladding to the core (normally there are 12-16 layers). A rough schematic of the expected OH^- concentration profile is shown in figure 7.1[153,154]. The high concentration of OH^- at the core periphery is expected to cause an excess loss to the high order modes at 0.95 μm, but not at other wavelengths. This enabled a study into the effect of differential mode attenuation on backscatter measurements.

The refractive index profile shown on figure 7.1 also exhibits a depression at the core centre caused by dopant 'burn-off' during the collapse stage of preform preparation[62,63]. This is a characteristic of MCVD fibres; the fraction of the core area involved, however, is usually quite small.

7.1.2 Diameter control details

The accuracy of a backscatter attenuation measurement relies on the constancy of longitudinal fibre parameters (see section 2.8). Recently reported was an advance in fabrication techniques at Southampton University which enabled fibre diameters to be programmed and controlled to an accuracy of <0.2 μm rms[159]. In the present instance fibre VD277/L was pulled with a constant diameter of 125 μm (core diameter 60 μm) for the first 1.7 km, after which a number of tapers were

programmed along its length.

The section of constant diameter is studied further in this chapter to ascertain the fundamental accuracy of the backscatter method. Following, in Chapter 8, the programmed diameter changes are analysed and the origin of previously-observed but unexplained features on some backscatter waveforms is identified[95] for the first time.

7.2 Length-dependent Loss of VD277/L at 1.0 μm

The quality and uniformity of fibre VD277/L may be determined by using the backscatter technique to probe the local loss along the entire length of the fibre. A detailed evaluation of the backscatter instrumentation is also desirable before proceeding to the comparative studies in later sections.

The length-dependent loss over the first 1.6 km of fibre VD277/L is shown on figure 7.2. The measurement was performed at a wavelength of 1.006 μm using the dye-laser and 2-channel instrumentation described in Chapter 4. Results are presented as attenuation versus position in the fibre, a much more useful format than the previously reported exponential or logarithmic plots[3,4,99,160].

Measurements were taken from both end A and end B of the fibre and are superimposed for comparison. The fibre input designated 'A' corresponds, in the preform-fabrication stage to the end of the deposition, and in the fibre-drawing stage to the beginning of the pull (i.e. z = 0). The input designated 'B' is the opposite end of the fibre and for the measurements shown on figure 7.2, corresponds to the point z = 3.2 km, although only the results for the first 1.6 km are displayed. Note that measurements were not performed in the first 200 m from end A due to the signal distortion resulting from the front-face reflection of the ∿1 μs optical-pedestal (see section 4.4).

The sample separation for the 2-channel technique was set at 50 m (ΔT = 480 ns) and measurements were taken at intervals of 20 m along the fibre. In order to account for possible drift, two complete scans of the fibre were executed, measuring

every 40 m in the first scan and the interleaving points in the second. The fibre was also kept in a refrigerator so as to remove any excess microbending and drift caused by pressure exerted from the drum (see section 6.3.1).

Figure 7.2 shows that the fibre attenuation is reasonably uniform along the entire 1.6 km length which perhaps, at this stage, could be said to be indicative of the high quality deposition and diameter control.

There is, however, a small decrease in the local attenuation when moving away from end A and this is confirmed by the end B measurement. In addition, there are some shall fluctuations along the length of the fibre, particularly in the first few hundred metres and these are anti-correlated when measured from the two fibre ends. That is, a slight increase in loss when measured from end A appears as a slight decrease when measured from end B. The anti-correlated features are most likely due to instabilities which were observed in the initial stages of the fibre drawing. The effect of the fibre drawing on backscatter measurements is pursued further in Chapter 8.

The results in figure 7.2 demonstrate the high resolution of the 2-channel technique for local loss measurements. Typically, the standard deviation of consecutive measurements on a 50 m section of fibre is better than 0.05 dB km^{-1}. It is interesting to compare this figure to the 0.1 dB km^{-1} reproducibility of the cutback method (see Chapter 6).

7.3 Effect of Launching Conditions on the Backscatter Method

In section 2.6 it is shown that the backscatter factor depends on the core energy distribution and may be modified by the presence of leaky or cladding modes. Furthermore, fibre loss depends on excitation due to differential mode attenuation, as demonstrated in the cutback measurements of Chapter 6 (see also section 2.3). Before proceeding to a comparison between the backscatter and cutback methods, it is necessary to clarify this effect. In particular, the sensitivity of backscatter measurements to variations in mode-scrambling and the dye-laser launching conditions are considered.

The mode scrambling technique used with the dye-laser is described in section 4.6 and the effect on backscatter measurements is shown in figure 7.3. One measure of the degree of mode conversion is the loss of the scrambler and curves are shown for 0, 3 and 6 dB losses in backscattered power. The fibre VD277/L was cut at 1.5 km from end A and results correspond to launching backwards from the cutting point, which is now designated as the end B.

The fluctuations in measured local attenuation shown in the figure are caused by differences in excitation at the fibre input (cf. figure 7.2 where the actual loss at 1.5 km from end A is shown to be constant). Mode scrambling corresponding to a 6 dB two-way loss of power is expected to convert modes most heavily and is seen to result in a greater initial attenuation. This may be attributed to the increased intrinsic losses of the highest-order modes[25-27].

It is also clear from figure 7.3 that independent of the degree of mode scrambling, transition losses due to launching quickly diminish and within about 400 m from the fibre input, the difference between the curves is reduced. The effect is presumably caused by the stabilization of power into an equilibrium mode distribution (see section 2.3) and is similar to the effect noted in section 6.4 for cutback measurements. This observation forms a basis upon which the two measurement techniques may be compared (see section 7.6).

7.4 Backscatter Spectral Measurements on Fibre VD277/L

7.4.1 Attenuation of the section 500-1500 m

A spectral attenuation measurement was performed on fibre VD277/L using the 2-channel backscatter technique and results are shown on figure 7.4. The fibre was kept in a refrigerator operating at about $0^{o}C$ so as to reduce microbending due to pressure exerted by the drum (see section 6.3.1). Light was launched into end A and the two sampling gates positioned at t_1= 5 μs and t_2= 15 μs on the backscatter waveform. Thus, results represent the attenuation over the 1 km section from 500-1500 m.

The wavelength of the dye-laser and parametric oscillator system was adjusted (see section 4.2) and attenuation measurements were taken at 5 nm intervals over the range 0.820-1.070μm.

In order to account for possible drift, measurements were performed in two cycles. The first consisted of increasing the wavelength in 10 nm steps until reaching the limits of the range. Then, a second scan was performed with the attenuations at the intermediate 5 nm wavelengths being measured. The smoothness of the curves is indicative of a negligible measurement drift and the standard deviation of consecutive results was better than 0.05 dB km^{-1}.

The fall in responsivity of the silicon avalanche photodiode above 1 μm determined the upper limit of the wavelength range[161,162]. In future it may be possible to extend measurements to longer wavelengths by using a germanium[163] or quaternary device[94].

Figure 7.4 shows the first comprehensive spectral measurement of fibre attenuation by the backscatter method[94]. It is apparent that the absorption peak at 0.95 μm and the smaller one at 0.88 μm, both due to the OH^- contaminent[17], have been resolved. In addition, the overall loss exhibits the λ^{-4} dependence which is characteristic of Rayleigh scattering (see section 2.2). Furthermore, confidence may be gained in the accuracy of the spectral measurement by a comparison with the length dependent loss shown in figure 7.2. It is clear that the average of the local attenuation over the section from 500-1500 m is equal to the measurement at 1.006 μm on figure 7.4.

This spectral backscatter measurement is considered further in section 7.6.2 where the result is compared to cut-back measurements on the same fibre section.

7.4.2 Attenuation of the sections 500-1000 m and 1000-1500 m

The spectral losses over the sections 500-1000 m and 1000-1500 m were determined to enable a comparison with results on figure 7.4, the latter which shows the loss over the whole section 500-1500 m.

Figure 7.5 displays the results of the 2-channel measurements. Curve 1 represents the loss measured over the 500-1000 m section, i.e. t_1= 5 μs, t_2= 10 μs; curve 3 is the loss

over the section 1000-1500 m, i.e. t_1= 10 μs, t_2= 15 μs; and curve 2 is the loss over the whole section 500-1500 m, i.e. t_1= 5 μs, t_2= 15 μs.

A number of interesting features are observed in the result. Firstly, it is reassuring to note a consistency in the measurements in that the loss shown on curve 2 is equal to the average of the losses on curve 1 and 3. Secondly, at 0.95 μm, curves 1 and 3 show that there is significant difference in the loss of the two fibre sections. This effect is unexpected since figure 7.2 shows that the attenuation measured at 1.006 μm is reasonably uniform along the fibre.

Two possible reasons for the discrepancy at 0.95 μm are:-

i) The diffusion profile of OH^- ions in the fibre core (sketched roughly in figure 7.1) causes an excess loss of power in the high order modes, which is not observed at wavelengths other than 0.95 μm. Thus, losses near the launching end are higher since there is a larger proportion of high-order modes than when compared to the remainder of the fibre[48].

ii) The concentration of OH^- ions in the core may also vary along the fibre. Possible causes may be a variation in the B_2O_3/SiO_2 buffer-layer thickness or due to an excessive heating being applied to some sections of the preform during fabrication. Both these factors affect the diffusion rate of OH^- ion into the core.

The origin of the discrepancy between curve 1 and curve 3 may be checked by measuring the length dependence of fibre loss at 0.95 μm.

7.5 Evolution of OH^- along the Length of Fibre VD277/L

The local attenuation of fibre VD277/L at the water-peak wavelength of 0.946 μm and at wavelengths on each side of the water peak at 0.906 μm and 1.006 μm, is shown on figure 7.6. Measurements were taken from both end A (z = 0) and end B (z = 1500 m) of the fibre and at intervals of 20 m with a sample separation of 50 m as described in section 7.2. For

clarity in the case of End B, results at only 0.946 μm are shown, since those at 0.906 and 1.006 μm were not significantly different from the End A measurements. This may be confirmed in the case of the 1.006 μm measurement by referring to figure 7.2.

Figure 7.6 shows that the fibre attenuation at 0.906 and 1.006 μm is reasonably uniform along the whole length. The reproducibility of the 2-channel approach is indicated by the correlation observed between the small loss-features on the two curves.

In contrast, the attenuation at 0.946 μm shows a marked variation with length, indicating a reduction in OH^- concentration from End A to B. This is confirmed in that measurements from both ends show good agreement, except close to either launch end. The latter effect was not significant at other wavelengths and can be attributed to differential mode attenuation, presumably caused by the diffusion profile of the absorbing OH^- ions which exist across the core (see figure 7.1).

The origin of variations in OH^- ion along the fibre length is investigated in the following two sub-sections.

7.5.1 Stereoscan studies of B_2O_3/SiO_2 buffer-layer

The diffusion of OH^- ions from the cladding to core depends on both the deposition temperature and the thickness of the B_2O_3/SiO_2 buffer layer. A variation in the buffer-layer often occurs due to the tapering of the deposited layer thickness which occurs at the beginning of each CVD pass[11,14,155,156]. In the present instance, however, End A represents the far-end of the CVD pass where such effects are not usually observed.

Photographs from a steroscan of the fibre cross-section are shown on figure 7.7. The left-hand side of the figure shows the cross-sections at points 0, 500, 1000 and 1500 m from End A. Clearly evident are the fibre core and cladding regions and the buffer-layer. Some of the individual deposited core layers can also be seen including the central dip in the index profile (also see figure 7.1). The right-hand side of figure 7.7 shows expanded views of the buffer-layer for each cross-section.

It is clear that there is no significant variation in either the buffer-layer thickness or the core diameter over the entire 1.5 km section. Thus, variation in the buffer-layer thickness is not the cause of changes in OH^- concentration along the fibre.

7.5.2 Thermal history

Increased OH^- ion diffusion may result during fibre fabrication due to:-

i) a temperature overshoot at the beginning of each CVD pass following the burner flyback in the preform preparation. However, this explanation may be eliminated since end A corresponds to the far end of the deposition where the temperature is usually well stabilized.

ii) excessive heating being applied to sections of the preform during the collapse stage. In a discussion with R. J. Mansfield[164] it was pointed out that when all the core layers had been deposited, the end A was subjected to an extremely high temperature ($\sim$1900^{o}C) for a period in order to collapse the hollow preform tube into a solid rod. The collapse of the remainder of the preform, however, was much faster due to the surface tension pull from the already-collapsed sections. The diffusion of OH^- through the buffer-layer is expected to be proportional to the temperature and the time spent at that temperature. Thus, it is perhaps not surprising that the end A exhibits a higher loss due to the OH^- absorption.

iii) excessive heating being applied to the preform in the pulling rig. Additional OH^- ion may diffuse from cladding to core in the draw-down zone in the pulling furnace. The end A of the preform is subjected slightly longer to the elevated temperature than other sections due to the time taken in setting up the pull. Thus, the increased diffusion during this period may also contribute to the excess OH^- absorption at end A.

It is clear from the above discussions that the origin of the longitudinal variation in OH^- ion is intimately related to the thermal history of the fibre and preform. In the present

instance, however, it was not possible to quantify the relative importance of the mechanisms described in (ii) and (iii). This may be an avenue for research in the future.

7.6 Absolute Accuracy of the Backscatter Technique by a Cutback Comparison

The backscatter measurements presented in the previous sections demonstrate both the utility and resolution of the method. The technique is used to determine several interesting features pertaining to the properties of fibre VD277/L. In the present section, the absolute accuracy of these measurements are determined by a comparison with the more-standard cutback method. The results of two such comparisons are described.

7.6.1 Formulation of a method for comparison

A proper comparison of the backscatter and cutback methods requires that an experiment be designed to compare them under like conditions. However, this is difficult since the two techniques are fundamentally different. The backscattered power depends on the average of the forward and backward losses as well as variations in scattering along the fibre. Conversely, the cutback method depends only on the forward fibre loss.

Furthermore, it is shown in section 6.4 that fibre attenuation comprises two components; firstly, a transition component resulting from over- or under-excitation and secondly, a base-line or equilibrium component which dominates when sufficiently far from the input, joints and other discontinuities. Thus, cutback and backscatter measurements are sensitive to the excitation conditions, microbending, mode-mixing and differential mode attenuation.

One method for implementing a comparison of the two techniques is to ensure the same excitation for both measurements. However, when different optical sources are used (e.g. dye-laser for backscatter and tungsten lamp for cutback) a difficulty arises in arranging the spot sizes and the launch numerical apertures to be identical in each case. A 'pigtail' fibre acting as a leader from the optical source or a mode-

scrambler (see section 4.6) may be used to control the excitation, but always there is some uncertainty as to the actual launch distribution[65,164,165].

It is noted in section 6.4 that cutback measurements could be made insensitive to launching conditions if the 'short-length' is sufficiently long. Furthermore, local backscatter measurements are also insensitive to launching conditions if the analysed section is sufficiently far from the input (see section 7.3). The attenuation measured under these circumstances represents the equilibrium fibre loss since the mode distribution is approximately stable in the sections under test, i.e. the equilibrium mode distribution (see section 2.3).

The backscatter and cutback measurements described in the following two sections are compared under equilibrium loss conditions. It is believed that this approach provides a sound basis for comparison and simultaneously removes experimental uncertainties due to fibre transition losses resulting from differences in both the nature of the optical sources and the excitation conditions at the fibre input.

7.6.2 Spectral comparison number 1

A comparison between the backscatter and cutback techniques is achieved by measuring the final 1 km of a 1.5 km length of the fibre VD277/L. The fibre was kept in a refrigerator so as to minimize microbending caused by pressure exerted from the drum (see section 6.3).

For the backscatter measurement a mode scrambler was used to excite the test fibre and the linear gates were sited at times corresponding to 500 m and 1500 m from the launch end, as described in section 7.4.1. For the cutback measurement, light from a tungsten lamp was focussed with a numerical aperture of 0.25 into the fibre and the output from 1500 m was compared to that after shortening to 500 m. Thus, the effective 'short-length' for both the backscatter and cutback measurements was 500 m and a comparison of the results under similar conditions was achieved, since in both cases a close-to equilibrium mode distribution should exist in the section under test.

The results of the measurements are shown in figure 7.8. It can be seen that the two techniques give remarkably similar results, the difference between the curves being within the experimental error at all wavelengths. Even in the region of the water peak at 0.95 μm, where differential mode attenuation might be expected to produce some variation, the agreement is excellent. This result is believed to be largely a consequence of the systematic attempt to compare the methods under like conditions and lends a considerable confidence to the efficacy of the backscatter technique.

7.6.3 Spectral comparison number 2

The spectral comparison on the 1.5 km length of VD277/L described in the previous section could only be performed once due to the destructive nature of the cutback method. As a result of the 'short-length' measurement the fibre was cut into two sections, one of 500 m and the other 1000 m. The former was discarded and the latter used in a further cutback comparison which is now described.

For the cutback measurement light from the tungsten lamp was launched into the 1 km fibre and the output was compared to that when the section was shortened to 500 m (i.e.'short-length' = 500 m). The result is shown in figure 7.9.

Also shown on the figure is the result of a backscatter measurement on the same 500 m section (see previous description in section 7.4.2 and curve 3 of figure 7.5). Note that the effective 'short-length' (i.e. t_1) for the backscatter measurement was 1000 m since it was carried out prior to the cutback comparison number 1 already described.

The difference between the backscatter and cutback curves shown on figure 7.9 is within the experimental error except in the region of the water peak at 0.95 μm where a small but significant difference is observed. The deviation here is believed to be due to the difference in launching conditions and in the effective'short-lengths' for the backscatter and cutback measurements. For the backscatter measurement the effective 'short-length' was 1000 m, whereas for the cutback result, the 'short-length' was only 500 m. The diffusion profile of the OH^- ions across the core (see section 7.1)

is expected to enhance the differential mode attenuation at 0.95 μm relative to other wavelengths. Thus, in the case of the cutback result, the transition loss at 0.95 μm is expected to be larger since the fibre is fully excited at the input and the short length is only half that for the back-scatter measurement. The agreement between the methods at other wavelengths is excellent.

7.7 Summary

The application of the 2-channel approach to backscatter waveform analysis is shown to give accurate and reproducable results. The technique is capable of providing high resolution attenuation data, as evidenced by its application to the measurement of fluctuations in local loss along the length of a fibre. The results presented in this chapter include the first comprehensive spectral measurements of fibre attenuation by the backscatter technique[94]. The utility of spectral backscatter measurements is demonstrated by tracking the evolution of the OH^- impurity along the length of a fibre. This measurement is important since it may enable the source of a contamination to be identified and lead to modifications and improvements in fibre fabrication methods.

The complete spectral comparison with the more-standard cutback method showed that under similar measurement conditions, virtually identical results can be obtained. It is believed that this excellent agreement is largely the result of a systematic attempt to compare the two methods under like conditions, and lends a considerable confidence to the efficacy of the backscatter technique.

The measured loss is affected slightly by launching conditions but appears to become insensitive within a few hundred metres of the fibre input. Thus, in long fibre links, launching effects will be of little concern.

Length dependent measurements at single wavelengths may be used to determine the magnitude and uniformity of local fibre loss. Thus, manufacturers can monitor the quality of production, and sub-standard fibres and fibre-sections may be identified. In the next chapter the backscatter technique is used to probe the length dependence of fibre loss. The ability

to vary the wavelength for this type of measurement, however, is not necessary and a semiconductor laser source is adequate (see Chapter 5).

Furthermore, the dye-laser system is not attractive for the field and factory due to its bulk and expense.

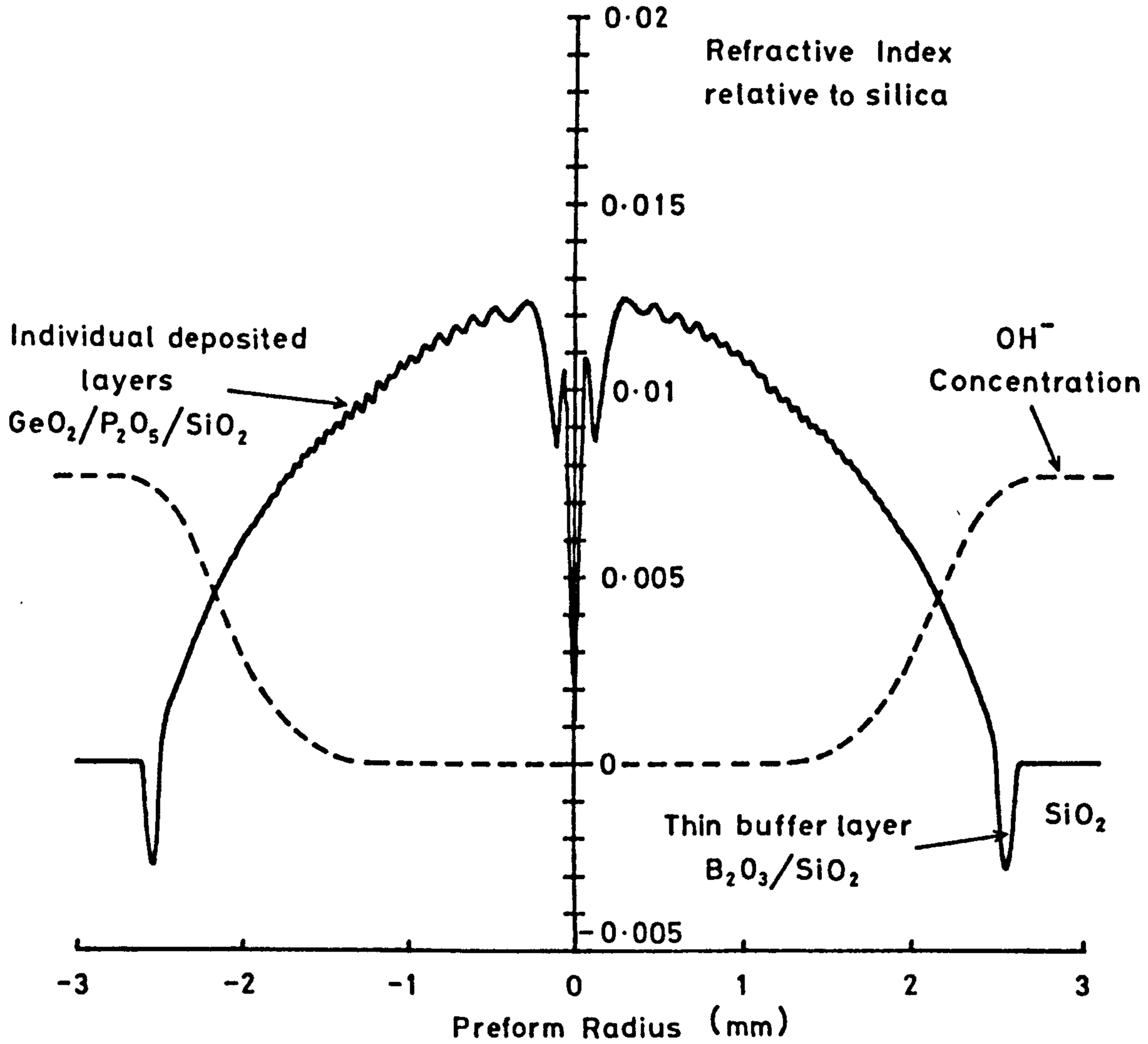

Refractive Index Profile of Fibre-Preform VD277/L (solid) measured by Mr. I. Sasaki , using a spatial-filtering technique (see text). Also shown (dashes) is a schematic of the expected OH^- concentration variation across the core.

Figure 7.1

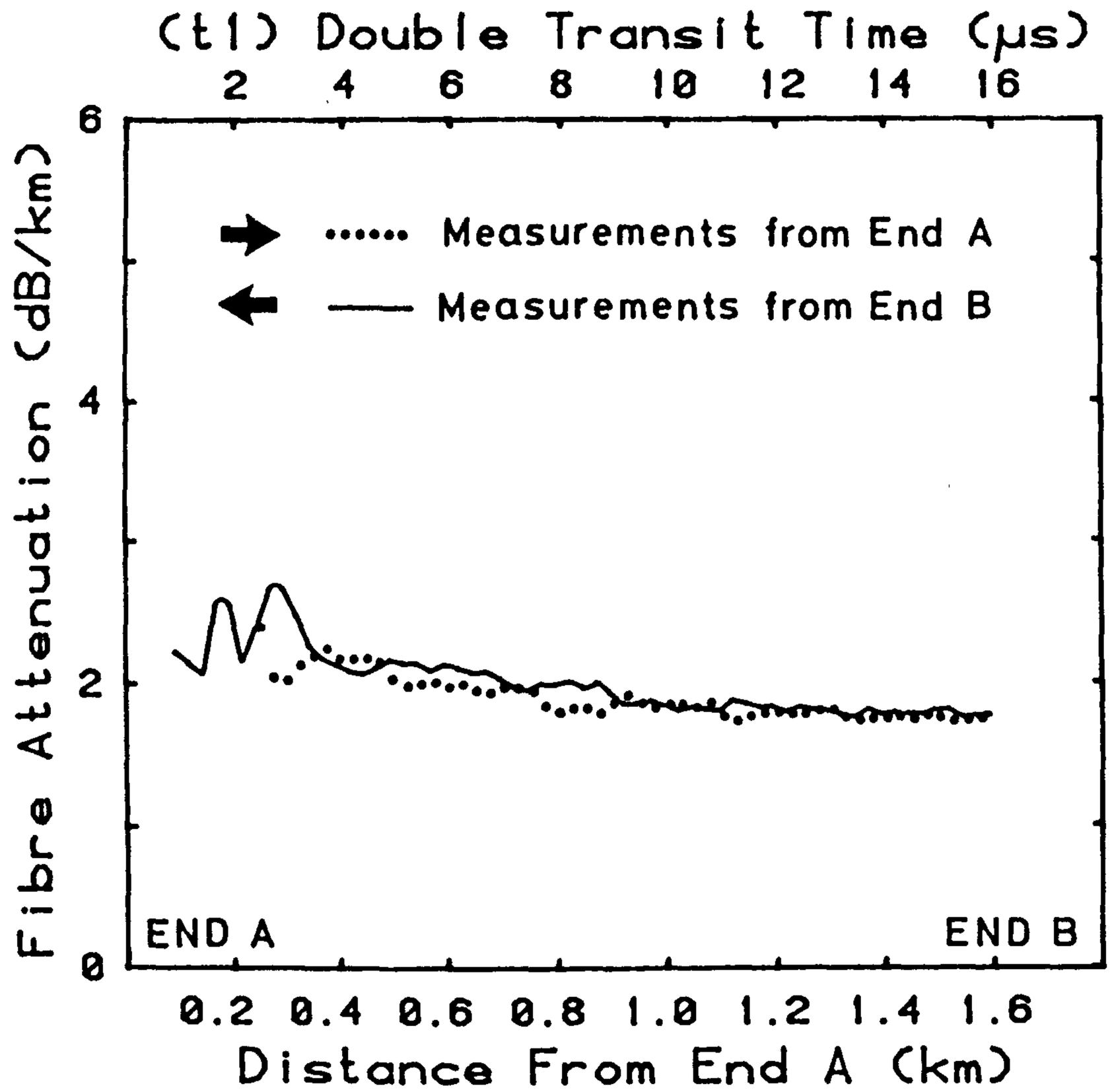

Length-dependent loss of the first 1.6 km of fibre VD277/L measured by the 2-channel backscattering technique. Results are shown for launching into the end designated A and the end designated B. The sample separation ΔT = 480 ns = 50 m and measurements are taken at 20 m intervals down the fibre. (λ = 1.006 μm)

Figure 7.2

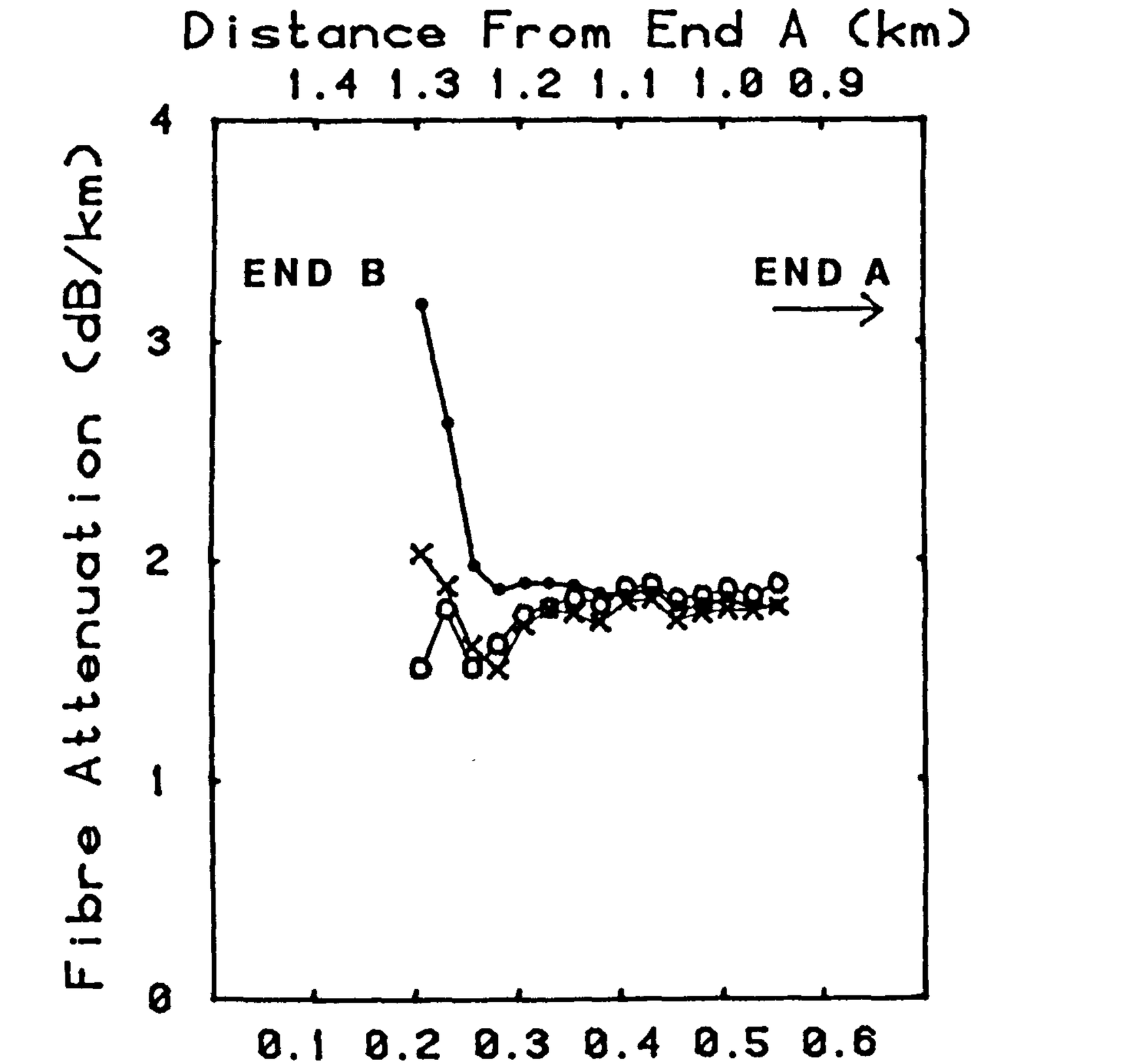

Effect of variation of mode-scrambling on the backscatter method. The measurement was performed by launching into end B of fibre VD277/L. The reduction in backscatter power due to the mode scrambler is 0 dB (circles), 3 dB (crosses) and 6 dB (dots).

Figure 7.3

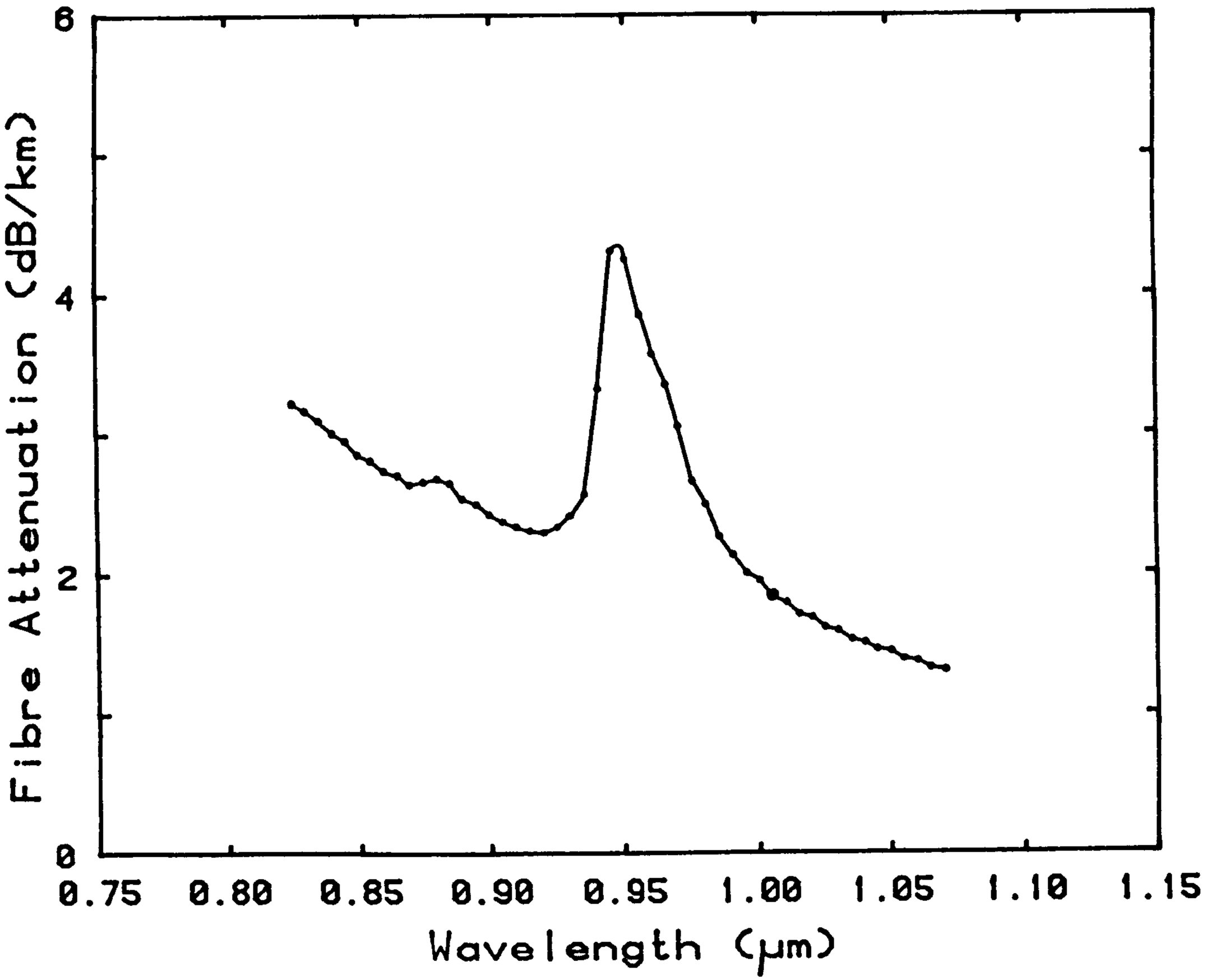

Spectral attenuation measurement of a fibre by the backscatter technique. The measurement was performed by the 2-channel method over the section 500-1500 m of fibre VD277/L.

Figure 7.4

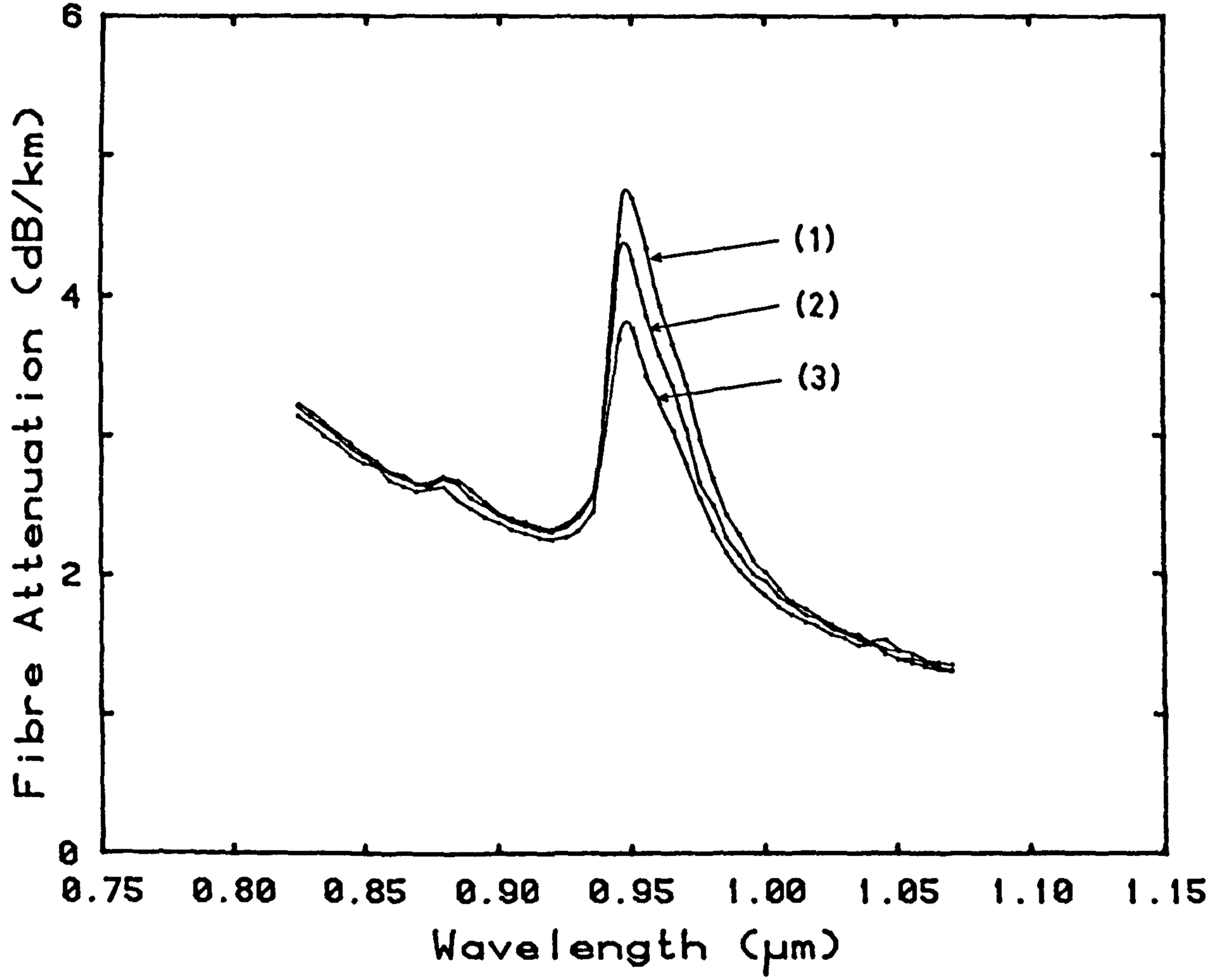

Spectral-attenuation of fibre VD277/L measured by the backscattering technique for the fibre sections 500-1000 m (curve 1), 500-1500 m (curve 2) and 1000-1500 m (curve 3).

Figure 7.5

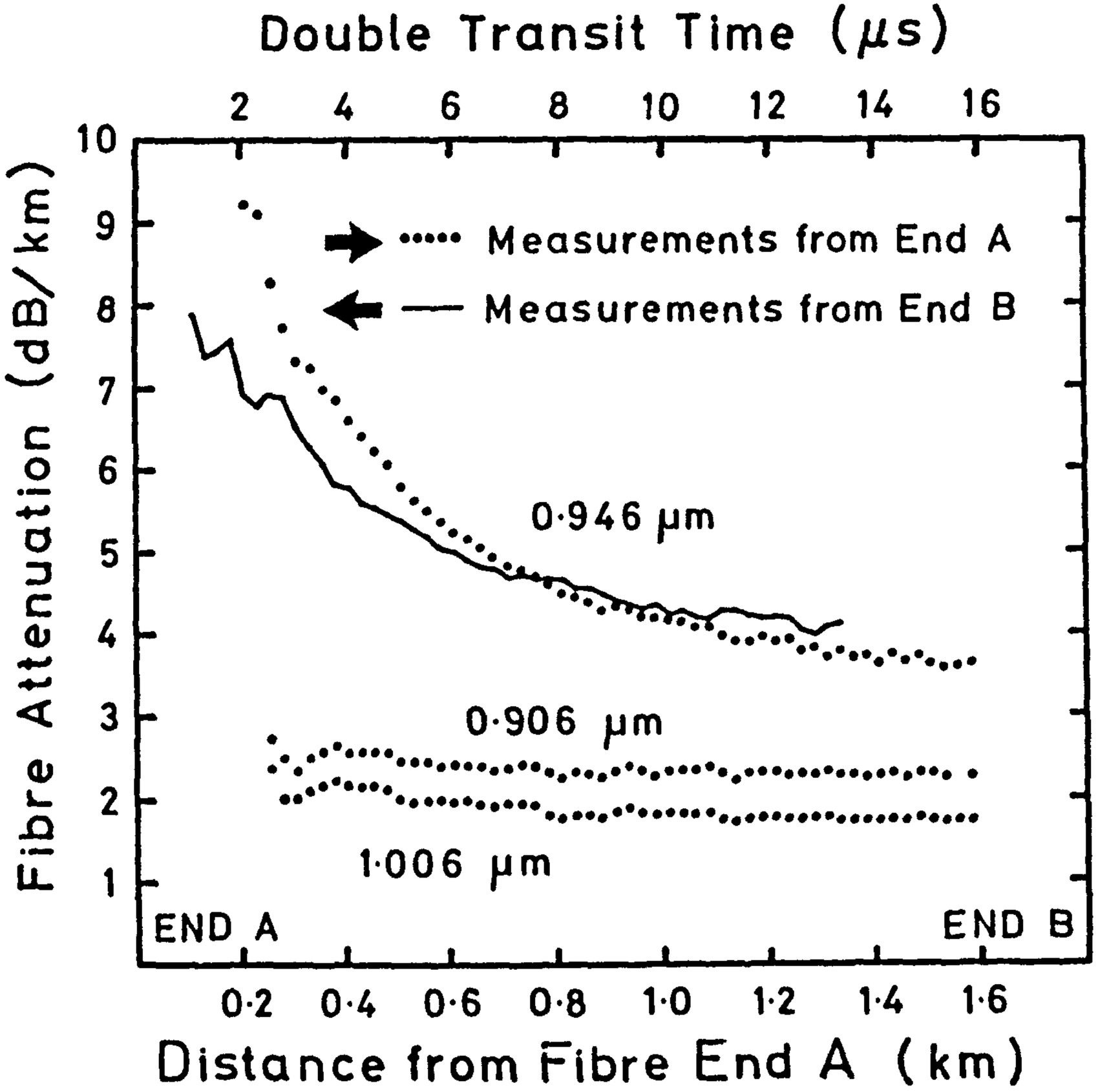

Length-dependence of fibre VD277/L attenuation measured by the backscattering technique at wavelengths 0.906, 0.946 and 1.006 μm by launching into end A. The measurement from end B is also shown at the wavelength 0.946 μm.

Figure 7.6

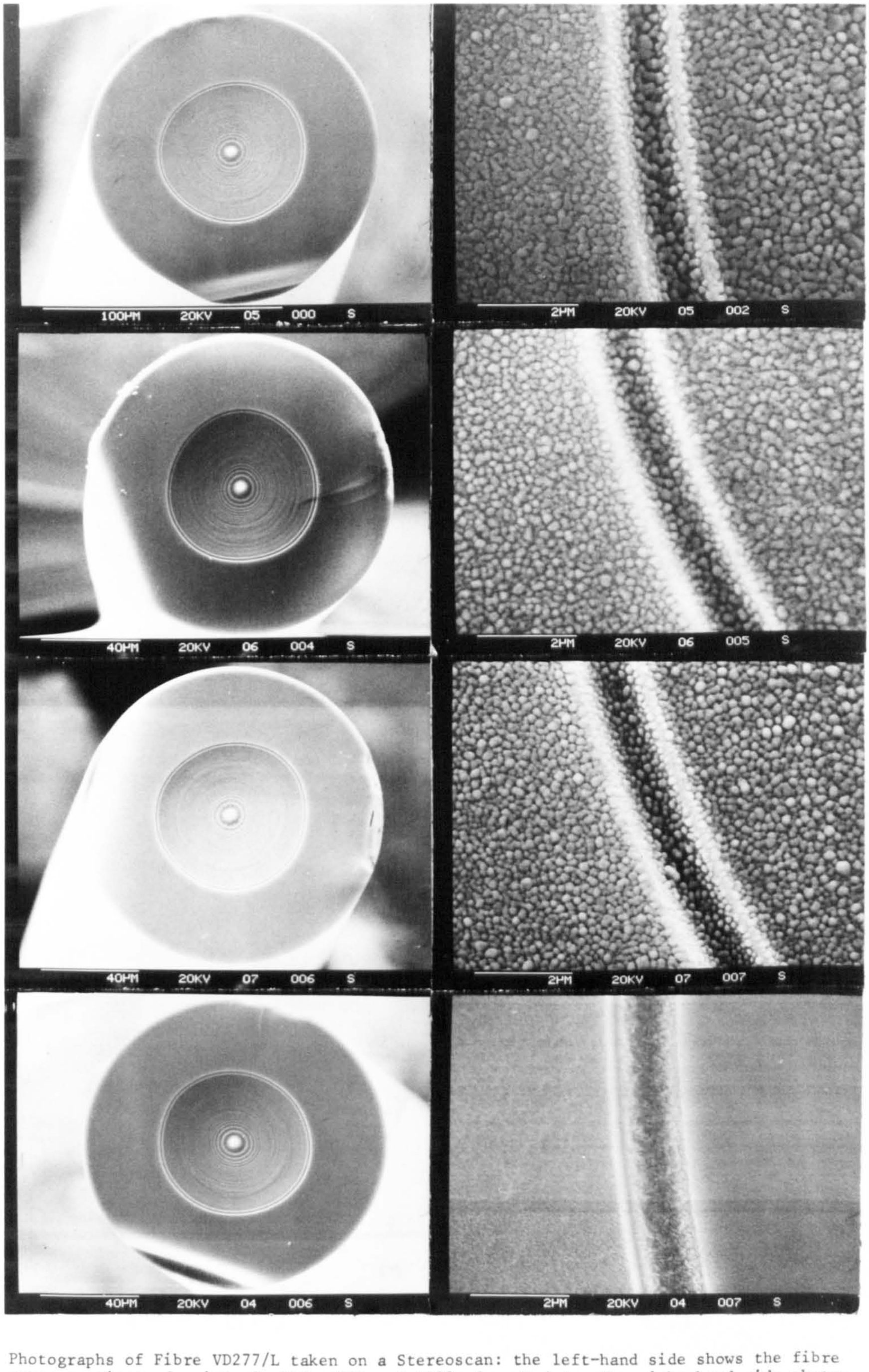

0m

500m

1000m

1500m

Photographs of Fibre VD277/L taken on a Stereoscan: the left-hand side shows the fibre cross-sections of points 0, 500, 1000 and 1500m from End A. The right-hand side photographs show a magnification of the B_2O_3/SiO_2 buffer layer in each case. The buffer layer slows the diffusion of OH^- ions from cladding to core during fibre fabrication. It can be seen that there is virtually no change in the buffer layer thickness over the 1.5km length.

Figure 7.7

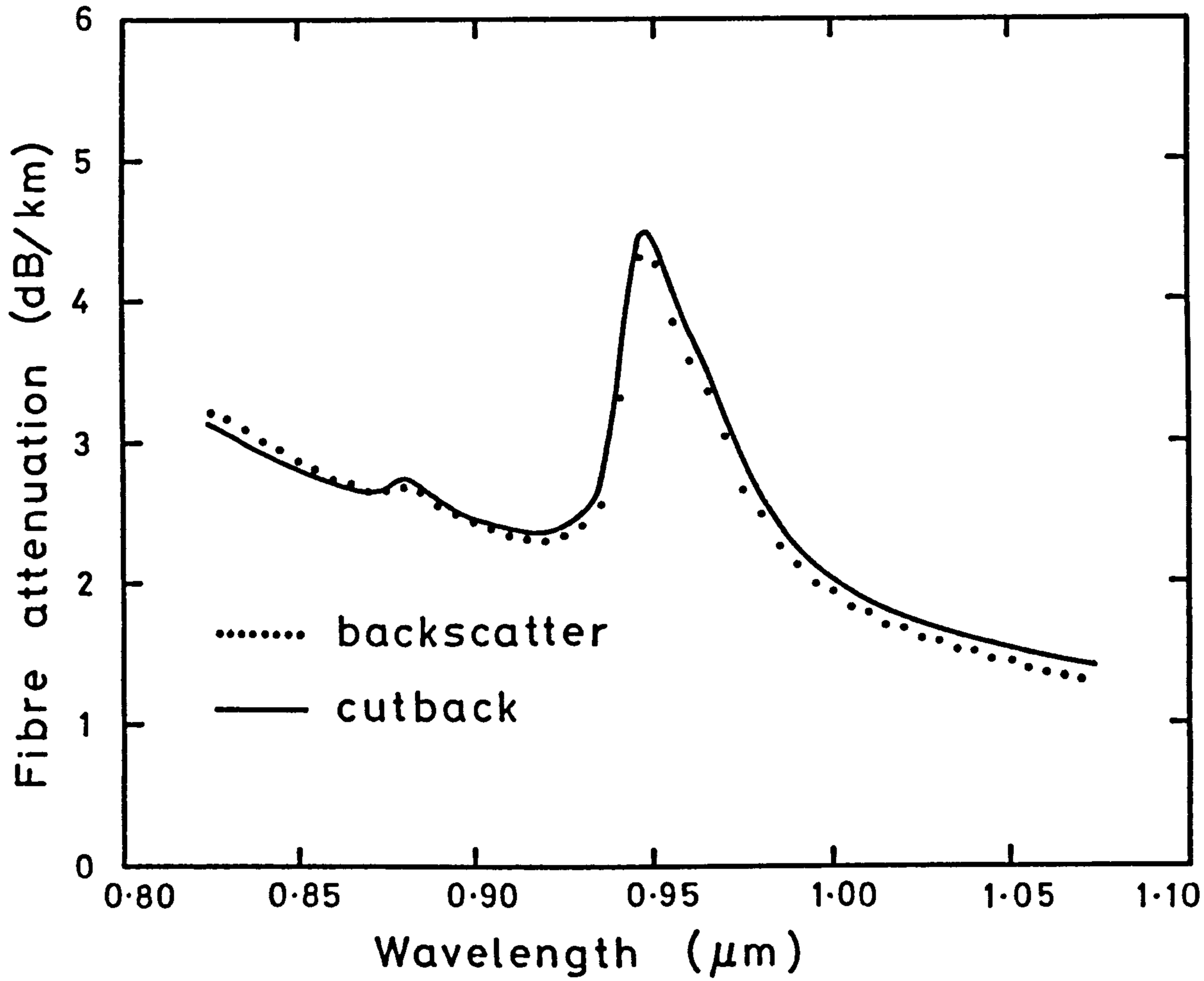

Spectral comparison of attenuation measured by the cut-back and backscatter techniques. The results represent the losses over the section 500-1500 m of fibre VD277/L.

Figure 7.8

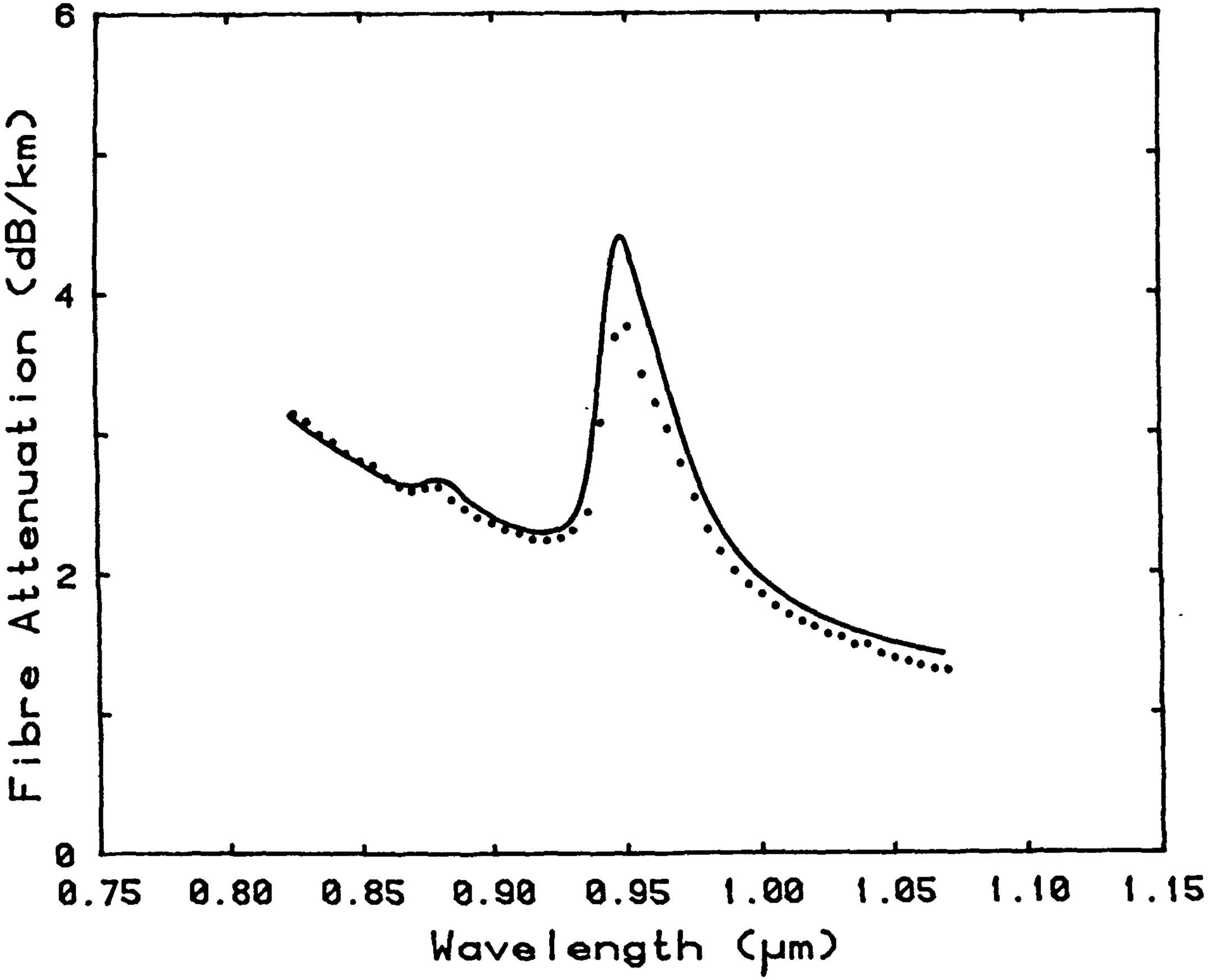

Spectral comparison of attenuation measurement by the cut-back and backscatter techniques. The results represent the losses over the section 1000-1500 m of fibre VD277/L.

Figure 7.9

CHAPTER 8

INTERPRETATION OF FEATURES IN BACKSCATTER WAVEFORMS

A major attraction of the backscatter technique is the ability to determine non-destructively the local fibre attenuation. Results from Chapter 7 indicate that the technique is capable of high resolution and accuracy in local loss measurement. The measurements described thus far were performed on a fibre of high quality and both the index-profile and fibre diameter were known to be uniform along the length. It is shown in section 2.5, however, that the accuracy of backscatter measurements depend critically on the constancy of the backscatter factor along the length.

In the present chapter, the dye and semiconductor laser systems (see Chapters 4 and 5 respectively for details of the instrumentation) are used to determine the effects on the backscattered power of non-uniformities in longitudinal fibre parameters. It is shown that depending on fibre quality, plots of local attenuation with length (the backscatter-loss signature) frequently exhibit severe fluctuations and anomalies such as negative values. In particular, backscatter-loss signatures are presented which clearly show correlation with programmed fibre defects[95-98] and indicate, in contrast to conclusions in the literature[7,81], that in many cases diameter fluctuations are the cause of unidentified features in backscatter waveforms. Moreover, it is possible to infer the nature of the fluctuation from its loss signature[95-98]. This latter point is most important since, in principle, a better understanding of the origin of fabrication-induced losses[86] could lead to improvements in fibre production techniques.

8.1 Fluctuations in Length-dependent Loss

Fluctuations in fibre attenuation can result from variations in either material or geometrical properties. These losses may be intrinsic to the glass, induced during fabrication or result from external influences (see section 2.1). The effects on backscatter measurements are determined by variations in the local backscatter factor (see equation

2.55). The latter may also be different when viewed from opposite ends of the fibre since it depends on the symmetry of the imperfection.

8.1.1 Correlated features

Material absorption and microbending variations are not expected to affect the local backscatter factor, unless also associated with a structural change in the glass or waveguide. These effects are symmetrical when viewed from opposite ends of the fibre. Figure 7.6, for example, demonstrates the ability of the backscatter method to accurately track the variation of the OH^- impurity[94].

8.1.2 Scatter centres

Point defects such as bubbles or phase changes may sometimes scatter light in the backward direction. In backscatter measurements these are usually characterized by individual non-Rayleigh pulse reflections superimposed on the Rayleigh 'exponential'.

Figure 8.1,for example,shows the effect of scatter centres on the backscattered power from two ends of a fibre. The measurement was performed with the dye-laser system operating at 0.9 μm and with a 10 ns pulse-width. A commercial multi-channel sampling system (Tektronix transient digitizer 7912AD) is used to acquire the waveforms. The fibre was manufactured by the Pilkington Glass Company using the 'phasil' process[174] (phase separation and leaching). Pulse reflections of 10 ns width are observed from the many scatter centres along the length of the fibre. It is believed that these scatter centres are indicative of incomplete leaching, incomplete dopant diffusion and/or the presence of voids in the glass.

8.1.3 Anti-correlated features

It is shown in section 2.8 that errors in local loss measurement depends on the derivative of the backscatter factor. Thus, variations in NA and diameter along the fibre may be expected to produce anti-correlation in the loss

signature when viewed from the ends A and B since the derivatives from the two ends are opposite in sign.

The backscatter loss signatures considered in Chapter 7, except for minor deviations, are symmetrical when viewed from opposite ends of the fibre and indicates that the backscatter factor is constant.

Consider figure 8.2 which displays the length-dependent loss of the MCVD fibre VD230/L. The 0.2 NA, graded-index fibre, 2.8 km in length was fabricated at Southampton University. Measurements were performed using the dye-laser operating at wavelengths of 1.00 and 0.87 μm, and for launching into both ends of the fibre, although for clarity the end B measurement at 0.87 μm is not shown. The sample separation for the 2-channel system was set at 50 m and measurements were taken at 20 m intervals down the fibre.

It is clear from the figure that the first 1.8 km of fibre possesses a reasonably uniform loss with only minor variations. However, the region thereafter exhibits a considerable oscillation with a period of ∿80 m and the loss appears to be anti-correlated when measured from the ends A and B. Actually, smaller anti-correlated features are also observed in the first 1.8 km section.

It is important that the origin of these fluctuations be determined in order to gain a better understanding of the backscatter method. Furthermore, this could lead to improvements and possibly the elimination of such features in future fibre production.

Di Vita[7,81] also reported the observation of anti-correlated features of somewhat larger magnitude and with a period ∿40 m and attributed them to fluctuations in fibre numerical aperture.

However, in the present instance (i.e. fibre VD 230/L) diameter variations appeared to be the more likely cause since it was known that at ∿1.8 km the feed weld-rod entered the drawing furnace and caused changes in the gas flow conditions in the hot zone. Diameter feedback control[159] had not been implemented at this time and therefore considerable diameter variations were observed in the final kilometre of

fibre due to changes in glass viscosity in the draw-down zone.

A consideration of MCVD fabrication methods indicated further that short-period fluctuations were more likely due to variations in fibre diameter.

8.1.3.1 Origin of variations in numerical aperture

For MCVD fibres[86], variations in numerical aperture may originate during preform fabrication due to an instability in deposition caused by a change in either the dopant flow or flame temperature. In addition, excessive heating during the collapse stage may lead to a loss of dopants from central core layers and result in small changes in numerical aperture (see figure 7.1).

Typically the hot zone of the deposition-torch extends over 3 cm of preform and any deposition fluctuations tend to be well dispersed. Thus, significant variations in numerical aperture are not expected over sections corresponding to less than one torch width. For a 1 cm diameter preform the torch width corresponds to approximately 300 m of fibre after drawing. In a high quality production the period of any numerical aperture variations is expected to be greater.

8.1.3.2 Origin of variations in diameter

In contrast to variations in numerical aperture, variations in fibre diameter may exhibit spatial oscillations of almost any period, however, if a good feedback control is used in fibre-drawing all but those of highest frequency may be eliminated[159].

An additional source of diameter variation may be a change in thickness of deposited core layers during the preform fabrication. If the overall fibre diameter is held constant then the variation in deposition will result in a taper of the core diameter. However, such effects usually occur only in the first few hundred metres of fibre which corresponds to the start of the deposition.

Re-consideration of figure 8.2 shows that fluctuations in loss in the final 1 km of fibre VD230/L are of short period (∿80 m) and therefore suggests a variation in the fibre

diameter. Further evidence to support this hypothesis is presented in the following sections.

It is noted here that the above discussion applies strictly only to MCVD fibres, since fibres fabricated by other techniques (e.g. VAD) may well also exhibit variations in numerical aperture over short lengths. This may be an avenue for a future investigation.

8.2 Effect of Programmed Diameter Changes in Fibre VD277/L

In order to determine the effect of variations in diameter on backscatter measurements, the fibre drawing was modified such that with the preform feed rate held constant, the drum speed could be modulated to produce a desired diameter profile. Initially, step changes of 1 μm at a time could be programmed on a thumbwheel switch, but in a later development the control was modified so that an analogue input could be used to give a continuous variation. In the latter instance, a flexibility was achieved by deriving the analogue input from a D-A converter under computer control.

The recent advances in fibre-drawing techniques at Southampton University[159] enables fibre diameters to be programmed and controlled to <0.2 μm rms over their whole length, thereby removing any uncertainties in backscatter measurements due to diameter features of unknown origin.

8.2.1 Programmed diameter profile

The characteristics of fibre VD277/L are presented in section 7.1, except for the details of the programmed diameter changes which are now described. The fibre was pulled with a constant diameter of 125 μm (core diameter 60 μm) over the first 1.7 km. It was then programmed with a double taper, a triple taper and a single taper, each separated by a section of constant diameter. Figure 8.3 shows the details of the diameter profile. The section of constant diameter between each taper enabled separation of the individual features and provided a base-line to determine the intrinsic fibre loss. Each taper was piece-wise continuous and comprised steps typically of 1 μm magnitude.

The double taper consisted of 10 decreasing 1 μm steps separated by 20 m, except for a 40 m section between the 8th and 9th steps. This was followed by 10 increasing 1 μm steps separated by 15 m.

The single taper consisted of 14 steps of 1 μm separated by 5 m, except for the 14th step which was of 2 μm magnitude and separated from the 13th by a distance of 10 m.

The triple taper consisted of steps of somewhat larger amplitude as shown in figure 8.3.

In practice, the step changes in diameter were not infinitely sharp and were determined by the response time of the control system. Typically, diameter transitions occurred over about 1 m of fibre during the pull.

8.2.2 Identification of backscatter features and correlation with programmed defects

Figure 8.4 shows the results of local attenuation measurements performed on the 3.2 km length of fibre VD277/L. The dye-laser and parametric oscillator system was operated at a wavelength of 1.006 μm and a 2-channel gate separation of 50 m was used with the local loss taken at every 20 m down the fibre. Measurements were performed from both fibre ends and the results are shown vertically displaced for clarity; end A (lower curve) and end B (upper curve) correspond to the left- and right-hand axes respectively and the arrows indicate the directions of launching. A schematic of the fibre diameter profile is also shown.

The loss in the well-controlled section of fibre is remarkably featureless when measured from either end and demonstrates both the accuracy of the measurement and the quality of the diameter control[159]. There is a considerable improvement when compared to the loss signature in figure 8.2 for the fibre VD230/L where no diameter feedback control was used.

In the tapered sections of fibre, however, strong fluctuations in loss are observed which are closely correlated to the programmed diameter variations. Moreover, the measurements from either end are in exact anti-correlation with one another and by examination clearly follow both the magnitude

and sign of the change in fibre diameter. For example, the curve measured from end A exhibits the infamous negative loss[7,81] at 2.4 km which can now be associated with a contracting fibre section (the inverse of what might have been expected), whereas from end B the same feature produces an apparent positive loss. Moreover, the double taper at 2.0 km gives both positive and negative losses but of smaller amplitude because the taper depth is less. Even the slope of the small triple taper at 2.2 km is faithfully reproduced, although in this case the 50 m gate separation of the sampling system has been unable to resolve properly the magnitude of the feature (see section 8.2.4).

Note that there is a strong peak at 1.8 km which is the only feature that correlates when measured from either end. Reference to the diameter charts for this fibre (not shown) revealed that at this point a major change in diameter occurred spontaneously for a few centimetres owing to the presence of a bubble in the preform. Although unprogrammed, this feature serves to show how regions of actual loss can be separated from diameter variations in the fibre loss-signature.

The origin of features in some backscatter waveforms may now be diagnosed. Re-consider figure 8.2 which shows the loss signature of VD230/L. Here, the reasonably flat section with minor anti-correlated features indicates good diameter stability and no scatter centres. However, the region from 1.8 km onwards exhibits considerable anti-correlated fluctuations of short period and therefore implies diameter variation. The signature taken at 0.87 μm shows virtually identical features.

8.2.3 Single-channel measurements

The relationship between the backscattered power and the loss signature is now considered by analysis of single-channel measurements from both ends of the fibre. Figure 8.5 shows the backscattered power and the corresponding local attenuation for the final 1.6 km of fibre VD277/L. The measurements were performed at a wavelength of 0.904 μm using a semiconductor laser. The backscattered power was measured

by single-channel sampling of the waveform (see section 3.1) and the local loss determined by the 2-channel method (see Chapter 5).

The sudden drop in backscattered power at 1.8 km caused by the bubble is clearly evident and is the only correlated defect in both the end A and end B results. Note that the 2-channel sampling which determines the incremental loss from the local time constant of the backscattered power, amplifies greatly the presence of the defect and causes some broadening due to the finite gate width (50 m). Using equation (2.41) and the results on figure 8.5, the loss at the fault is found to be ∿2 dB and is identical for launching into the two ends.

The triple and single tapers, on the other hand, clearly produce anti-correlation in the loss-signature. The single taper at 2.4 km which is contracting when measured from end A causes an increase in backscattered power and therefore appears to produce a negative loss. In contrast, from end B the taper is expanding and results in decreased back-scattered power and an apparent increase in loss. The two effects are the opposite of that which is normally expected since uni-directional propagation through a contracting taper causes power loss, whereas with an expanding taper no loss is observed[175].

The apparent anomaly can be attributed to the fact that in backscatter measurements light passes through the taper in both the forward and backward directions. In addition, the local backscatter factor is modified by the combined effects of the taper, cladding modes and differential mode attenuation. This effect is described in more detail in section 8.3 where a model for the mechanism is proposed.

8.2.4 High resolution measurements

Before modelling the effects of diameter fluctuations, it is instructive to analyse each feature in greater detail. The double taper is removed by cutting the fibre at 2105 m from end A (see figure 8.3). Figures 8.6-8.8 show high resolution backscatter measurements on the single and triple tapers of fibre VD277/L. Light at a wavelength of 0.9 μm

from the dye-laser and parametric oscillator system was launched into the fibre and data for both end A and end B measurements was acquired and averaged using a commercial multi-channel sampling system (Tektronix transient digitizer 7912AD). The pulse width of the laser was shortened to 10 ns by modifying the length of the high voltage delay line shown in figure 4.2 and this enabled smaller fibre sections to be resolved.

The results are now compared to the diameter profile shown in figure 8.3. Figure 8.6 shows the backscattered power in the region of the triple and double tapers. Figures 8.7 and 8.8 show higher resolution measurements of the triple and double tapers respectively.

In the case of the single taper, figure 8.8, the measurement from end A shows clearly that each decrease of 1 μm in fibre diameter produces a small increase in backscattered power. The effect, however, becomes smaller as the taper deepens; eventually the intrinsic attenuation appears to dominate and the backscattered power decays once more. The net effect of the taper is that there appears to be a decrease in loss when measured from end A. In the reverse direction (end B) each increase of 1 μm in fibre diameter produces a small decrease in the backscattered power. The individual steps are not so pronounced, however, since the losses are superposed on a decaying exponential. Also note that the 13th step of the single taper which is of larger magnitude (see figure 8.3) is clearly evident in both the end A and end B results of figure 8.8.

In a similar way, the backscattered power from the triple taper, shown on figure 8.7, displays the effects of both the positive and negative increments in the fibre diameter. The magnitudes of the steps in backscattered power are proportional to the changes in fibre diameter. Furthermore, there is no significant change in the level of the backscattered power after, than before the taper, other than that accounted by the intrinsic fibre loss over the section. Forward propagating power is therefore not affected by small diameter changes, a result which is believed to be due to the under-excitation of the guide. This important observation forms the basis of the model formulated in the next section.

8.3 Modelling the Effect of Diameter Variations

For a fully excited fibre uni-directional propagation through a contracting taper causes power loss, whereas with an expanding taper no loss occurs[175]. However, in back-scatter measurements the opposite effect is observed (see section 8.2). The model developed here shows that this is caused by attenuation of the backscattered light which, since it contains high-order modes, is sensitive to mode conversion and differential mode attenuation (DMA). The model is supported by experimental evidence to be described in the following sections.

The backscattered power P_R received by the detector is affected by both forward losses of the probe pulse and reverse attenuation of the scattered light. For simplicity, assume that the fibre base-line loss α, is equal in both directions and thus the returned power, from equation (2.31), is

$$P_R = P_o \exp(-2\alpha\ell) \qquad \ldots (8.1)$$

where ℓ is the distance to the scatter point and P_o is now re-defined as the backscattered power from the start of the fibre. Furthermore, assume that the forward propagating pulse only partially excites the guide so that it is able to negotiate small diameter changes without loss.

8.3.1 Expanding taper

In the case of an expanding taper (see figure 8.9(i)) the probe pulse propagating to the right passes through the taper without loss; high-order modes in the left-hand guide are converted to lower-order modes in the right-hand guide. However, the light returned to the detector from a scatter point within or beyond the taper region suffers an additional loss as the high-order modes of the larger waveguide, which have been excited by the scattering process, are lost by radiation.

If we assume that the scattering excites all reverse-propagating modes equally, the magnitude of the loss is given simply by the reduction in area of the guide[175].

SOUTHAMPTON UNIVERSITY LIBRARY

$$\text{Thus} \quad P_R = P_o \frac{d_o^2}{d(\ell)^2} \exp(-2\alpha\ell) \qquad \ldots (8.2)$$

where $d(\ell) = d_o$ for $\ell < \ell_o$, $d(\ell) = d_1$ for $\ell > \ell_1$ and $d(\ell)$ varies linearly for $\ell_o < \ell < \ell_1$.

8.3.2 Contracting taper with differential mode attenuation (DMA)

The situation for propagation into a contracting taper (see figure 8.9(ii)) is more complex. Low-order modes constituting the probe pulse to the left of the contracting taper are converted by the taper to higher-order modes in the right-hand guide. However, if the fibre section before the taper is under-excited and if the diameter change is small then a negligible loss of forward power may be observed.

The mechanism[95-98] which leads to an increased back-scattered power level being received at the source for scatter points following a contracting taper involves mode conversion, followed by DMA. Light scattered into high-order modes from a point after the taper is converted to lower-order modes on traversing the taper, since it appears expanding to the reverse propagating light. Thus light from beyond the taper returns to the fibre input with a greater proportion of lower-order modes when compared to the scattering from a point prior to the taper.

Since the fibre has a lower loss when partially excited,[25-27] a greater proportion of the light from beyond the taper arrives at the source than from before the taper, giving an apparent reduction in loss. Note that the cause of the DMA may be intrinsic to the fibre, mode selection at the optical receiver, or a reduction in fibre diameter between the point of interest and the detector. In the latter case, the effect of the contracting taper is to recoup returning power which for points prior to the taper had previously been lost at the diameter reduction.

If the DMA is introduced by a prior diameter reduction with minimum core-diameter d_{min}, (see figure 8.9(ii)), and assuming that the scattering process excites all modes equally, then the received power on traversing a contracting taper will increase in proportion to the area change.

$$P_R = P_o \frac{d_o^2}{d(\ell)^2} \exp(-2\alpha\ell) \qquad \text{for } d(\ell) > d_{min} \qquad \ldots(8.3)$$

$$= P_o \frac{d_o^2}{d_{min}^2} \exp(-2\alpha\ell) \qquad \text{for } d(\ell) \leq d_{min} \qquad \ldots (8.4)$$

Note that for DMA introduced by mechanisms other than diameter changes the relationship will be slightly different, but is expected to depend on a function which links the area change to the particular type of DMA. This, however, has not been pursued.

8.3.3 Contracting taper with cladding effect

For a contracting fibre section a second mechanism can contribute to an increase in received power after the taper (figure 8.9(iii)). A scattering point following the taper excites both the fibre core and cladding, and backscattered light propagates in the two regions, particularly if the cladding loss is low (e.g. if the fibre is silicone coated). When the cladding light encounters the taper,which now appears expanding in the reverse direction, it is able to enter the core. By reciprocity with the case described by equation (8.2) above, the power which can enter the core is proportional to the area change.

Thus

$$P_R = P_o \frac{d_o^2}{d(\ell)^2} \exp(-2\alpha\ell) \qquad \ldots (8.5)$$

There is now no requirement for DMA in the reverse path and the limitation on the increase in power level given by equation (8.4) is no longer present. Note that the magnitude of the effect is identical to that of equation 8.3 and exactly reciprocal to that for pulse propagation in the reverse direction (equation (8.2)).

In practice, the DMA and cladding mode mechanisms often co-exist. However, cladding modes suffer a higher loss than power in the core and this provides a means whereby the two power-increasing mechanisms can be distinguished. This is described further in the following sections.

8.3.4 Computer simulation

Assuming all core modes are equally excited by the scattering process, the observed loss α as a function of length is expected to be proportional to the change in core area. Thus, from equations (8.2)-(8.5)

$$\alpha(\ell) = \alpha_o - \frac{1}{2}\frac{d}{d\ell}\left[10 \log_{10} \frac{d_o^2}{d(\ell)^2}\right] \quad \ldots (8.6)$$

where α_o is the intrinsic fibre loss.

In a computer simulation described here, tapers comprised N sections of length $\delta\ell$ and with core radii r_o to r_N. A convention is established whereby contracting sections are analysed by launching into end A and expanding sections are probed from end B (see figure 8.10(a) and (b) respectively). The results of analyses from the two fibre ends are then easily superimposed for comparison.

For the expanding taper shown in figure 8.10(b), the backscattered power at position ℓ in section N (see Appendix II) is

$$P_R = P_o \frac{r_o^2}{r_N^2} \exp(-2\alpha_c \ell) \quad \ldots (8.7)$$

Note that cladding modes do not influence the backscattered power in the case of an expanding taper.

Similarly, for a contracting fibre section the back-scattered power from a point at position ℓ in section N (see Appendix III) is

$$P_R = P_o\, e^{-2\alpha_c \ell}\left(1 + \sum_{n=1}^{N} e^{-\Delta\alpha(\ell - x - (n-1)\delta\ell)} \cdot \left[\frac{r_{n-1}^2}{r_n^2} - 1\right]\frac{r_n^2}{r_N^2}\right) \quad \ldots (8.8)$$

where $\Delta\alpha = \alpha_{cl} - \alpha_c$; and α_{cl}, α_c represent the attenuation coefficients of the cladding and core respectively and the other parameters are defined on figure 8.10(a). The sum-mation term in equation (8.8) accounts for the additional backscattered power due to the coupling from cladding to core. Note that in the limit of small δr and with zero differential

cladding loss, the summation becomes an integral and equation (8.8) reduces to the expression in equation (8.5).

In order to assist in comparison with experimental results the fibre and taper parameters used in the following computer calculations (the latter which are based on equations (8.7) and (8.8)), are chosen to be similar to those of the single taper in fibre VD277/L (see figure 8.3).

8.3.4.1 Effect of step changes in fibre diameter

Figure 8.11, upper curves, show the backscattered power for simulated launching into two ends of a tapered fibre with core and cladding losses of 2.5 and 10 dB km^{-1} respectively. The dimensions of the fibre at the end A are 60 μm-core and 125 μm-cladding. The solid curves show the effect of a taper consisting of 3 μm steps in the outside diameter (o/d) at 15 m intervals over a 75 m length of fibre. Also shown is a taper with the same average slope but consisting of 0.2 μm steps at 1 m intervals over the same section (i.e. slope = 0.2 μm/m o/d).

It is clear from the figure that at each diameter step in the contracting section coupling of power from the cladding to core results in an increase in received backscatter level. The effect from the opposite end (i.e. for the expanding section) is step decreases in backscattered power, although the mechanism does not involve interaction with cladding modes.

The lower curves in figure 8.11 show the calculated local attenuation for the 75 x 0.2 μm stepped-taper. The loss-signature measured from the two ends is anti-correlated in the region of the diameter variation and agrees generally with previous experimental results (e.g. figure 8.4). An apparent decrease in loss is observed for a contracting taper whilst an expanding taper results in an apparent increase in loss.

8.3.4.2 Effect of cladding loss

The effect of cladding loss on the backscattered power and calculated local attenuation is shown in figure 8.12. The fibre core/cladding dimensions are 60/125 μm at the end A and the core loss is 2.5 $dB.km^{-1}$ as before. The taper consists of 75 x 0.2 μm steps in the fibre outside diameter separated by 1 m intervals (i.e. slope = 0.2 μm/m o/d). Curves are shown for cladding losses of 10 and 100 $dB.km^{-1}$ and are smoothed to simulate a receiver bandwidth of 5 MHz.

It can be seen that for the end A measurement (contracting taper), the increase in backscattered power fades back to the normal level (dashes) for scatter points downstream from the taper as a result of preferential attenuation of power returning in the cladding. The effect on the loss-signature is firstly to produce a negative loss and then, after the taper, a positive overshoot of magnitude proportional to the excess cladding attenuation (see figure 8.12 lower solid curve). In the limiting case of equal core and cladding losses, however, no positive overshoot is observed.

If the increase in backscattered power at the contracting taper is caused by DMA introduced, for example, by a prior diameter restriction with $d_{min} < d(\ell)$ (see section 8.3.2), then the effect is similar to the dotted curve in figure 8.12 except that once again no positive overshoot is observed in the loss-signature.

The result from end B (expanding taper) shows a decrease in backscattered power and an apparent increase in fibre loss at the taper. The effect is independent of cladding mode attenuation.

8.3.4.3 Effect of taper slope

The effect of taper slope on the backscattered power and local attenuation is shown in figure 8.13. The fibre core/cladding dimensions at end A and the attenuations are 60/125 μm and 2.5/10 $dB.km^{-1}$ respectively. Each taper consists of 75 steps at 1 m intervals along the fibre but with differing step sizes. Curves are shown for average taper slopes of 0.2, 0.1 and 0.05 μm/m (o/d) and are smoothed

to simulate a receiver bandwidth of 5 MHz.

It can be seen that the increase/decrease in backscattered power and the apparent attenuation change for contracting/ expanding fibre sections is proportional to the taper slope.

8.4 Comparison of Model and Experimental Results

There appears to be a general agreement between the model (figures 8.11-8.13) and experimental results (figures 8.3-8.8). Diameter variations give rise to anti-correlated features in backscatter loss signatures; a contracting/expanding taper causes an apparent decrease/increase in loss.

However, for fibre VD277/L, the loss signature of the single contracting taper (see figures 8.4 and 8.5) does not exhibit a positive overshoot due to excess cladding attenuation (cf. prediction of model, e.g. lower solid curve in figure 8.12 where α_{cl}= 100 dB.km^{-1}). This indicates that either the cladding loss is small or that the negative loss feature is caused by the DMA mechanism. The response is therefore similar to that shown on figure 8.12 (dots) except that no positive overshoot occurs. The double taper in fibre VD277/L with d_{min}= 115 μm occurs prior to the single taper (see figures 8.3 and 8.4) and therefore provides a mechanism for DMA (see section 8.3.2). In principle, the DMA can be removed by cutting the fibre at 2105 m from end A (see figure 8.3). The backscatter from the triple and single tapers remeasured is shown on figure 8.6. It can be seen that for the single contracting taper the increase in backscattered power now fades back to the normal level for scatter points downstream from the taper, indicating a preferential cladding attenuation of ∿100 dB.km^{-1}, a not unlikely figure for a silicone-clad fibre. Thus, the removal of the double taper caused a reduction in DMA and enabled the effect of coupling from cladding modes to be observed. The measurement from end B (expanding section) remains unchanged.

A further example of a single taper is shown in figure 8.14. The fibre VD314/L is a 0.2 NA graded-index MCVD fibre and was pulled with a 120 μm outside diameter over the first 1 km and then tapered down to a diameter of 105 μm at a rate

of 0.2 μm/m. The taper consisted of 1 μm steps at 5 m intervals over a length of 75 m. There was also a bubble in the fibre at approximately 1.5 km from end A. Backscatter measurements were performed with a semiconductor laser operating at 0.9 μm and results for both the 2-channel and multi-channel techniques are shown (see figures 8.14 (a) and (b) respectively).

It can be seen that the bubble produces a correlated feature on the backscatter waveform when measured from the two ends. In contrast, the taper gives rise to an anti-correlated feature which for the contracting section exhibits firstly a negative-going loss and then a positive overshoot. The latter effect is predicted by the model and may be attributed to the excess loss of power travelling in the cladding. The response for the expanding taper is an increase in loss and the mechanism does not involve cladding modes.

8.4.1 Magnitude of features

For small diameter variations it is predicted that the change in backscattered power is proportional to the change in core area. This is now tested by analysing the back-scattered power and diameter profile of the triple taper shown in figure 8.7. Step changes of -2, -2, +8 and -4 μm are programmed into the fibre of nominal diameter 125 μm. The step changes were not instantaneous but each occurred over a distance of approximately 1 m (see section 8.2). It can be seen that a decrease in fibre diameter causes an increase in backscattered power and vice-versa, but for each diameter step the change in fibre area exceeds the change in back-scattered power by a factor of 2. This factor appears to be consistent throughout all experimental results.

The discrepancy is believed to be due to the assumption in the theory that the backscattered power fully excites the fibre (see section 8.3). In practice, however, high order skew rays are not fully excited in the backward direction since the forward propagating light only partially excites the guide. Thus, the effective mode volume of the back-scattered light is reduced and calculations based simply on

core area changes become inaccurate. Nevertheless, the model appears to be generally successful in describing the back-scatter response of a fibre with diameter variations.

8.4.2 Effect of DMA on contracting tapers

In order to test the interaction of the DMA and cladding mode mechanisms a step index fibre VD304/L was programmed with a single taper of slope 0.2 μm/m over a 70 m section. The fibre was 115 μm in diameter at the end A and reduced to 101 μm after the taper. DMA could be artifically induced by placing an aperture between the photodiode-focussing lens and the beam-splitter (refer to figure 2.1).

The results of 2-channel measurements on the contracting section are shown on figure 8.15. Curve 1 is the loss measured with full reception (i.e. aperture wide open). A feature characteristic of the cladding-mode mechanism is apparent; i.e. a negative-going loss followed by a positive overshoot.

Curve 2 shows the effect of a restricted photodiode reception (i.e. small aperture) with an effective NA of 0.04. It can be seen that the DMA introduced by the aperture results in an enhanced negative-going loss and a reduction in positive overshoot. The latter effect indicates that the detected cladding power in the backscatter is reduced due to discrimination of the aperture against high-order modes. Note that the positive overshoot did not disappear completely with restricted aperturing and this is believed to be due to mode-mixing of the backward travelling light.

The backscatter measurement using a restricted aperture necessarily invoked a significant penalty in the level of detected power. In order to remove measurement uncertainty which might arise due to the dynamic range performance of the instruments, the aperture was subsequently replaced by an attenuator with an equivalent loss (but no mode-selection). The measurement was repeated and found to give an identical result to curve 1.

The effect of launching with a restricted numerical aperture was tested by placing the aperture between the lens

adjacent to the laser and the beam-splitter (refer to figure 2.1). However, a negligible difference was observed between the measurement and that of curve 1 on figure 8.15, a result which underscores the dominance of backward propagating light relative to the forward light in determining the characteristics of the observed backscatter features.

8.4.3 Verification of coupling from cladding modes

Further experimental evidence for the influence of cladding modes on backscattered power may be obtained by removing the primary silicone coating and placing the fibre in a medium of high refractive index (e.g. liquid glycerol). The experiment was performed on the single taper of fibre VD277/L using a semiconductor laser operating at 0.9 μm. In order to remove any DMA introduced by the triple taper (see figure 8.3), the fibre was cut at 2280 m.and measurements were performed only on the remaining section (2280-3280 m).

Figure 8.16(a) shows a photograph of the backscatter waveform measured from the end A (i.e. contracting taper) before the silicone coating was removed. Figure 8.17, curve 1, shows the waveform recorded on the multi-channel transient digitizer. The increase in backscattered power at the contracting taper returns to the normal backscatter level after a distance of 100 m, indicating a preferential cladding attenuation of $\sim$100 dB km^{-1}, a not unlikely figure for a silicone-clad fibre. Curve 4 of figure 8.17 shows the result for propagation in the reverse direction, i.e. into the expanding taper.

Evidence of the effect of cladding modes was obtained by removing sections of silicone coating in concentrated sulphuric acid. Firstly, $\sim$8 cm of silicone was removed at the 2490 m point (see figure 8.3) and the section was index-matched in liquid paraffin to remove the cladding power. Figure 8.16(b) is a schematic of the expected backscatter response for the contracting taper based on the model prediction. The actual response is shown in the photograph of figure 8.16(c). The cladding power from sections beyond the taper no longer contributes to the feature and the waveform returns to the normal scattering level immediately after

the taper. (Unfortunately there is no multi-channel record of this waveform.)

The whole taper section was then immersed in concentrated acid and the silicone coating removed. As the silicone slowly dissolved the end A response altered and a number of peaks became evident in the region of the taper (see figures 8.16(d) and (e)). The response was also recorded on the multi-channel transient digitizer and is shown on figure 8.17, curve 2. In the latter measurement a 10ns-width pulse from the semiconductor laser was used to resolve the individual peaks. Relative to curve 1 there is a marked increase in backscattered power in the region of the taper. However, for the end B measurement (i.e. expanding taper) no such effects were observed and the response remains identical to that before acid immersion (curve 4).

The origin of the peaks is believed to be due to scattering of the cladding modes at the fibre/acid interface. This power is able to enter the core at the contracting section since it appears expanding in the reverse direction. Consideration of figure 8.3 for the single taper shows that the peaks may be attributed to individual steps in the fibre diameter profile. Note that the peaks were also quasi-stable and the response could be modified by agitating the fibre in the acid-bath. Figure 8.18 shows three of the many responses that could be generated in this way. This effect underscores the complexity of the scattering process at the fibre/acid interface.

In order to strip the cladding power and thereby eliminate the effect of interface-scatter, the fibre was removed from the acid and immersed in a bath of index-matching liquid (glycerol). The effect on the contracting taper is shown on figure 8.17, curve 3. The backscattered power at the taper is reduced due to the loss of cladding modes. The feature is not removed completely however, an observation which emphasizes the persistence of the low-order cladding modes which contribute to the effect. It should be noted that there was no change in the end B response due to the index-matching (in accordance with the model prediction).

In a further experiment a step index fibre VD304/L programmed with a similar single taper was subjected to the same process. Figure 8.19 shows photographs of the effect of acid immersion on the response for the contracting section. Sharp quasi-stable peaks were again observed in the back-scatter response from the contracting taper. No change was observed in backscatter measurements from end B (expanding taper).

8.4.4 Effect of taper slope

The tapers considered thus far comprised a number of diameter steps, typically of 1 μm amplitude. A modification to the fibre drawing enabled smooth diameter variations to be achieved by modulating the drum speed with an analogue voltage, the latter derived from a D-A converter under computer control.

Two 1 km lengths of fibre VD335/L were programmed with 5 μm-deep smooth tapers with slopes of 0.1 and 0.2 μm/m (o/d) at approximately 500 m from the ends designated A. The end A and end B fibre diameters were 125 and 120 μm respectively.

The result of backscatter measurements and the local-loss calculations performed by the multi-channel transient digitizer are shown on figure 8.20. It is clear that the change in backscatter loss is proportional to taper slope in accordance with theoretical predictions (figure 8.13). However, once again the magnitude of the effect is half of that which might be expected from the change in guide area (see section 8.4.1). The noise on the loss curves is due to digital noise in the acquired data and the small gate separations used for 2-point calculations.

8.5 Oscillatory Diameter Variations

Large oscillations in backscattered power of ∿40 m period were reported in the literature[7,81] and their origin was attributed to variations in fibre numerical aperture. It is suggested here that for MCVD fibres these features are more likely due to fluctuations in diameter. The effects of diameter changes are modelled and demonstrated experimentally.

As a further example, a fibre was fabricated with short-period sinusoidal diameter variations. Figure 8.21, upper curve, shows the diameter-profile of a graded-index, 0.2 NA MCVD fibre programmed with 4 cycles of a sinusoid, 5 μm peak-to-peak, over a length of 200 m. An additional un-programmed diameter change also appears at a further 50 m down the fibre. Backscatter measurements were performed using a semiconductor laser operating at 0.9 μm and a multi-channel digitizer acquired the data.

The backscattered power (figure 8.21, centre curves) measured from the two ends follows closely the variations in fibre diameter; a decrease in diameter results in an increase in backscattered power and vice-versa. Furthermore, the plots of local attenuation (lower curves) are anti-correlated for both programmed and unprogrammed features. Also shown (dashed) is the theoretical result calculated from equation (8.6) and it is clearly of similar form but of somewhat reduced amplitude when compared to the experimental result. The latter effect is believed to be due to partial excitation of the guide by the backscattered light and is in accordance with previous results.

Note that the backscattered power in figure 8.21 returns to the exponential decay after the diameter variations and the local attenuation curves are symmetric about a fibre median loss of 2.5 $dB.km^{-1}$. This indicates that no forward loss was caused by the diameter variations and again confirms the basic assumption in the model. Thus, the observed features are predominantly caused by the sensitivity of backscattered light to diameter changes.

8.6 Length-dependent Measurement of Microbending Loss

Point defects such as bubbles can be distinguished from diameter variations by analysing the backscattered power from two ends of a fibre. Point defects and diameter variations give rise to correlated and anti-correlated features respectively. The effect of a distributed loss on the back-scatter waveform is now considered.

A 1 km length of a 0.2NA, graded-index MCVD fibre was pulled and wound tightly on a polystyrene drum. Usually, a

silicone protective coating is applied to the fibre to act as a buffer against external forces which can induce micro-bending loss. However, no protective jacketing was applied to this fibre. In addition, the fibre was programmed with a single smooth taper of slope 0.2 μm/m (o/d), contracting when viewed from end A. The diameters at end A and end B are 125 and 120 μm respectively. Backscatter measurements were performed using a semiconductor laser operating at 0.9 μm and a multi-channel digitizer acquired the data.

The fibre was slowly unwound from the drum and coiled loosely on the floor, end A first. Curves 1-6 of figure 8.22 show the results of consecutive measurements from end A of the backscattered power and calculated loss at various stages of unwinding. It is clear from the figure that as the fibre is unwound from the drum, the local attenuation is reduced from 3.8 to 2.3 dB km^{-1}. Thus, microbending on the drum contributed 1.5 dB km^{-1} to the total fibre loss. This indicates the value of using a soft protective jacket to ensure good transmission performance.

Curve 7 of figure 8.22 shows a measurement taken from end B at the same stage of unwinding as that of curve 4. Comparison of results shows that the diameter variation causes an anti-correlation feature whilst the microbending loss produces a symmetrical imperfection and is correlated from the two ends.

Thus, in backscatter measurements faults may be separated into two categories, correlated and anti-correlated. Correlated defects such as microbends, bubbles, breaks and absorption centres are symmetrical when viewed from both ends of a fibre and cause attenuation of forward propagating light. On the other hand, variations in numerical aperture and fibre diameter may be identified since their loss signatures are anti-correlated from the two ends.

8.7 Summary

The change in backscattered power levels associated with variations in longitudinal fibre parameters is considered in

this chapter. Backscatter waveforms are presented which for the first time clearly show the relationship between features and programmed fibre defects. It is shown that analysis of the backscattered power from two ends of an optical fibre can lead to the location and diagnosis of imperfections.

Two general classifications of feature are identified; firstly, there is the correlating feature caused, for example, by absorption losses, microbending and point defects which result in an identical loss of power when measured from the two fibre ends. Secondly there is the anti-correlating feature caused by variations in the backscatter factor which result generally in mode conversion but not necessarily an immediate power loss. Imperfections which fall into this category are, for example, variations in numerical aperture, diameter and refractive index profile. Anti-correlated features exhibit an apparent positive or negative error in backscatter-loss measurements which depends on the direction of launching.

A consideration of fabrication methods indicates that for MCVD fibres, oscillations in backscattered power of short period ($\lesssim$300 m) are most likely caused by diameter variation. Note that this conclusion contrasts the hypothesis in reference 7 where the origin of similar fluctuations is attributed to numerical aperture variations.

Measurements presented in this chapter on fibres with programmed diameter variations confirm anti-correlation in backscatter-loss signatures. It is shown that propagation through a contracting taper results in an increase in backscattered power and an apparent reduction in loss. Conversely, an expanding taper results in a decrease in backscattered power and an apparent increase in loss. Both these effects are the opposite of that which might be intuitively expected by a consideration of uni-directional light propagation.

A simple mathematical model to describe the phenomenon has been developed and compared to experimental results. It is shown that the effect is caused by attenuation of the backscattered light which, since it contains high-order modes, is sensitive to mode conversion and differential mode attenuation.

Cladding modes also play a significant part in the production of negative-going loss features which are characteristic of contracting sections.

Results from the model are in general agreement with observed experimental behaviour, however, it was found that the change in backscattered power is only half that predicted by the change in fibre area. This is believed to be due to the assumption that the backscattered power fully excites the fibre. In practice, however, the fibre is not fully excited in the backward direction since forward propagating power only partially excites the guide.

Fibres with diameter variations of the type described in this chapter are perhaps not indicative of those produced by high quality fabrication methods. However, the fibre shown in figure 8.21 is within the CCITT specification for tolerance in outside diameter[89]. Thus, it is interesting to speculate as to the quality of some of the lower-grade fibres that may be manufactured and accepted for telecomms-applications in the future.

The utility of the backscatter technique in the diagnosis of faults has been demonstrated. The method is likely to be invaluable for fibre quality control and will aid in the isolation of fabrication induced faults.

This terminates the presentation of backscatter attenuation measurements in multimode optical fibres. In the next chapter a new measurement technique based on time domain reflectometry is described and is used to determine the residual stress levels in jacketed fibres.

For further discussions and a review of backscatter measurements refer to the concluding chapter (Chapter 10). A small section which describes the backscatter response in single-mode fibres is also included in Appendix IV.

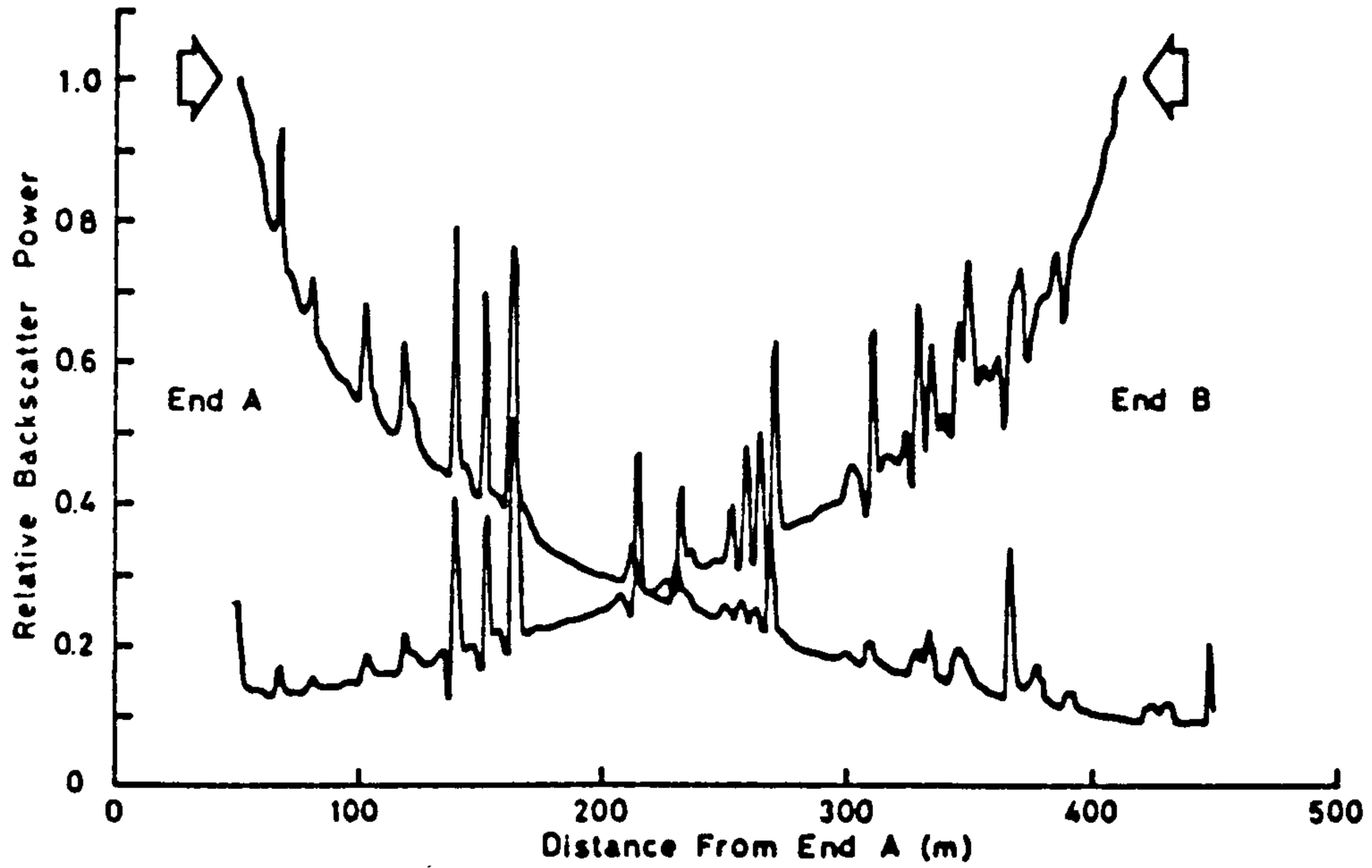

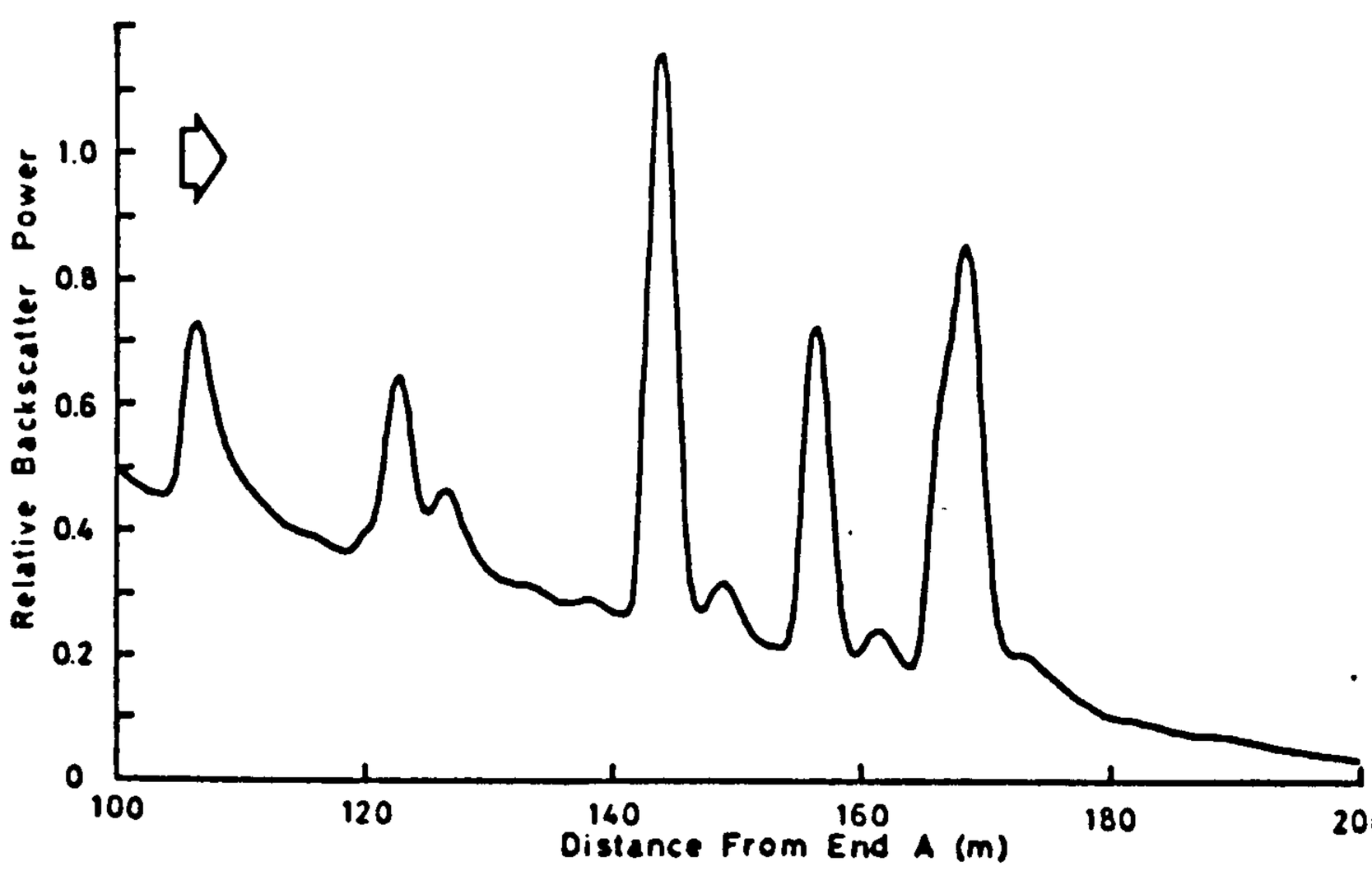

The upper diagram shows the backscattered power measured at $\lambda = 0.9$ μm from two ends of a fibre manufactured by the Pilkington Glass Company using the 'phasil' process. The lower diagram shows an expanded view of the region from 100-200 m measured from end A. The spikes are due to reflections from the many scatter centres along the fibre.

Figure 8.1

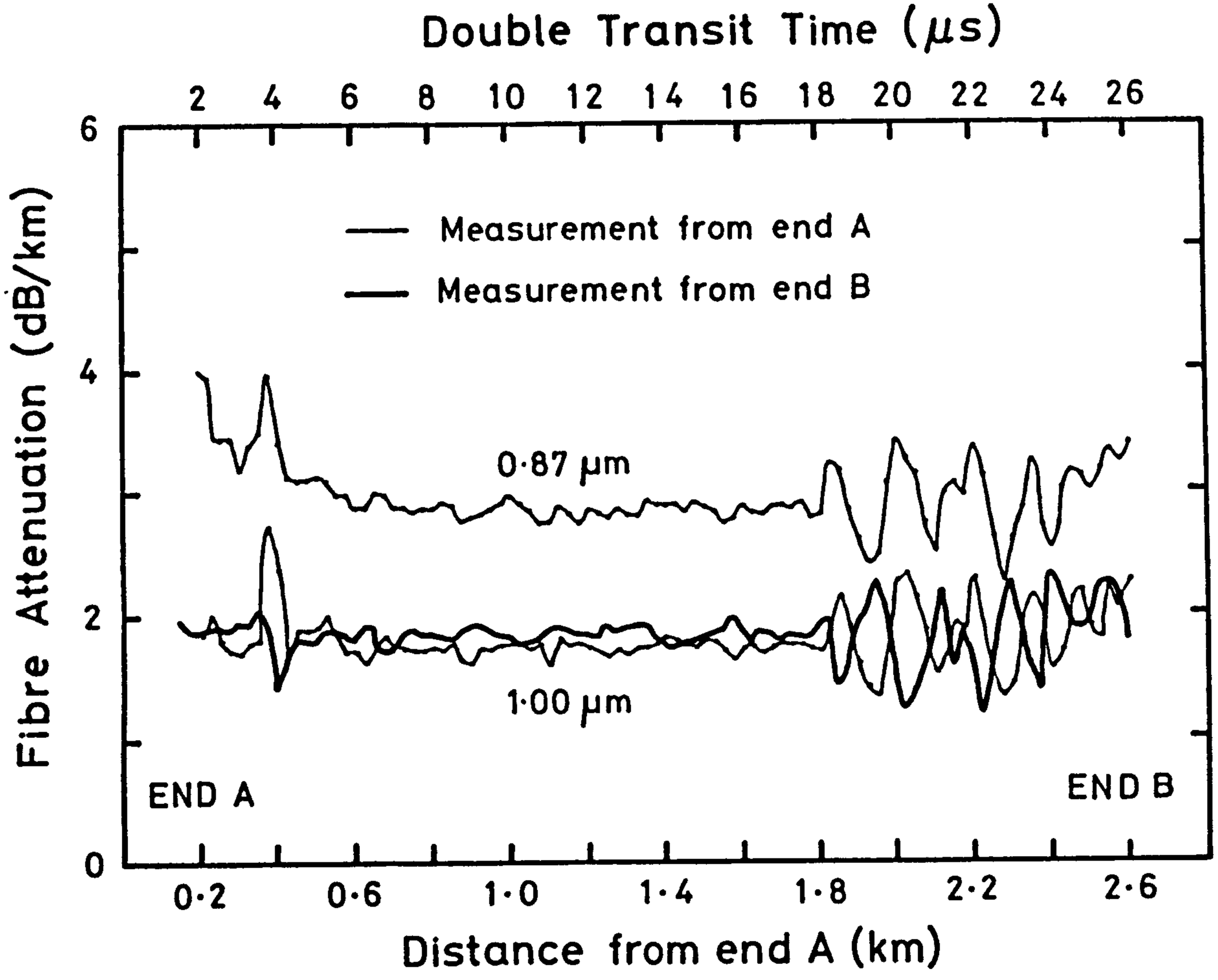

Backscatter loss signature of fibre VD 230/L measured using the 2-channel technique and the dye laser system. The region of fibre after 1.8 km clearly exhibits large anti-correlated fluctuations when measured from the two ends.

Figure 8.2

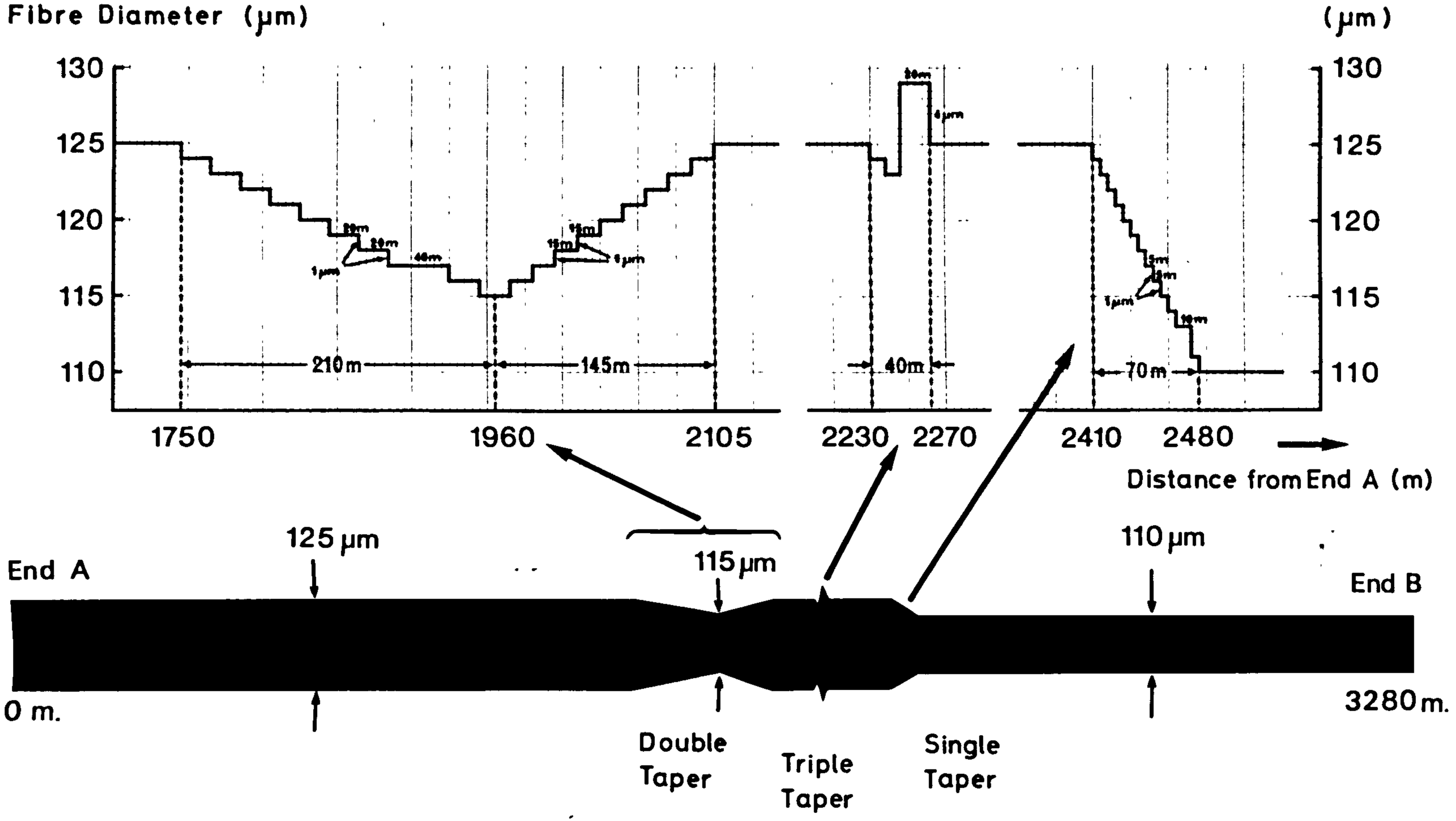

Figure 8.3 Programmed Diameter Profile of Fibre VD277/L

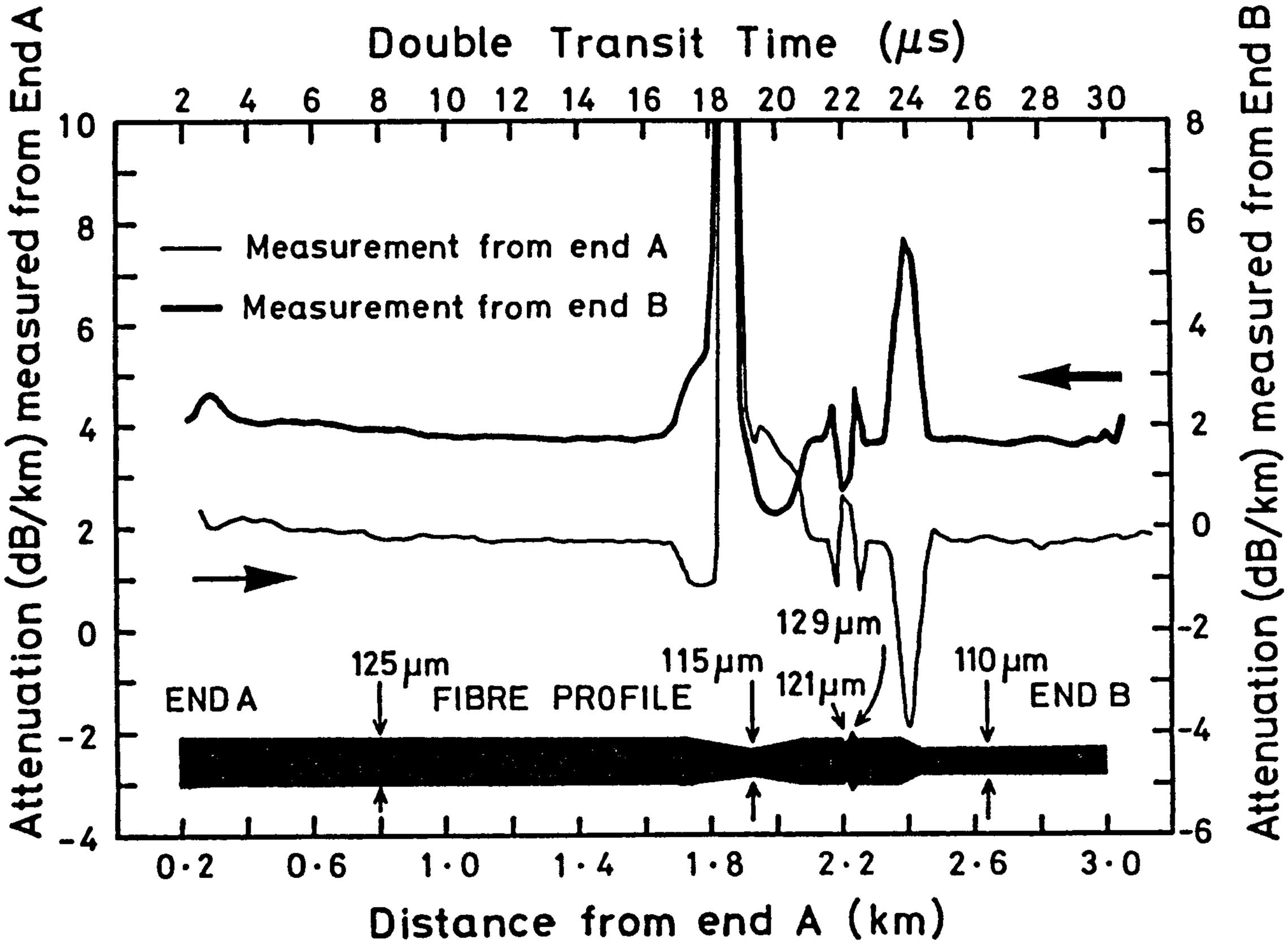

Effect of programmed diameter changes in fibre VD 277/L. Measurements performed with the dye laser at $\lambda = 1.006$ μm.

Figure 8.4

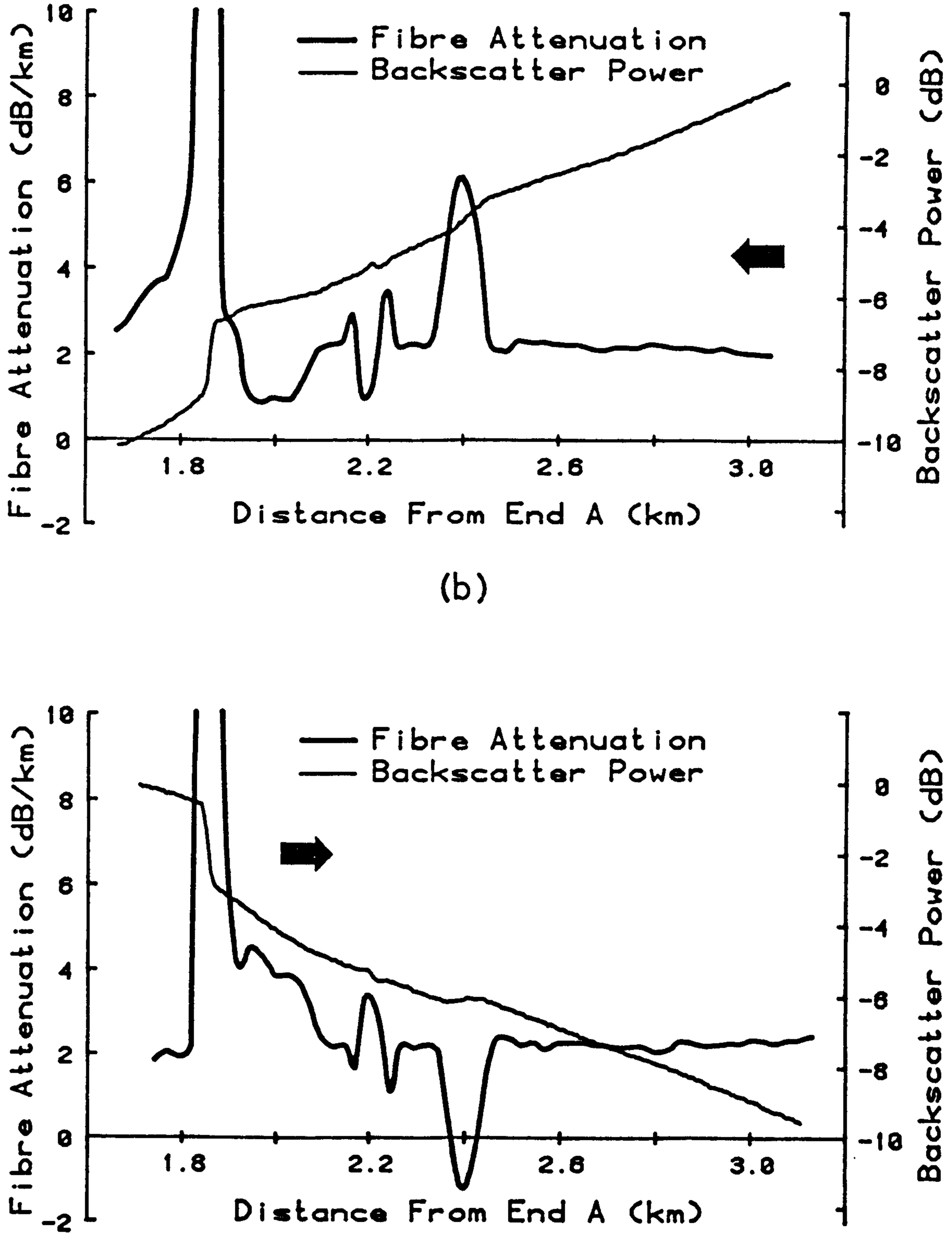

Backscatter measurements on fibre VD 277/L showing the back-scattered power (single-channel sampling) and local loss (2-channel sampling) (a) measurements from end A and (b) measurements from end B. (A semiconductor laser is used operating at λ = 0.9 μm)

Figure 8.5

Backscatter power in the region of the triple (2250 m) and single (2450 m) tapers in the fibre VD 277/L (also see figure 8.3). Measurements were performed using a 10 ns dye laser at $\lambda = 0.9$ μm and Tektronix 7912 AD transient digitizer. Contracting fibre sections clearly produce an increase in backscatter power and vice-versa.

Figure 8.6

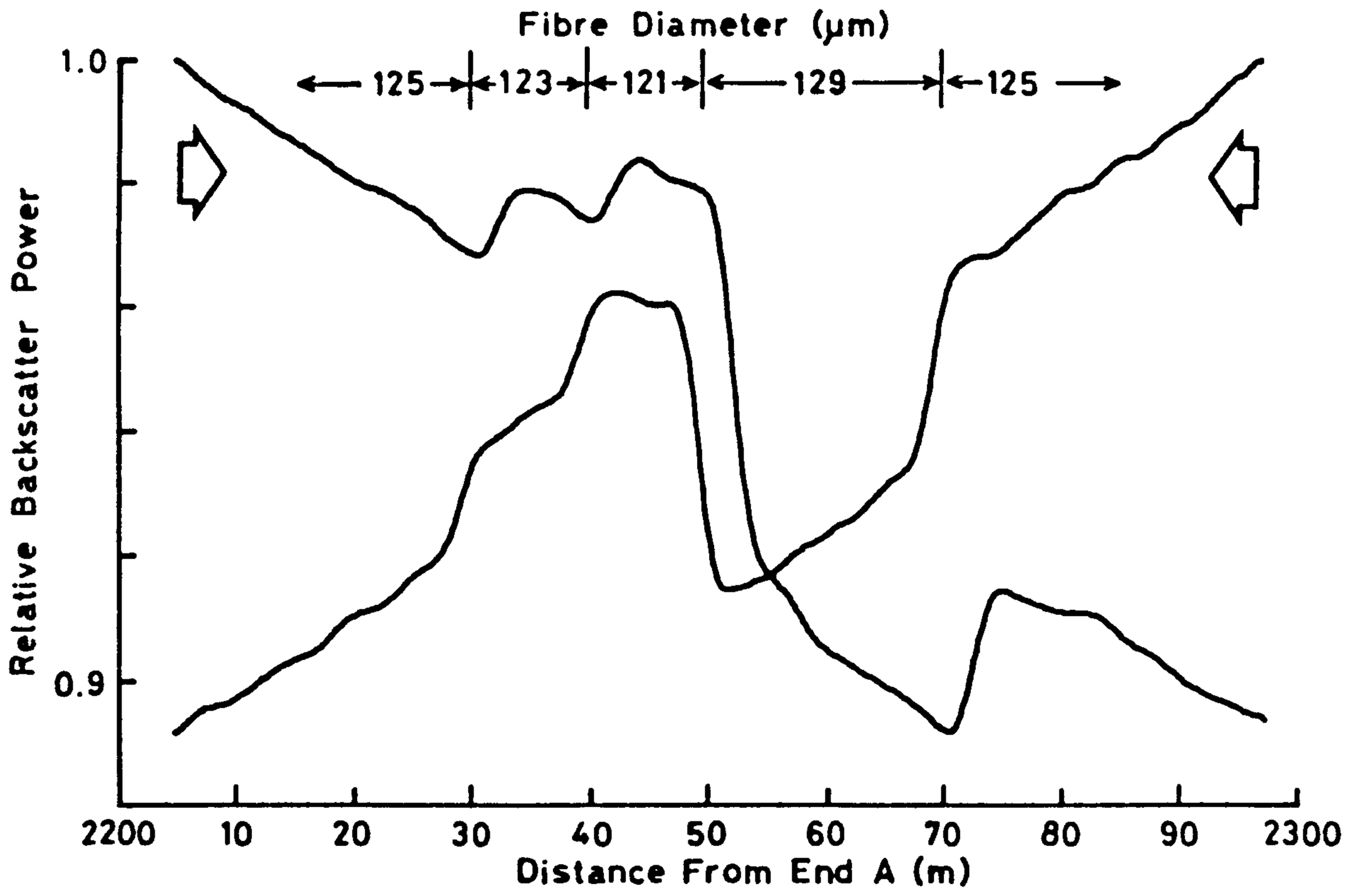

High resolution measurement of the triple taper in fibre VD 277/L at $\lambda = 0.9$ μm (also see figure 8.3). The backscatter power clearly follows the positive and negative increments in fibre diameter.

Figure 8.7

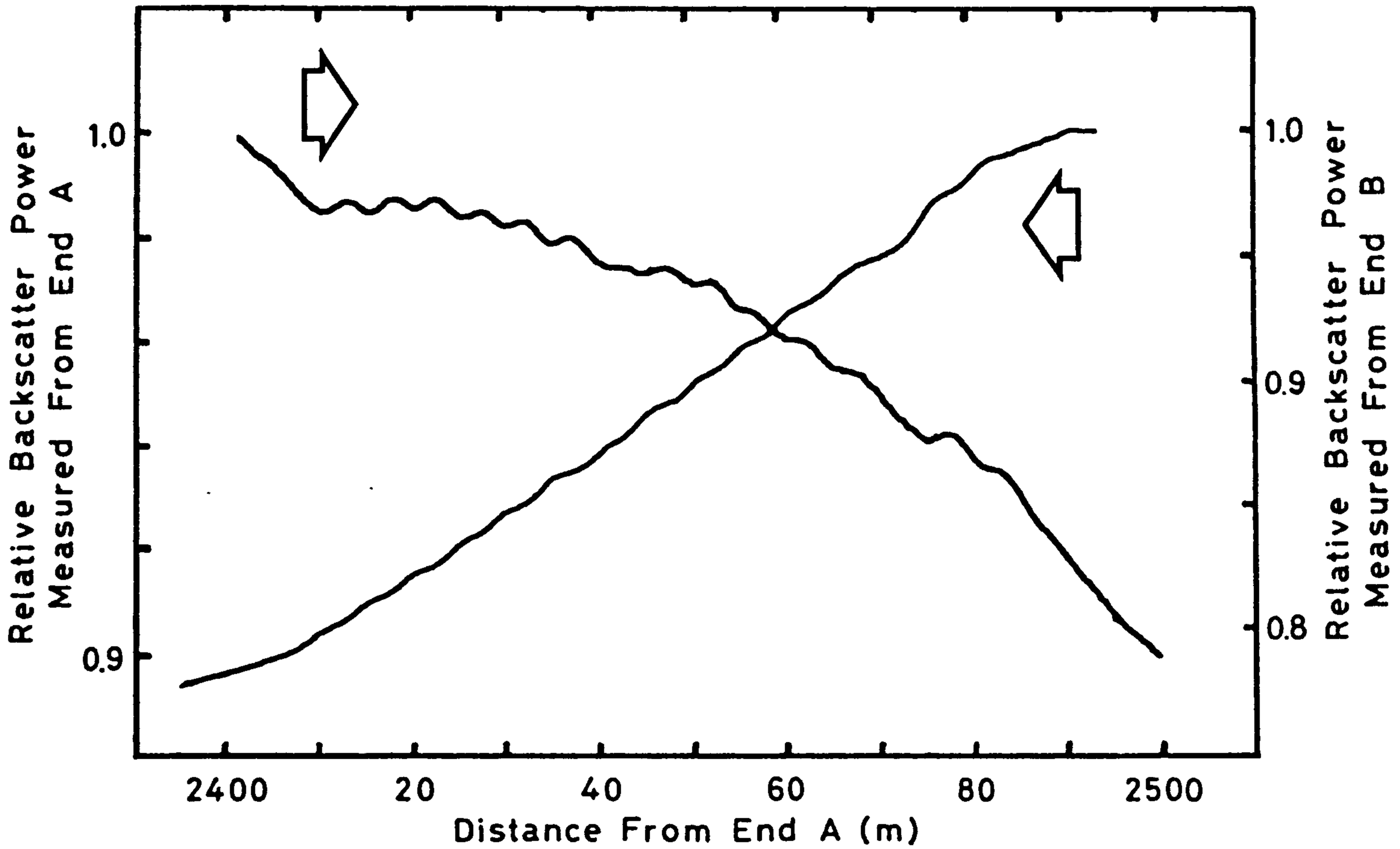

High resolution measurement of single taper in fibre VD 277/L at $\lambda = 0.9$ μm (also see figure 8.3). The backscatter power clearly follows the increments in fibre diameter.

Figure 8.8

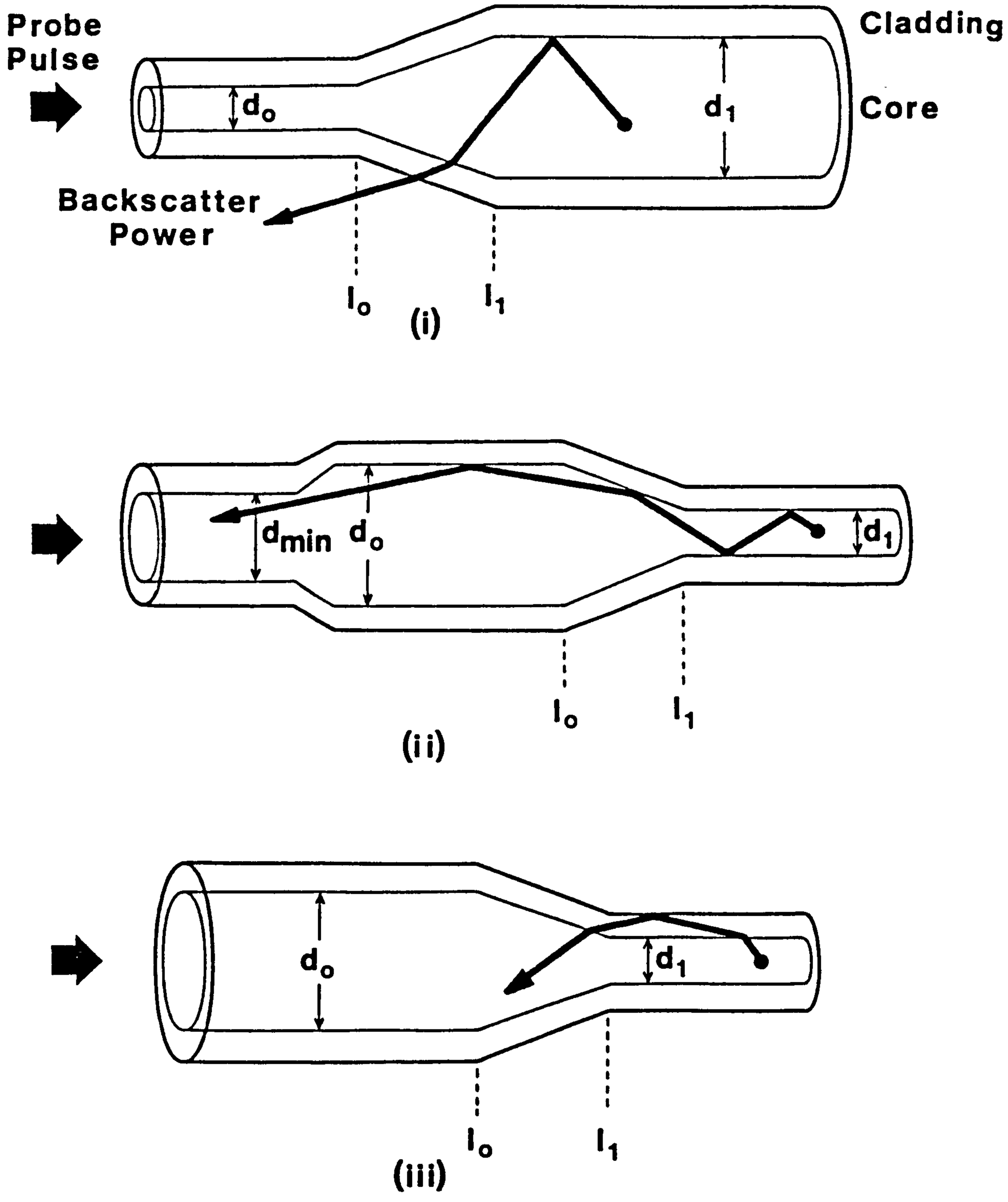

Schematic representation of the effect of fibre tapers on backscattered light (i) expanding taper between ℓ_o and ℓ_1 (ii) contracting taper between ℓ_o and ℓ_1 with differential mode attenuation (DMA) introduced by prior diameter change (iii) contracting taper between ℓ_o and ℓ_1 with coupling from cladding modes.

Figure 8.9

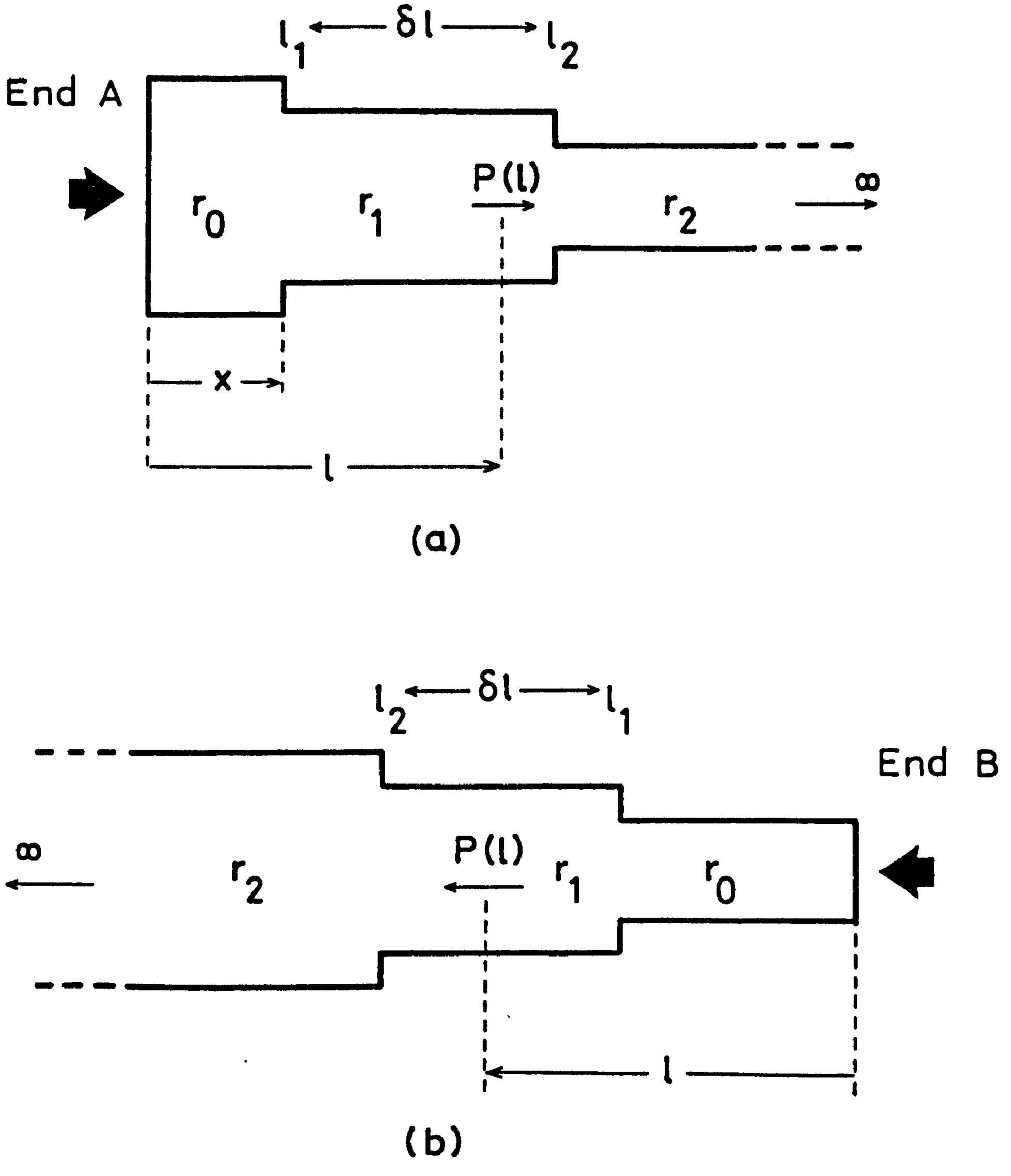

Modes for (a) contracting and (b) expanding fibre sections. Tapers are composed of N sections of length $\delta\ell$ and with core radii r_0 to r_N. A convention is established here whereby a contracting section is analysed by launching into End A and and expanding section is probed from End B.

Figure 8.10

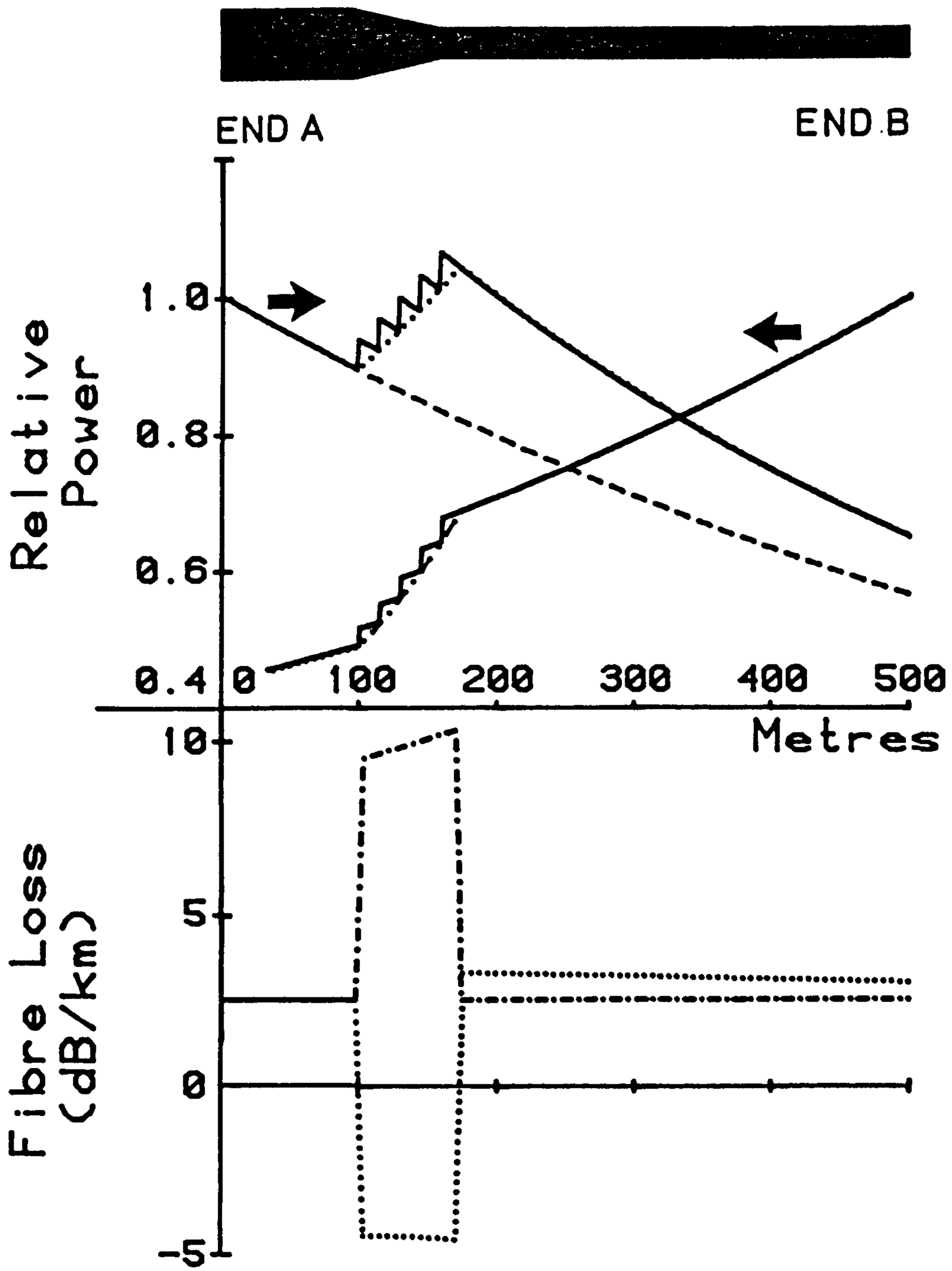

Computer simulation of backscatter power from tapered fibre with intrinsic core attenuation 2.5 dB km^{-1} and cladding loss 10 dB km^{-1} and core/cladding dimensions 60/125 μm at End A. Upper curves give relative backscatter power and the lower curves calculated fibre loss. The solid curve shows the effect of 3 μm steps in fibre o/d at 15 m intervals over a 75 m section. Also shown is a taper with the same average slope but consisting of 0.2 μm steps at 1 m intervals. For the latter simulation (.....) represents the End A result and (·-·) the End B result.

Figure 8.11

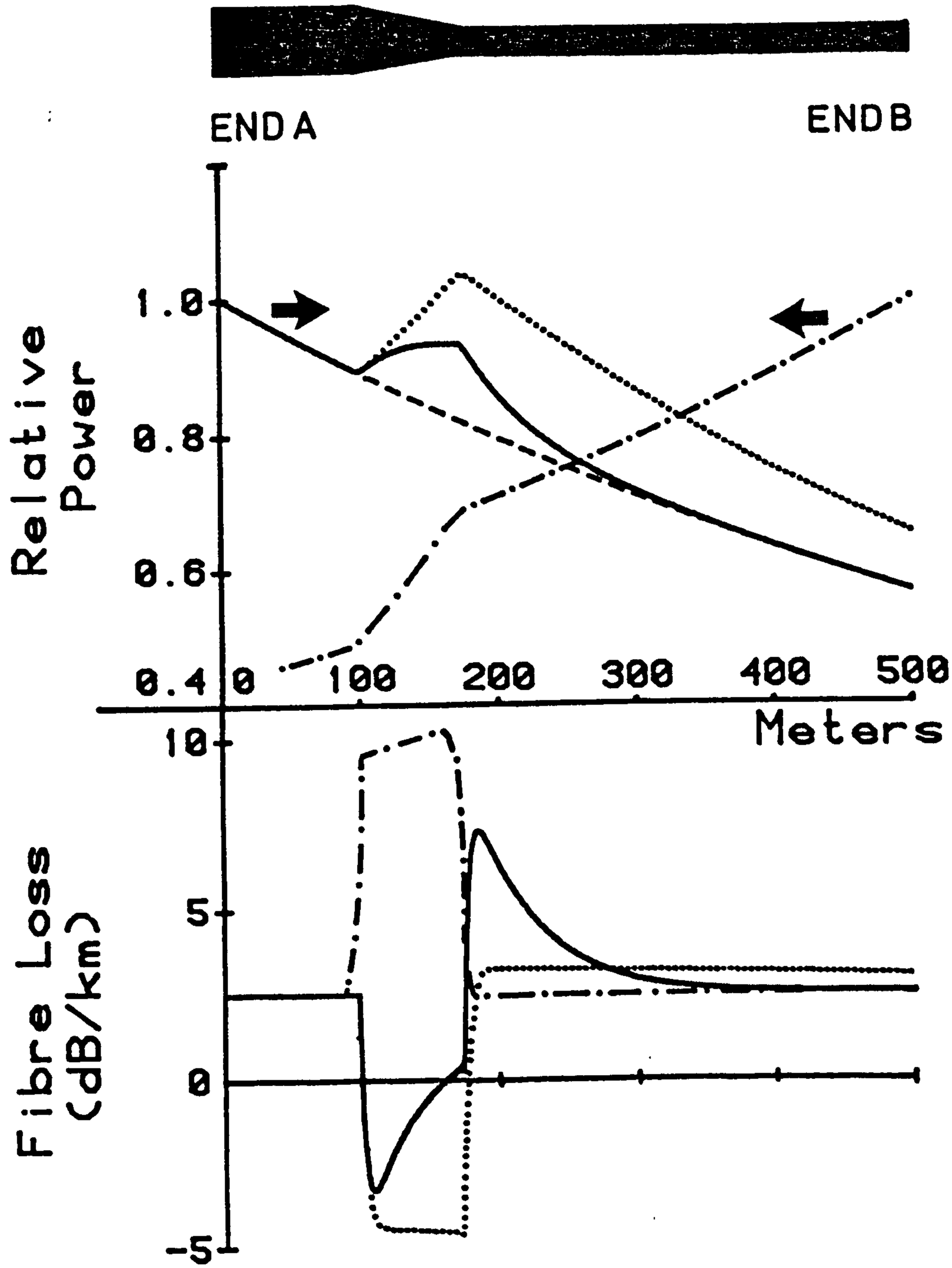

Cladding mode attenuation

..... 10 dB km^{-1}

——— End A 100 dB km^{-1}

-.-.- End B

Computer simulation of effect of cladding losses on backscatter power from tapered fibre with intrinsic core attenuation 2.5 dB km^{-1} and core/cladding dimensions 60/125 μm at End A. The taper slope is 0.2 μm/m (o/d) over a 75 m section.

Figure 8.12

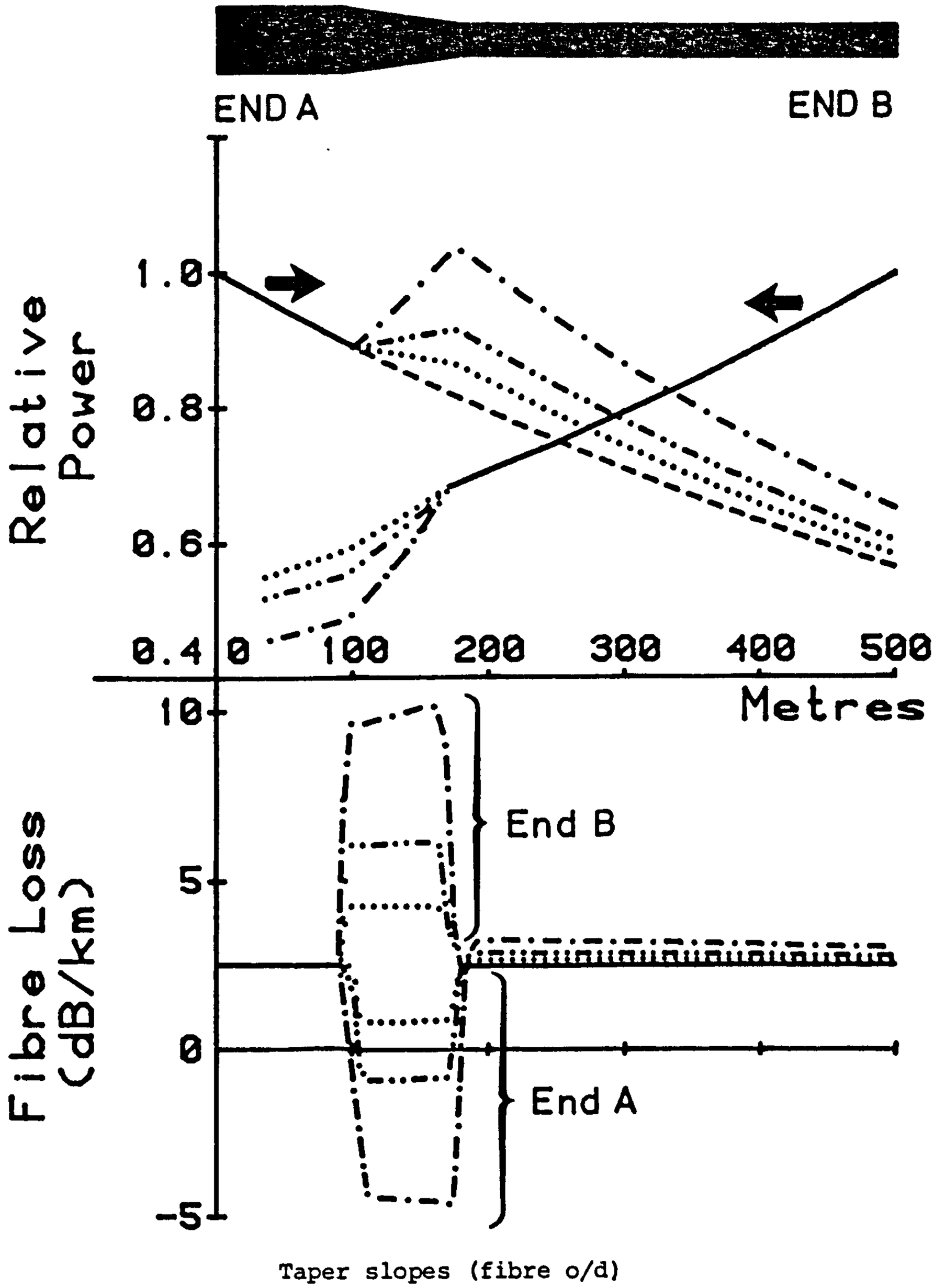

Taper slopes (fibre o/d)

—.—.— 0.2 μm/m

—..—.. 0.1 μm/m

..... 0.05μm/m

Computer simulation of backscatter power from tapered fibre with intrinsic core attenuation 2.5 dB km^{-1} and core/cladding dimensions 60/125 μm at End A. The curves show the effect of taper slope on the backscatter-loss signature and assume a cladding mode attenuation 10 dB km^{-1}.

Figure 8.13

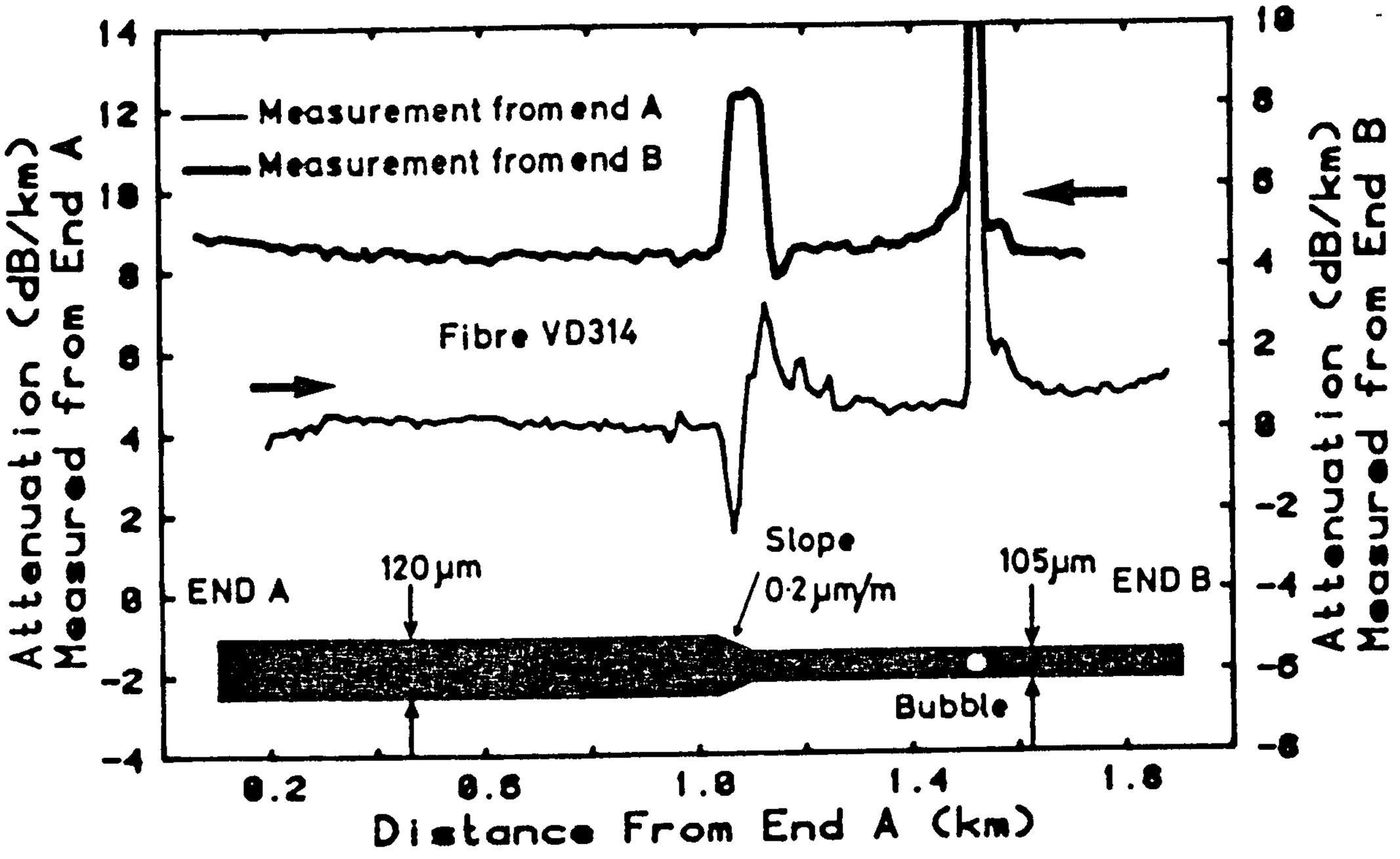

(a)

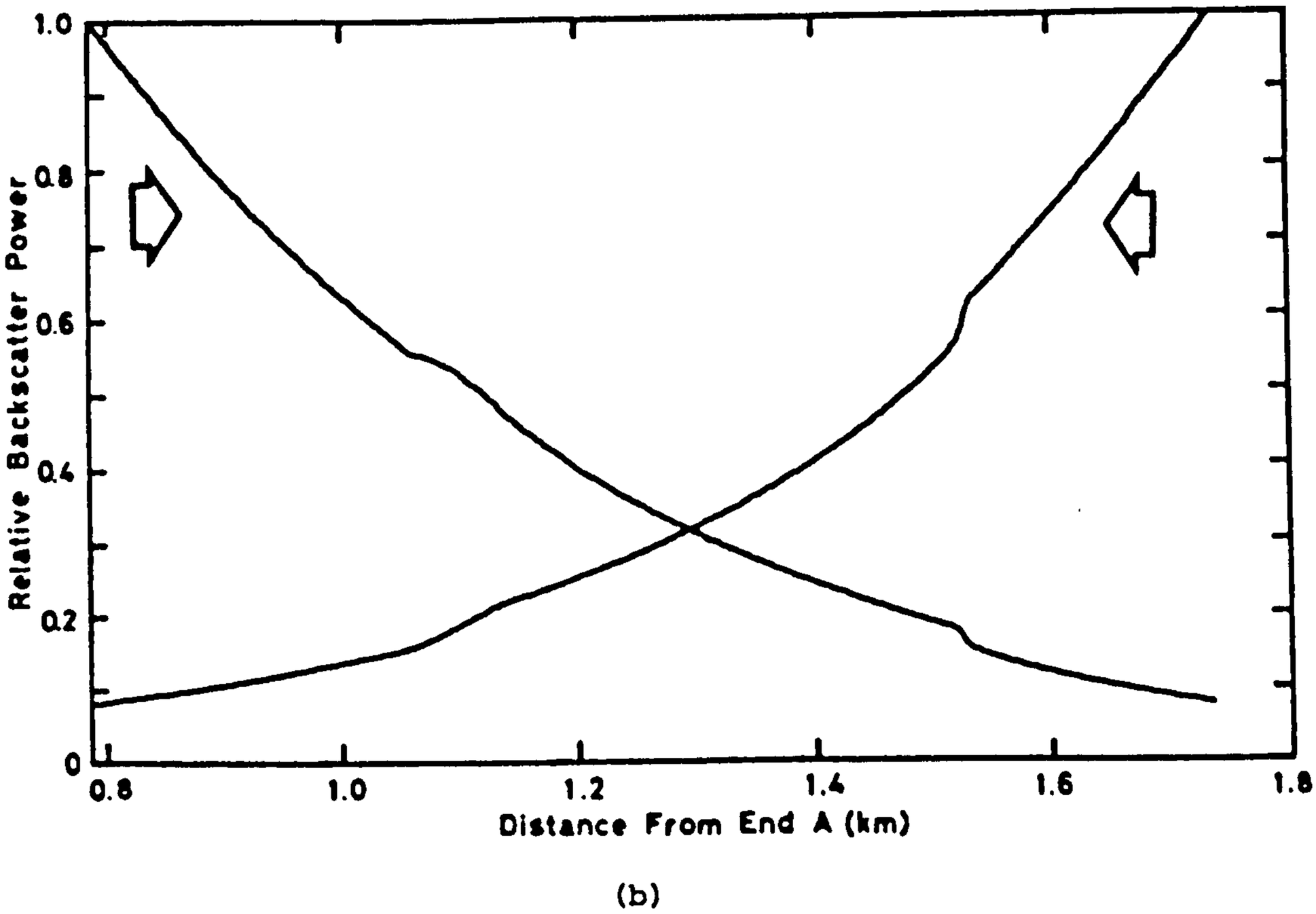

(b)

Backscatter response of fibre VD 314 measured with a semiconductor laser at $\lambda = 0.9$ μm. (a) fibre profile and loss signature, (b) relative backscatter power. The contracting section when measured from End A exhibits a positive overshoot which corresponds to an excess cladding loss. The only correlated defect is that produced by the bubble at 1.5 km.

Figure 8.14

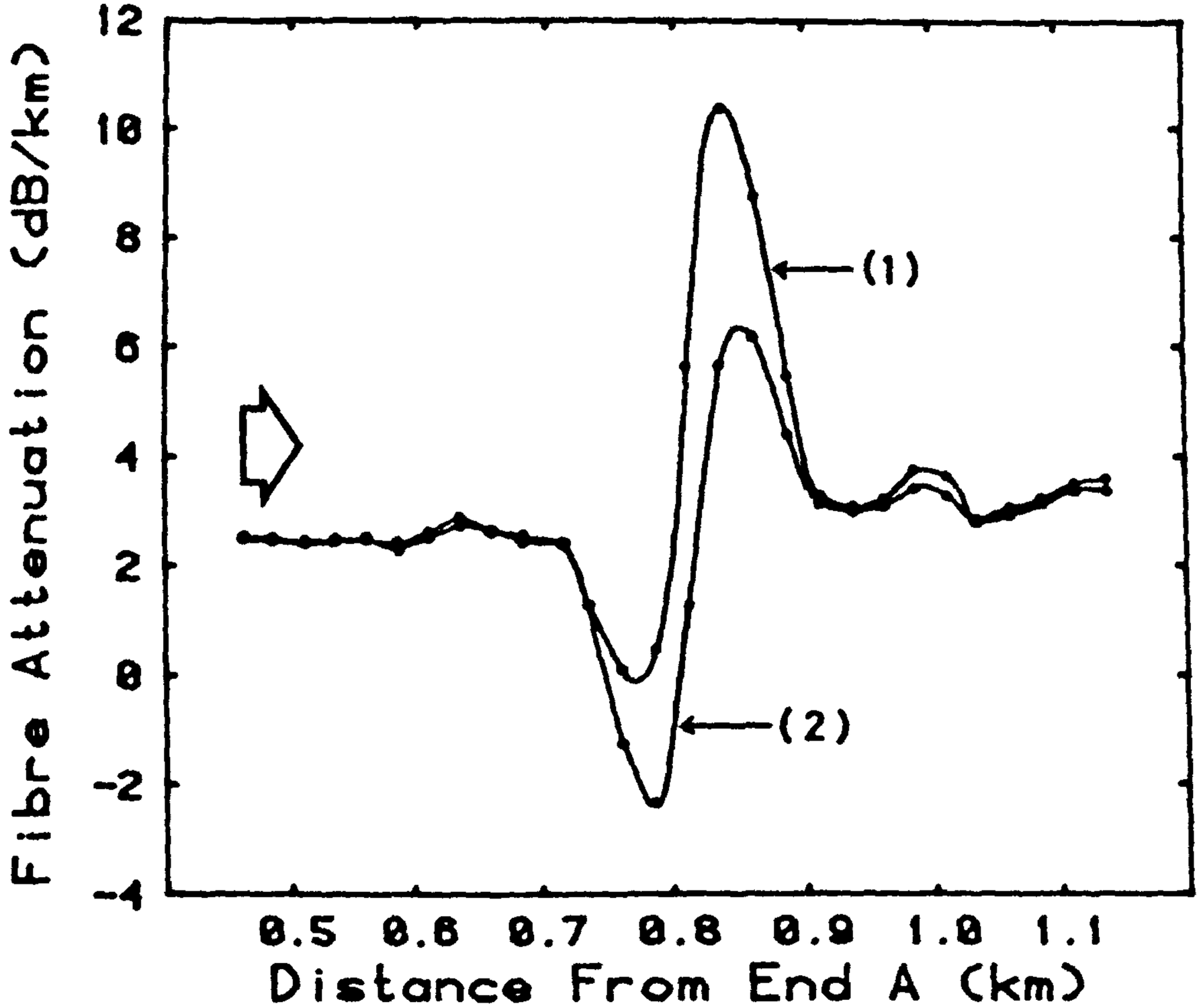

Effect of contracting fibre section in step-index fibre VD 304/L. Curve 1 shows the results of measurement with full backscatter reception and curve 2 shows the response when DMA in the form of an aperture is placed between the fibre and photodetector. The source is a semiconductor laser at $\lambda = 0.9$ μm. (see text for further details)

Figure 8.15

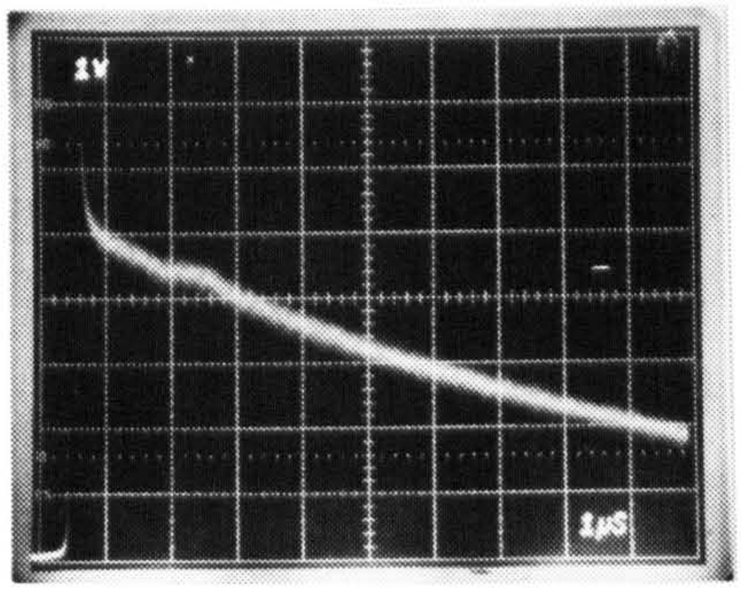

(a)

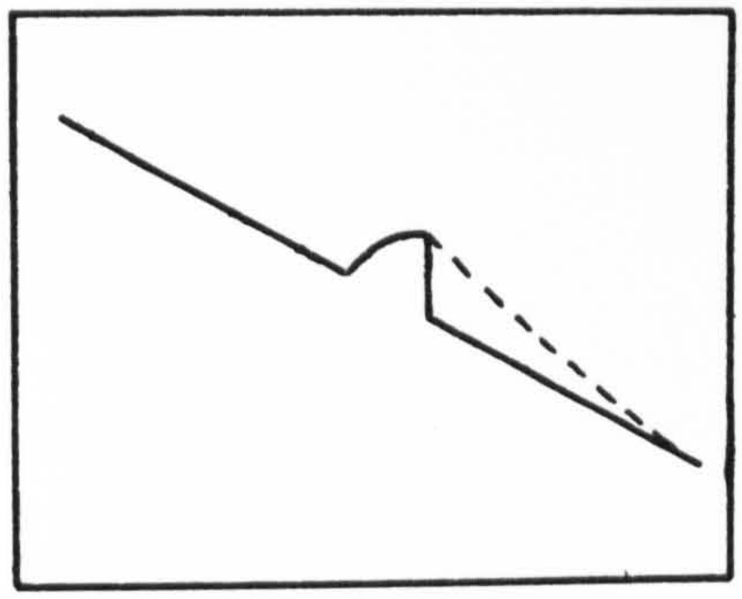

(b)

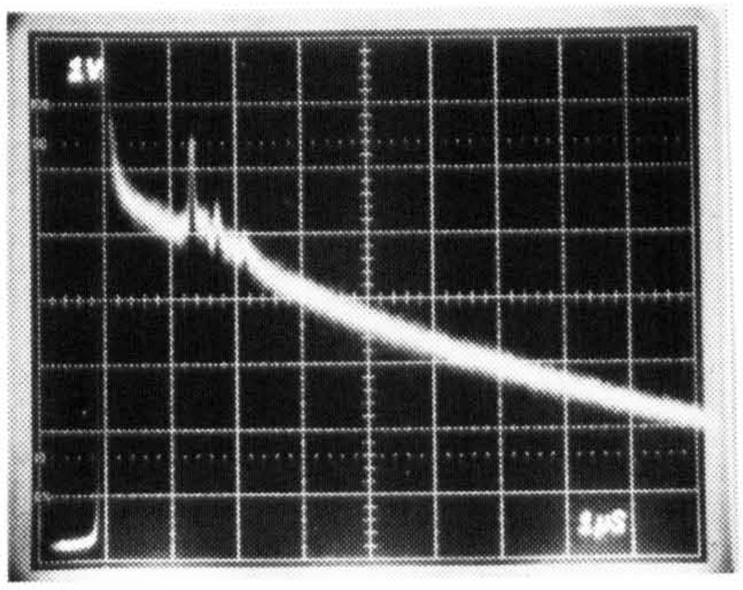

(d)

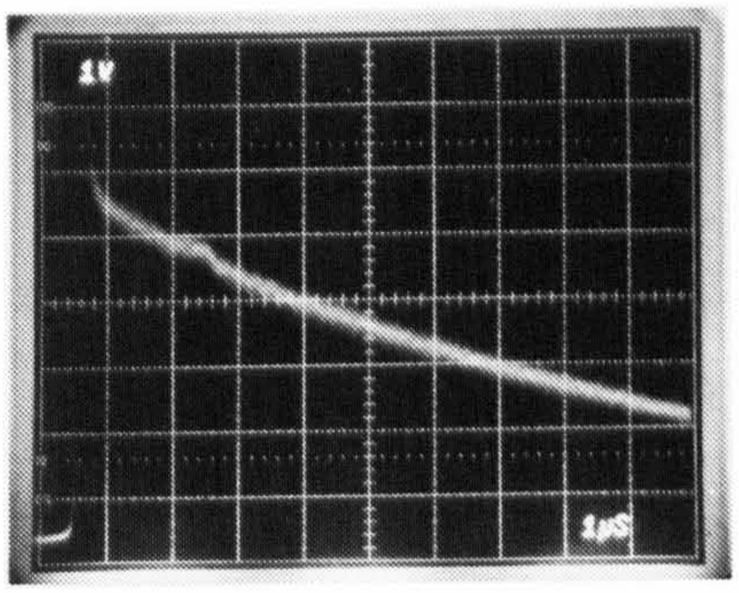

(c)

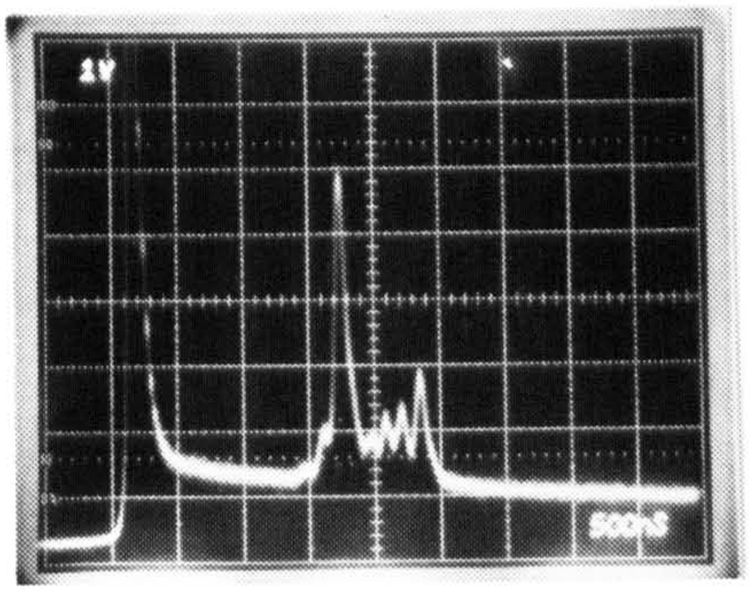

(e)

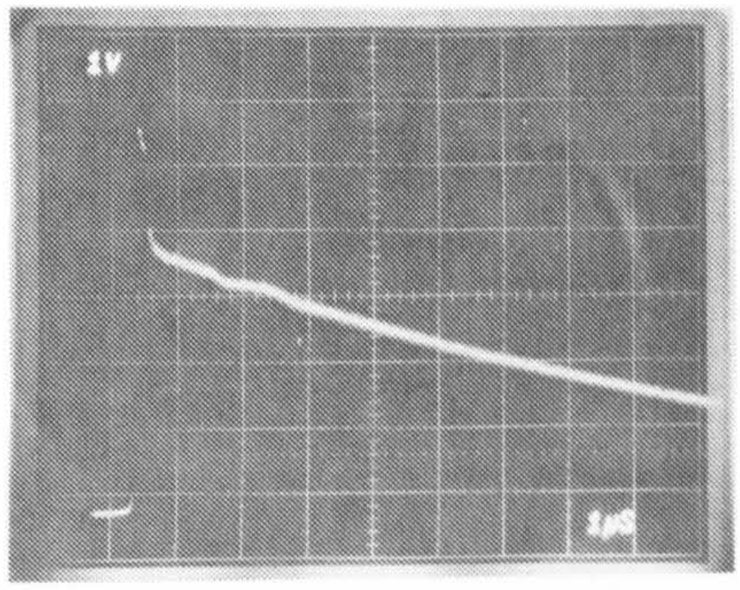

(f)

Verification of coupling from cladding modes for the single contracting taper in fibre VD277/L. Measurements are of the section from 2280-3280 m (see Figure 8.3). Light at 0.9 μm from a semiconductor laser is launched into the end A at the 2280 m point.

(a) response of silicone coated fibre

(b) schematic of expected response after ∿8 cm of silicone is removed and index-matched at the 2490 m point (see Figure 8.3)

(c) actual response

(d), (e) responses when tapered section is immersed in acid and silicone coating removed

(f) response of unclad fibre in index-matching liquid.

Refer to Section 8.4.3 in text for full description of the above.

FIGURE 8.16

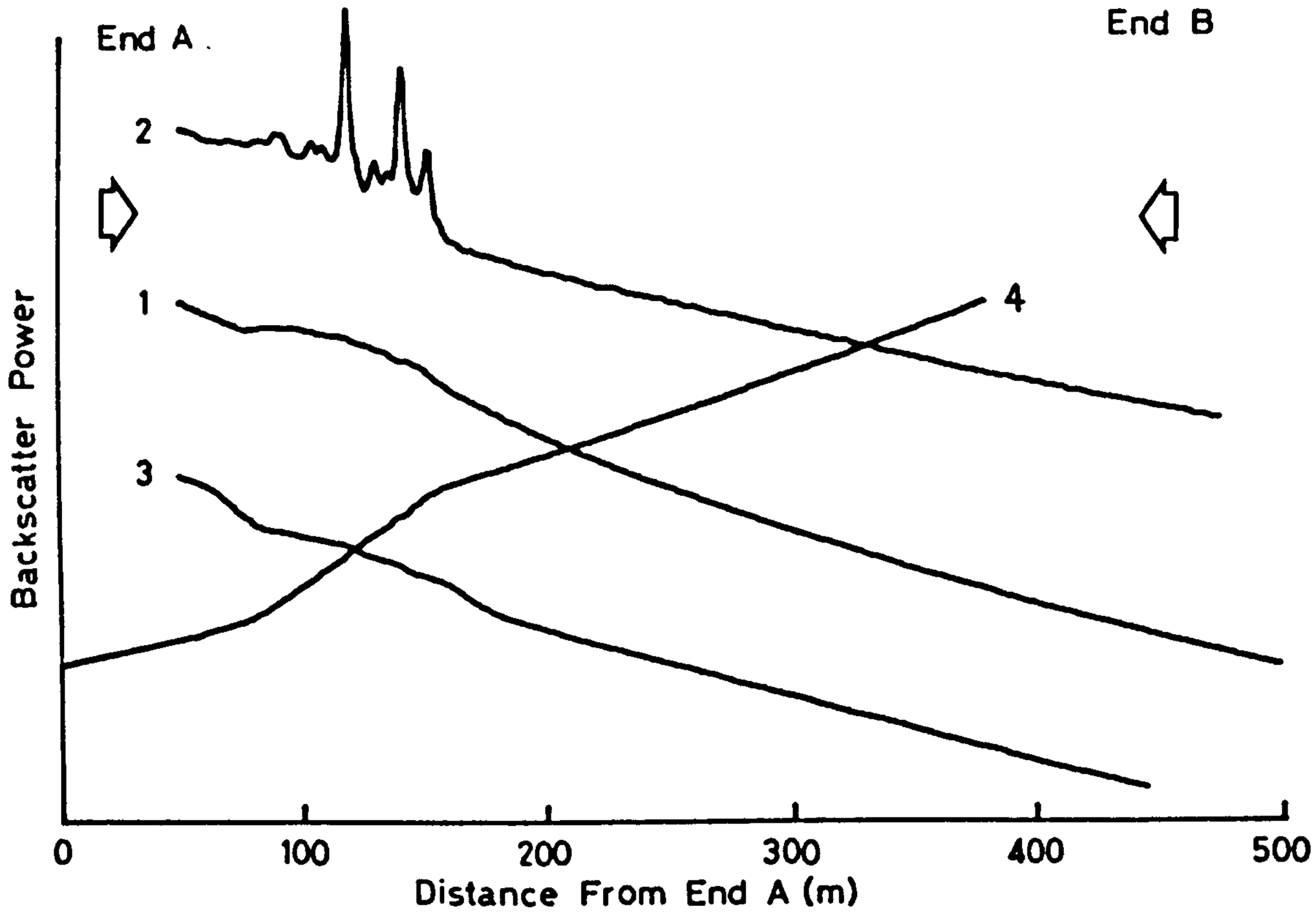

Verification of coupling from cladding modes for fibre VD 277/L, single taper.
Curve 1, response of contracting taper with silicone primary over-jacket.
Curve 2, response with fibre immersed in acid-bath to remove silicone jacket.
Curve 3, response with fibre immersed in index-matching liquid (glycerol).
Curve 4, measurement from End B (expanding taper) and remained unchanged throughout the above measurements.

Figure 8.17

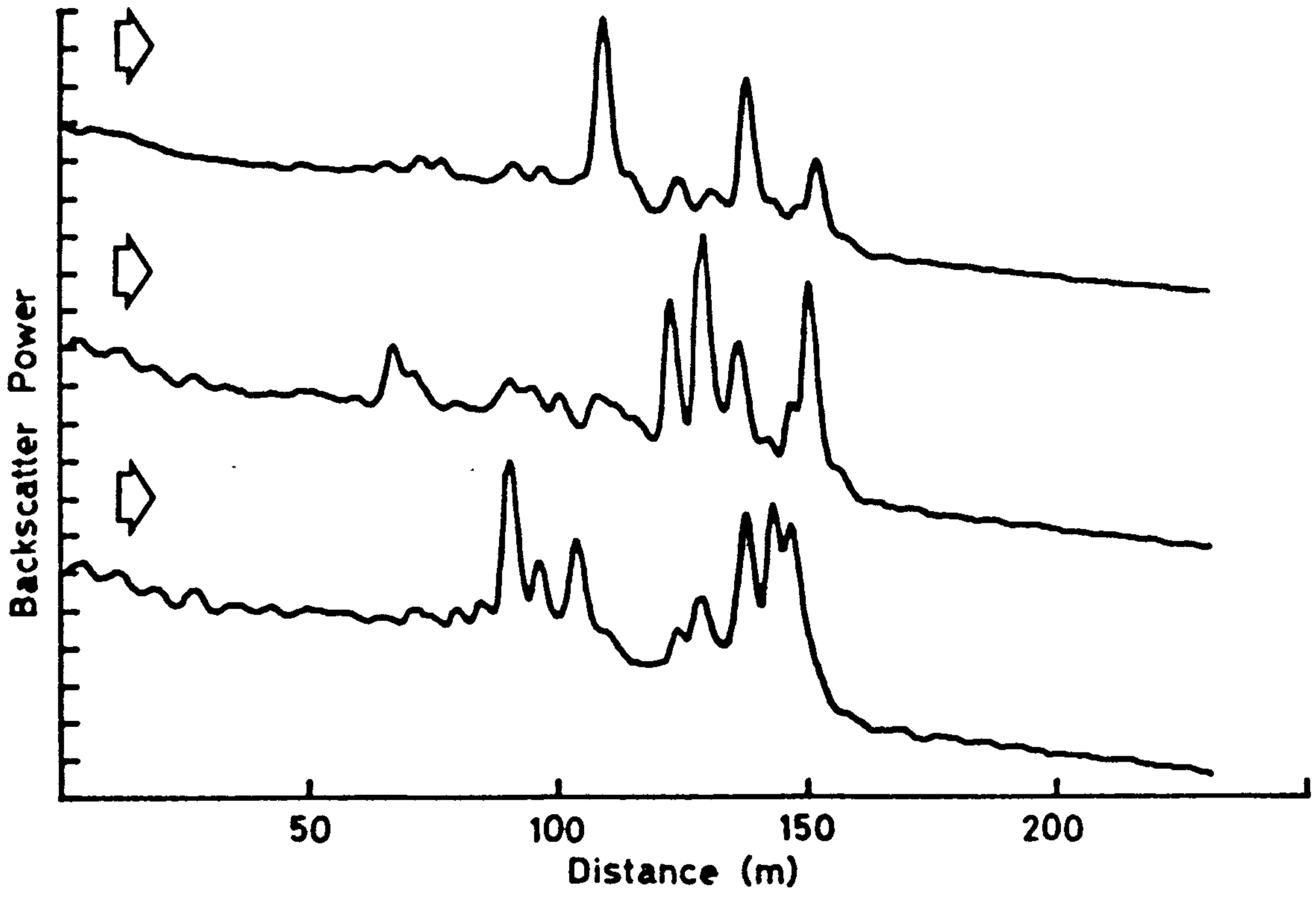

Fibre VD 277/L, single contracting taper immersed in acid bath. Agitation of the fibre in the acid bath caused a shift of power between the peaks in in the taper region. Measurements performed with a 10 ns pulse from a semiconductor laser at λ = 0.9 μm and recorded on Tektronix 7912 AD transient digitizer.

Figure 8.18

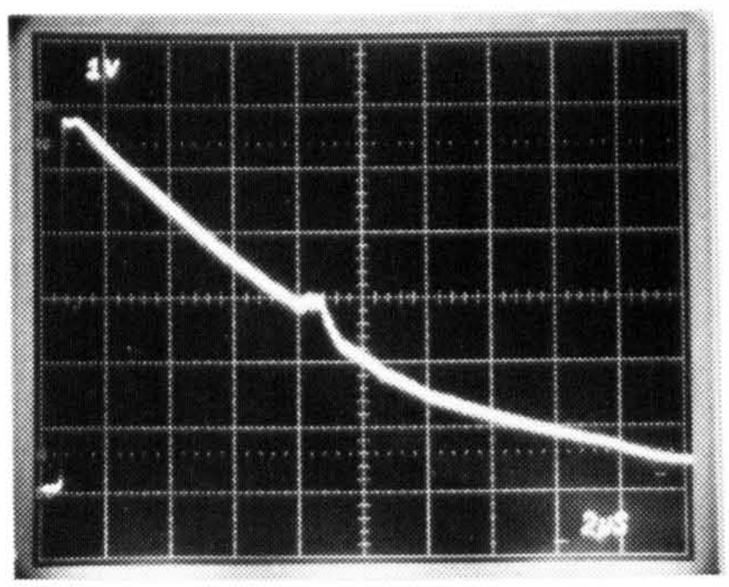

(a)

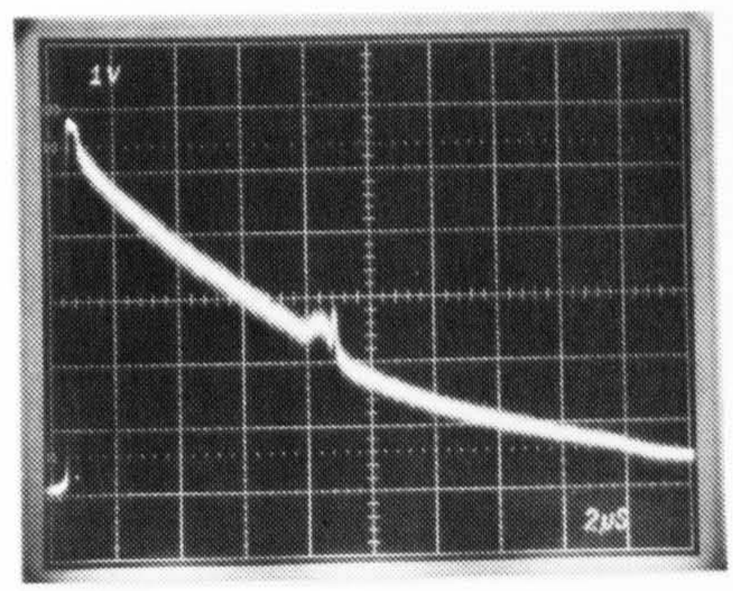

(b)

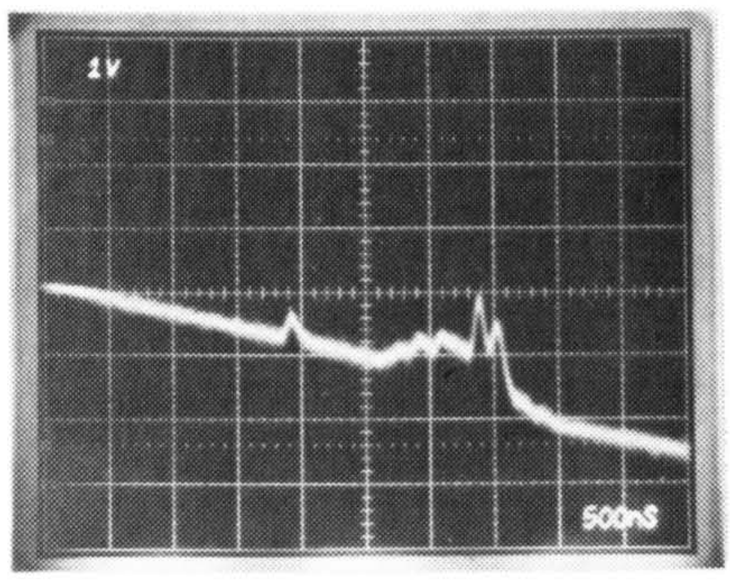

(d)

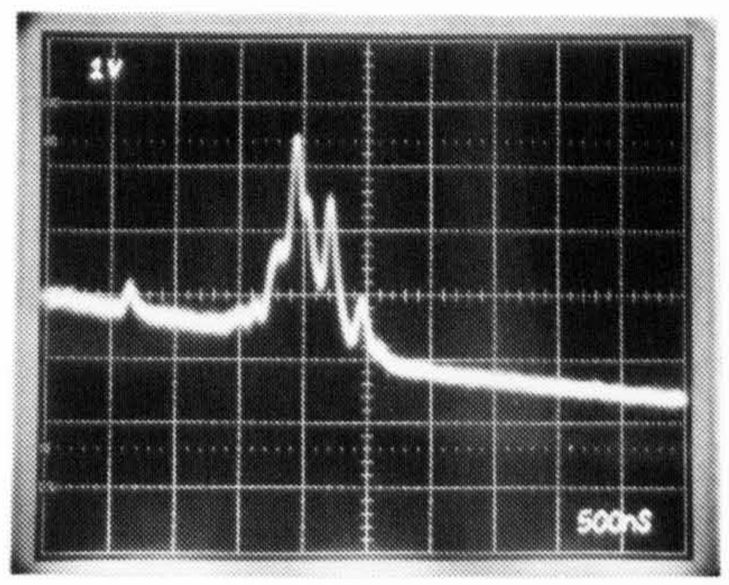

(c)

Verification of coupling from cladding modes for a single contracting taper in fibre VD304/L.

(a) response of silicone coated fibre

(b) response soon after immersion in concentrated acid which begins to dissolve the silicone coating

(c) } show responses with the silicone completely
(d) } removed. Agitating the fibre in the acid bath caused transfer of power from one peak to another. Many quasi-stable responses could be generated in this way.

Refer to Section 8.4.3 in text for full description.

FIGURE 8.19

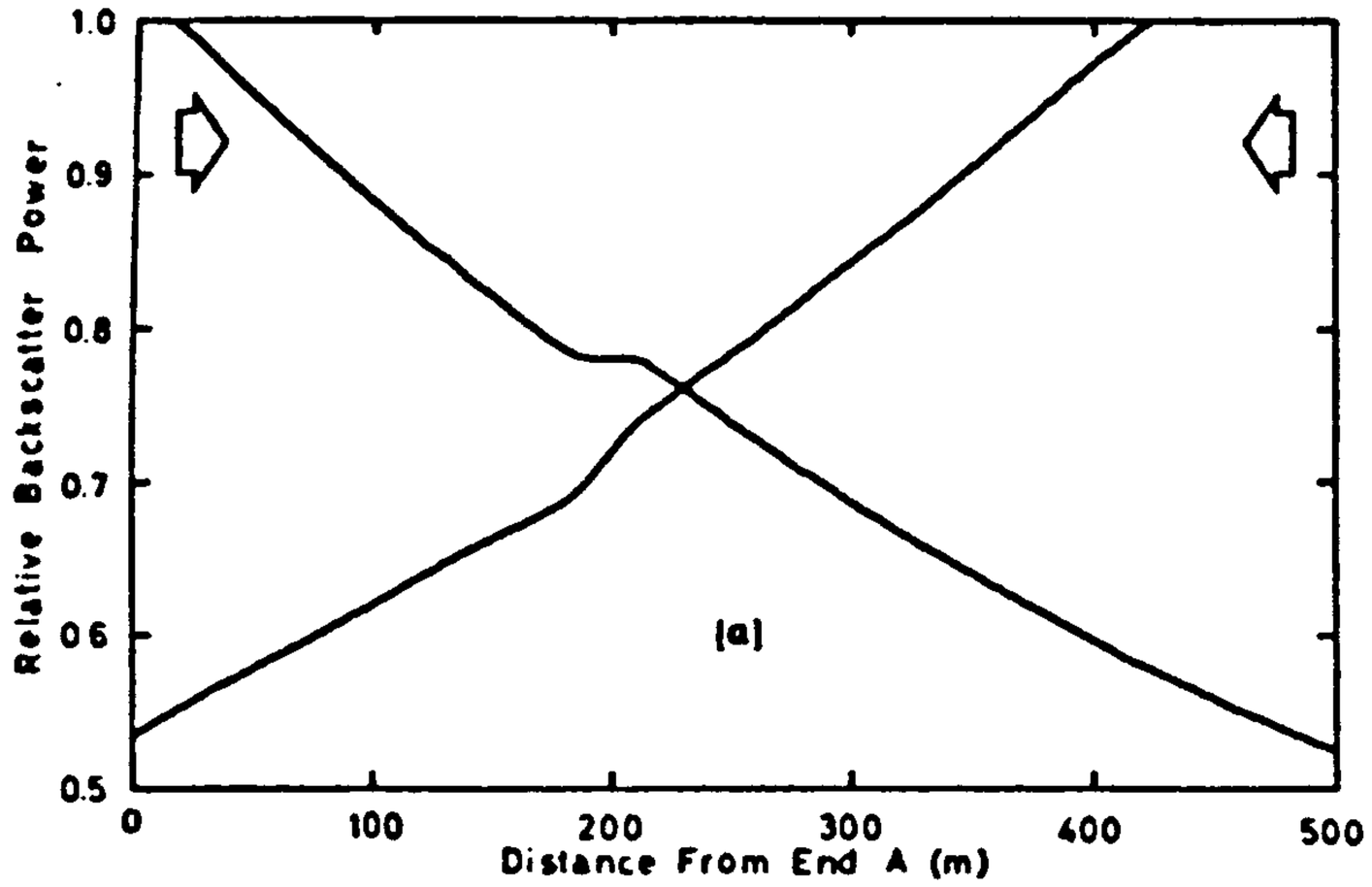

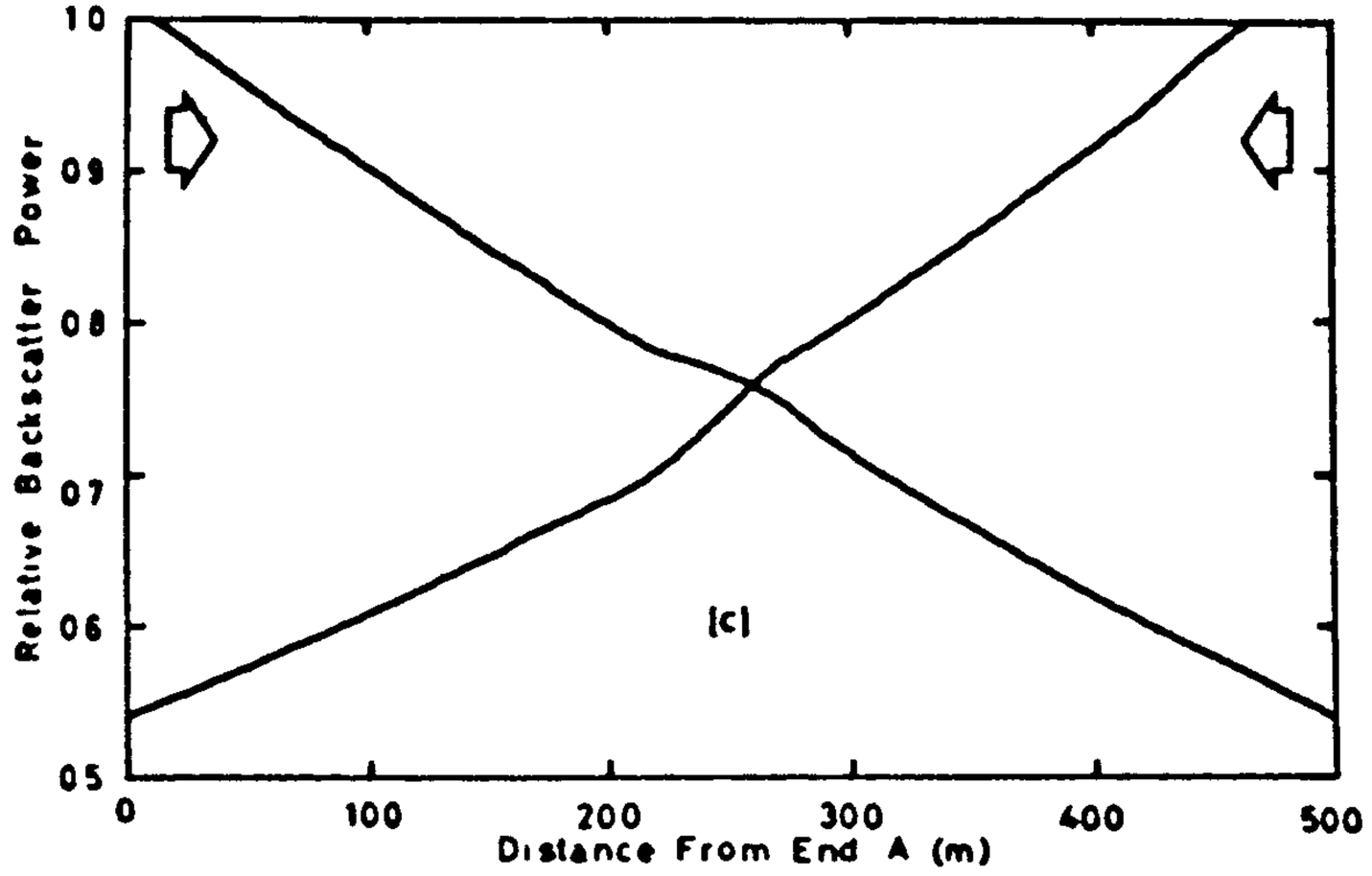

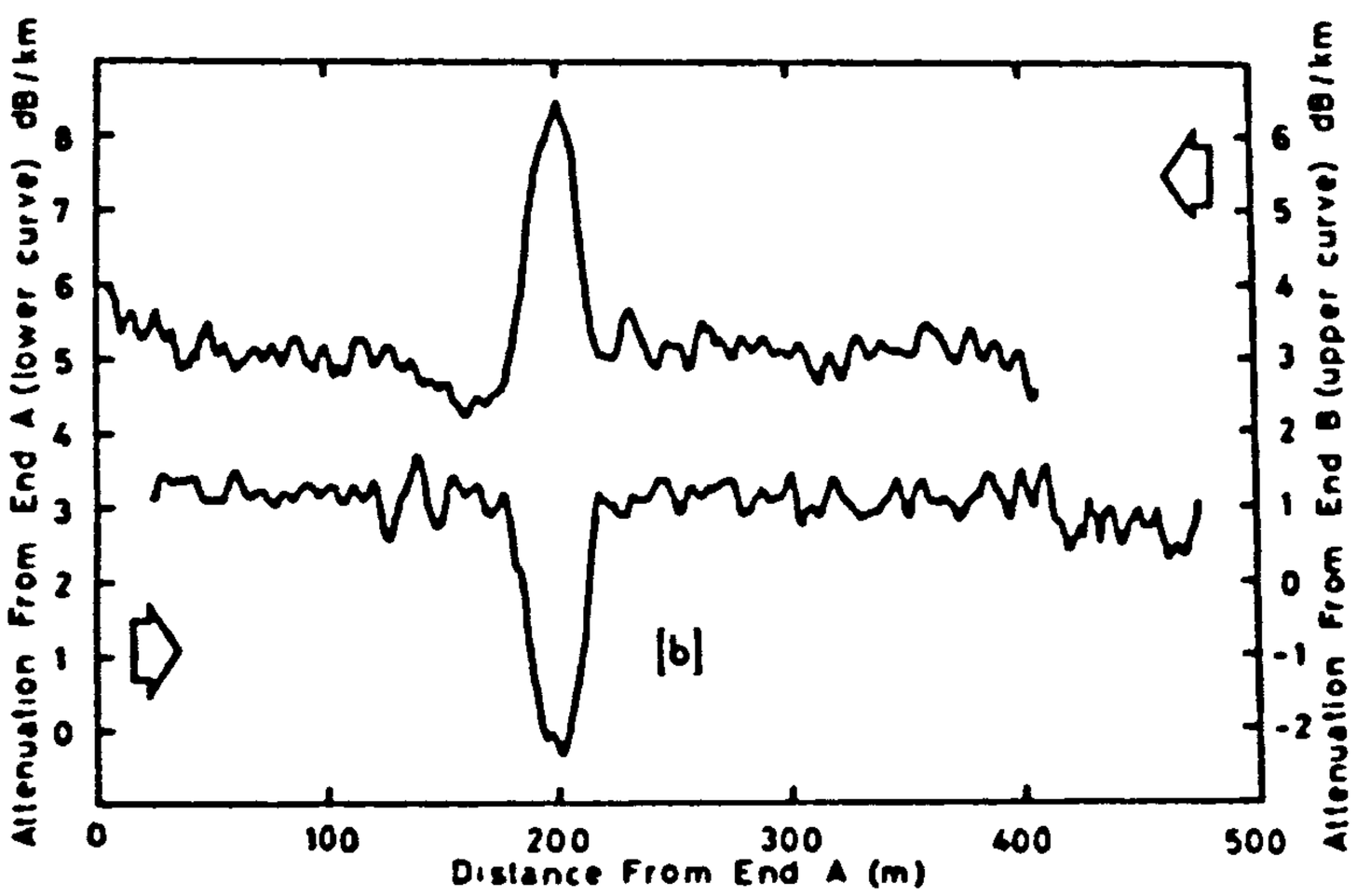

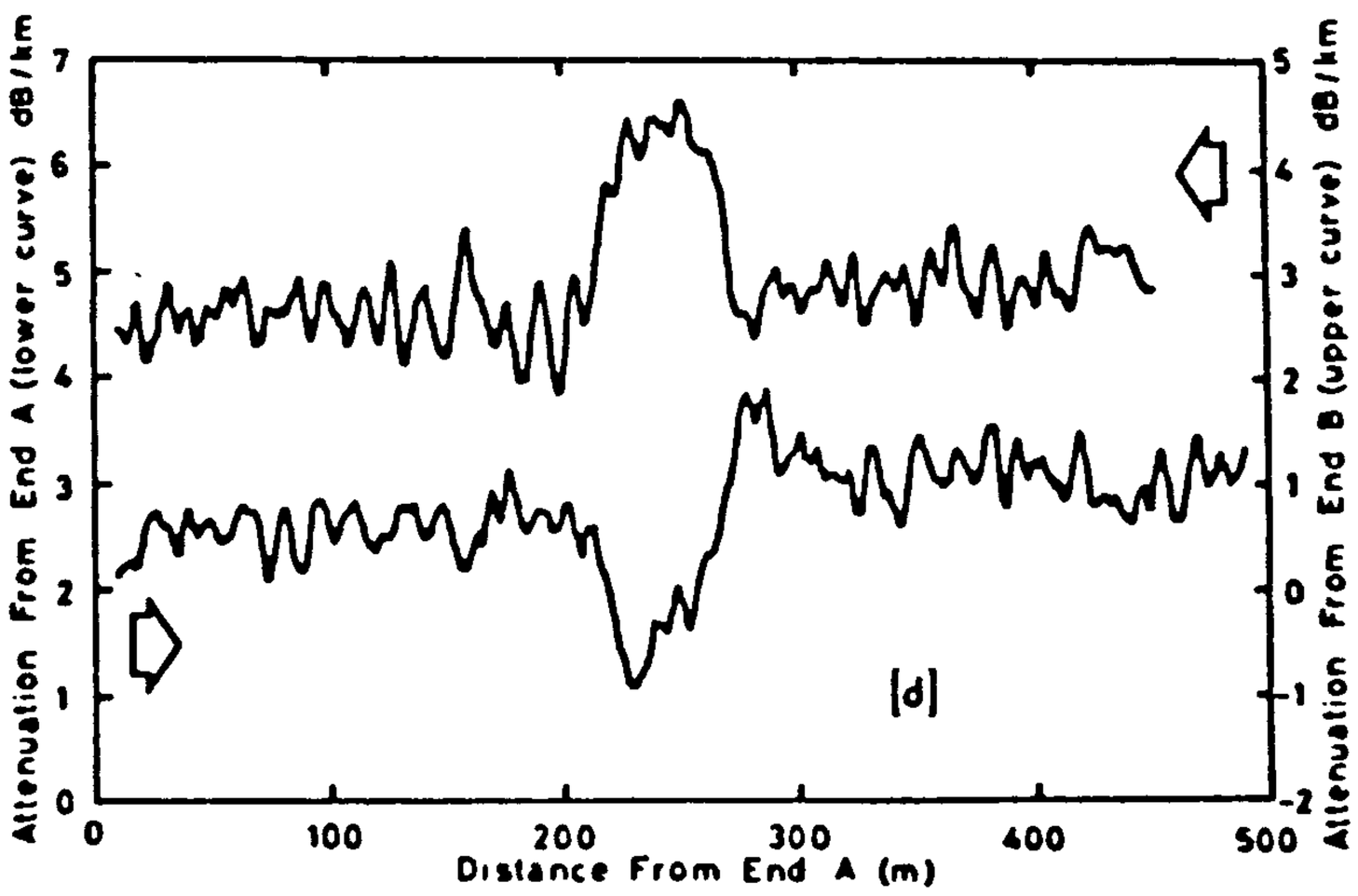

Effect on the backscattered power and loss signature of smooth tapers with differing slopes : (a) and (b) are for a taper of slope 0.2 μm/m over a 25 m section, (c) and (d) are for a taper of slope 0.1 μm/m over a 50 m section. The fibre diameters are 125 μm and 120 μm at the Ends A and B respectively.

Figure 8.20

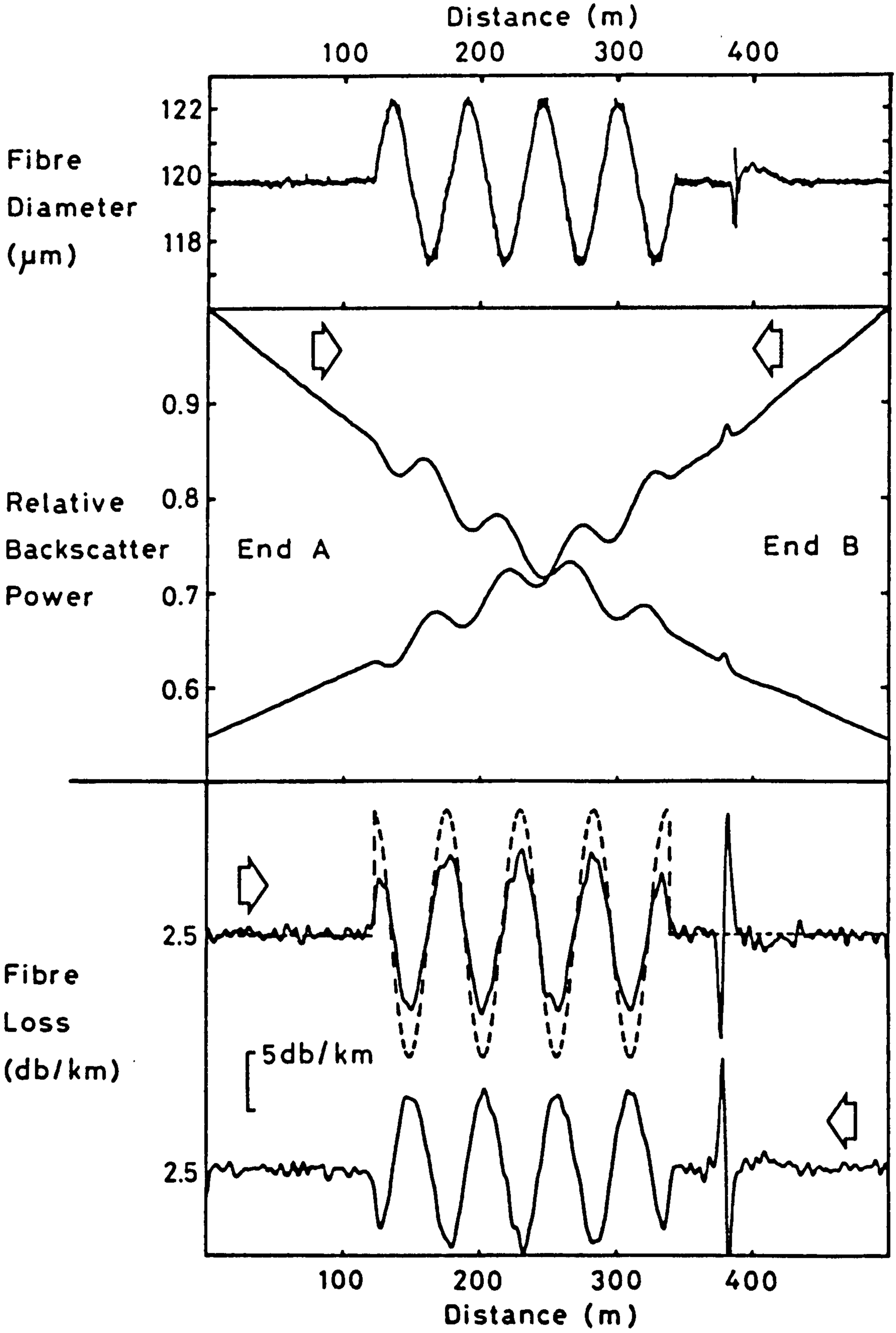

Effect of programmed oscillatory diameter variations of short period. Upper curve, diameter profile. (Also note small unprogrammed feature at ∿380 m). Centre curves, backscatter power. Lower curves, calculated loss. Dashed curve shows theoretical prediction of the model.

Figure 8.21

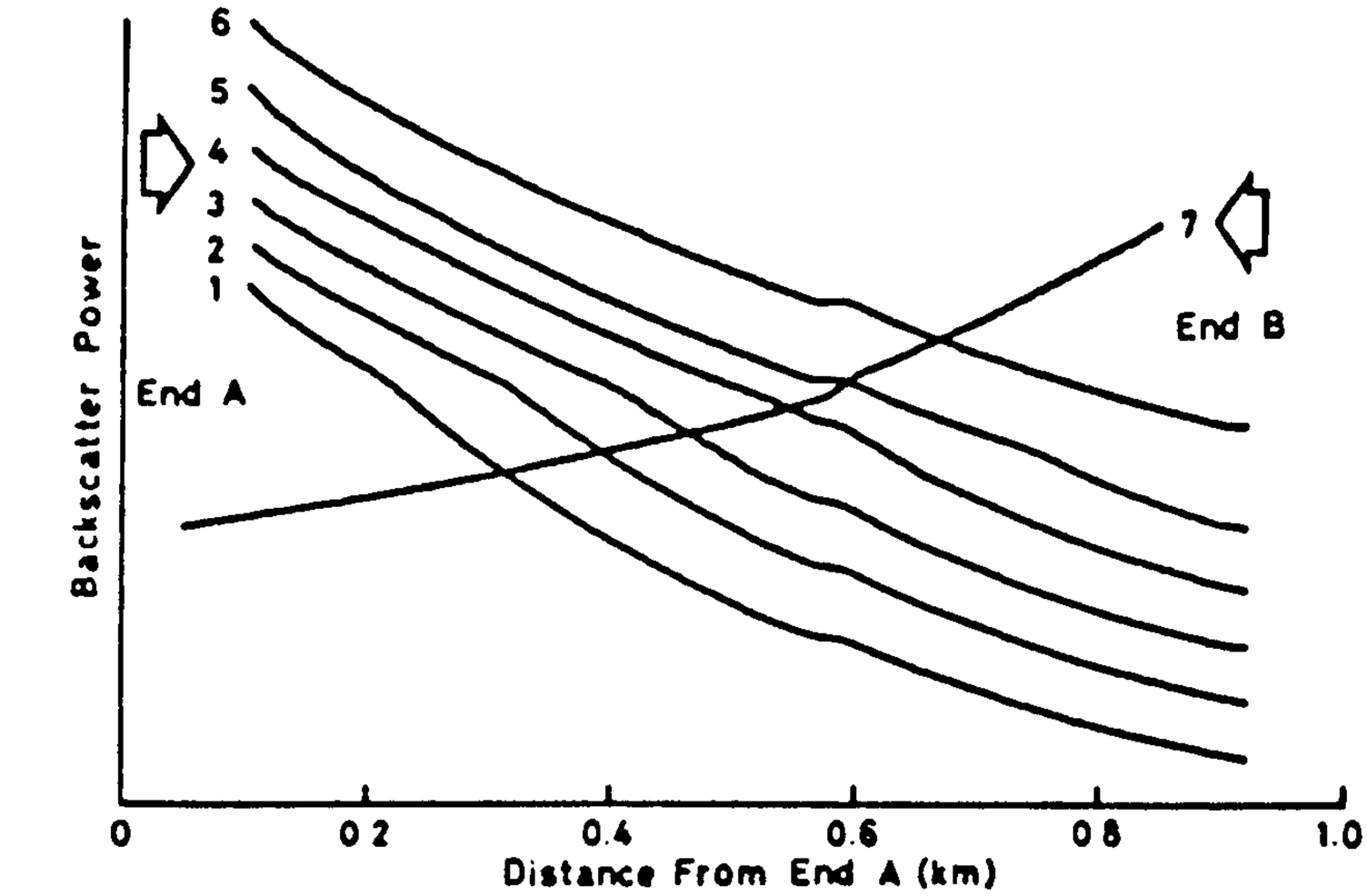

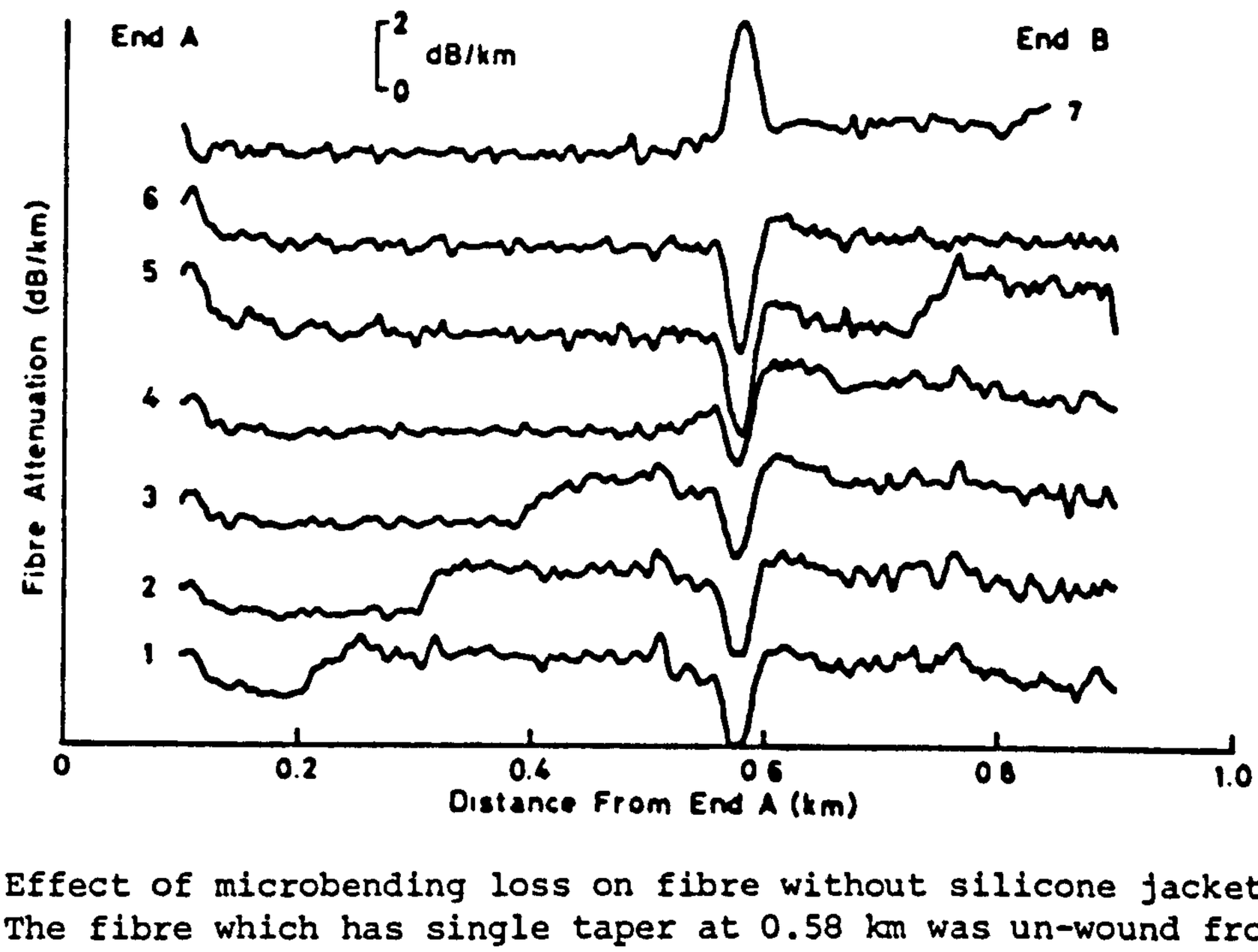

Effect of microbending loss on fibre without silicone jacket. The fibre which has single taper at 0.58 km was un-wound from drum and coiled loosely on floor, End A first. Curves 1-6 show consecutive measurements from End A of backscatter power (upper diagram) and loss (lower diagram) at various stages of un-winding. Uncoiling from drum causes reduction of local attenuation from 3.8 to 2.3 dB km^{-1}. Curve 7 shows result from End B at same stage of un-winding as curve 4.

Figure 8.22

CHAPTER 9

VARIATION OF PULSE DELAY WITH STRESS AND TEMPERATURE IN JACKETED AND UNJACKETED OPTICAL FIBRES

Measurements of the pulse transit time in an optical fibre can be used to reveal several interesting properties relevant to the transmission medium. For example, the wavelength dependence of pulse delay has been used to determine the material dispersion parameter in multimode fibres[42] and the chromatic dispersion in single-mode fibres[185]. Moreover, the inherent stability of the delay and the high bandwidth attainable has led to the employment of optical fibres as delay lines in signal processing applications[186]. Delay-bandwidth products of greater than 5000 are possible. The high delay stability has also suggested the use of fibres as strain gauges[187] and for synchronizing of remote events in high energy physics. In telecommunications, delay stability is also important if a clock for several digital channels is carried over a separate fibre[188].

Measurements on pulse transit time described in this section were performed with a dual objective. Firstly, the stability of the time delay has been evaluated for variations in temperature and axially-applied stress in order to provide data for the design of optical delay lines. Both unjacketed and plastic-clad fibres have been tested and it is shown that the application of a secondary coating of Nylon 6 considerably degrades the delay stability. These results were of particular significance to Mr. A. H. Hartog who required a high stability in fibre delay in order to accurately measure the location of the zero of material dispersion[42].

A second objective results from the observation that the pulse delay is dependent on fibre tension, suggesting the use of the measurement as a diagnostic test for residual stress levels in optical cables. The latter measurement is of some importance to cable designers, since ideally the fibre should be neutrally stressed in order to avoid static fatigue and microbending effects. Refinements to the previously reported delay-measurement technique[42], based on a time-domain reflectometry principle, have resulted in improved long-term stability and this has permitted experiments to be undertaken to determine

the residual compressive stress level in the fibre following the application of a Nylon 6 over-jacket. In addition, the effect of water ingress on the cable has been assessed.

9.1 Theory

The pulse transit time τ in a fibre of length L may be found approximately from

$$\tau = \frac{L}{c} N_1 \qquad \ldots (9.1)$$

where c is the speed of light in vacuo and

$$N_1 = n_1 - \lambda \frac{dn_1}{d\lambda} \qquad \ldots (9.2)$$

is the material group index. Here n_1 is the refractive index at core centre and λ the wavelength. Longitudinally-applied stress σ and temperature T produce changes in both fibre length and refractive index, each of which affect the transit time. The variation of pulse delay with temperature is given by

$$\frac{d\tau}{dT} = \frac{1}{c}\left(N_1 \frac{dL}{dT} + L \frac{dN_1}{dT}\right) \qquad \ldots (9.3)$$

and the variation with stress by

$$\frac{d\tau}{d\sigma} = \frac{1}{c}\left(N_1 \frac{dL}{d\sigma} + L \frac{dN_1}{d\sigma}\right) . \qquad \ldots (9.4)$$

Values for the thermal expansion coefficient dL/dT and the temperature coefficient of refractive index dn_1/dT ($\simeq dN_1/dT$) are given in reference[189] for bulk fused silica. The respective contributions of the two terms to the total variation of pulse delay are shown in Table 9.I. It may be seen that the two effects are the same in sense and that the refractive index variation dominates. Summing the two effects leads to a combined change with temperature of 40 ps $km^{-1}K^{-1}$.

The change in refractive index with applied stress is a result of the stress-optical effect. For a purely axial stress, the photo-elastic theory developed in Appendix V gives

$$\frac{dN_1}{d\sigma} \sim \frac{dn_1}{d\sigma} = \frac{1}{3}(A - B) \qquad \ldots (9.5)$$

where A is the isostatic pressure dependence of index[190] and B is the stress-induced birefringence[191]. In addition, fibre tension produces an elongation which may be found from Young's

modulus $E = L\frac{d\sigma}{dL}$. Table 9.I gives the time-delay components resulting from the known values of $dn_1/d\sigma$ and $dL/d\sigma$ for silica[190,191] and reveals that the two terms contribute an effect of opposite sense to the overall variation of time delay with applied axial stress. In contrast to the dependence on temperature, it is now the change in fibre length which dominates the change in index, giving an overall effect of 62.2 ps km^{-1} for a stress of 1 MPa.

Departures from the above calculated values are expected in practice due to the presence of graded concentrations of P_2O_5 and GeO_2 in the fibre cores[192], and the chilled state of the fibres. The latter is a result of the rapid cooling experienced during the fibre drawing process.

The application of a close-fitting polymer over-jacket to the fibre modifies the temperature dependence of pulse delay, owing to the large expansion coefficient of plastic materials. Using a simplified elastic model of fibre and coating, which neglects any radial stress component, it can be shown that the effect of temperature on a jacketed fibre is

$$\left(\frac{d\tau}{dT}\right)_{jacketed} = \frac{A_P}{A_F} E_P k_P \left(\frac{d\tau}{d\sigma}\right)_F + \left(\frac{d\tau}{dT}\right)_F \qquad \ldots (9.6)$$

where A is the cross-sectional area, E is the Young's modulus and k the expansion coefficient. The subscripts P and F refer respectively to the plastic over-jacket and the fibre. For a typical fibre of 125 μm diameter having a primary silicone coating of 250 μm diameter and a 500 μm diameter nylon over-jacket, for which $E_p = 3.1 \times 10^9$ Pa, $k_p = 8.3 \times 10^{-5} K^{-1}$, the variation of pulse delay with temperature is estimated to be 185 ps $km^{-1}K^{-1}$ (neglecting the contribution of the soft silicone buffer layer). The delay stability is thus expected to be nearly an order of magnitude worse than for an unjacketed fibre.

9.2 Experimental Procedure

An optical pulse of 0.35 ns duration from a GaAs injection laser operating at 0.9 μm is launched into the fibre and the pulse transit time measured using a time-delay generator and

sampling oscilloscope. In order to improve the timing stability and eliminate errors which may result from long-term variations in the laser turn-on time, a technique has been evolved which uses a marker pulse reflected from the input to the test fibre to provide a time reference. As shown in figure 9.1, the laser output is focused into a 25 m 'pigtail' of graded-index fibre, to which the test fibre is butt-coupled. The 8% Fresnel reflection which occurs at the joint returns a pulse to the fibre input, from where it is directed to a silicon avalanche photodetector by means of a 50% beam splitter. An aluminium mirror butted against the far end of the test fibre similarly returns a pulse to the APD. The time difference between the two pulses is found by positioning each to the same point on a sampling oscilloscope display using a variable pulse-delay generator. The electrical delay introduced in each case is then accurately determined with a time interval counter. The difference between the readings obtained for the reference pulse and the pulse returned from the remote end of the test fibre gives double the fibre transit time.

The advantage of the above technique is that long-term trigger-delay drifts in the timing circuitry can be eliminated, since they are common to both measurements. Furthermore, the back-reflection technique improves the sensitivity of the experiment, since it doubles the effective length of the fibre. Two further considerable advantages for field measurements are that access to only one end of the fibre is required and that test fibres may be easily interchanged without the necessity for re-alignment of the optics. There is an obvious similarity with the previously described backscatter measurement technique, however in the present instance, the reflection from the far end of the fibre is many decibels above the scattered return.

Pulse-delay measurements were performed on fibres having only a primary coating of silicone rubber and on fibres jacketed with a secondary coating of Nylon 6. The former were made to assess the intrinsic effects of tension and temperature on silica-based fibres (the silicone rubber contributes little to the observed delays) and to compare the results with those calculated previously. The measurements on nylon-jacketed fibres could then be interpreted in the light of the known

behaviour of the fibre under stress.

The variation of pulse delay with applied tension in unjacketed fibres was evaluated by horizontally suspending the fibre between two sheaves of eight low-friction pulleys spaced up to 90 m apart. Intermediate supports were provided for the fibre strands at intervals of approximately 20 m so as to reduce sag. A calibrated tension could be evenly distributed amongst the fibre sections by applying a known force to one of the pulley blocks and the resulting elongation determined by noting the block displacement. Measurements were made on three graded-index fibres having similar GeO_2/P_2O_5/SiO_2 core compositions in effective lengths (2 x actual length) ranging from 0.67-1.6 km.

The temperature-dependence of delay was assessed in both unjacketed and jacketed fibres by removing them from the drum and freely suspending the coils in a chamber whose temperature could be controlled over the range -30 to +100^{o}C to within $\pm$ 0.5^{o}C. The chamber consisted of a commercial freezer modified by the addition of heating elements, fans and thermocouples. Care was taken to ensure that no additional stresses were applied to the fibre. The effect of water and salt water on the jacketed fibres over the temperature range 0-50^{o}C was determined by immersing the freely coiled fibres in a temperature-controlled liquid bath. The jacketed fibres were conditioned to their environments (air or liquid) by performing a stabilizing soak at elevated temperature for periods of up to a few days.

9.3 Experimental Results

9.3.1 Effect of applied tension on unjacketed fibres

Transit time measurements were made on an unjacketed, silicone coated fibre, Fibre A, with characteristics given in Table 9.II. The experimental results for the variation of both pulse delay and fibre elongation with tension are shown in figure 9.2. For a fibre of 122.5 μm diameter, a tension of 1 g-wt corresponds to a stress and a strain of approximately 0.83 MPa and 1.2 x 10^{-5} respectively.

The extension curve exhibits a zero offset which is attributed to the uptake of the sag in the fibre at low values of tension; the absence of such an effect in the time-delay indicates that the measured tension accurately reflects that applied to the fibre.

A straight line least-squares fit to the data of figure 9.2 reveals a value of 53.7 ps $km^{-1}MPa^{-1}$ for the variation of time delay with applied tensile stress. This is substantially larger than the calculated figure of 62.2 ps $km^{-1}MPa^{-1}$ for fused silica given in Table 9.I, even taking into account the uncertainty in the experimental value of 3%, resulting mainly from the error in the fibre diameter measurement. On the other hand, the least-squares fit to the extension data indicates that the contribution of the change in length to the variation time delay is 70.6 ps $km^{-1}MPa^{-1}$, which is in close agreement with the value of 68.7 ps $km^{-1}MPa^{-1}$ calculated from the published results for pure silica[190].

The major difference from the fused silica values lies in the effect of stress on the glass refractive index where a much larger sensitivity than expected is found (Table 9.I). The stress-optical contribution to pulse delay given in the table is obtained by subtracting two measured values of similar magnitude. However, it should be noted that one of these values, the delay due to elongation, is not so accurate as the combined pulse delay due to the difficulty in precisely measuring the displacement of the block and pulleys. Thus, the present measurement is not sufficiently accurate to provide a precise determination of the longitudinal stress-optical effect. Nevertheless, it is clear that the fibre exhibits a stress-optical effect which is significantly larger than is predicted from silica data. This is perhaps not surprising in view of the presence of P_2O_5 and GeO_2 in the fibre core and the large differences found in practice between the stress-optical coefficients of glasses having different compositions. Measurements on two other fibres having GeO_2/P_2O_5-doped cores produced similar results, indicating that the discrepancy could be attributed to a material property.

9.3.2 Effect of temperature on unjacketed fibres

Pulse delays were measured as a function of temperature in a 600 m length of silicone-coated fibre, Fibre B (Table 9.II) produced from the same preform as Fibre A. The results over the temperature range -30 to +100°C are shown in figure 9.3 normalized to a fibre length of 1 km. The actual experimental length was determined by measuring the time delay at 20°C and comparing this with the delay measured in an accurately known short length of fibre. The latter gave a value for the group index of 1.4798 ±0.04%.

The least-squares fit to the data of figure 9.3 gives a delay variation of 35.7 ps $km^{-1}K^{-1}$, a value which is somewhat smaller than the calculated figure of 40 ps $km^{-1}K^{-1}$ for pure silica. The experiment repeated in the reverse temperature direction produced a similar result and showed no hysteresis in the measurement.

9.3.3 Residual fibre stress introduced by jacketing with Nylon 6

During the cabling process, stresses are unavoidably applied to the optical fibre and some of these may remain in the finished product. For example, the high-temperature extrusion of the secondary coating is expected to result in longitudinal compression of the fibre on cooling, owing to the difference in expansion coefficients between glass and plastic. Although compressive stresses applied to the fibre may possibly result in improved strength characteristics, they may also have detrimental effects such as increased microbending losses.

An experiment was conducted on 600 m of fibre, Fibre C, (Table 9.II) from the same production batch as those used previously, in order to determine the residual stresses within the fibre and thus demonstrate the use of pulse-delay measurements for cable diagnostics. Initially, the silicone-coated fibre was freely suspended in a stress-free state and the pulse transit time determined. A secondary layer of Nylon 6 was then applied by extrusion to give an outer diameter of 0.5 mm. Care was taken to ensure that all fibre pieces broken off during the extrusion process and for the purposes

of end preparation were taken into account.

It was found that the transit time after jacketing had decreased by 2.44 ns km^{-1} which from the stress/pulse delay calibration previously performed (section 9.3.1) indicates a residual compressive stress of 45 MPa (a compressive force of 58 g-wt). Such a figure is an order of magnitude less than that estimated from the known[193] expansion coefficient and Young's modulus of Nylon 6, although it should be noted that an exact analysis is complicated by the fact that the remaining stress is dependent on the extrudate cooling conditions and the time allowed for stress relief by plastic creep. The relatively low level of residual compression found in the fibre indicates that considerable stress relief had taken place in the period immediately following extrusion.

9.3.4 Delay stability in jacketed fibres

The temperature stability of pulse delay was investigated in Fibre C, after jacketing with Nylon 6 as described above. After an initial annealing period during which the transit time decreased slightly, the fibre was freely suspended in air and the time delay monitored as the temperature was cycled over the range -30 to +50°C. Several interesting effects were observed which could be attributed to the known creep behaviour of plastic materials. The thermal history of the fibre/plastic composite and the duration of the experiment were found to influence the time delay measured at any point in the temperature range. For example, static measurements at -30°C following a prolonged period spent at 50°C would result in an upward drift in pulse delay of as much as 4 ns km^{-1}. Conversely, measurements at 50°C after stabilization at -30°C produced a downward drift of similar magnitude. Furthermore, the delay was observed to exhibit hysteresis.

This behaviour is illustrated in figure 9.4. The curves show an experiment in which the temperature was continuously cycled at a rate of approximately 10°C/hour. One and three-quarter cycles were performed under these conditions (solid lines, curves 1-4) and are seen to produce almost coincident time-delay hysteresis loops. Curve 5 (dashed), on the other

hand, shows a measurement taken in the direction of increasing temperature after the above temperature cycles had been interrupted at -30°C for 12 hours. The static period has resulted in an upward drift in pulse delay of 1 ns, which, on resumption of temperature cycling, leads to a curve lying above those previously determined, although tending towards them at higher temperatures. Similarly, curve 6 (dashed) shows the effect of a 12 hour pause at 50°C, which produced a 0.5 ns drop in delay. The difference is gradually eliminated as the temperature is cycled.

The departure of the delay curves in figure 9.4 from the simple straight-line characteristic exhibited by the unjacketed fibre (figure 9.3) is the result of the mechanical properties of the secondary coating and the forces it exerts on the fibre. Plastics by their very nature do not exhibit simple elastic and thermal behaviour[193-196]; unlike silica, they are non-Hookean and such quantities as Young's modulus and thermal expansion coefficient are dependent on the magnitude of the applied load, the time scale and the temperature of the experiment. Furthermore, the thermal history, water content and degree of crystallinity of the plastic affect their properties.

Clearly, the hysteresis and time-dependent behaviour of the pulse delay shown in figure 9.4 are a result of stress relief in the fibre caused by plastic creep of the Nylon 6 over-jacket. The reason, however, for the marked change in slope at approximately 30°C is not at present understood, although we note that both the expansion coefficient and tensile modulus of nylon vary non-linearly with temperature. As a consequence of the effect, the temperature coefficient of time delay is no longer uniquely defined, being both time and temperature dependent. Nevertheless, averaging the slopes of curves 1 and 2 below 10°C leads to a working figure of 170 ps $km^{-1}K^{-1}$. This is in good agreement with the value of 185 ps $km^{-1}K^{-1}$ calculated previously.

The temperature stability of time delay in the jacketed fibre, Fibre C, should be compared with that of the primary-coated fibre, Fibre B, for which a value of 35.7 ps $km^{-1}K^{-1}$ was found. The application of the protective jacket degrades

the stability by nearly a factor of five. Furthermore, it should be recognised that the incorporation of the jacketed fibre into a larger cable structure having the same high expansion coefficient will produce a still greater variation.

9.3.5 Effect of water ingress on jacketed fibres

The influence of moisture ingress on the performance of jacketed fibres was assessed by immersing Fibre C loosely coiled in a water bath. Experiments were also conducted whilst immersed in a 20 wt% aqueous NaCl solution. Sufficient time was allowed for the fibre to reach equilibrium (72 hours and 36 hours at 50°C for water and NaCl solutions, respectively[193]). The pulse-delay performance for temperature cycles over the range 0-50°C is given in figure 9.5. Also shown are the results previously presented (figure 9.4) for the same fibre, Fibre C, suspended in air and, to aid comparison, for the unjacketed fibre, Fibre B (figure 9.3). The results are all normalized to a length of 1 km. This was achieved as outlined in section 9.3.2 by precisely determining the time delay in the unjacketed fibre and comparison with the delay in a known short length of the same fibre. The length of Fibre C was known from the results obtained prior to extrusion of the plastic jacket. However, confirmation of the measurement was obtained by removal of the jacket in concentrated nitric acid on completion of the temperature experiments. This also served to verify the effect found in section 9.3.3, namely that the time delay decreased after jacketing. It was ascertained that removal of the jacket now produced an increase in pulse delay and that the final value was in close agreement with that found prior to extrusion of the nylon.

The curves of figure 9.5 show that both water and salt solutions produce a marked increase in time delay, suggesting that a release of residual compressive fibre stress has occurred. Hysteresis behaviour is observed and curve gradients are closer to that of the unjacketed fibre, indicating that the liquids have caused a softening of the jacketing plastic, i.e. reduced its modulus. In addition,

the curve for water immersion lies above that of the unjacketed fibre, indicating that the fibre is in fact in tension. This may be seen more clearly by noting that at any temperature the time-delay difference between the jacketed fibre and the unjacketed one is an indication of the stress that the sheath is applying to the fibre. With the aid of the calibration figure for the dependence of time delay with stress for these fibres, we may map figure 9.5 into the residual stress versus temperature curves shown in figure 9.6, where the negative sign indicates fibre compression.

Figure 9.6 reveals that at room temperature the residual compressive longitudinal force exerted on the fibre by dry Nylon 6 (after conditioning) is in the region of 100 g-wt. The ingress of water into the plastic has relieved the initial compression which existed after extrusion and in fact has caused the fibre to become tensioned. This effect is consistent with the known[193] volume expansion and reduction of Young's modulus which accompanies water saturation (9.5 wt%) of Nylon 6.

The subsequent immersion in a salt solution caused the fibre to return to compression, although not to the level observed in air. This was accompanied by a significant increase in attenuation (6 dB km^{-1}) with little change in pulse dispersion, an effect which was not observed in water. Furthermore, on removal from the salt solution and drying, the attenuation became so high as to render further measurements impossible. This was found even if the fibre was rinsed in de-ionized water for two days prior to drying; however, re-immersion in water restored the transmission. Similar behaviour was found in aqueous $CaCl_2$ solutions. Clearly the effect is attributable to an increase in microbending loss in the fibre caused by a change in the nylon characteristics. The mechanism whereby such kinking can occur as a result of increased radial pressure exerted by the plastic, but with little change in stress in the axial direction is not at present clear.

Although the levels of salt concentration used in these experiments are high, the effects observed are indicative of

the performance of Nylon 6 as a jacketing material in hostile environments. A more appropriate choice in these cases would be polypropylene, which exhibits a low level of hygroscopy and high resistance to chemical attack.

Experiments performed on Nylon 6 jacketed fibres immersed in organic solvents such as formaldehyde and glycol-methanol (1:1) similarly produced changes in the fibre stress levels, although their effect on pulse dispersion and attenuation have not been measured.

9.4 Summary

Measurements of the stability of the optical pulse delay in both unjacketed and jacketed fibres have been presented. In the case of unsheathed fibres, an evaluation of the dependence of delay on fibre tensile stress and temperature reveals that the effects are linear, having values of 53.7 ps $km^{-1}MPa^{-1}$ and 35.7 ps $km^{-1}K^{-1}$, respectively. Calculation of the expected values for bulk fused silica indicates that the variation with stress is dominated by the physical change in fibre length and that with temperature by the change in refractive index. Comparison of the silica values with those determined experimentally demonstrates significant departures for P_2O_5/GeO_2-doped fibres,particularly for the stress-induced index change.

For fibres jacketed with Nylon 6, it was observed that the presence of the sheath produced much larger and non-linear excursions of time delay with temperature. The departure of the performance of the jacketed fibre from that of the unclad fibre was used to evaluate the effect of the sheath on residual fibre stress levels. The physical properties of the plastic jacketing material were shown to induce time-delay drift and hysteresis following temperature variations. In addition, the ingress of water modifies the plastic properties and causes significant delay variations. Furthermore, immersion in salt and $CaCl_2$ solutions irreversibly impairs optical transmission, indicating that Nylon 6 is unsuitable for use as a cladding material in hostile environments.

From the above we see that the temperature stability of the transit time can be severely degraded by encapsulation of the fibre in plastic materials having a high expansion coefficient. This is a consequence of the sensitivity of the delay to applied longitudinal stress. Thus plastic-jacketed fibres or epoxy-potted coils should not be used in applications which require high time stability, for example in fibre delay lines and strain gauges.

On the other hand, the stress dependence of delay can be used to provide a powerful diagnostic tool for cable stress analysis. This was demonstrated by an experiment to determine the fibre compression induced by application of a Nylon 6 jacket, where a residual compressive force of 58 g-wt was found. Application of the method to determine residual stress after each stage of cable manufacture is possible; for example, after stranding, sheathing and armouring. In addition, it is envisaged that periodic tests on installed cables could be used to provide information on long-term cable creep effects.

Component	With temperature ($ps\ km^{-1}K^{-1}$)	With stress ($ps\ km^{-1}MPa^{-1}$)
effect on delay due to variation of index N_1	38	-6.5 (-16.9)
effect on delay due to variation of length L	2	68.7 (70.6)
combined calculated effect on delay	40 (35.7)	62.2 (53.7)

Calculated components of the temperature and stress dependence of time delay in bulk fused silica. The bracketed figures refer to the experimentally determined values for unjacketed silica fibres doped with P_2O_5/GeO_2.

Table 9.I

Property	Fibre A	Fibre B	Fibre C
approximate length, m	800	600	600
numerical aperture	0.21	0.21	0.21
core diameter, μm	65	65	65
fibre diameter, μm	122.5	122.5	125
silicone coating diameter, μm	250	250	250
nylon diameter, μm	unjacketed	unjacketed	500

Properties of fibres used in pulse-delay measurements. All fibres have $P_2O_5/GeO_2/SiO_2$ cores and a B_2O_3/SiO_2 buffer layer.

Table 9.II

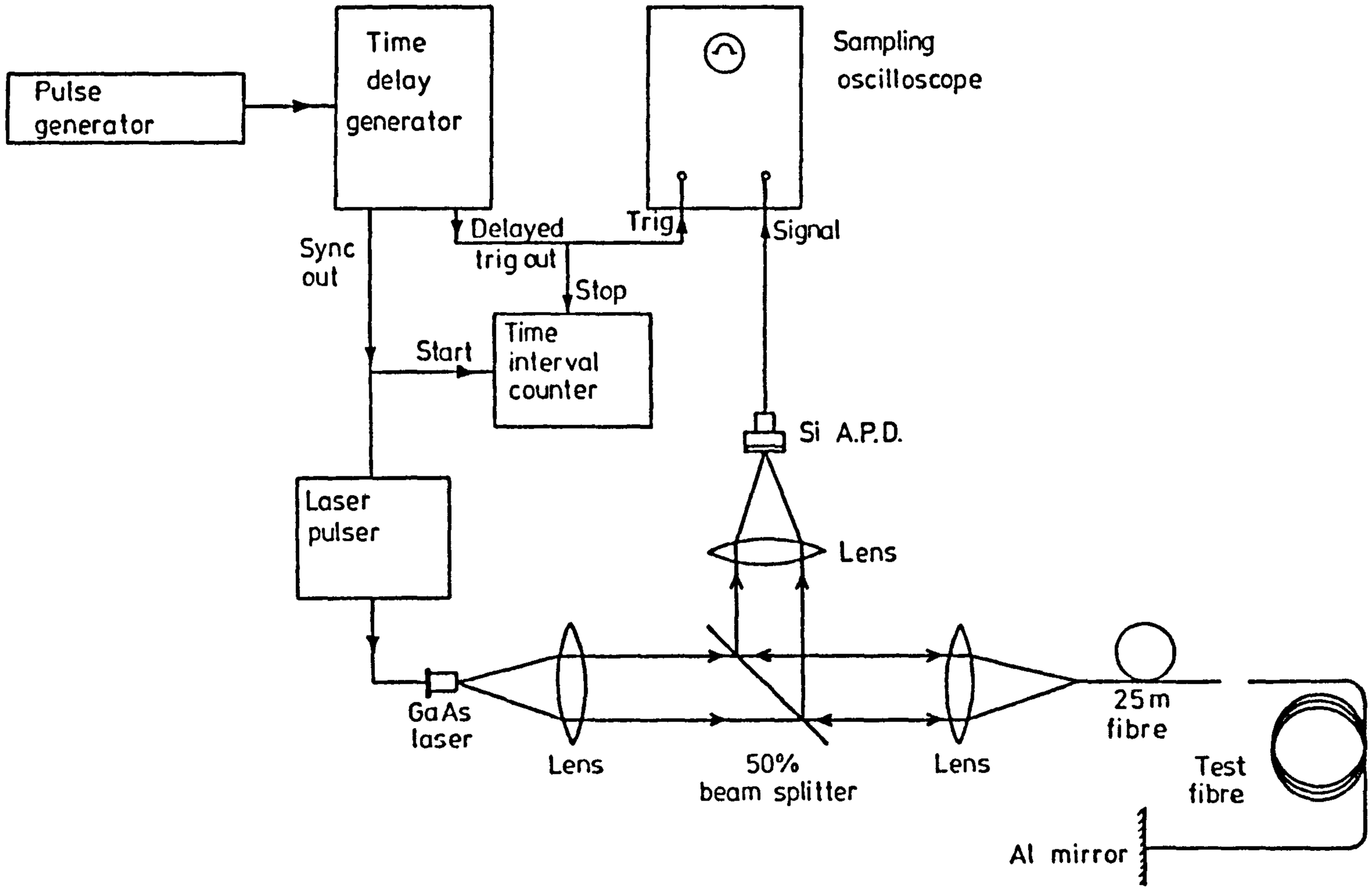

Schematic diagram of optical pulse-delay measurement experiment

Figure 9.1

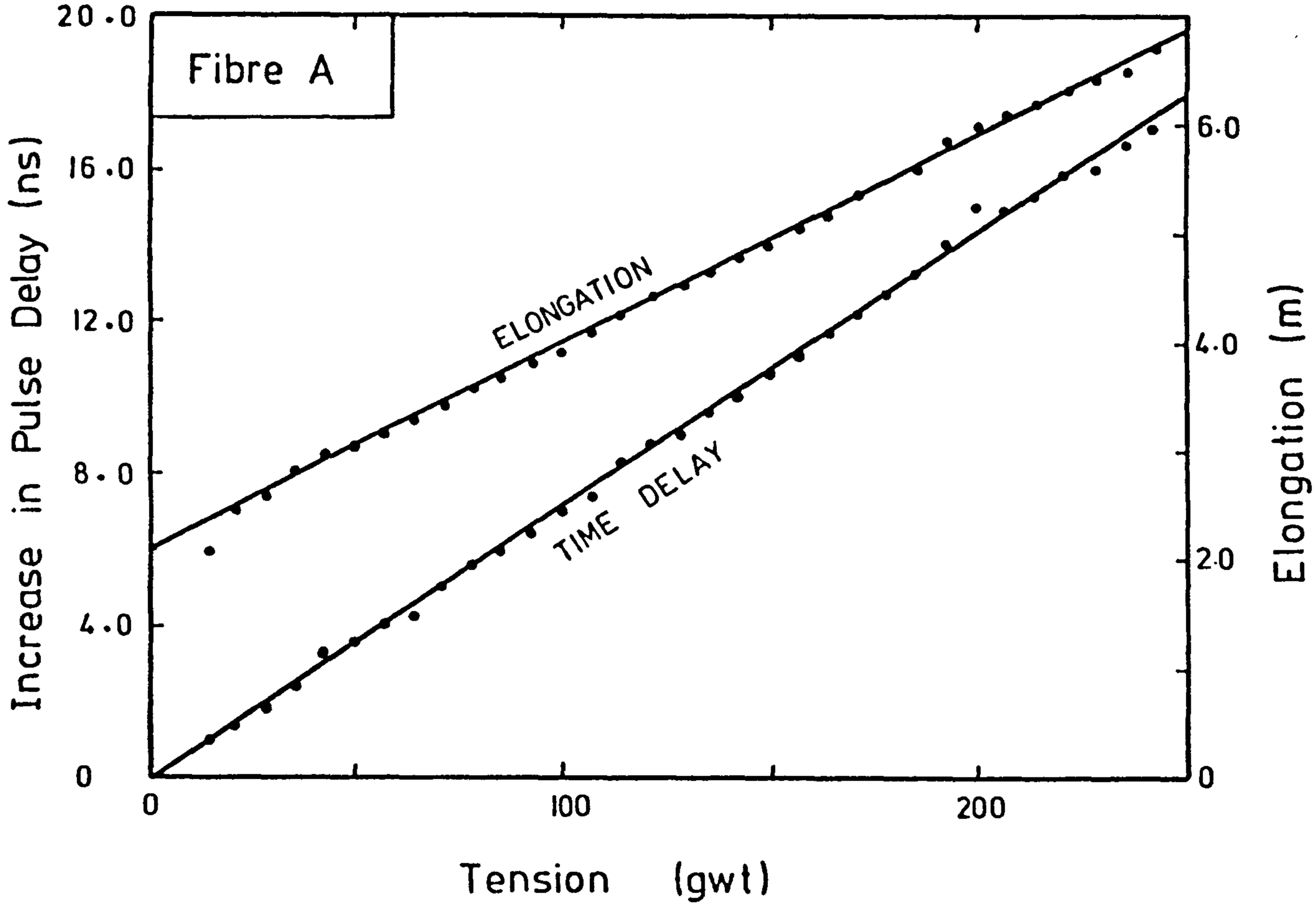

Variation of pulse-delay and fibre extension with applied tension for Fibre A (Table 9.II) The fibre is unjacketed and has an effective length of 1.6 km.

Figure 9.2

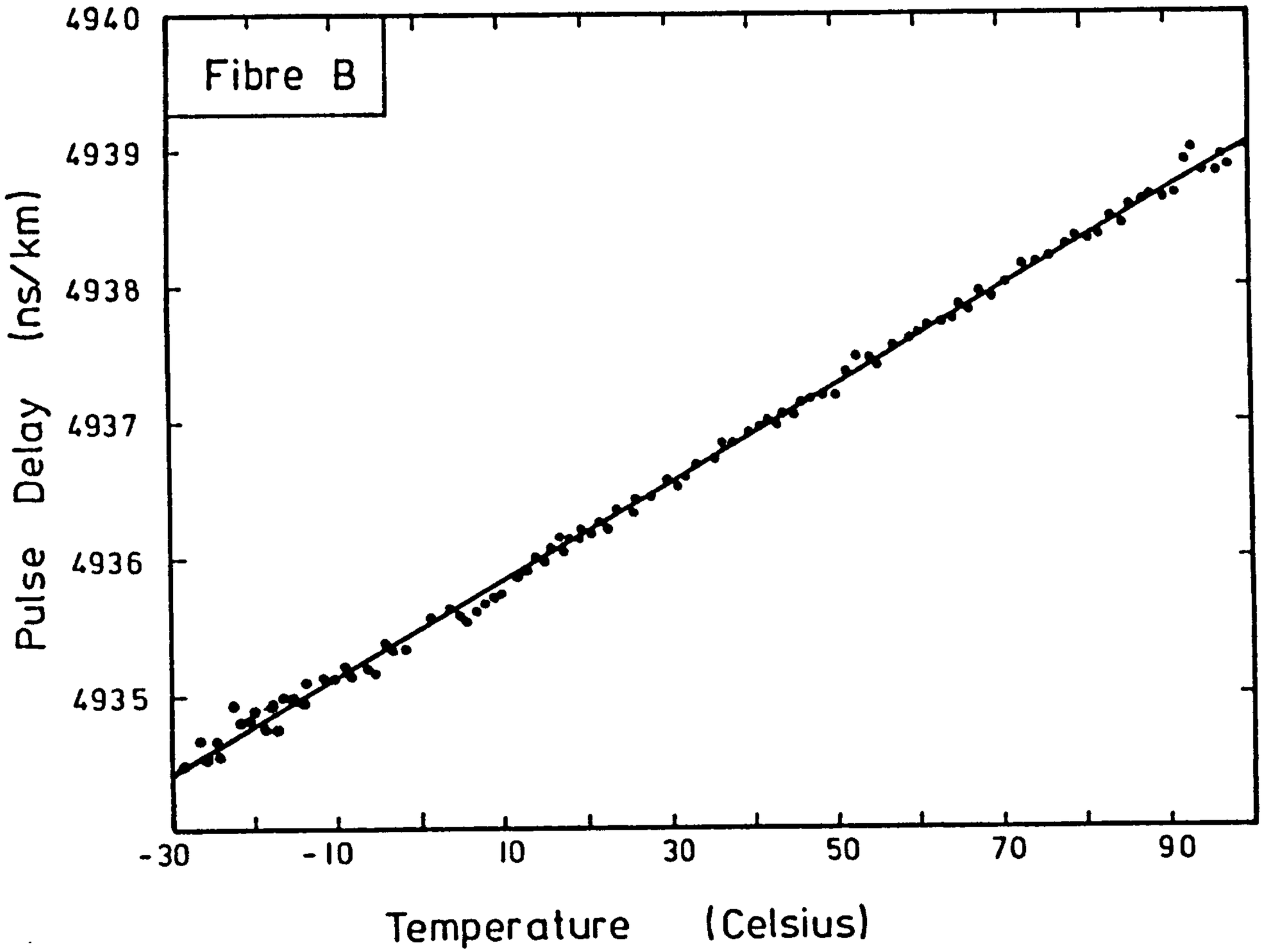

Pulse delay normalized to a length of 1 km as a function of temperature for an unjacketed fibre, Fibre B (Table 9.II).

Figure 9.3

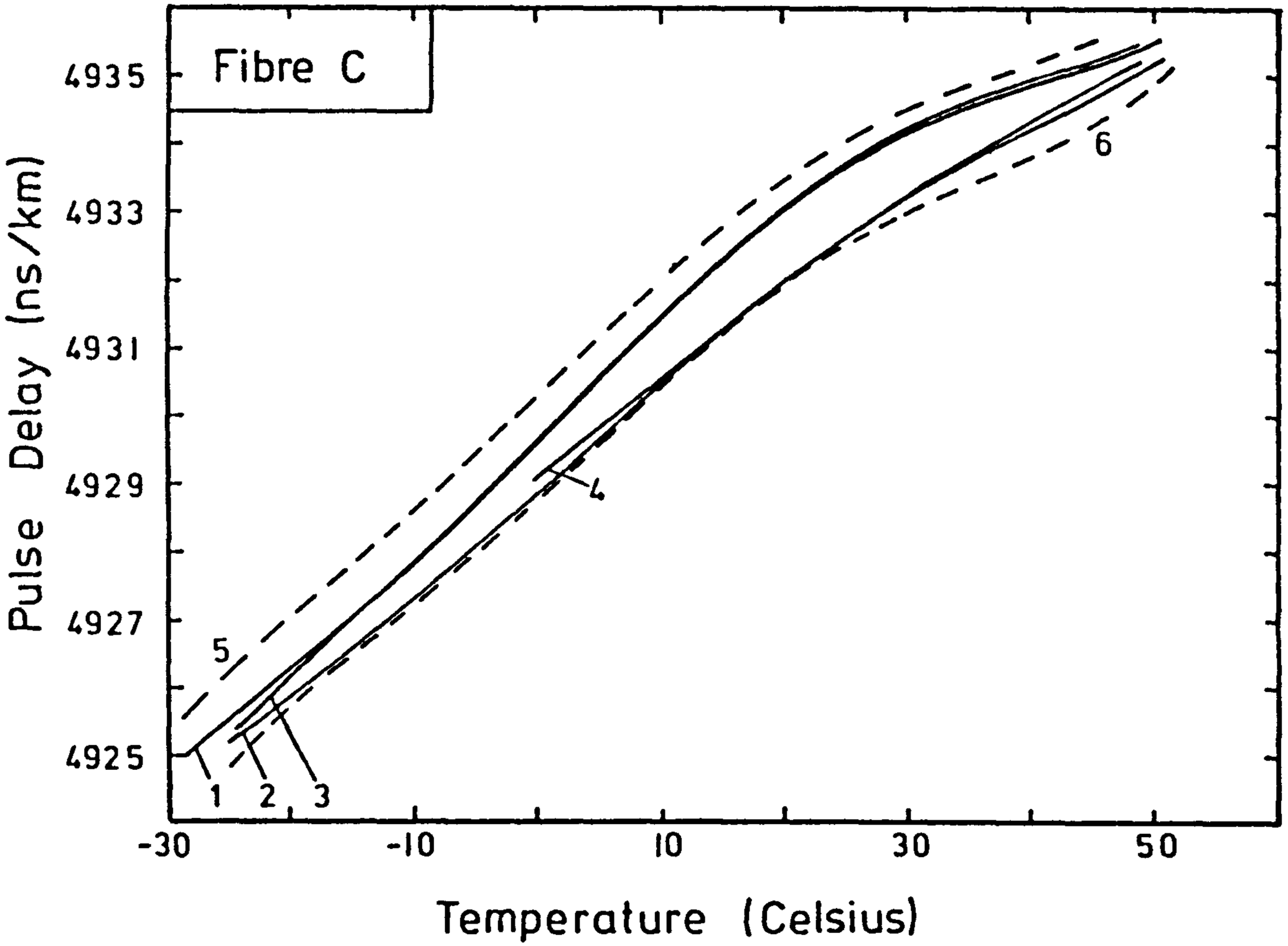

Variation of pulse-delay with temperature for Fibre C, having a nylon jacket. The delay is normalized to a fibre length of 1 km. Solid lines are for continuous temperature cycling, dashed lines show effect of pausing at -30^{o}C and 50^{o}C.

Figure 9.4

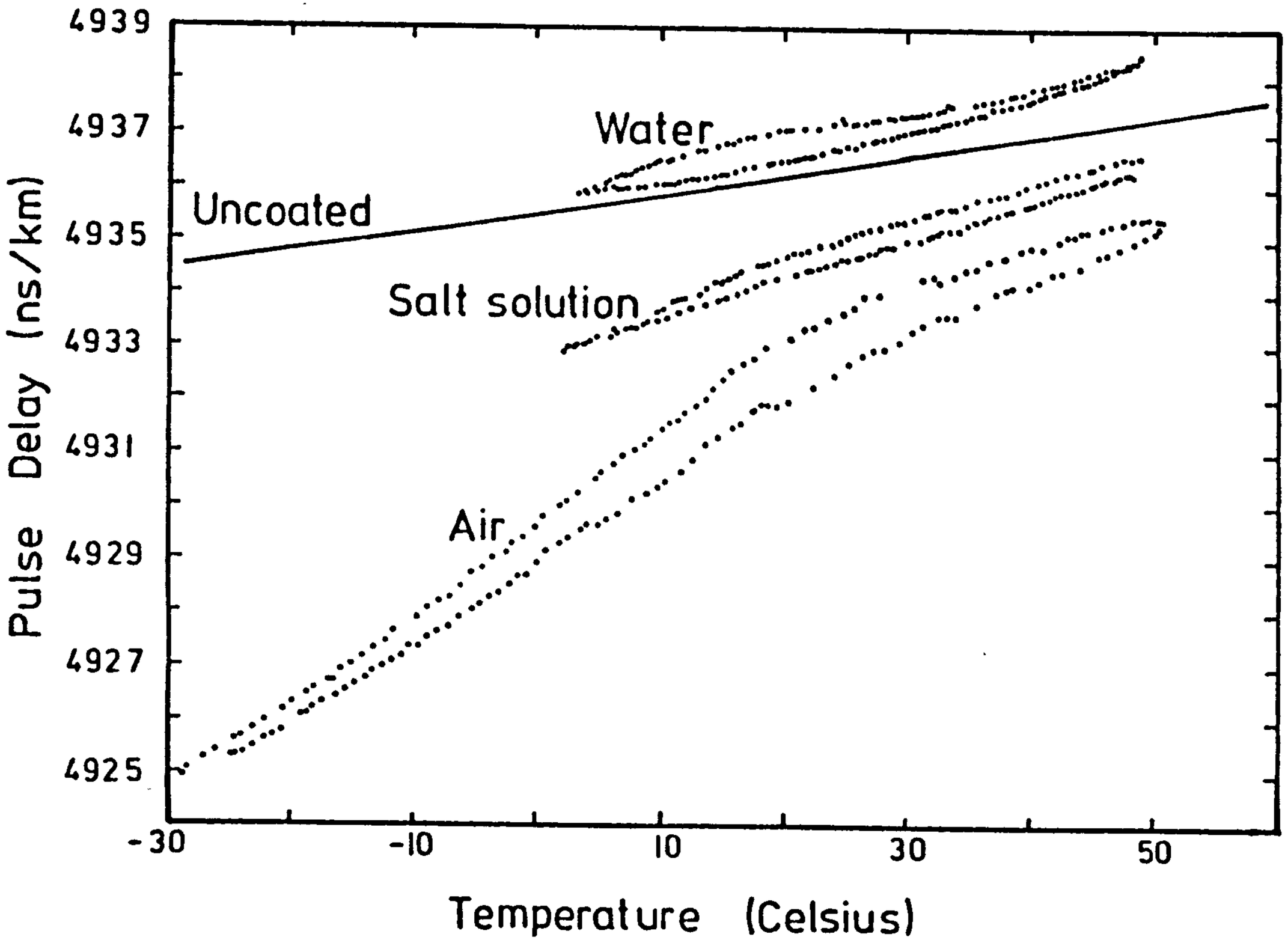

Measured values of pulse-delay versus temperature for a nylon-jacketed fibre, Fibre C (Table 9.II), under various environmental conditions (dots). The solid curve gives time delay for unjacketed fibre, Fibre B (Table 9.II). All curves are normalized to 1 km.

Figure 9.5

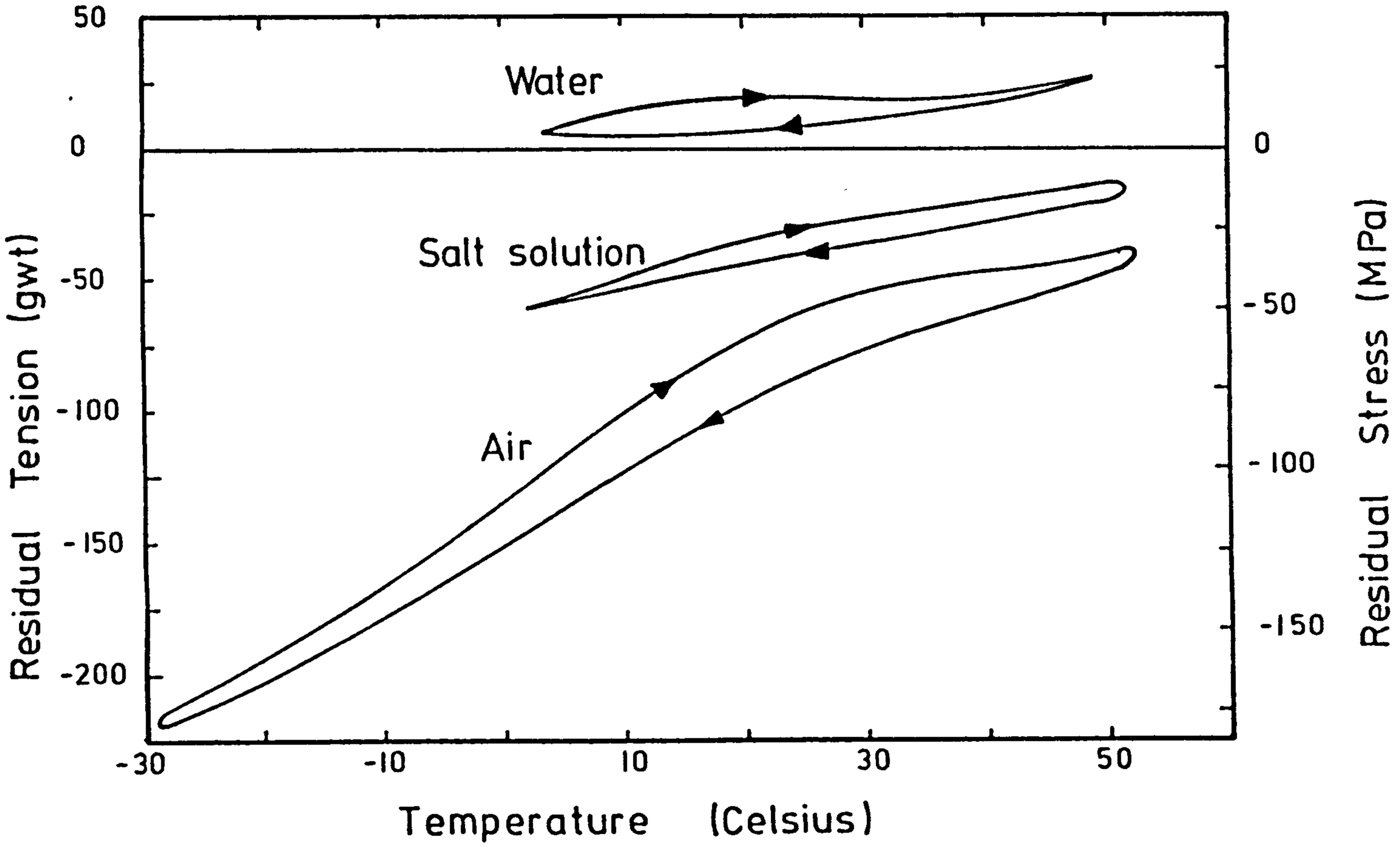

Stress and force exerted on Fibre C by the nylon jacket for various environmental conditions

Figure 9.6

CHAPTER 10

CONCLUSION

Applications of Time Domain Reflectometry to optical fibre measurements have been described. Firstly, the Back-scatter Technique for measuring local fibre attenuation is analysed and constitutes the bulk of the study. Secondly, a modification of the Shuttle Pulse Technique is used to determine the dependence of pulse transit time on stress and temperature in jacketed and un-jacketed fibres.

Fibre properties were carefully assessed under varying conditions of fabrication, excitation and environment. This was aided by a detailed consideration of the theoretical aspects and by a number of innovations in instrumentation, the latter which enabled the achievement of high measurement accuracy.

10.1 The Backscatter Technique

The backscatter technique is shown to be a powerful method for determining the fibre length, locating faults and measuring the local fibre loss.

10.1.1 Optimization of measurement

An important consideration in backscatter measurements is the absolute accuracy of the instrumentation (see Chapter 3). The analysis presented here indicates that an optimum operating strategy exists in terms of the choice of the sample separation such that the accuracy with which local fibre attenuation can be measured is maximized[93].

The implication of this is that a compromise is necessary between the achievement of overall attenuation accuracy and the resolution of short-length fluctuations, since the latter requires small gate separations. This results from the difficulty in determining the slow decay in the back-scatter signal when the difference between the power levels $p(t_1)$ and $p(t_2)$ is small. On the other hand, relatively large localized power fluctuations are found at fault points and imperfections, leading to significant differences in signal levels if gates are positioned immediately before and after the point of interest. Thus, relatively small gate

separations are permitted and accurate loss measurements of such discontinuities is not precluded.

A further consequence of the existence of an optimum gate separation is that greatest accuracy in the determination of overall link attenuation is obtained by summing the attenuation of individual fibre sections having lengths corresponding to ΔT_{opt}. It is shown in Chapter 2 that the accuracy of local attenuation measurements depend critically on the constancy of the backscatter factor S, along the fibre. Thus, the measurement of sections of length approximately equal to ΔT_{opt} may well have a further advantage in that it should allow both sample points to be sited within the same fibre section in a jointed link, thus avoiding problems which may result from variations in S between fibre sections.

10.1.2 Developments in instrumentation

A new 2-channel method for backscatter waveform analysis is proposed[93] and shown to be capable of high resolution in the determination of local fibre loss. The advantages of the 2-channel technique are numerous (see Chapter 3) and make this approach very attractive for commercial exploitation. The technique is insensitive to drift and instability in the optical source and detector. Furthermore, when near maximum range the receiver gain can be adjusted to increase the signal amplitude and thereby maximize measurement accuracy.

The instrument 'range' defined as the maximum fibre length over which measurements can be performed to a desired accuracy is calculated. It is inevitable that when near maximum range, the signal-to-noise ratio is low and measurements must be averaged to attain the desired accuracy. The availability of inexpensive microprocessors suggests numerical averaging as a better alternative to analogue techniques used in the past. Accordingly parameters pertaining to digital data acquisition are taken into account.

The development of two measurement systems based on the 2-channel principle is described. The first utilized boxcar sampling and a tunable dye laser (see Chapter 4) and the second consisted of fast sample-holds, A-D converters and a

semiconductor laser (see Chapter 5). The equipments were used extensively for the measurements described in Chapters 7 to 8 and the latter system was also demonstrated as part of a contribution by Southampton University to the British Telecom Exhibition of Optical Fibre Technology[176].

10.1.3 Accuracy of the method

The ability of the backscatter method to resolve accurately the fibre loss was assessed by a comparison with the more standard cutback method over a wide wavelength range (see Chapter 7). This measurement represents the first comprehensive spectral analysis of the backscattered power[94] and comparison with the cutback method showed that for a high quality optical fibre virtually identical results can be obtained. The excellent agreement is believed to be largely the result of a systematic attempt to compare the two methods under like conditions and lends a considerable confidence to the efficacy of the backscatter technique.

The utility of spectral backscatter measurements is also demonstrated by tracking the evolution of the OH^- impurity along the length of a fibre. This measurement is important since it may enable the source of a contamination to be identified.

10.1.4 Analysis of backscatter-loss signatures

The effects on the backscattered power of variations in longitudinal fibre parameters is considered (see Chapter 8). It is shown that depending on fibre quality, plots of local attenuation with length may exhibit severe fluctuations in loss and anomalies such as negative values. Two general classifications of loss feature are identified: Firstly, there is the correlating feature caused, for example, by absorption losses, microbending and point defects, which result in an identical loss of power when measured from the two fibre ends. Secondly, there is the anti-correlating feature where the apparent loss change is of opposite sign from the two fibre ends. Features of the latter type are caused by variations in the backscatter factor which result from changes in numerical aperture, diameter and refractive index profile.

Backscatter waveforms are presented which for the first time clearly show the relationship between features and programmed fibre defects. A consideration of fabrication methods indicates that for MCVD fibres, anti-correlated oscillations in backscattered power of short period ($\lesssim$300 m) are most likely caused by diameter variation. Note that this conclusion contrasts the hypothesis in reference 7 where the origin of similar fluctuations is attributed to numerical aperture variations.

A simple mathematical model to describe the phenomenon has been developed and compared to experimental results. It is shown that propagation through a contracting fibre section results in an increase in backscattered power and an apparent reduction in loss. Conversely, an expanding taper results in a decrease in backscattered power and an apparent increase in loss. Both these effects are the opposite of that which might be intuitively expected by a consideration of uni-directional light propagation.

This advance in understanding of the backscatter process means that it is now possible to infer the nature of a fibre fluctuation from its loss signature. Backscatter measurements may, therefore, be used for the diagnosis of faults in the factory and field. In the factory results may possibly assist the improvement of fabrication techniques and increase fibre yield.

10.1.5 Single mode measurements

The feasibility of polarization optical time-domain reflectometry in single-mode fibres is demonstrated. Polarization analysis of the backscattered light clearly shows the evolution of the state of polarization in the fibre. The technique could be invaluable in the study of the properties of polarization-maintaining fibres for sensor applications (e.g. gyroscopes, hydrophones) and of low-birefringence fibres for the Faraday Current Monitor and telecommunications.

Furthermore, it is shown that polarization effects can cause substantial errors in conventional backscatter attenuation measurements on monomode fibres. Consequently, care

must be taken to eliminate the polarization sensitivity of the measurement and caution exercised in the interpretation of backscatter results.

10.1.6 Current status and future prospects for the backscatter technique

The backscatter technique has proven capable of resolving accurately the local attenuation of high quality optical fibres for wavelengths up to ∿1.1 μm. It appears likely that a commercial instrument can be developed to cover the maximum repeater span (∿40 dB) of first generation fibre links[177].

Present technology dictates that single and 2-channel scanning schemes provide for best instrumentation accuracy in resolving the fibre attenuation. The advantages of the 2-channel approach in particular have been emphasised in this study. However, in the future, provided lower cost and higher resolution sequential digitizers can be realised then a better alternative will be the m-channel processing technique (see Chapter 3).

Further development in backscatter measurements will undoubtedly be affected by moves towards long wavelength operation and the use of single-mode fibres. Modified back-scatter methods based on photon counting[125] and new correlation[178,179] and frequency domain techniques[180] operating at about 1.3 μm are currently under investigation. Rayleigh scatter levels at the long wavelengths are lower and the backscatter slope is expected to be dominated by variations in the backscatter factor and in the case of single-mode fibres also the birefringence. Thus, the local attenuation will be difficult to resolve. However, the measurement and location of faults is not precluded and it is important that an instrument possessing this limited but important facility is developed.

Backscatter measurement methods are therefore yet to mature and further intensive investigation is still warranted.

10.2 Pulse Delay Measurements

The incorporation of an optical fibre into a cable results in a level of residual stress within the fibre which depends upon the materials, cable structure and method of manufacture. The remanent stress is of some importance from the cable static-fatigue and microbending viewpoints. A method based on a time domain reflectometry principle is described for the measurement of longitudinal stress. The long term stability of the method enables manufacturers to evaluate the stresses applied to the fibres at the various stages of the manufacturing process and throughout the life-time of the cable. The method is attractive for field applications since access to only one end of the fibre is required and test fibres can be easily interchanged without re-alignment of the optics.

Application of the method to determine the residual stress in a fibre after the extrusion of a Nylon 6 over-jacket indicated a residual compressive force of 58 g-wt. It was shown that the presence of the jacket also produced much larger and non-linear excursions of time-delay with temperature than in the un-clad fibre. The physical properties of the plastic jacketing material were shown to induce time-delay drift and hysteresis following temperature variations. In addition, the ingress of water modifies the plastic properties and causes significant delay variations. It is clear that the temperature stability of transit time can be severely degraded by encapsulation of the fibre in plastic materials having a high expansion coefficient. Thus plastic-jacketed fibres should not be used, for example, in fibre delay lines and strain gauges where a high time stability is required.

The pulse transit time has proved to be a sensitive indicator of physical changes in fibre jacketing materials and therefore in the future could be used to evaluate a wide range of new materials under various environmental conditions.

10.3 Closing Remark

It is hoped that the results described in this thesis have contributed to an advancement in the understanding of Time-Domain Reflectometry Techniques in optical fibres.

APPENDIX I MEASUREMENT ERRORS DUE TO NOISE CLIPPING

This appendix quantifies the effects of noise-clipping on sampling accuracy in backscatter measurements. It is stated in section 3.7 that the amplifier gain must not be so large as to cause truncation of the noise at the sample points t_1 and t_2. This causes a bias in the mean since the noise cannot average to zero, even after an infinite number of samples.

Consider a waveform which consists of a signal x_o and a superimposed Gaussian noise of variance σ^2. Let the waveform be inputed to an A-D converter with dynamic range limits $\pm K$. The probability density function for the combined signal and noise is

$$P_x(\gamma) = \frac{1}{\sqrt{2\pi}\,\sigma} \exp -\left[(\gamma - x_o)^2/2\sigma^2\right] \qquad \ldots(I.1)$$

However, the probability density for the clipped waveform becomes

$$P_z(\gamma) = \begin{cases} P(\gamma) & |\gamma| < K \\ \delta(\gamma - K)\int_K^{\infty} P_x(\gamma)d\gamma & \gamma \geq K \\ \delta(\gamma + K)\int_{-\infty}^{-K} P_x(\gamma)d\gamma & \gamma \leq -K \end{cases} \qquad \ldots(I.2)$$

where 'δ' is the dirac-delta function. The mean, after an infinite number of samples is given by

$$\bar{z} = \int_{-\infty}^{\infty} \gamma P_z(\gamma)d\gamma \qquad \ldots(I.3)$$

and the error, or bias in the mean due to truncation of the noise is

$$\varepsilon = |x_o - \bar{z}| \qquad \ldots(I.4)$$

Combining equations (I.1-I.3) and using the variable transformation $\beta = \frac{\gamma - x_o}{\sigma}$ results in

$$\bar{z} = \int_{\frac{-K-x_o}{\sigma}}^{\frac{K-x_o}{\sigma}} (\sigma\beta + x_o) \frac{1}{\sqrt{2\pi}} e^{-\beta^2/2} d\beta$$

$$+ K \left[\int_{\frac{K-x_o}{\sigma}}^{\infty} \frac{1}{\sqrt{2\pi}} e^{-\beta^2/2} d\beta - \int_{-\infty}^{\frac{-K-x_o}{\sigma}} \frac{1}{\sqrt{2\pi}} e^{-\beta^2/2} d\beta \right] \quad \ldots (I.5)$$

The bias in the mean of the waveform may be determined from equation (I.5). Thus

$$\bar{z} - x_o = (K - x_o) \int_{\frac{K-x_o}{\sigma}}^{\infty} \frac{1}{\sqrt{2\pi}} e^{-\beta^2/2} d\beta$$

$$-(K + x_o) \int_{\frac{K+x_o}{\sigma}}^{\infty} \frac{1}{\sqrt{2\pi}} e^{-\beta^2/2} d\beta \quad \ldots (I.6)$$

$$-\sigma \int_{\frac{K-x_o}{\sigma}}^{\frac{K+x_o}{\sigma}} \frac{1}{\sqrt{2\pi}} e^{-\beta^2/2} d\beta$$

This reduces to

$$\bar{z} - x_o = \frac{K - x_o}{2} \operatorname{erfc}\left[\frac{K - x_o}{\sqrt{2}\ \sigma}\right] - \frac{K + x_o}{2} \operatorname{erfc}\left[\frac{K + x_o}{\sqrt{2}\ \sigma}\right]$$

$$+ \frac{\sigma}{\sqrt{2\pi}} \left(\exp\left[-\tfrac{1}{2}\left(\frac{K + x_o}{\sigma}\right)^2\right] - \exp\left[-\tfrac{1}{2}\left(\frac{K - x_o}{\sigma}\right)^2\right] \right) \quad \ldots (I.7)$$

where the error function is defined as

$$\operatorname{erfc}\ y = \frac{2}{\pi} \int_y^{\infty} e^{-t^2/2} dt = 1 - \operatorname{erf}\ y \quad \ldots (I.8)$$

Dividing both sides of equation I.7 by x_o, and expressing σ in terms of x_o and the signal-to-noise ratio (SNR) via equation (3.20), results in the normalized expression

$$\frac{\bar{z} - x_o}{x_o} = \tfrac{1}{2}\left(\frac{K}{x_o} - 1\right) \operatorname{erfc}\left[\left(\frac{K}{x_o} - 1\right)\sqrt{\frac{SNR}{2}}\right]$$

$$- \tfrac{1}{2}\left(\frac{K}{x_o} + 1\right) \operatorname{erfc}\left[\left(\frac{K}{x_o} + 1\right)\sqrt{\frac{SNR}{2}}\right] \qquad \ldots \text{ (I.9)}$$

$$- \frac{1}{\sqrt{2\pi(SNR)}}\left(\exp\left[-\left(\frac{K}{x_o} - 1\right)^2 \frac{SNR}{2}\right]\right.$$

$$\left. -\exp\left[-\left(\frac{K}{x_o} + 1\right)^2 \frac{SNR}{2}\right]\right)$$

In Chapter 3, the backscatter signal level $p(t_1)$ is substituted for x_o in equation (I.9) and results in the fractional sampling error $\frac{\varepsilon}{p(t_1)}$, shown in equation (3.23). This equation forms the basis for many of the discussions in the remainder of the chapter.

APPENDIX II COMPUTER SIMULATION OF EXPANDING FIBRE SECTION

Figure 8.10(b) shows an expanding taper comprised of N sections of length $\delta\ell$ and with core radii r_o to r_N, and core attenuation α_c.

The probe pulse propagating to the left passes through the tapers without loss. However, light returned to the detector from a scatter point within or beyond the tapered region suffers an additional loss as the high-order modes of the larger waveguide, which have been excited by the scattering process, are lost by radiation. Assuming the guide is fully excited in the backward direction, the additional loss is expected to be proportional to the change in core area[175].

The power returning to the input P_R, for scatter points at positions ℓ in taper sections 0 to N are given below (refer also to figure 8.10(b)).

Section 0 :

$$P_R = KP(\ell) \qquad \ldots (II.1)$$

Section 1 :

$$P_R = KP(\ell)\frac{r_o^2}{r_1^2}e^{-\alpha_c\ell} \qquad \ldots (II.2)$$

Section 2 :

$$P_R = KP(\ell)\frac{r_o^2}{r_2^2}e^{-\alpha_c\ell} \qquad \ldots (II.3)$$

Section N :

$$P_R = KP(\ell)\frac{r_o^2}{r_N^2}e^{-\alpha_c\ell} \qquad \ldots (II.4)$$

where K is a constant of proportionality.

Now
$$P(\ell) = P(0)e^{-\alpha_c\ell} \qquad \ldots (II.5)$$

Thus, the backscattered power returned to the input from a point at position ℓ in section N is

$$P_R = KP(0)\frac{r_o^2}{r_N^2}e^{-2\alpha_c\ell} \qquad \ldots (II.6)$$

Re-define P_o as the backscattered power from the start of the fibre. Thus,

$$P_R = P_o\frac{r_o^2}{r_N^2}e^{-2\alpha_c\ell} \qquad \ldots (II.7)$$

This equation is used in the calculations in section 8.3.4.

APPENDIX III COMPUTER SIMULATION OF CONTRACTING FIBRE SECTION

Figure 8.10(a) shows a contracting taper comprised of N sections of length $\delta\ell$ and with core radii r_o to r_N. The core and cladding attenuations are given by α_c and α_{cl} respectively.

Low-order modes constituting the probe pulse to the left of the contracting taper are converted by the taper to higher-order modes in the right hand guide. However, if the fibre section before the taper is under-excited and if the diameter change is small then a negligible loss of forward power may be observed.

A scatter point following the taper excites both fibre core and cladding, and backscattered light propagates in the two regions. When the cladding light encounters the taper, which now appears expanding in the reverse direction, it is able to enter the core. By reciprocity with the case described in Appendix II, the power which can enter the core is proportional to the area change.

Consider a point in tapered-section 2 of figure 8.10(a). Scattering excites both core and cladding modes in the backward direction. A fraction of the cladding light can re-enter the core at each of the diameter transitions $x + \delta\ell$ and x, and therefore contributes to the received power.

The power P_R(at x) received at point x for scatter points in sections 1, 2 and 3 is given in Table III.1. The table shows clearly the various core and cladding components along with the core re-entry points for the cladding modes. Multiplying the values in the table by $e^{-\alpha c(\ell+x)}$ gives the received power P_R relative to the launched power P(0) at the fibre input. The factor K is merely a constant which relates the forward and backscattered light.

In general, the power received at the fibre input from a point ℓ in section N is

$$P_R = P_o\, e^{-2\alpha_c \ell}\left(1 + \sum_{n=1}^{N} e^{-\Delta\alpha(\ell-x-(n-1)\delta\ell)} \cdot \left[\frac{r_{n-1}^2}{r_n^2} - 1\right]\frac{r_n^2}{r_N^2}\right) \quad \ldots \text{(III.1)}$$

where $\Delta\alpha = \alpha_{cl} - \alpha_c$ is the difference between the cladding and core losses and P_o is the backscatter power from the start of the fibre.

The validity of the above derivation may be tested by putting $\Delta\alpha = 0$ and considering the limit of equation (III.1)

$$\lim_{\delta r \to 0} \left(1 + \sum_{n=1}^{N} \left[\frac{r_{n-1}^2}{r_n^2} - 1 \right] \frac{r_n^2}{r_N^2} \right)$$

$$= 1 + \lim_{\delta r \to 0} \sum_{n=1}^{N} \frac{(r_n - \delta r)^2 - r_n^2}{r_N^2}$$

$$= 1 + \int_{r_o}^{r(\ell)} \frac{-2r}{r^2(\ell)}\, dr$$

$$= \frac{r_o^2}{r^2(\ell)} \qquad \ldots \text{(III.2)}$$

Thus, in the limit equation (III.1) reduces to equation (8.5) and shows that the change in backscattered power associated with diameter fluctuations is proportional to the variation in guide area.

Taper section number	Backscattered power received at x $\frac{P_R(\text{at } x)}{KP(\ell)}$	Propag-ation path	Re-entry point into core
1	$e^{-\alpha_c(\ell-x)}$	c	-
	$+\left[\frac{r_o^2}{r_1^2}-1\right] e^{-\alpha_{c1}(\ell-x)}$	c1	x
2	$e^{-\alpha_c(\ell-x)}$	c	-
	$+\left[\frac{r_o^2}{r_1^2}-1\right]\frac{r_1^2}{r_2^2}\ e^{-\alpha_{c1}(\ell-x)}$	c1	x
	$+\left[\frac{r_1^2}{r_2^2}-1\right] e^{-\alpha_c\ \delta\ell}\ e^{-\alpha_{c1}(\ell-x-\delta\ell)}$	c1+c	x+$\delta\ell$
3	$e^{-\alpha_c(\ell-x)}$	c	-
	$+\left[\frac{r_o^2}{r_1^2}-1\right]\frac{r_1^2}{r_3^2}\ e^{-\alpha_{c1}(\ell-x)}$	c1	x
	$+\left[\frac{r_1^2}{r_2^2}-1\right]\frac{r_2^2}{r_3^2}\ e^{-\alpha_c\delta\ell}\ e^{-\alpha_{c1}(\ell-x-\delta\ell)}$	c1+c	x+$\delta\ell$
	$+\left[\frac{r_2^2}{r_3^2}-1\right] e^{-\alpha_c 2\delta\ell}\ e^{-\alpha_{c1}(\ell-x-2\delta\ell)}$	c1+c	x+2$\delta\ell$

Contracting fibre section: the backscattered power P_R(at point x) relative to the propagating power $P(\ell)$ at point ℓ in taper sections 1, 2 and 3 (refer also to figure 8.10(a)). Also shown are the various core and cladding components along with the core re-entry points for the cladding modes.

Table III.1

APPENDIX IV BACKSCATTER MEASUREMENTS IN SINGLE MODE FIBRES

The following paper was presented at the Sixth European Conference on Optical Communication (post-deadline session) at York in September 1980.

POLARISATION OPTICAL TIME-DOMAIN REFLECTOMETRY: EXPERIMENTAL RESULTS AND APPLICATION TO LOSS AND BIREFRINGENCE MEASUREMENTS IN SINGLE-MODE OPTICAL FIBRES

A. H. HARTOG, D. N. PAYNE AND A. J. CONDUIT

DEPARTMENT OF ELECTRONICS, SOUTHAMPTON UNIVERSITY, SOUTHAMPTON, ENGLAND

1. INTRODUCTION

Optical time-domain reflectometry[1,2] is now a well established means of examining the length-dependence of attenuation in multimode optical fibres. Theoretical work[3] has shown that the technique is similarly applicable to monomode fibres and experimental results have lately appeared in the literature[4]. It has recently been noted that in monomode fibres the scatter return contains additional information concerning the local state of polarisation (SOP) in the fibre, since at any point the scattered light mirrors the SOP at that position. A polarisation optical time-domain reflectometry technique (POTDR) has thus been proposed[5], in which the backscattered light is analysed by means of a polariser to reveal the variation of polarisation along a monomode fibre. Such a technique would be invaluable in the study of the properties of polarisation - maintaining fibres for sensor applications (e.g. gyroscopes, hydrophones) and of low-birefringence fibres for the Faraday Current Monitor and telecommunications. In the latter case, information could be obtained relating to the polarisation dispersion in the fibre and to the variation of the SOP with time, an effect which is expected to produce problems when interfacing to integrated-optics devices.

We present here the first measurement to be made using POTDR. Our results clearly establish the feasibility of the technique and, furthermore, show that polarisation effects can cause substantial errors in conventional backscatter attenuation measurements on monomode fibres. Consequently, care must be taken to eliminate the polarisation sensitivity of the measurement and caution exercised in the interpretation of backscatter curves.

2. EXPERIMENT

The experimental arrangement is shown in Fig. 1. An optical parametric oscillator (OPO) pumped by a dye laser produced pulses of ∿200W peak power which are truncated to a duration of 10ns by an electro-optic modulator. The light is launched into the fibre via a beamsplitter, a focusing lens and a launching cell. The receiver consists of a Si APD followed by a 15MHz transimpedance amplifier. The signal is fed to a transient recorder where the complete waveform is digitised and sent to a computer for averaging and processing.

This arrangement retains the advantages of the two-channel technique[2] while reducing the measurement time by acquiring samples from many parts of the fibre simultaneously (i.e. a 'multi-channel' technique).

The characteristic feature of the POTDR experiment is the polariser placed in front of the receiver to analyse the time variation of the SOP in the backscatter trace. The analyser converts polarisation information to intensity variations; thus in a fibre having only, say, linear birefringence, the backscatter signal is expected to vary sinusoidally with a period determined by the characteristic polarisation beat length. Note also that the beamsplitter is used at near-normal incidence so that its reflectivity is almost polarisation-independent.

3. POTDR MEASUREMENTS

Measurements were made on the final 150m section of a 450m length of germano-borosilicate fibre having a cutoff wavelength of 860nm. Typical results measured at 885nm are shown in Fig. 2. POTDR traces taken with the receiving polariser parallel (upper curve) and orthogonal (middle) to the input polarisation exhibit strong and rapid fluctuations of power along the length, corresponding to the evolution of the SOP in the fibre. Note that the POTDR traces measured at orthogonal polarisations are precisely anti-correlated and thus sum to a near-constant value; the fluctuations which are observed thus correspond to variations in the polarisation of the received power and are not found in the total intensity of the backscattered light. This is confirmed by a conventional backscatter trace (lower) which was measured without the receiving polariser; the curve is almost featureless by comparison.

A detailed analysis of the POTDR returns is complex since several mechanisms contribute simultaneously to the length-dependence of the SOP. The backscattered light, does, however, contain sufficient information[5] to describe fully the polarisation retardance and rotation characteristics of a particular section of fibre. For example, it can be seen that a characteristic frequency exists in the traces which corresponds to a polarisation beat-length of 10m, a typical figure for this series of low-birefringence fibres.

4. DISTORTION OF BACKSCATTER LOSS BY POLARISATION EFFECTS

Light backscattered in single-mode fibres is almost inevitably polarised. It is therefore of utmost importance that backscatter test equipment designed for single-mode fibres should not contain polarisation-sensitive components. Insufficient attention to this point would lead to spurious features in the loss/distance curves. For example, a semitransparent beamsplitter at an angle of 45° is commonly used in backscatter experiments to separate the forward and backward-travelling light. Figure 3 shows a measurement of the same length of fibre as in Fig. 2 made in this way.

The result (upper) shows a large number of spurious features which are not real attenuation features (e.g. Fig. 2 lower curve) but which are associated with the variation of reflectivity of the beamsplitter with the SOP of the incident light. This interpretation is confirmed by the correlation which exists between these features and those of the POTDR curve (Fig. 3 lower curve).

5. SUMMARY

We have demonstrated the feasibility of POTDR and have presented the first measurements using the technique. In addition to revealing the potential of POTDR for polarisation studies, our measurements show that extreme care must be exercised in interpreting conventional OTDR loss measurements on monomode fibres owing to the presence of polarisation effects.

Acknowledgements are made to Dr. A. J. Rogers for useful discussions, to CERL for sponsoring the work and to S. R. Norman for supplying the fibre.

REFERENCES

1. M. K. Barnoski and S. M. Jensen: Appl. Opt. 15, 2112, 1976
2. A. J. Conduit, A. H. Hartog & D. N. Payne: Electron. Letts. 16, 77, 1980
3. E. Brinkmeyer: Electron. Letts. 16, 329, 1980
4. P. Healey and P. Hensel: Electron. Letts. 16, 831, 1980
5. A. J. Rogers: Electron. Letts. 16, 489, 1980

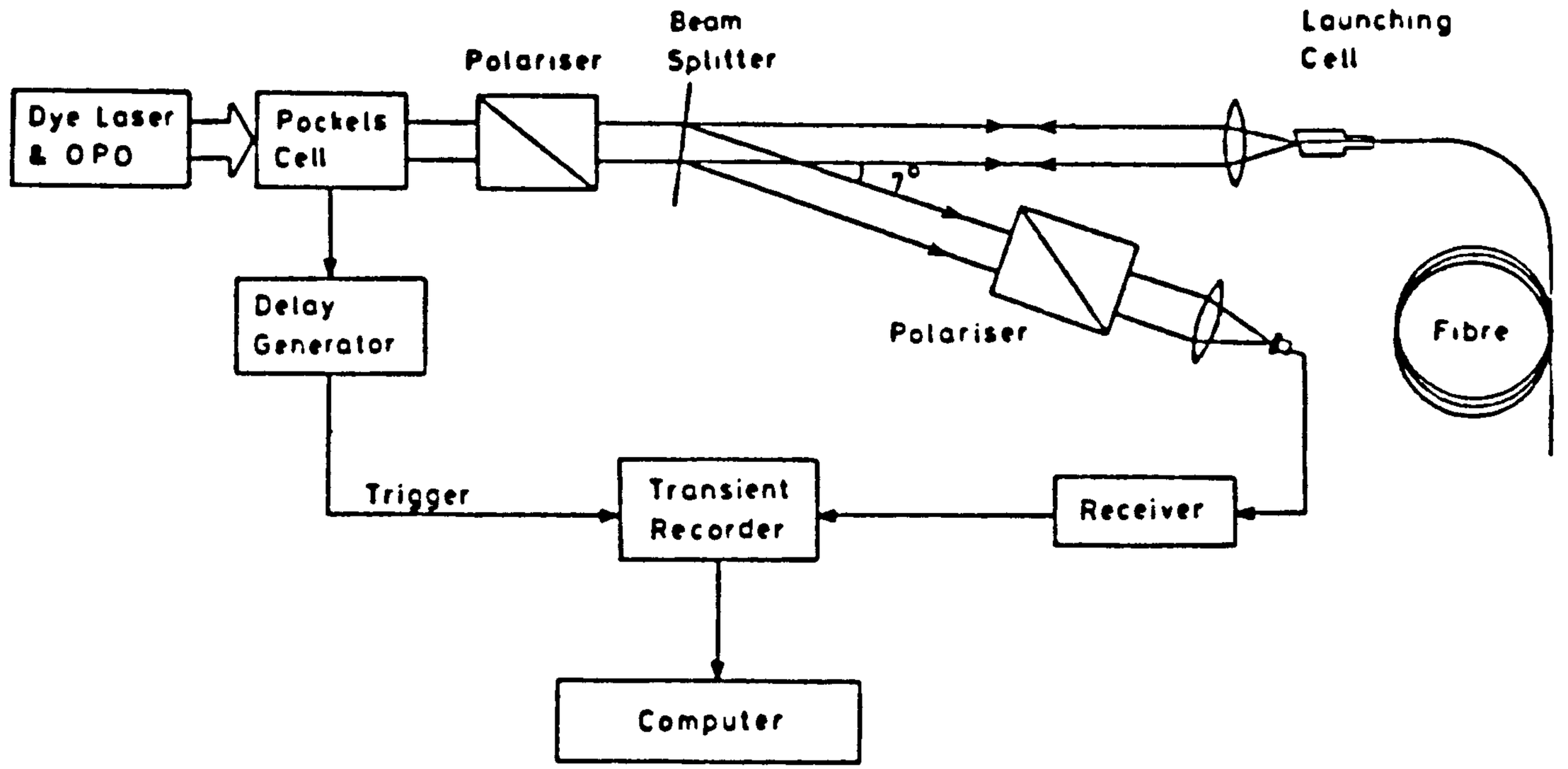

Experimental arrangement

Figure 1

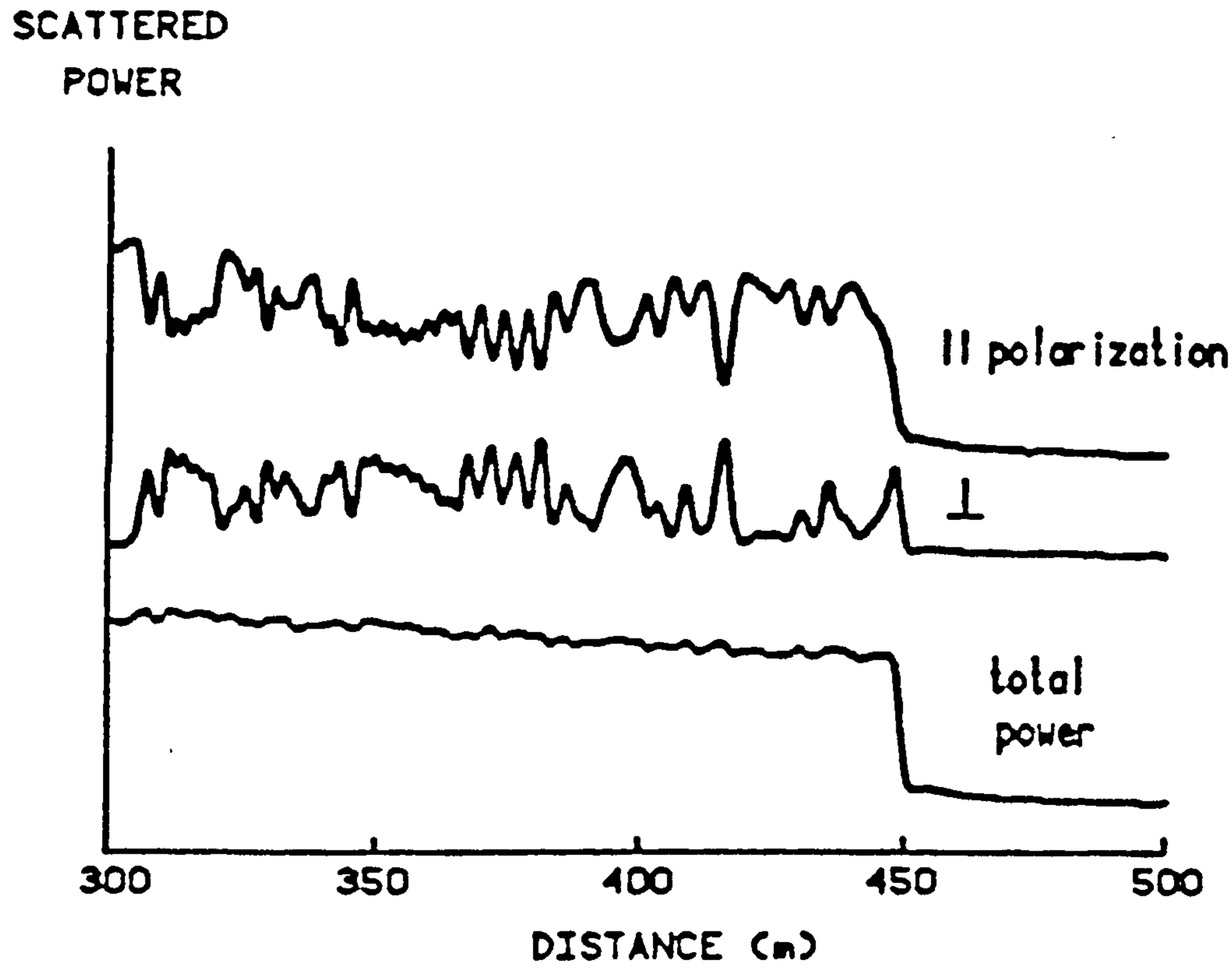

POTDR traces recorded with two Orthogonal orientations of the receiving polariser (upper and middle curves) and measured total scattered return (lower curve)

Figure 2

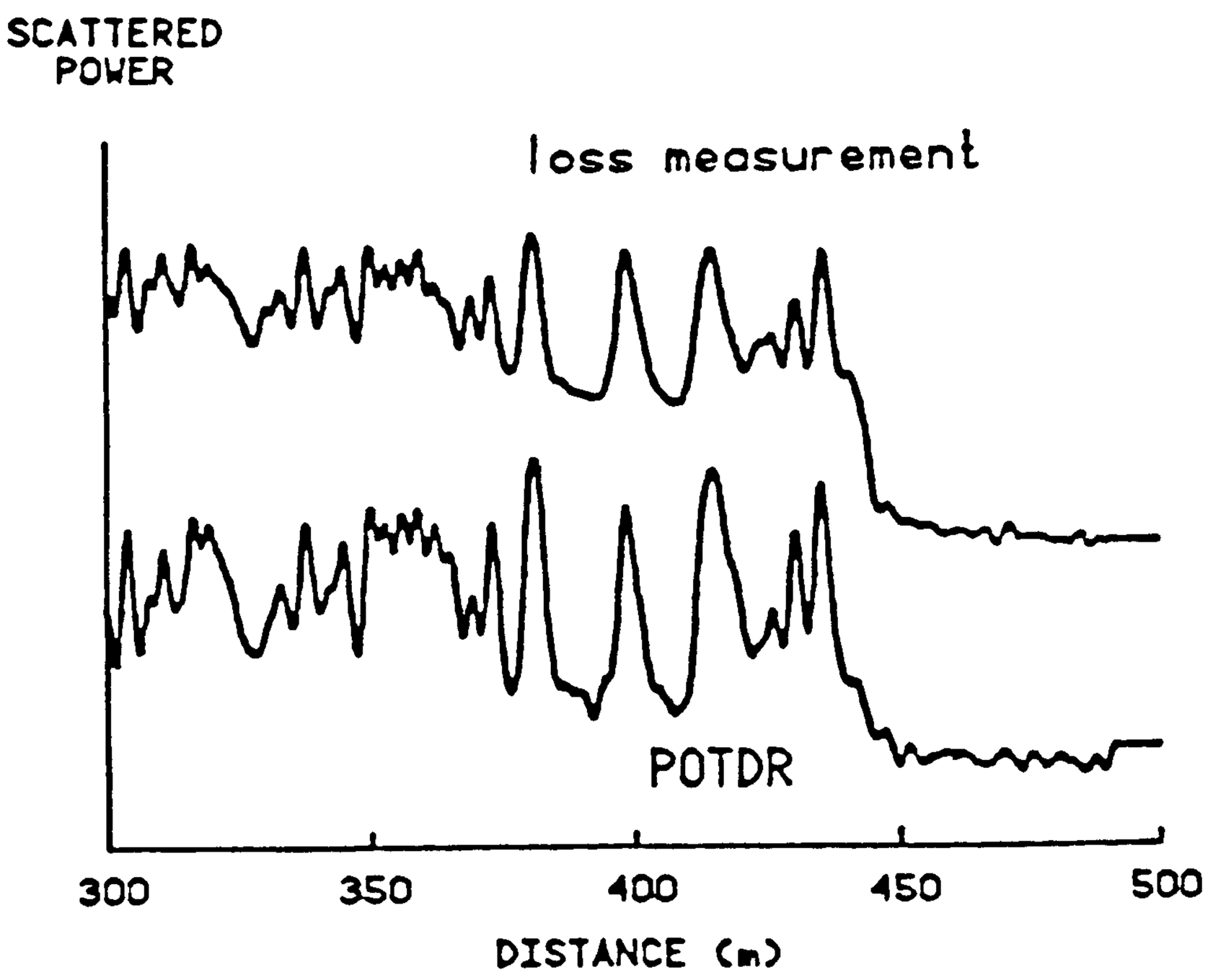

Effect of polarisation-sensitive components on backscatter loss measurements in monomode fibres. Upper curve: total received power, lower curve: corresponding POTDR trace

Figure 3

APPENDIX V STRESS-OPTICAL EFFECT

Stress applied externally to an optical fibre results in a change in the core refractive index and this affects the pulse transit time. The phenomenon which links the applied stress to the refractive index is known as the 'stress-optical effect'. In the present section, the relationship between refractive index change and stress is determined and expressed in terms of easily measured quantities. Using published data for the effect of stress on bulk glass, the dependence of time delay is calculated and in Chapter 9 compared to delay measurements in germano-silicate fibres.

V.1 Stress Optical-effect in Bulk Glass

Following Morey[192], consider a cube of glass, as shown in figure V.1. Stresses denoted T_x, T_y and T_z are applied and result in dilations (strains) x_x, y_y, z_z along each axis. The influence of the deformation on light propagation can be expressed as

$$\begin{bmatrix} v_x \\ v_y \\ v_z \end{bmatrix} = v + \begin{bmatrix} q & p & p \\ p & q & p \\ p & p & q \end{bmatrix} \begin{bmatrix} x_x \\ y_y \\ z_z \end{bmatrix} \qquad \ldots \text{(V.1)}$$

where $v = \frac{c}{n}$ is the phase velocity of light in the unstressed material; v_x, v_y and v_z are the velocities of light waves having electric field vectors parallel to the axes $\underset{\sim}{x}$, $\underset{\sim}{y}$ and $\underset{\sim}{z}$ respectively. The strain-optical matrix appearing in equation V.1 is particularly simple for glasses, since it contains only two coefficients p and q.

The strains are related to the compressive stresses by

$$\begin{bmatrix} x_x \\ y_y \\ z_z \end{bmatrix} = -\frac{1}{E} \begin{bmatrix} 1 & -\sigma & -\sigma \\ -\sigma & 1 & -\sigma \\ -\sigma & -\sigma & 1 \end{bmatrix} \begin{bmatrix} T_x \\ T_y \\ T_z \end{bmatrix} \qquad \ldots \text{(V.2)}$$

where E is the Young's modulus and σ is the Poisson's ratio.

If n is the refractive index of the un-stressed medium and n_x, n_y and n_z are the refractive indexes for light with electric vectors parallel to the axes, then

$$nv = n_x v_x = n_y v_y = n_z v_z \qquad \ldots (V.3)$$

Thus, for small changes in refractive index

$$\frac{v_x - v}{v} = \frac{n - n_x}{n}$$

$$\frac{v_y - v}{v} = \frac{n - n_y}{n} \qquad \ldots (V.4)$$

$$\frac{v_z - v}{v} = \frac{n - n_z}{n}$$

Combining equations (V.1) to (V.4) gives the relationship between the applied stress and the resulting index change. Thus

$$\begin{bmatrix} \frac{n_x - n}{n} \\ \frac{n_y - n}{n} \\ \frac{n_z - n}{n} \end{bmatrix} = \frac{n}{cE} \begin{bmatrix} (q-2\sigma p) & p-\sigma(p+q) & p-\sigma(p+q) \\ p-\sigma(p+q) & (q-2\sigma p) & p-\sigma(p+q) \\ p-\sigma(p+q) & p-\sigma(p+q) & (q-2\sigma p) \end{bmatrix} \begin{bmatrix} T_x \\ T_y \\ T_z \end{bmatrix} \qquad \ldots (V.5)$$

Two special cases of applied stress are:-

i) <u>isotropic pressure</u> - causes a change in refractive index which is the same in all directions. Substituting $T_x = T_y = T_z = T$ in equation (V.5) gives

$$\Delta n = \frac{n^2}{cE}(1 - 2\sigma)(2p + q)\,T \qquad \ldots (V.6)$$

where $\Delta n = n_x - n = n_y - n = n_z - n$.

The coefficient

$$A = \frac{n^2}{cE}(1 - 2\sigma)(2p + q) \qquad \ldots (V.7)$$

describes the isotropic pressure dependence of refractive index and may be determined from measurements on bulk glass. From the literature[197] the value for silica is

$$A = 0.925 \times 10^{-11}\ Pa^{-1} \qquad \ldots (V.8)$$

ii) <u>uni-axial pressure</u> - causes the glass to become birefringent. Substituting $T_x = T_y = 0$ in equation (V.5) and re-arranging gives

$$n_z - n_x = n_z - n_y = \frac{n^2}{cE}(1+\sigma)(q - p)T_z \quad \ldots (V..9)$$

The strain induced birefringence is defined as

$$B = \frac{n^2}{cE}(1 + \sigma)(q - p) \quad \ldots (V.10)$$

This quantity may also be measured and for pure silica is[191]

$$B = 0.341 \times 10^{-11}\ Pa^{-1} \quad \ldots (V.11)$$

The stress-optical effects p and q can be expressed in terms of A and B using equations (V.7) and (V.10). Substituting the result into equation (V.5) gives

$$\begin{bmatrix} n_x - n \\ n_y - n \\ n_z - n \end{bmatrix} = \frac{1}{3}\begin{bmatrix} A + 2B & A - B & A - B \\ A - B & A + 2B & A - B \\ A - B & A - B & A + 2B \end{bmatrix}\begin{bmatrix} T_x \\ T_y \\ T_z \end{bmatrix} \quad .. (V.12)$$

Note that the stress-optical relationship no longer explicitly depends on the Young's modulus and Poisson's ratio, but is expressed directly in terms of the measured quantities A and B.

V.2 Stress-optical Effect in Glass Fibres

Consider now the propagation of light in an optical fibre. In accordance with convention let $\underset{\sim}{z}$ be the direction of propagation. For a weakly guiding fibre[25], electric vectors are almost perpendicular to the z-axis and therefore only the refractive index parallel to $\underset{\sim}{x}$ need be considered.

The effect of a purely axial stress on the pulse transit time in an optical fibre is considered in Chapter 9. This is usually the dominant stress in cabled fibres since the glass is normally buffered against transverse forces by a soft primary protective jacket, such as a silicone rubber. Thus, if T_z is the applied longitudinal stress and $T_x \simeq T_y \simeq 0$, the change in refractive index, from equation (V.12) is

$$n_x - n = \frac{1}{3}(A - B)T_z \quad \ldots (V.13)$$

The analysis of the effects of longitudinal stress is continued in Chapter 9.

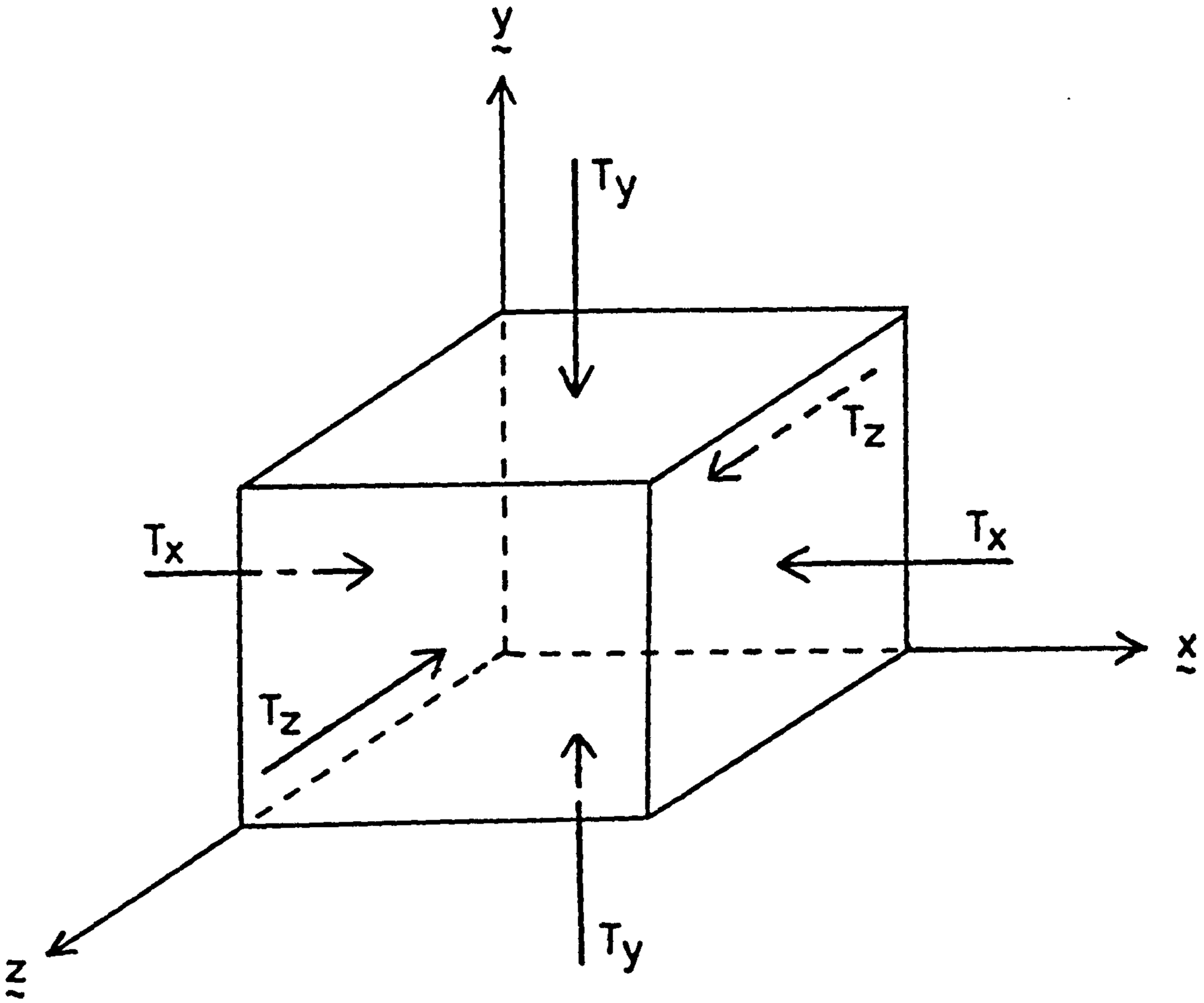

Schematic of a cube of glass subjected to compressive stresses T_x, T_y, T_z.

Figure V.I

APPENDIX VI PUBLICATIONS, CONFERENCE PAPERS AND EXHIBITIONS

The following publications and conference presentations have been the result of work described in this thesis.

VI.1 Publications and Conference Presentations

1. A. J. Conduit, A. H. Hartog, D. N. Payne:
Measurement of longitudinal internal stress in cabled fibres
IEE Colloquium on Measurement Techniques for Optical Fibre Systems, London. Digest No. 1979/33, 3 May 1979.

2. A. H. Hartog, A. J. Conduit, D. N. Payne:
Variation of pulse delay with stress and temperature in jacketed and unjacketed optical fibres
Opt. & Quant. Electron., 1979, 11, 265-273.

3. A. J. Conduit, A. H. Hartog, D. N. Payne:
Residual stress diagnosis in jacketed optical fibres by a pulse delay technique.
Proc. Fifth Europ. Conf. Opt. Commun., Amsterdam 1979.

4. A. J. Conduit, A. H. Hartog, D. N. Payne:
Spectral- and length-dependent losses in optical fibres investigated by a two-channel backscatter technique
Electron. Lett., 1980, 16, 77-78.

5. A. J. Conduit, J. L. Hullett, A. H. Hartog, D. N. Payne:
An optimized technique for backscatter attenuation measurements in optical fibres.
Opt. & Quant. Electron., 1980, 12, 169-178.

6. A. J. Conduit, D. N. Payne, A. H. Hartog:
Optical fibre backscatter-loss signatures: Identification of features and correlation with known defects using the two-channel technique
Proc. Sixth Europ. Conf. Opt. Commun., York 1980.

7. A. H. Hartog, D. N. Payne, A. J. Conduit:
Polarization optical time domain reflectometry: experimental results and application to loss and birefringence measurements in single-mode optical fibres.
Proc. Sixth Europ. Conf. Opt. Commun. (post-deadline session) York 1980.

8. A. J. Conduit, D. N. Payne, A. H. Hartog, M. P. Gold:
Optical fibre diameter variations and their effect on backscatter loss measurements
Electron. Lett., 1981, 17, 308-310.

9. A. J. Conduit, D. N. Payne, A. H. Hartog:
Fibre diameter variations and their effect on backscatter loss measurements
Proc. Third Int. Conf. Integr. Opt. & Opt. Fib. Commun. San Francisco 1981.

10. A. J. Conduit, A. H. Hartog, M. R. Hadley, D. N. Payne, M. P. Gold, R. J. Mansfield, E. J. Tarbox:
High-resolution measurement of diameter variations in optical fibres by the backscatter method
Electron. Lett., 1981, 17, 742-744.

11. A. H. Hartog, D. N. Payne, A. J. Conduit:
Polarization measurements on monomode fibres using optical time-domain reflectometry
IEE Proc. Part H, 1981, 128, 168-170.

VI.2 Exhibitions

The 2-channel backscatter instrument described in Chapter 5 was demonstrated at the British Telecom Exhibition of Optical Fibre Technology as part of a Southampton University Contribution.
The exhibition was held concurrently with the Sixth European Conference on Optical Communication at York, U.K., in September 1980.

APPENDIX VII REFERENCES

1. F. P. Kapron, R. D. Maurer, M. P. Teter:
Theory of backscattering effects in waveguides
Appl. Opt., 1972, 11, 1352-1356.

2. M. K. Barnoski, S. M. Jensen:
Fibre waveguides: a novel technique for investigating attenuation characteristics
Appl. Opt., 1976, 15, 2112-2115.

3. M. K. Barnoski, M. D. Rourke, S. M. Jensen, R. T. Melville:
Optical time domain reflectometer
Appl. Opt., 1977, 16, 2375-2379.

4. S. D. Personick:
Photon probe - an optical-fiber time-domain reflectometer
Bell Syst. Tech. J., 1977, 56, 355-366.

5. E.-G. Neumann:
Optical time domain reflectometer: comment
Appl. Opt., 1978, 17, 1675.

6. E.-G. Neumann:
Theory of the backscattering method for testing optical fibre cables
Electron. Commun. AEÜ, 1980, 34, 157-160.

7. P. DiVita, U. Rossi:
The backscattering technique: its field of applicability in fibre diagnostics and attenuation measurements
Opt. and Quant. Electron., 1980, 11, 17-22.

8. D. B. Keck, R. D. Maurer, P. C. Schultz:
On the ultimate lower limit of attenuation in glass optical waveguides
Appl. Phys. Lett., 1973, 22, 307-309.

9. H. Osanai, T. Shioda, T. Moriyama, S. Araki, M. Horiguchi, T. Izawa, H. Takata:
Effects of dopants on transmission loss of low-OH-content optical fibres
Electron. Lett., 1976, 12, 549-550.

10. S. Kobayashi, N. Shibata, S. Hibata, T. Izawa:
Characteristics of optical fibres in infrared wavelength region
NTT Rev. of Elect. Commun. Labs.,1978, 26, 453-467.

11. T. Edahiro, K. Chida, Y. Omori, H. Ozaki:
Fabrication technique for graded index optical fibres
NTT Rev. of Elect. Commun. Labs., 1979, 27, 165-175.

12. P. Dean, R. J. Bell:
Atomic vibrations in vitreous silica
Faraday Soc. Discussions, Meeting on Vitreous State, Sept. 22-24, 1970, 55-61.

13. P. H. Gaskell., D. W. Johnson:
The optical constants of quartz, vitreous silica and neutron-irradiated vitreous silica
J. Non-Cryst. Solids, 1976, 20, 171-191.

14. D. N. Payne, W. A. Gambling:
A borosilicate-cladded phosphosilicate-core optical fibre
Opt. Comm., 1975, 13, 422-425.

15. H. Ibach, J. E. Rowe:
Electron orbital energies of oxygen on silicon surfaces and of silicon dioxide
Phys. Rev. B., 1974, 10, 710-718.

16. D. B. Keck, P. C. Schultz, F. Zimar:
Attenuation of multimode glass optical waveguides
Appl. Phys. Lett., 1972, 21, 215-217.

17. P. Kaiser, A. R. Tynes, H. W. Astle, A. D. Pearson, W. G. French, R. E. Jaeger, A. H. Cherin:
Spectral losses of unclad vitreous silica and soda-lime silicate fibres
J. Opt. Soc. Am., 1973, 63, 1141-1148.

18. K. J. Beales, J. E. Midwinter, G. R. Newns, C. R. Day:
Materials and fibre for optical transmission systems
Post Off. Elec. Eng. J., 1974, 67, 80-87.

19. D. N. Payne, W. A. Gambling:
Preparation of water-free silica-based optical-fibre waveguide
Electron. Lett., 1974, 10, 335-337.

20. M. Horiguchi, H. Osanai:
Spectral losses of low-OH content optical fibres
Electron. Lett., 1976, 12, 310-312.

21. A. D. Pearson, R. L. Barns, E. A. Chandros, C.M. Melliar-Smith:
Hydroxyl contamination of optical fibres and its control in the MCVD process and
Photochemical purification of reagents used in the MCVD optical process (combined presentation)
Proc. Sixth Europ. Conf. Opt. Commun, York 1980.

22. T. Moriyama, O. Fukuda, K. Sanada, K. Inada, S. Tanaka:
Fabrication of ultra-low content optical fibres with VAD method
Proc. Sixth Europ. Conf. Opt. Commun., York 1980.

23. I. L. Fabelinskii:
'Molecular Scattering of Light'
(Plenum Press, N.Y., 1968).

24. M. Kerker:
'The Scattering of Light and Other Electromagnetic Radiation'
(Academic Press, N.Y., 1969).

25. D. Gloge:
Weakly guiding fibres
Appl. Opt. 1971., 10, 2252-2258.

26. J. P. Dakin, W. A. Gambling:
Theory of scattering from the core of a multimode fibre waveguide.
Opt. Commun., 1974, 10, 195-199.

27. M. H. Reeve, M. C. Brierley, J. E. Midwinter, K. I. White:
Studies of radiative losses from multimode optical fibres
Opt. & Quant. Electron., 1976, 8, 39-42.

28. A. W. Snyder, D. J. Mitchell:
Leaky rays on circular optical fibers
J. Opt. Soc. Am., 1974, 64, 599-607.

29. M. J. Adams, D. N. Payne, F. M. E. Sladen:
Leaky rays on optical fibres of arbitrary (circularly symmetric) index profiles
Electron. Lett., 1975, 11, 238-240.

30. J. J. Ramscov-Hansen, A. Ankiewicz, M. J. Adams:
Attenuation of leaky modes in graded index non-circular multimode fibres
Electron. Lett., 1980, 16, 94-96.

31. R. Olshansky, D. A. Nolan:
Mode-dependent attenuation of optical fibres: excess loss
Appl. Opt., 1976, 15, 1045-1047.

32. D. Gloge:
Bending loss in multimode fibres with graded and ungraded core index
Appl. Opt., 1972, 11, 2506-2513.

33. D. Marcuse:
Losses and impulse response of a parabolic fibre with random bends
Bell Syst. Tech. J., 1973, 52, 1423-1437.

34. W. B. Gardiner:
Microbending loss in optical fibres
Bell Syst. Tech. J., 1975, 54, 457-465.

35. A. R. Tynes, A. D. Pearson, D. L. Bisbee:
Loss mechanisms and measurements in clad glass fibres and bulk glass
J. Opt. Soc. Am., 1971, 61, 143-153.

36. P. Kaiser:
Drawing-induced coloration in vitreous silica fibres
J. Opt. Soc. Am., 1974, 64, 475-481.

37. E. D. Ippen:
Low power quasi-cw Raman oscillator
Appl. Phys. Lett., 1970, 16, 303-305.

38. R. G. Smith:
Optical power handling capacity of low loss optical fibres as determined by stimulated Raman and Brillouin scattering
Appl. Opt., 1972, 11, 2489-2494.

39. R. H. Stolen, E. P. Ippen, A. R. Tynes:
Raman oscillation in glass optical waveguide
Appl. Phys. Lett., 1972, 20, 62-64.

40. E. P. Ippen, R. H. Stolen:
Stimulated Brillouin scattering in optical fibres
Appl. Phys. Lett., 1972, 21, 539-541.

41. R. Plonsey, R. E. Collin:
'Principles and Applications of Electromagnetic Fields'
(McGraw-Hill Inc., N.Y., 1961).

42. D. N. Payne, A. H. Hartog:
Determination of the wavelength of zero material dispersion in optical fibres by pulse-delay measurements
Electron. Lett., 1977, 13, 627-629.

43. D. L. Weinberg:
Absolute intensity measurements in small-angle X-ray scattering
Rev. Sci. Instrum., 1963, 34, 691-696.

44. D. L. Weinberg:
X-ray scattering measurements of long range thermal density fluctuations in liquids
Phys. Lett., 1963, 7, 324-325.

45. D. A. Pinnow, T. C. Rich, F. W. Ostermayer,Jr., M. DiDomenico, Jr.:
Fundamental optical attenuation limits in the liquid and glassy state with application to fibre optical waveguide materials
Appl. Phys. Lett., 1973, 22, 527-529.

46. P. B. O'Connor, J. B. MacChesney, P. V. DiMarcello, P. Kaiser, C. A. Burrus, H. M. Presby, L. G. Cohen:
Large numerical-aperture, germanium-doped fibres for LED applications
Proc. Second Europ. Conf. Opt. Commun., Paris 1976.

47. F. W. Ostermayer,Jr., D. A. Pinnow:
Optimum refractive-index difference for graded-index fibres resulting from concentration-fluctuation scattering
Bell Syst. Tech. J., 1974, 53, 1395-1402.

48. P. Kaiser:
Numerical aperture dependent spectral loss measurements of optical fibres
Proc. Int. Conf. Integr. Opt. & Opt. Fib.Commun., 1977.

49. J. Schroeder, R. Mohr, P. B. Macede, C. J. Montrose:
Rayleigh and Brillouin scattering in K_2O-SiO_2 glasses
J. Am. Ceram. Soc., 1973, 56, 510-514.

50. M. A. Karr, T. C. Rich, M. DiDomenico,Jr.:
Lightwave fibre tap
Appl. Opt., 1978, 17, 2215-2218.

51. S. R. Norman, D. N. Payne, M. J. Adams, A. M. Smith:
Fabrication of single-mode fibres exhibiting extremely low polarization birefringence
Electron. Lett., 1979, 15, 309-311.

52. M. J. Adams, D. N. Payne, C. M. Ragdale:
Birefringence in optical fibres with elliptical cross-section
Electron. Lett., 1979, 15, 298-299.

53. V. Ramaswamy, R. H. Stolen, D. M. Divine, W. Phebel:
Birefringence in elliptically clad borosilicate single-mode fibres
Appl. Opt., 1979, 18, 4080-4084.

54. H. Matsumura, T. Katsuyama, T. Suganuma:
Fundamental study of single polarization fibres
Proc. Sixth Europ. Conf. Opt. Commun., York 1980.

55. A. J. Rogers:
Polarization optical time domain reflectometry
Electron. Lett., 1980, 16, 489-490.

56. A. J. Rogers:
Polarization optical time domain reflectometry: a technique for the measurement of field distributions
Appl. Opt., 1981, 20, 1060-1074.

57. A. H. Hartog, D. N. Payne, A. J. Conduit:
Polarization optical time-domain reflectometry: experimental results and applications to loss and birefringence measurements in single-mode optical fibres
Proc. Sixth Europ. Conf. Opt. Commun. (post deadline session) York 1980.

58. A. H. Hartog, D. N. Payne, A. J. Conduit:
Polarization measurements on monomode fibres using optical time-domain reflectometry
IEE Proc., Part H, 1981, 128, 168-170.

59. R. Olshansky, S. M. Oaks:
Differential mode attenuation measurements in graded-index fibres
Appl. Opt., 1978, 17, 1830-1835.

60. D. Gloge:
Impulse response of clad optical multimode fibres
Bell Syst. Tech. J., 1973, 52, 801-816.

61. D. Marcuse:
'Theory of Dielectric Optical Waveguides'
(Academic Press, N.Y., 1974),173

62. W. A. Gambling, D. N. Payne, H. Matsumura:
Effect of dip in the refractive index profile on the cut-off frequency of a single-mode fibre
Electron. Lett., 1977, 13, 173-175.

63. H. M. Presby:
Axial refractive index depression in preforms and fibres
Fib. & Integr. Opt., 1979, 2, 111-126.

64. P. Kaiser, A. C. Hart, L. L. Blyler, Jr.:
Low loss FEP-clad silica fibres
Appl. Opt., 1975, 14, 156-162.

65. M. Eve, A. M. Hill, D. J. Malyon, J. E. Midwinter,
B. P. Nelson, J. R. Stern, J. V. Wright:
Launching-independent measurements of multimode fibres
Proc. Second Europ. Conf. Opt. Commun., Paris 1976.

66. D. Marcuse:
Derivation of coupled power equations
Bell Syst. Tech. J., 1972, 51, 229-237.

67. W. A. Gambling, D. N. Payne, H. Matsumura:
Mode conversion coefficients in optical fibres
Appl. Opt., 1975, 14, 1538-1542.

68. M. Miyagi, S. Kawakami, M. Ohashi, S. Nishida:
Measurement of mode conversion coefficients and mode dependent losses in multimode fibre
Appl. Opt., 1978, 17, 3238-3244.

69. L. G. Cohen:
Shuttle pulse measurements of pulse spreading in an optical fibre
Appl. Opt., 1975, 14, 1351-1356.

70. L. G. Cohen, S. D. Personick:
Length dependence of pulse dispersion in a long multimode optical fibre
Appl. Opt., 1975, 14, 1357-1360.

71. L. G. Cohen:
Pulse transmission measurements for determining near optimal profile gradings in multimode borosilicate fibres
Appl. Opt., 1976, 15, 1808-1814.

72. I. Nouchi, A. Jacques, L. D'Auria:
Characteristics against length of silicone-clad silica optical fibres
Electron. Lett., 1979, 15, 315-316.

73. M. Eve, P. C. Hensel, D. J. Malyon, B. P. Nelson,
J. R. Stern, J. V. Wright, J. E. Midwinter:
Transmission studies on three graded-index fibre cable links installed in operational ducts
Opt. & Quant. Electron., 1978, 10, 253-265.

74. M. Eve, A. H. Hartog, R. Kashyap and D. N. Payne:
Wavelength dependence of light propagation in long fibre links
Proc. Fourth Europ. Conf. Opt. Commun., Genoa 1978.

75. A. H. Hartog, M. J. Adams, F. M. E. Sladen, D. N. Payne,
A. Ankiewicz:
Comparison of measured and predicted bandwidth of graded-index multimode fibres
IEEE J. Quant. Electron., to be published.

76. S. Sentsui:
Length-addition-law of spliced fibres
Proc. Nat. Conf. IECE, Japan 1979.

77. Y. Kohanzadeh:
Hot splices of optical waveguide fibres
Appl. Opt., 1976, 15, 793-795.

78. D. L. Bisbee:
Splicing silica fibres with an electric arc
Appl. Opt., 1976, 15, 796-798.

79. P. Matthijsse, C. M. DeBlok:
Measurement of splice insertion loss using the back-scattering method
Proc. Fifth Europ. Conf. Opt. Commun., Amsterdam, 1979.

80. P. Matthijsse, C. M. DeBlok:
Field measurement of splice loss applying the back-scattering method
Electron. Lett., 1979, 15, 795-797.

81. P. DiVita, U. Rossi:
Backscattering measurements: Separation of power decay from imperfection contribution
Electron. Lett., 1979, 15, 467-469.

82. D. Gloge, E. A. J. Marcatili:
Multimode theory of graded-core fibres
Bell Syst. Tech. J., 1973, 52, 1563-1579.

83. A. W. Snyder, D. L. Love:
Attenuation coefficient for tunnelling leaky rays in graded fibre
Electron. Lett., 1976, 12, 324-326.

84. K. Petermann:
Leaky mode behaviour of optical fibres with non-circularly symmetric refractive index profile
Electron. Commun. AEÜ, 1977, 31, 201-204.

85. M. J. Adams, D. N. Payne, F. M. E. Sladen:
Splicing tolerances in graded-index fibres
Appl. Phys. Lett., 1976, 28, 524-526.

86. F. V. DiMarcello, J. C. Williams:
Reproducibility of optical fibres prepared by a modified chemical vapor deposition process
Bell Syst. Tech. J., 1978, 57, 1723-1734.

87. E. Brinkmeyer:
Backscattering in single-mode fibres
Electron. Lett., 1980, 16, 329-330.

88. E. Brinkmeyer:
Analysis of the backscattering method for single-mode optical fibres
J. Opt. Soc. Am., 1980, 70, 1010-1012.

89. International Telegraph and Telephone Consultative Committee (CCITT)
VIIth Plenary Assembly - Document 75, Study Group XV - Contribution 370, Recommendation G651 , 1980.

90. R. Olshansky, D. B. Keck:
Pulse broadening in graded-index fibres
Appl. Opt., 1976, 15, 483-491.

91. F. M. E. Sladen, D. N. Payne, M. J. Adams:
Measurement of profile dispersion in optical fibres: a direct technique
Electron. Lett., 1977, 13, 212-213.

92. L. Stensland, G. Borak:
Raman time-domain reflectometry
Proc. Third Int. Conf. Integr. Opt. & Opt. Fib. Commun., San Francisco 1981.

93. A. J. Conduit, J. L. Hullett, A. H. Hartog, D. N. Payne:
An optimized technique for backscatter attenuation measurements in optical fibres
Opt. & Quant. Electron., 1980, 12, 169-178.

94. A. J. Conduit, A. H. Hartog, D. N. Payne:
Spectral- and length-dependent losses in optical fibres investigated by a two-channel backscatter technique
Electron. Lett., 1980, 16, 77-78.

95. A. J. Conduit, D. N. Payne, A. H. Hartog:
Optical fibre backscatter-loss signatures: Identification of features and correlation with known defects using the two-channel technique.
Proc. Sixth Europ. Conf. Opt. Commun., York 1980.

96. A. J. Conduit, D. N. Payne, A. H. Hartog, M. P. Gold:
Optical fibre diameter variations and their effect on backscatter loss measurements
Electron. Lett., 1981, 17, 308-310.

97. A. J. Conduit, D. N. Payne, A. H. Hartog:
Fibre diameter variations and their effect on backscatter loss measurements
Proc. Third Int. Conf. Integr. Opt. & Opt. Fibre Commun., San Francisco 1981.

98. A. J. Conduit, A. H. Hartog, M. R. Hadley, D. N. Payne, M. P. Gold, R. J. Mansfield, E. J. Tarbox:
High-resolution measurement of diameter variations in optical fibres by the backscatter method
Electron. Lett., 1981., 17, 742-744.

99. B. Costa , B. Sordo:
Experimental study of optical fibres attenuation by a modified backscattering technique
Proc. Third Europ. Conf. Opt. Commun., Munich 1977.

100. M. P. Klein, G. W. Barton,Jr:
Enhancement of signal-to-noise ratio by continuous averaging: Application to magnetic resonance
Rev. Sci. Instrum., 1963, 34, 754-759.

101. J. Reichert, J. Townsend:
Gated integrator for repetitive signals
Rev. Sci. Instrum., 1964, 35, 1692-1697.

102. R. R. Ernst:
Sensitivity enhancement in magnetic resonance.
I. Analysis of the method of time averaging
Rev. Sci. Instrum., 1965, 36, 1689-1695.

103. W. G. Clark, A. L. Kerlin:
Solid state gated integrator
Rev. Sci. Instrum., 1967, 38, 1593-1596.

104. J. D. W. Abernethy:
The boxcar detector
Wireless World, December 1970.

105. T. Coor
Signal averaging computers
Industrial Research, May 1972.

106. F. G. Collins, R. Katchinoski:
Boxcar attachment for oscilloscopes useful for low level signals
Rev. Sci. Instrum., 1973, 44, 1178-1181.

107. K. Neelakantan, S. Dottagupta
Analysis of signal-to-noise enhancement of Box-Car averagers
Pramana, 1978, 11, 295-306.

108. E.G. & G. Brookdeal Ltd:
Boxcar Detector 9415/9425 Instruction Manual.

109. E.G. & G. Princeton Applied Research Corporation
Model 162 Boxcar averagers system research manual

110. Teledyne Philbrick Ltd:
Designing high speed data acquisition systems
Applications Bulletin AN-21, 1976.

111. Teledyne Philbrick Ltd:
Specifying and testing sample-hold amplifiers
Applications Bulletin AN-30, 1977.

112. J. L. Hullett, R. D. Jeffrey:
Noise in optical fibre backscatter measurement
Opt. & Quant. Electron., 1981, 13, 117-124.

113. Teledyne Philbrick Ltd:
Specifying and testing analog to digital converters
Applications Bulletin AN-24, 1976.

114. W. K. Bucklen:
A monolithic (single-chip) video A/D converter
SMPTE, 1980, 89, 573-578.

115. W. K. Bucklen:
Digitize with monolithic flash A-D converters
Electronic Design, Sept. 13, 1980, 93-98.

116. L. Walter:
75 MHz A-D converter relies on 8-bit chip with 1 μm line widths
Electronics, Aug.11, 1981, 37-38.

117. B. Paulson:
Television gathers speed on its way from A to D
Broadcast Commun., Aug. & Sept. 1979.

118. T. E. Linnenbrink, D. A. Gradl, G. J. DeWitte, D. N. Metzger, E. K. Hodson, D. R. Thayer, J. W. Balch, C. F. McConaghy:
A one gigasample per second transient recorder
IEEE Trans. Nuc. Sci., 1979, 26, 4443-4449.

119. Tektronix Ltd:
New digitizers for a new decade
Handshake, Spring/Summer 1980, 5, 1, 3-6.

120. L. E. Brennan, S. I. Reed:
Quantization noise in digital moving target systems
IEEE Trans. Aerospace & Electron. Syst., 1980,2,655-658.

121. B. M. Gordon:
Linear electronic analog/digital conversion architectures, their origins, parameters, limitations and applications
IEEE Trans. Circ. & Syst., 1978, 25, 391-418.

122. J. E. Goell:
An optical repeater with high input impedance
Bell Syst. Tech. J., 1974, 53, 629-643.

123. J. L. Hullett, T. V. Muoi:
A feedback amplifier for optical transmission systems
IEEE Trans. Comm., 1976, 24, 1180-1185.

124. S. Moustakas, J. L. Hullett:
Noise modelling for broadband amplifier design
IEE Proc., Part G, 1981, 128, 67-76.

125. P. Healey:
OTDR in monomode fibres at 1.3 μm using a semiconductor laser
Electron. Lett., 1981, 17, 62-64.

126. R. J. Turner:
Preliminary engineering design of digital transmission systems using optical fibre
Post. Off. Elec. Eng. J., 1975, 68, 7-14.

127. RCA Solid State Division:
Optoelectronic Products, Application Note AN-4741.

128. H. Kressel, H. Nelson:
Close confinement gallium arsenide pn junction lasers with reduced optical loss at room temperature
RCA Review, 1969, 30, 106-113.

129. R. D. Jeffrey, J. L. Hullett:
N-point processing of optical fibre backscatter signals
Electron. Lett., 1980, 16, 82-83.

130. E. G. Hanson:
Origin of temperature dependence of microbending attenuation in fibre optic cables
Fib. & Integr. Opt.,1980, 3, 113-148.

131. M. C. Brain:
Responsivity and noise characterization of Ge avalanche photodiode through wavelength range 1.1-1.7 μm.
Electron. Lett., 1979, 15, 821-823.

132. D. R. Smith, R. C. Hooper, I. Garrett:
Receivers for optical communications: A comparison of avalanche photodiodes with PIN-FET hybrids
Opt. & Quant. Electron., 1980, 10, 293-300.

133. K. Ahmad, J. W. Burgess, D. R. Jenkins, A. W. Mabbitt R. Nicklin:
Optimised PIN photodiodes for longer wavelength fibre-optic systems
Proc. Sixth Europ. Conf. Opt. Commun.,York 1980.

134. R. C. Hooper, M. A. Z. Rejman, S. T. D. Ritchie, D. R. Smith, B. R. White:
PIN-FET hybrid optical receivers for longer wavelength optical communications systems
Proc. Sixth Europ. Conf. Opt. Commun., York 1980.

135. K. Kishino, Y. Suematsu, Y. Haya:
Mesa-substrate buried heterostructure GaInAsP/InP injection lasers
Electron. Lett., 1979, 15, 134-136.

136. H. Kawaguchi, K. Takehei Y. Toyoshima, H. Nagai, G. Iwane:
Room temperature C.W. operation of InGaAsP/InP double heterostructure diode lasers emitting at 1.55 μm
Electron. Lett., 1979, 15, 669-670.

137. S. Arai, M. Asada, Y. Suematsu, Y. Itaya, T. Tambun-Ek, K. Kishino:
1.6 μm wavelength GaInAsP/InP BH lasers fabricated by a new process
Proc. Sixth Europ. Conf. Opt. Commun., York 1980.

138. M. Arbranowitz, I. A. Stegan:
'Handbook of Mathematical Functions'
(Dover Publications Inc., 1972).

139. Chromatix CMX-4 Dye-laser and Optical-Parametric Oscillator Instruction Manual.

140. A. H. Hartog:
Wavelength dependent effects in optical fibre waveguides
Ph.D. Thesis, Dept. of Electronics, University of Southampton, May 1981.

141. R. C. Fletcher:
Production and measurement of ultra-high-speed impulses
Rev. Sci. Instrum., 1949, 20, 861-869.

142. M. Eve, P. C. Hensel, D. J. Malyon, B. P. Nelson, J. V. Wright:
Techniques for measuring the transmission properties of optical fibre cables
Post. Off. Elec. Eng. J., 1978, 71, 122-129.

143. K. Okada, K. Hashunoto:
Optical cable fault location using correlation technique
Electron. Lett., 1980, 16, 629-630.

144. M. Ikeda, A. Sugimura, T. Ikegami:
Multimode optical fibres: Steady-state mode exciter
Appl. Opt., 1976, 15, 2116-2120.

145. H. Murata:
Broadband optical cable and connecting
Proc. Second Europ. Conf. Opt. Commun., Paris 1976.

146. A. J. Conduit
Aspects of optical communications
Minithesis, Dept. of Electronics, University of Southampton, April 1979.

147. E. M. Cherry, D. W. Hooper:
'Amplifying Devices and Low-Pass Amplifier Design'
(J. Wiley & Sons, N.Y., 1968).

148. D. B. Keck, A. R. Tynes:
Spectral response of low-loss optical waveguides
Appl. Opt., 1972, 11, 1502-1506.

149. A. R. Tynes:
Measuring loss in optical fibres
Bell Lab. Record, 1972, 50, 302-310.

150. P. Kaiser, H. W. Astle:
Measurement of spectral total and scattering losses in unclad optical fibres
J. Opt. Soc. Am., 1974, 64, 469-474.

151. D. J. Malyon:
Techniques for the measurement of optical fibre insertion loss
B.P.O. Research Dept. Report No. 803, 1979.

152. S. Tanaka, K. Inada, T. Akimoto, M. Kozima:
Silicone-clad fused-silica-core fibre
Electron. Lett., 1975, 11, 153-154.

153. M. Kawachi, M. Horiguchi, A. Kawana, T. Miyashita
OH-ion distribution profiles in rod preforms of high silica optical waveguide
Electron. Lett., 1977, 13, 247-248.

154. M. Horiguchi, M. Kawachi:
Measurement technique of OH-ion distribution profile in rod preform of silica-based optical fibre waveguides
Appl. Opt., 1978, 17, 2570-2574.

155. D. N. Payne, W. A. Gambling
New silica-based low-loss optical fibre
Electron. Lett., 1974, 10, 289-290.

156. J. B. MacChesney:
Preparation of low loss optical fibres using simultaneous vapor phase deposition and fusion
Proc. Tenth Int. Congr. Glass, 1974, 6, 40.

157. I. Sasaki, D. N. Payne, M. J. Adams:
Measurement of refractive-index profiles in optical fibre preforms by spatial filtering technique
Electron. Lett., 1980, 16, 219-221.

158. I. Sasaki, D. N. Payne, R. J. Mansfield, M. J. Adams:
Variation of refractive-index profiles in single-mode fibre preforms measured using an improved high-resolution spatial-filtering technique
Proc. Sixth Europ. Conf. Opt. Commun., York 1980.

159. M. R. Hadley, D. N. Payne, R. J. Mansfield:
Identification of sources of diameter fluctuations in smooth optical fibres by analysis of their spatial power spectrum
Proc. Sixth Europ. Conf. Opt. Commun., York 1980.

160. B. Costa, C. DeBernadi, B. Sordo:
Investigation of scattering characteristics and accuracy of the backscattering technique by wavelength dependent measurements
Proc. Fourth Europ. Conf. Opt. Commun., Genoa 1978.

161. E.G. & G. Inc., Electro-Optics Div., Mass.,U.S.A.:
Silicon Photodiode Applications Note D 3000C-1.

162. H. Melchior:
Detectors for lightwave communications
Physics Today, Nov. 1977, 30, 32-39.

163. H. Melchior, W. T. Lynch:
Signal and noise response of high speed Germanium avalanche photodiodes
IEEE Trans. Electron Devices, 1966, 13, 829-838.

164. R. J. Mansfield:
Southampton University, Private Communication.

165. H. Murata:
Broadband optical cable and connecting
Proc. Second Europ. Conf. Opt. Commun., Paris 1976.

166. C. Kao:
Fibre optics - Worldwide
Telephone Engineer & Management, Sept 1, 1980.

167. R. L. Gallawa, J. E. Midwinter, S. Shimada:
A survey of world-wide optical waveguide systems
Proc.Int.Conf.Integr.Opt. & Opt.Fib.Commun.,Washington 1979.

168. J. E. Midwinter:
Potential broadband services
IEEE Proceedings, 1980, 68, 1321-1327.

169. National Bureau of Standards
Technical Digest-Symp. Opt. Fib. Measurements, 1980
NBS Special Publication 597.

170. Hewlett Packard:
Selected articles on time domain reflectometry applications
Application Note 75, March 1966.

171. L. G. Cohen:
Shuttle pulse measurements of pulse spreading in an optical fibre
Appl. Opt., 1975, 14, 1351-1356.

172. Orionics Inc:
Optical time domain reflectometer
34368 Frontage Rd., Bozeman, Montana, 59715,U.S.A.

173. ITT Components Group:
Optical time domain reflectometer
Opto-Electronics Div., Westfield Mill, Leeds LS13 3HA.

174. P. B. Macedo, J. H. Simmons, J. Olson, R. K. Mohr, M. Samanta, P. K. Gupta, T. A. Litaritz:
Molecular stuffing of Phasil glasses for graded-index optical fibres
Proc. Second Europ. Conf. Opt. Commun., Paris 1976.

175. H.-G. Unger:
'Planar Optical Waveguides and Fibres'
(Clarendon Press, Oxford, 1977) pp 723-727.

176. British Telecom Exhibition of Optical Fibre Technology:
The exhibition was held concurrently with the Sixth Europ. Conf. Opt. Commun, York 1980.

177. J. L. Hullett, R. D. Jeffrey:
Long-range optical-fibre backscatter-loss signatures using two-point processing
Proc. Int. Conf. Integr. Opt. & Opt. Fib. Commun., San Francisco 1981.

178. K. Ohada, K. Hashimoto, T. Shibata, Y. Nagaki:
Optical cable fault location using correlation technique
Electron. Lett., 1980, 16, 629-630.

179. P. Healey:
Pulse compression coding in optical time domain reflectometry
Proc. Seventh Europ. Conf. Opt. Commun.,Copenhagen 1981.

180. W. Eickhoff, R. Ulrich:
Optical frequency domain reflectometry in single mode fibres
Proc. Int. Conf. Integr.Opt. & Opt.Fib.Commun., San Francisco 1981.

181. J. R. Andrews:
Inexpensive diode pulse generator for optical waveguide studies
Rev. Sci. Instrum., 1974, 45, 22-24.

182. RCA Solid State Division, Optoelectronic Products:
Application Note AN-4741.

183. F. Szarka, A. Lightstone, J. Lit, R. Hughes:
A review of biconical taper couplers
Fib. & Integr. Opt., 1981, 3, 285-298.

184. Canstar Communications:
1240 Ellesmere Rd, Scarborough, Ontario, Canada M1P2X4.

185. K. Daikoku, R. Sugimura:
Direct measurements of wavelength dispersion in optical fibres - difference method
Electron. Lett., 1978, 14, 149-151.

186. C. T. Chang, J. A. Cassaboom, H. F. Taylor:
Fibre-optic delay line devices for RF signal processing
Electron. Lett., 1977, 13, 678-680.

187. M. Johnson, R. Ulrich:
Fibre-optical strain guage
Electron. Lett., 1978, 14, 432-433.

188. E. F. Anderson:
Temperature effects on dispersion and propagation delay in multifibre cables
Proc. Sixth Europ. Conf. Opt. Commun., York 1980.

189. 'American Institute of Physics Handbook'
(McGraw-Hill, N.Y., 1972) pp 4-138.

190. R. Brückner:
Properties and structure of vitreous silica, Part I
J. Non-Crystl. Solids,1970, 5, 123-175.

191. W. Primak, D. Post:
Photoelastic constants of vitreous silica and its elastic coefficient of refractive index
J. Appl. Phys. ,1959, 30, 779-788.

192. G. W. Morey:
'Properties of Glass'
(Rheinhold Publishing Corporation, N.Y., 1938).

193. S. Gross (Editor):
'Modern Plastics Encyclopedia'
(McGraw-Hill, N.Y., 1969).

194. L. E. Nielsen:
'Mechanical Properties of Polymers'
(Rheinhold Publishing Corporation, N.Y., 1962).

195. R. M. Ogorkiewicz:
'Engineering Properties of Thermoplastics'
(J. Wiley & Sons Ltd., N.Y., 1970).

196. N. G. McCrum, B. E. Read, G. Williams:
'Anelastic and Dielectric Effects in Polymeric Solids'
(J. Wiley & Sons Ltd., N.Y., 1967).

197. K. Vedam, E. D. D. Schmidt, R. Roy:
Nonlinear variation of refractive index of vitreous silica with pressure to 7 kbars
J. Am. Ceram. Soc., 1966, 49, 531-535.